Biochemical and structural characterization of *Myxococcus xanthus* Frz chemosensory receptor complex

विद्या वाचस्पति की
उपाधि की अपेक्षाओं की आंशिक पूर्ति में प्रस्तुत शोध प्रबंध

A thesis submitted in partial fulfillment of the requirements of the degree of Doctor of Philosophy

द्वारा / By
अपूर्ब दास/ Apurba Das

पंजीकरण सं. / Registration No.:
२०१९३६४०/ 20193640

शोध प्रबंध पर्यवेक्षक / Thesis Supervisor:

डॉ. गायत्री पनांघट/ Dr Gayathri Pananghat



भारतीय विज्ञान शिक्षा एवं अनुसंधान संस्थान पुणे
INDIAN INSTITUTE OF SCIENCE EDUCATION AND RESEARCH PUNE
2026

CERTIFICATE

Certified that the work incorporated in the thesis entitled **"Biochemical and structural characterization of *Myxococcus xanthus* Frz chemosensory receptor complex"** submitted by **Apurba Das** was carried out by the candidate, under my supervision. The work presented here or any part of it has not been included in any other thesis submitted previously for the award of any degree or diploma from any other University or institution.



Dr. Gayathri Pananghat

Date: 19.3.2026

Declaration by Student

Name of Student: Apurba Das

Reg. No.: 20193640
Thesis Supervisor(s): Dr. Gayathri Pananghat

Department: Biology
Date of joining program: 1 August 2019

Date of Pre-Synopsis Seminar: 9 July 2025

Title of Thesis: Biochemical and structural characterization of *Myxococcus xanthus* Frz chemosensory receptor complex

I declare that this written submission represents my idea in my own words and where others' ideas have been included; I have adequately cited and referenced the original sources. I declare that I have acknowledged collaborative work and discussions wherever such work has been included. I also declare that I have adhered to all principles of academic honesty and integrity and have not misrepresented or fabricated or falsified any idea/data/fact/source in my submission. I understand that violation of the above will be cause for disciplinary action by the Institute and can also evoke penal action from the sources which have thus not been properly cited or from whom proper permission has not been taken when needed.

The work reported in this thesis is the original work done by me under the guidance of Dr. Gayathri Pananghat.



Apurba Das

Date: 19.3.2026

Declaration by Student

Thesis editing using artificial intelligence:

I declare that the use of Generative AI in this thesis did not extend beyond what is described in Section 4.6.1 of the ‘Guidelines for Generative AI usage at IISER Pune’, and accordingly, no attribution is required.

Grammarly and formalizer subroutine in goblin.tools were used to edit and improve text of some sections of the thesis.



Apurba Das

Date: 19.3.2026

Acknowledgements

I express my deepest gratitude to my supervisor, Dr. Gayathri Pananghat, for her continuous support, keen interest, and invaluable guidance. I am truly thankful for the opportunity to work in her laboratory. Her support and guidance have been instrumental in shaping my research, and her critical insights have allowed me to grow as a researcher during the course of my PhD work.

I am deeply grateful to my collaborators Dr. Emilia Mauriello and Prof. Ben Luisi. I thank Dr. Emilia Mauriello and her group for their collaboration in *in vivo* studies. I thank Prof. Ben Luisi for hosting me in his laboratory, where I had the opportunity to carry out cryoEM studies.

I sincerely thank my Research Advisory Committee (RAC) members, Dr. Jeetender Chugh, Dr. Janesh Kumar and Prof. M. S. Madhusudhan, for their insights and inputs during our meetings. I also thank Prof. Saikrishnan Kayarat for valuable insights during lab group meetings.

I gratefully acknowledge the financial support provided by CSIR, India, for my PhD fellowship. I am also grateful to DBT, India, for financial support, and to the SPARC grant for providing the opportunity and funding for my travel and accommodations during my stay at Cambridge.

This research would not have been possible without the facilities and instruments at IISER Pune. I would like to thank the IISER Pune Biology office, the academic office, and the housekeeping staff for their daily assistance with lab-related and official procedures.

A special thanks to the Frz group, both past and present members: Dr. Mutum Yaikhomba, Dr. Jaya Sharma, Jazleena P J, Meenakshi PV, Punam Pawara, Shefali Sonarkar, Tiyasa Bain, Shankar, Achyutan, Hari Sunder, Abrar Bhat, Nandini Majumdar and Prerna Gupta for their hard work, assistance and insightful discussions.

I thank the following facilities for assistance with cryoEM or crystal diffraction data collection: Cryo TEM Pune BioCluster facility; National Electron Cryo-Microscopy Facility NCBS Bangalore; Cryo-Electron Microscopy Facility CCMB Hyderabad; Cryo-Electron Microscopy Facility IIT Delhi; Cryo-Electron Microscopy Facility, Dept of Biochemistry, Cambridge

University; Elettra-Synchrotron Trieste and Raja Ramanna Centre for Advanced Technology Indore.

I am very thankful to the past and present lab members: Vani, Sukanya, Mrinmayee, Joyeeta, Soumyajit, Puja, Rinku, Saurabh, Shivang, Nandini, Nikhil and Omkar. They have always taken the time to assist me in troubleshooting my experiments, to listen to my ideas and hypotheses, and to make my lab days enjoyable and memorable. Their insightful discussions and constructive feedback have significantly contributed to the progress of my work. They have provided me with memories that I will treasure for a lifetime.

I am thankful to all members of Saikrishnan Lab and Jayant Lab for their help with troubleshooting experiments and insightful discussions, especially Mahesh, Om, Vishal, Vinayak, Akhilesh, Rushik and Suman.

I thank my supervisor, Dr. Gayathri, and my lab mates Rinku, Tiyasa, Nikhil, Suyog and Nandini for proofreading my thesis and suggesting improvements.

To my friends and batchmates, especially Madhu, Arnab, Atreyi, Raunak, Pooja, and Ankit, thank you for your advice, suggestions, support and encouragement during this journey.

Finally, and most importantly, I wish to thank my family. I am grateful to my parents, Mr. Ashis Kumar Das and Mrs. Sumita Das, and my sister, Arpita, for their unconditional love, encouragement, motivation and support.

Apurba

Table of contents

List of figures		7 – 9
List of tables		9
List of abbreviations		10 – 11
Abstract		12
Synopsis		13 – 18
Chapter 1	**Introduction: Chemotaxis in Bacteria**	19 – 53
1.1	Background	20 – 21
1.2.	Bacterial motility by 'run' and 'tumble'	21 – 24
1.3.	Chemosensory receptors: methyl-accepting chemotaxis proteins	24 – 25
1.4.	Phosphotransfer signalling cascade by histidine kinase	25 – 26
1.5.	Sensory adaptation	26 – 29
1.6	Gain in signal	29 – 30
1.7	Architecture of chemosensory complex	30 – 33
1.8	Diversity in chemosensory systems	33 – 35
1.9	Diversity in chemosensory arrays	35 – 37
1.10	Concluding remarks and motivation	38 – 41
1.11	References	42 – 53
Chapter 2	**Biochemical characterization of cytoplasmic FrzCD chemosensory receptor from *M. xanthus***	54 – 83
2.1	Introduction	55 – 59
2.2	Materials and Methods	60 – 64
2.2.1	Domain architecture prediction for FrzCD	60
2.2.2	Bioinformatics analysis and modelling of FrzCD	60 – 61
2.2.3	Cloning	61
2.2.4	Protein purification	61 – 62
2.2.5	Circular dichroism spectroscopy	62
2.2.6	Fluorescence anisotropy	62 – 63
2.2.7	Electrophoretic mobility shift assay (EMSA)	64
2.3	Results	65 – 74
2.3.1	Domain organization of FrzCD consists of a DNA-binding helix, di-HAMP domains and a methyl-accepting domain	65 – 68

2.3.2	Homology model of FrzCD confirms an elongated structure	68
2.3.3	Standardization of EMSA for small DNA fragments	68
2.3.4	DNA-binding properties of FrzCD resemble a leucine zipper domain	71 – 72
2.3.5	Deletion of MA domain of FrzCD affects supershift in EMSA with longer DNA	73 – 74
2.4	Discussion	75 – 78
2.5	Acknowledgements	79
2.6	References	79 – 83
Chapter 3	**Diversity of HAMP and ligand-binding domains in different MCP heptad classes**	84 - 109
3.1	Introduction	85 – 89
3.2	Methods	90 – 92
3.2.1	Data Source	90
3.2.2	Classification of MCPs into heptad classes	90 – 91
3.2.3	Identification of HAMP domains	92
3.3	Results and Discussion	93 – 101
3.3.1	Prevalence of different MCP heptad classes in membrane-bound and cytoplasmic MCPs	93 – 94
3.3.2	HAMP domain is predominantly present in membrane-bound MCPs	94 – 95
3.3.3	Poly-HAMP MCPs mostly have concatenated HAMP domains	97
3.3.4	Not all MCPS possess an exclusive LBD	97 – 98
3.3.5	LBDs are either membrane-bound or cytoplasmic depending on the diffusion and intracellular accessibility features of the ligand	99
3.4	Conclusions	102 – 103
3.5	References	104 – 109
Chapter 4	**Regulation of cytoplasmic chemosensory cluster formation by adaptor proteins**	110 – 143
4.1	Introduction	111 – 115
4.2	Materials and Methods	116 – 120
4.2.1	Cloning	116
4.2.2	Purification of receptor-adaptor complex	118 – 119

4.2.3	Mass photometry of purified receptor-adaptor complexes	119
4.2.4	Pull-down assays	120
4.2.5	Electrophoretic mobility shift assay	120
4.2.6	*In vitro* competition assay	120
4.3	Results	122 – 134
4.3.1	Adaptor protein FrzA forms a stable complex with FrzCD	122
4.3.2	FrzA interacts at the signalling tip of dimeric FrzCD	122 – 123
4.3.3	FrzA and FrzB interact at same interface on FrzCD	124 – 125
4.3.4	Hydrophobic and salt-bridge interactions mediate receptor-adaptor complexes	128 – 130
3.4.5	Receptor-adaptor complex is a dynamic assembly	132 – 134
4.4	Discussion	135 – 138
4.5	Acknowledgements	139
4.6	References	139 – 143
Chapter 5	**Structure of receptor-adaptor complex suggests presence of an asymmetric interface at the signalling tip**	144 – 172
5.1	Introduction	145 – 149
5.2	Materials and Methods	150 – 154
5.2.1	CryoEM Sample Preparation and Data Acquisition	150
5.2.2	CryoEM data processing and modelling	151 – 152
5.3	Results	155 – 164
5.3.1	CryoEM trials and observation	155
5.3.2	Structure of receptor-adaptor complexes	156 – 157
5.3.3	Glycine hinge contributes to a curved structure of the MCP coiled-coil domain	160 – 162
5.3.4	Conformational changes between $FrzCD^{\Delta DB}$-FrzA and $FrzCD^{\Delta DBH2}$-FrA complexes	162 – 163
5.3.5	Flexibility of di-HAMP domains	163 – 164
5.4	Discussion	165 – 168
5.5	Acknowledgements	169
5.6	References	169 – 173
Chapter 6	**Conclusions and Future Prospects**	174 – 180

6.1	Summary of major findings	175 – 178
6.2	Future prospects	178 – 179
6.2.1	Co-evolution studies on interface residues at receptor-adaptor complex	178
6.2.2	Mechanism of signal transduction in FrzCD	178
6.2.3	Significance of asymmetric interface on FrzCD	179
6.2.4	*In vitro* reconstitution and structure of CSU	179
6.3	References	179 – 180

List of figures

Figure 1.1 Observation of bacterial chemotaxis.	21
Figure 1.2 Motility is mediated by flagellar rotation in *E. coli.*	22
Figure 1.3 'Run' and 'Tumble' in *E. coli*.	23
Figure 1.4 Sensory adaptation of chemosensory systems.	25
Figure 1.5 Che pathway in *E. coli.*	27
Figure 1.6 Signalling adaptation of chemoreceptors by interplay between methyltransferase 'CheR' and methylesterase 'CheB'.	28
Figure 1.7 Architecture and significance of chemosensory complex.	31
Figure 1.8 Structural organization of chemosensory arrays.	33
Figure 1.9 Chemoreceptors from *E. coli*.	34
Figure 1.10 Alternative chemosensory arrays.	36
Figure 1.11 Alternative chemosensory arrays *in vivo*.	37
Figure 1.12 Chemosensory arrays resolved using CryoET.	38
Figure 1.13 Frz pathway in *M. xanthus*.	40
Figure 2.1 Social life cycle of *M. xanthus* involves complex coordinated group behaviour to effectively manage nutrient availability	56
Figure 2.2 Motility in *E. coli* and *M. xanthus*.	57
Figure 2.3 Frz chemosensory system of *M. xanthus* is homologous to the Che pathway from *E. coli*.	58
Figure 2.4 Workflow for generating a homology model of FrzCD dimer.	60
Figure 2.5 FrzCD has an N-terminal DNA-binding domain with conserved positively charged residues.	66
Figure 2.6 Domain architecture of FrzCD.	67
Figure 2.7 Homology model of FrzCD.	69
Figure 2.8 Standardization of EMSA for small DNA fragments.	70
Figure 2.9 FrzCD binds short lengths of double-stranded or single-stranded DNA.	72
Figure 2.10 MA-domain deletion construct does not exhibit a supershift upon binding longer lengths of DNA, unlike wild-type FrzCD.	73
Figure 2.11 Model for the regulation of oligomerization and signalling by HAMP domains.	76

Figure 3.1 Domains and features of a methyl-accepting chemotaxis protein.	86
Figure 3.2 Schematic representation of the workflow for the classification of MCPs and identification of the HAMP domain.	90
Figure 3.3 Representative alignment showing classification of MCPs into heptad classes and identification of HAMP domains.	91
Figure 3.4 Classification of MCPs into different classes.	93
Figure 3.5 Prevalence and distribution of HAMP domains.	95
Figure 3.6 Distribution of HAMP domains in different MCP heptad classes.	96
Figure 3.7 Distribution of LBDs across MCPs.	98
Figure 3.8 Distribution of LBDs across different MCP classes.	101
Figure 4.1 *M. xanthus* Frz chemosensory system.	111
Figure 4.2 FrzB lacks β4 and β5 in subdomain 2.	113
Figure 4.3 Standardization of receptor-adaptor complex formation.	121
Figure 4.4 Purification strategy for receptor-adaptor complex.	123
Figure 4.5 FrzCD-FrzA forms a more stable complex than FrzCD-FrzB.	124
Figure 4.6 Mass estimation of receptor adaptor complexes.	125
Figure 4.7 Interface of receptor-adaptor complex from AlphaFold3 predicted models.	126
Figure 4.8 FrzA and FrzB interact at the signalling tip of FrzCD**.**	127
Figure 4.9 $FrzCD^{\Delta 261\text{-}267_\Delta 286\text{-}292}$ (FrzCD*) formed a stable dimer and shows DNA binding in mobility shift assay	128
Figure 4.10 Hydrophobic interactions at receptor-adaptor interaction interface.	129
Figure 4.11 Salt-bridge interactions between FrzCD and FrzA.	130
Figure 4.12 Salt-bridge interactions between FrzCD and FrzB.	131
Figure 4.13 FrzA interacts with different Frz signalling states dictated by HAMP domain.	132
Figure 4.14 Receptor-adaptor complex is a dynamic assembly.	133
Figure 4.15 Mechanism of regulation of chemosensory array formation by FrzA and FrzB.	137
Figure 5.1 Core signalling unit of chemosensory array and regulation of signal transduction by HAMP domain in MCPs.	146
Figure 5.2 Cryo-electron tomography studies of chemosensory arrays.	147
Figure 5.3 AlphaFold3 predicted models of receptor adaptor complexes.	152

Figure 5.4 Workflow for processing of dataset of FrzCD$^{\Delta DBH2}$-FrzA complex in CryoSPARC.	153
Figure 5.5 Workflow for processing of dataset of FrzCD$^{\Delta DBH2}$-FrzA complex in CryoSPARC.	154
Figure 5.6 Representative cryoEM micrographs of receptor-adaptor complexes.	156
Figure 5.7 Atypical clusters observed for receptor-adaptor complex.	157
Figure 5.8 CryoEM density map of receptor-adaptor complex.	158
Figure 5.9 Structure of receptor-adaptor complex.	159
Figure 5.10 Glycine hinge contributes to the curvature of FrzCD.	160
Figure 5.11 Curvature of FrzCD dimer.	161
Figure 5.12 Conformational changes in receptor-adaptor complexes.	163
Figure 5.13 3D classification of FrzCD$^{\Delta DB}$-FrzA electron density at a filter resolution of 8 Å reveals movement of the HAMP1 domain.	164
Figure 5.14 Model showing asymmetric interface of FrzCD which might result in a preferential FrzA binding interface at concave side and FrzE binding or oligomerization at convex interface.	167

List of tables

Table 2.1 List of DNA sequences used for EMSA.	64
Table 3.1 Prevalence and distribution of LBDs between Cy-MCPs and M-MCPs.	100
Table 4.1 Plasmids used in this study.	116 - 117
Table 4.2 Primers used for restriction-free cloning.	117 - 118
Table 5.1 CryoEM samples and data collection parameters	151

List of Abbreviations

Abbreviation	Full form
°C	Degree Celsius
µg	Microgram
µL	Microliter
µM	Micromolar
µm	Micrometre
Å	Angstrom
BCA	Bicinchoninic Acid
bp	Base pair
CCW	counter-clockwise
CryoEM	Cryogenic electron microscopy
CryoET	Cryogenic electron tomography
CSS	Chemosensory system
CSU	Core signalling unit
CV	Column volume
CW	clockwise
DB	DNA-binding
DNA	Deoxyribonucleic acid
dsDNA	Double stranded deoxyribonucleic acid
EDTA	Ethylenediaminetetraacetic acid
EMSA	Electrophoretic mobility shift assay
EtBr	Ethidium bromide
HAMP	histidine kinase, adenylyl cyclase, MCP, and phosphatase
HEPES	4-(2-hydroxyethyl)-1-piperazineethanesulfonic acid
IAA	Isoamyl alcohol
iPTM	Interface predicted template modelling
KC	Kinase control region/module
K_D	Dissociation constant
kDa	Kilo Dalton
LB	Luria Bertani
LBD	Ligand-binding domain
MA	Methyl-accepting
MCP	Methyl-accepting chemotaxis protein
mL	Millilitre
MW	Molecular weight
NaCl	Sodium chloride
Ni-NTA	Nickel nitrilotriacetic acid
nm	Nanometre
PAE	Predicted aligned error
PAGE	Polyacrylamide gel electrophoresis
PCR	Polymerase chain reaction
pLDDT	Predicted local distance difference test
pTM	Predicted template modelling
RMSD	Root mean square deviation

SDS	Sodium dodecyl sulphate
SEC	Size exclusion chromatography
ssDNA	Single strand deoxyribonucleic acid
TEM	Transmission electron microscopy
TM	transmembrane
Tris	Tris(hydroxymethyl)aminomethane

Abstract

In bacterial chemotaxis, methyl-accepting chemotaxis proteins (MCPs) detect environmental cues and initiate a phosphorelay signal. In *Myxococcus xanthus*, the Frz pathway regulates motility in response to these cues. MCPs form organized hexagonal arrays on the bacterial membrane, composed of receptors, adaptor proteins, and histidine kinase. These arrays amplify, integrate, and transmit signals cooperatively, but the precise mechanism of signal propagation remains unclear.

Unlike canonical membrane-bound MCP arrays, Frz pathway has a cytoplasmic MCP FrzCD, which uses the nucleoid as a scaffold for oligomerization. In *M. xanthus*, FrzA and FrzB are adaptor proteins linking FrzCD to the histidine kinase FrzE. We identified di-HAMP domains between the DNA-binding and signalling domains of FrzCD. *In vitro*, the signalling domain promotes the stable oligomerization of FrzCD in the presence of DNA. The di-HAMP domains influence DNA binding and regulate FrzCD oligomerization. Together with *in vivo* studies, we found that the di-HAMP domains control nucleoid array formation and regulates downstream signalling, influencing bacterial motility and development. To understand the significance of di-HAMP domains observed in FrzCD and identify a possible signalling input module in FrzCD, we analyzed MCP sequences from the Pfam database. We observed that cytoplasmic receptors predominantly lacked HAMP domains and identified the prevalence of certain LBDs for cytoplasmic MCPs that can sense small diffusible molecules or intracellular metabolites.

Next, we reconstituted the receptor-adaptor complex *in vitro*. Through cryoEM studies of the FrzCD-FrzA complex, combined with AlphaFold-generated models, we have identified the interacting interface. Mutational analysis confirmed that hydrophobic and salt-bridge interactions mediate receptor-adaptor complexes. FrzA and FrzB interact at the same interface on FrzCD, but FrzCD-FrzA forms a more stable complex than FrzCD-FrzB. This may explain a mechanism for regulating the number and size of clusters on the nucleoid. Additionally, the dimeric receptor in the complex has a curvature mediated by a glycine hinge. We believe that the curvature induces an asymmetric interface on the dimeric FrzCD signalling tip, potentially resulting in separate preferred binding sites for adaptor proteins, histidine kinase or oligomerization. Interestingly, we observed a rotational shift of the adaptor protein at the signalling tip in the absence of HAMP2 domain, which suggests a mechanism of signal transduction in chemosensory complexes. Our work supports that this cytoplasmic chemosensory system can serve as a model for studying the mechanism of structural changes in signal transduction within bacterial chemosensory complexes.

Synopsis

Biochemical and structural characterization of *Myxococcus xanthus* Frz chemosensory receptor complex

Name: Apurba Das

Reg. No.: 20193640

Thesis Supervisor: Dr. Gayathri Pananghat

Date of joining program: 1 August 2019

Chemosensory signalling in motile bacteria enables the temporal sensing of environmental cues to track spatial gradients of signals in the environment, thereby biasing motility modules to facilitate the exploration of favourable environments *(Hazelbauer, 2012; Wadhams & Armitage, 2004)*. Chemoreceptors perceive signals, and together with adaptor protein and histidine kinase, form the core signalling unit (CSU) *(Li et al., 2011)*. A phosphorelay cascade initiated by the CSU regulates motility *(Parkinson et al., 2015)*. The signalling pathway and the architecture of arrangement of CSUs into hexagonal arrays are conserved in bacteria and archaea *(Gumerov et al., 2021; Briegel et al., 2015, 2012, 2009)*. Such architecture plays a key role in signal integration, amplification and cooperativity *(Piñas et al., 2022, 2016; Li & Hazelbauer, 2014; Sourjik & Berg, 2004)*. Limited by resolution from structural studies of mostly membrane-bound bacterial chemosensory complexes and arrays *(Riechmann & Zhang, 2023)*, the mechanisms involved in signal detection and transduction that regulate kinase activity, methylation adaptation of receptor in signalling regulation, as well as cooperative signal amplification within chemosensory arrays, are not yet fully understood.

In our work we studied a novel cytoplasmic Frz chemosensory complex from *M. xanthus*, which forms chemosensory clusters on the nucleoid *(Guiseppi et al., 2019; Moine et al., 2017)* and regulates polarity reversals in the bacterium *(Bustamante et al., 2004)*. Our motivation was to reconstitute this soluble chemosensory complex *in vitro* for structural studies to investigate the mechanism of signal transduction in chemosensory macromolecular complexes. This thesis is divided into six chapters with specific aims and objectives as discussed below:

Chapter-wise summary:

Chapter 1. Introduction: Chemotaxis in Bacteria

This chapter provides an overview of our current understanding of bacterial chemotaxis signalling pathways. It briefly summarises key historical discoveries that have shaped our understanding of bacterial movement, the molecular mechanisms behind "run and tumble" motility, the proteins that regulate the pathway and result in sensory adaptation. Additionally, the chapter discusses the architecture and diversity of protein assemblies into macromolecular complexes that play essential roles in signal integration, amplification, and cooperativity within chemosensory systems. Overall, this chapter offers readers a concise background on bacterial chemotaxis, establishing foundational concepts for the subsequent chapters.

Chapter 2. Biochemical characterization of cytoplasmic FrzCD chemosensory receptor from *M. xanthus*

Here we characterized a novel cytoplasmic chemosensory complex from *Myxococcus xanthus* that forms clusters on the nucleoid. Very few cytoplasmic chemosensory systems (CSSs) are characterized to date. The domain architecture of the receptor FrzCD was initially characterized using multiple sequence alignment and homology modelling. FrzCD has an N-terminal DNA binding domain connected to the coiled-coil signalling domain by di-HAMP domains. We showed that the signalling domain stabilizes higher-order oligomeric assemblies upon DNA binding. Di-HAMP domains were found to influence DNA binding and cluster formation on nucleoid followed by regulation of downstream signalling in the bacterium. The HAMP domains were found to regulate group motility and development in the bacterium. A rotation model of the coiled-coil signalling domain regulated by DNA binding and di-HAMP domains was proposed as a mechanism of signalling regulation in the bacterium. Thus, this chapter highlights that HAMP domains of cytoplasmic MCPs may play a role beyond signal transduction between sensory and output domains, and might regulate architecture of assemblies of CSSs.

Chapter 3. Diversity of HAMP and Ligand-binding domains in different MCP heptad classes

We looked into the diversity of HAMP and ligand-binding domains (LBDs) in different receptor heptad classes, as well as any preferences between membrane-bound and cytoplasmic

receptors. We wanted to understand the prevalence of multiple HAMP domains in MCPs and the significance of the observation of di-HAMP domains in FrzCD. Additionally, we aimed to identify a sensory input module based on trends of ligand-binding domains in MCPs. We did not identify any MCP with an architecture and DNA binding domain similar to FrzCD. We observed that cytoplasmic receptors predominantly lack HAMP domains and do not belong to higher heptad MCP classes. We noticed the prevalence of certain LBDs for cytoplasmic MCPs that can sense small diffusible molecules or intracellular metabolites. FrzCD did not harbour canonical LBDs, and we think FrzCD may detect intracellular signals, such as changes in osmolarity or small, diffusible molecules like short-chain alcohols.

Chapter 4. Regulation of cytoplasmic chemosensory cluster formation by adaptor proteins

Next, we reconstituted receptor-adaptor complex *in vitro*. Both the adaptor proteins in this CSS bind to the same interface on the FrzCD signalling tip, and they form a dynamic assembly. We identified key residues that mediate hydrophobic and salt-bridge interactions between the receptor and adaptor. Between the two adaptors, we observed FrzCD-FrzA complex was more stable than FrzCD-FrzB complex. We proposed a model where there is division of labour between the two adaptor proteins, FrzA promoting array formation while FrzB inhibiting array formation, thereby regulating the size and distribution of cluster formation on the nucleoid.

Chapter 5. Structure of receptor-adaptor complex suggests presence of an asymmetric interface at the signalling tip

In this chapter, we performed cryoEM studies on receptor-adaptor complexes. The structure was solved to a resolution of 6.13 Å. FrzA molecules interact at the signalling tip of dimeric FrzCD. The structure confirmed the presence of N-terminal di-HAMP domains, which is continuous with the coiled-coil signalling domain. The HAMP1 domain exhibits significant flexibility, likely due to a helical linker between HAMP1 and HAMP2. The receptor displays a curvature induced by the glycine hinge, resulting in an asymmetric interface at the signalling tip. Our observations indicate that FrzA binding is preferentially present at the concave interface, with a more pronounced density of FrzA at this site. We propose a model in which asymmetry at the signalling tip of dimeric FrzCD might result in preferential binding of adaptor protein FrzA at the concave interface. The convex interface might prefer binding of histidine kinase FrzE or support oligomerization of the receptor. Interestingly, we observed a rotational shift of FrzA at the signalling tip in absence of the HAMP2 domain, possibly due to

conformational changes in the coiled-coil domain. This suggests a mechanism of signal transduction in receptor adaptor complexes.

Chapter 6. Conclusions and Future Prospects

This chapter summarizes major findings and conclusions from my PhD work. Our results show that FrzCD chemosensory assembly can act as a model for structural studies to understand the mechanism of signal transduction in CSSs. Future experimental plans in this regard are discussed.

List of publications

- Jazleena PJ*, **Das A*,** Guiseppi A*, Debard F, Sharma J, Yaikhomba M, Mignot T, Mauriello EM, Gayathri P. Di-HAMP domains of a cytoplasmic chemoreceptor modulate nucleoid array formation and downstream signalling. mBio, 2025
- Jani J, Mochi J, Shah S, **Das A**, Patel D, Pananghat G, Pappachan A. Unravelling the plasticity of substrate recognition by Staphylococcus aureus lysyl-tRNA synthetase and its implications for misacylation. FEBS J. 2025

  * Denotes equal contribution

Manuscripts under preparation:

- **Das A**, Sharma J, Gayathri P. Comprehensive analysis of diversity, distribution and prevalence of HAMP and Ligand-binding domains in different MCP classes.
- **Das A**, Bain T, Mauriello EM, Gayathri P. Regulation of cytoplasmic chemosensory cluster formation by adaptor proteins.
- **Das A**, Bain T, Luisi BF, Gayathri P. Mechanism of signal transduction in chemosensory receptor-adaptor complexes.

References

1. Briegel, A., Li, X., Bilwes, A. M., Hughes, K. T., Jensen, G. J., & Crane, B. R. (2012). Bacterial chemoreceptor arrays are hexagonally packed trimers of receptor dimers networked by rings of kinase and coupling proteins. *Proceedings of the National Academy of Sciences*, *109*(10), 3766–3771. https://doi.org/10.1073/pnas.1115719109

2. Briegel, A., Ortega, D. R., Huang, A. N., Oikonomou, C. M., Gunsalus, R. P., & Jensen, G. J. (2015). Structural conservation of chemotaxis machinery across Archaea and Bacteria. *Environmental Microbiology Reports*, *7*(3), 414–419. https://doi.org/10.1111/1758-2229.12265

3. Briegel, A., Ortega, D. R., Tocheva, E. I., Wuichet, K., Li, Z., Chen, S., Müller, A., Iancu, C. V., Murphy, G. E., Dobro, M. J., Zhulin, I. B., & Jensen, G. J. (2009). Universal architecture of bacterial chemoreceptor arrays. *Proceedings of the National Academy of Sciences*, *106*(40), 17181–17186. https://doi.org/10.1073/pnas.0905181106

4. Gumerov, V. M., Andrianova, E. P., & Zhulin, I. B. (2021). Diversity of bacterial chemosensory systems. *Current Opinion in Microbiology*, *61*, 42–50. https://doi.org/10.1016/j.mib.2021.01.016

5. Hazelbauer, G. L. (2012). Bacterial Chemotaxis: The Early Years of Molecular Studies. *Annual Review of Microbiology*, *66*(Volume 66, 2012), 285–303. https://doi.org/10.1146/annurev-micro-092611-150120

6. Li, M., & Hazelbauer, G. L. (2014). Selective allosteric coupling in core chemotaxis signaling complexes. *Proceedings of the National Academy of Sciences of the United States of America*, *111*(45), 15940–15945. https://doi.org/10.1073/pnas.1415184111

7. Li, M., Khursigara, C. M., Subramaniam, S., & Hazelbauer, G. L. (2011). Chemotaxis kinase CheA is activated by three neighbouring chemoreceptor dimers as effectively as by receptor clusters. *Molecular Microbiology*, *79*(3), 677–685. https://doi.org/10.1111/j.1365-2958.2010.07478.x

8. Parkinson, J. S., Hazelbauer, G. L., & Falke, J. J. (2015). Signaling and sensory adaptation in Escherichia coli chemoreceptors: 2015 update. *Trends in Microbiology*, *23*(5), 257–266. https://doi.org/10.1016/j.tim.2015.03.003

9. Piñas, G. E., DeSantis, M. D., Cassidy, C. K., & Parkinson, J. S. (2022). Hexameric rings of the scaffolding protein CheW enhance response sensitivity and cooperativity in *Escherichia coli* chemoreceptor arrays. *Science Signaling*, *15*(718), eabj1737. https://doi.org/10.1126/scisignal.abj1737

10. Piñas, G. E., Frank, V., Vaknin, A., & Parkinson, J. S. (2016). The source of high signal cooperativity in bacterial chemosensory arrays. *Proceedings of the National Academy of Sciences of the United States of America*, *113*(12), 3335–3340. https://doi.org/10.1073/pnas.1600216113

11. Riechmann, C., & Zhang, P. (2023). Recent structural advances in bacterial chemotaxis signalling. *Current Opinion in Structural Biology*, *79*, 102565. https://doi.org/10.1016/j.sbi.2023.102565

12. Sourjik, V., & Berg, H. C. (2004). Functional interactions between receptors in bacterial chemotaxis. *Nature*, *428*(6981), 437–441. https://doi.org/10.1038/nature02406

13. Wadhams, G. H., & Armitage, J. P. (2004). Making sense of it all: Bacterial chemotaxis. *Nature Reviews Molecular Cell Biology*, *5*(12), Article 12. https://doi.org/10.1038/nrm152

Chapter 1

Introduction: Chemotaxis in Bacteria

Seeking a favourable environment for growth and development is fundamental across all domains of life. Motile bacteria can sense and adapt to transient environmental changes by monitoring surrounding chemoeffector molecules like attractants and repellents. This behaviour, termed as chemotaxis, allows bacteria to respond to chemoeffector cues through highly sensitive and adaptable chemosensory systems. The chemosensory systems initiate phosphorelay pathways to motility modules, facilitating movement toward favourable chemical gradients *(Porter et al., 2011; Wadhams & Armitage, 2004)*. Chemotaxis in bacteria is important for various processes like biofilm formation, quorum sensing, cell adhesion, symbiotic association with plants as well as pathogenesis in hosts *(Keegstra et al., 2022; Karmakar, 2021; Matilla & Krell, 2018)*.

1.1 Background

Leeuwenhoek, in the late 1600s, first observed and recorded movement in bacteria using his self-made single-lensed microscope, as documented in his notebook **(Figure 1.1A)** *(Lane, 2015)*. Two centuries later in late 1800s, chemotaxis, the movement towards or away from chemicals, was discovered in bacteria. Engelmann noted the accumulation of *Bacterium termo*, a rod-shaped, flagellated bacterium, in high oxygen areas around photosynthesizing plant cells. He also observed *Bacterium phatometricum* swam in light but stopped in darkness *(Berg, 1975)*. Pfeffer pioneered a technique in which he introduced a capillary tube filled with an attractant solution into a bacterial culture suspension. He observed bacterial migration and accumulation at the orifice of the capillary, followed by subsequent movement into the capillary as the attractant diffused within the suspension **(Figure 1.1B)** *(Berg, 1975)*.

In 1960s, Alder and colleagues did pioneering work in understanding bacterial chemotaxis on *Escherichia coli (Hazelbauer, 2012)*. They used "Pfeffer Assay" to survey compounds to identify attractants and repellents responsible for chemotaxis in *E. coli*. They observed distinct visible bands in capillary tubes or rings on agar plates, indicating migration of cells along a concentration gradient of nutrients and oxygen **(Figure 1.1C, D)** *(Adler, 1966a, 1966b; Adler & Templeton, 1967)*. Based on response to attractants and repellents potential receptors were identified in *E. coli* and it was also revealed that chemotaxis to attractants was independent of its metabolism value *(Adler, 1969)*. Chemoeffector molecules that are sensed by *E. coli* were identified *(Adler et al., 1973; Mesibov & Adler, 1972; Tso & Adler, 1974)*. Mutant strains with chemotactic deficiencies were then used to identify the *che* (chemotaxis) genes and their

associated Che proteins *(Parkinson, 1978, 1976, 1975)*. These observations led to questions and decades of extensive work on how bacteria could perceive the environment and move along a favourable chemical gradient, making the chemotaxis system the most comprehensively characterized signalling pathway in biology.

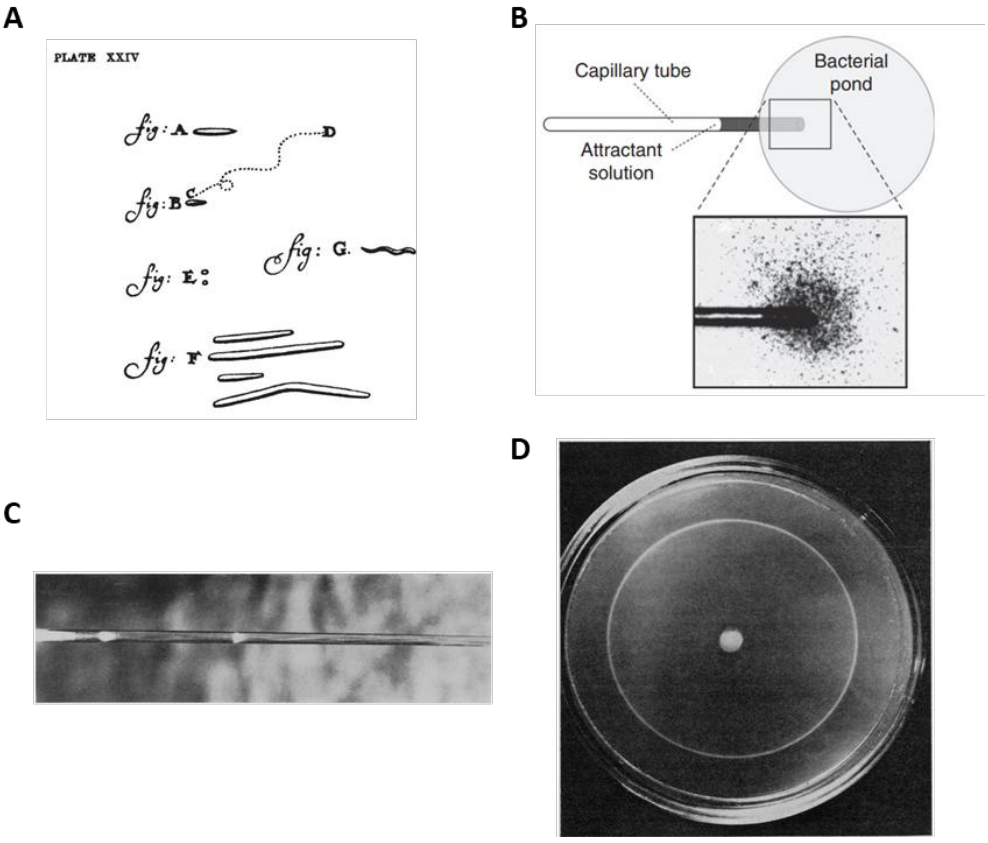


Figure 1.1 Observation of bacterial chemotaxis. (A) Bacteria observed by Leeuwenhoek. Dotted line shows movement from point C to D (fig: B). Adapted from *Lane, 2015*. (B) "Pfeffer Assay" shows accumulation of bacteria at the tip of an attractant-filled capillary. Adapted from *Parkinson, 2013*. Migration *E. coli as* (C) distinct bands in capillary tube, and (D) ring on agar plate. Adapted from *Adler, 1966a*.

1.2 Bacterial motility by 'run' and 'tumble'

Bacteria can sense various chemicals, including amino acids, sugars, salts, bases, alcohols, dipeptides, and metal ions. In addition to chemical gradients, they can perform aerotaxis and respond to signals such as pH, oxygen, temperature, redox status, and toxins *(Á. Ortega et al., 2017)*. Extensive studies on *E. coli* have established it as a model organism for investigating the mechanisms underlying chemotaxis. Three-dimensional tracking experiment using light microscopy of motile *E. coli* cells in isotropic solution by Berg and Brown highlighted how bacteria modulate their swimming trajectory *(Berg & Brown, 1972)*. *E. coli* cells move with an alternating sequence of intervals during which there is an abrupt or gradual change in direction,

termed as 'runs' and 'tumbles', which collectively define a 'random walk' pattern **(Figure 1.2A)** *(Berg & Brown, 1972)*. The motility appendages, flagella, are long filaments that extend outside the cell **(Figure 1.2B)**. It is anchored to the cell wall envelope via hook to a basal body, images of which were recorded under the electron microscope in early 1970s **(Figure 1.2C, D)** *(DePamphilis & Adler, 1971b, 1971a)*. Rotation of flagella was proposed to propel bacteria forward *(Berg & Anderson, 1973)*. In 1974, Silverman and Simon observed rotation of one cell bound to another or tethered to glass slides by anti-polyhook antibody **(Figure 1.2E)**. There was a variation in duration, direction and speed of rotation of the cells *(Silverman & Simon, 1974)*. Subsequent work in the same year confirmed flagellar rotation and revealed that the sensory system dictates the direction of that rotation to modulate swimming trajectory *(Berg, 1974; Larsen et al., 1974)*.

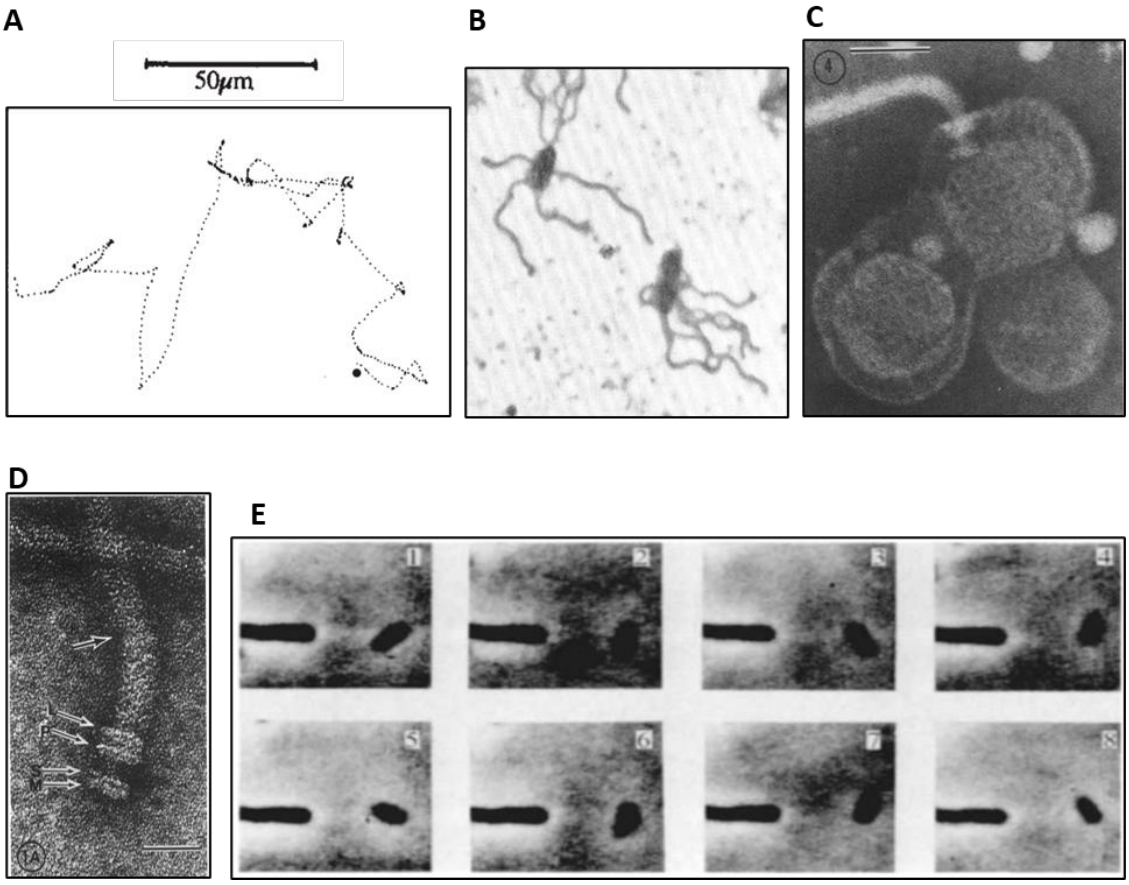


Figure 1.2 Motility is mediated by flagellar rotation in *E. coli*. (A) Three-dimensional tracking experiment of motile *E. coli* cells using light microscopy reveals an alternating sequence of intervals in motility during which there is an abrupt or gradual change in direction. Adapted from *Berg & Brown, 1972*. (B) *E. coli* cells. Adapted from (Adler & Templeton, 1967). (C) Flagellum attached to vesicle by basal body (Scale bar 60 nm). Adapted from *DePamphilis & Adler, 1971a*. (D) Flagellum connected to the basal body by hook (marked by top arrow, scale bar 30 nm). Adapted from *DePamphilis & Adler, 1971b*. (E) Rotation of cell bound by anti-polyhook antibody to a glass slide. The images are frames every 1/12 second. Stationary cell on the left acts as a reference point. Adapted from *Silverman & Simon, 1974*.

E. coli cells exhibit a 'random walk' in the absence of any attractants or repellents in the medium. The propulsion is due to the counter-clockwise (CCW) rotation of flagella, referred to as a 'run', which is subsequently followed by a 'tumble' when the flagella rotate clockwise (CW), resulting in the cell being reoriented in a random direction due to Brownian motion within the solution **(Figure 1.3A)**. Studies conducted between the late 1970s and early 1980s demonstrated a bias in the frequency of tumbles in the presence of attractants or repellents in the medium. As attractant concentration increased or repellent decreased, tumbling frequency of the bacterium decreased. Conversely, tumbling frequency of the bacterium rose as attractant decreased or repellent increased *(Berg, 1975)*. Thus, in the presence of an attractant or repellent source, *E. coli* engages in a 'biased random walk' **(Figure 1.3B)**. Consequently, bacteria detect the presence of chemoeffectors within the medium and adjust the frequency of tumbling, thereby determining whether to engage in a 'random walk' in isotropic surroundings or a 'biased random walk' in the presence of attractants or repellents *(Berg, 1975)*.

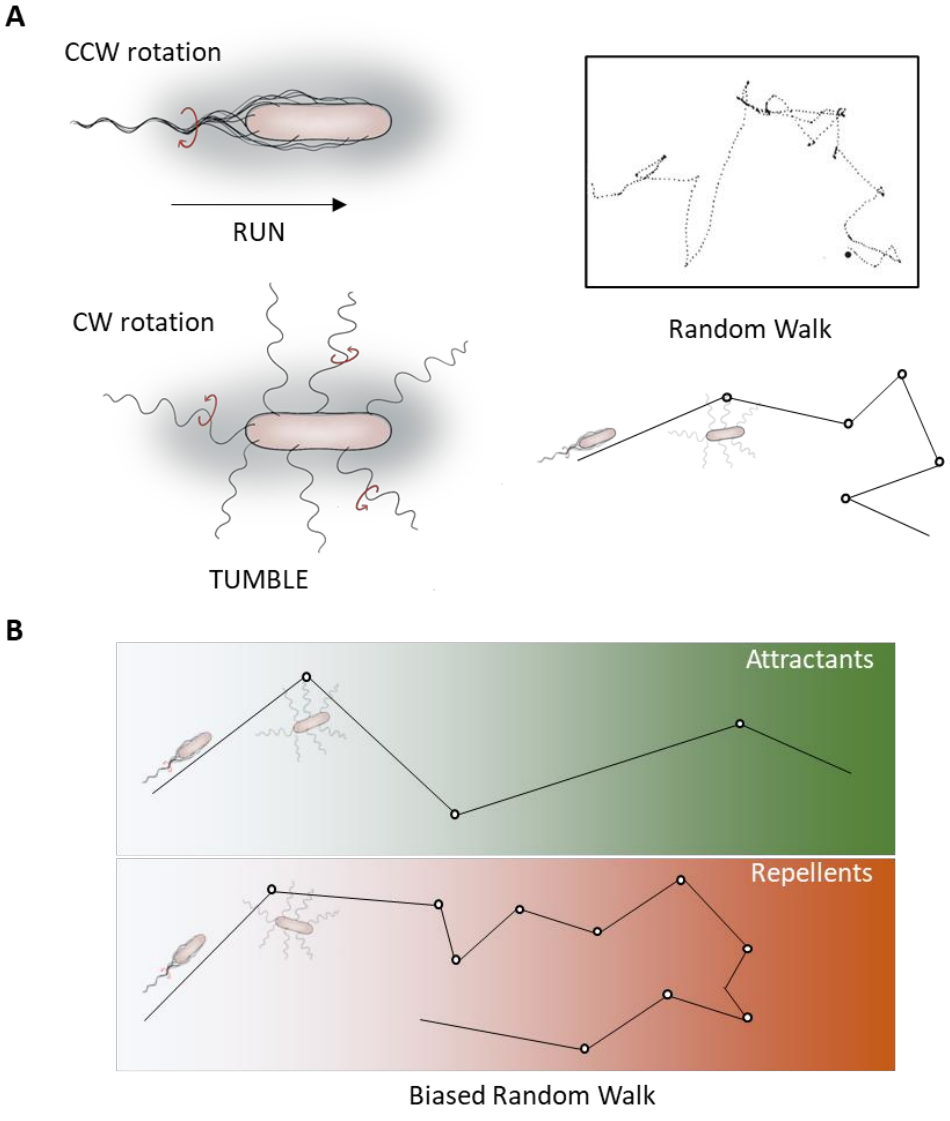


Figure 1.3 'Run' and 'Tumble' in *E. coli*. (A) Random walk in *E. coli* characterized by 'Run' (CCW flagellar rotation) and 'Tumble' (CW flagellar rotation). Inset of random walk is adapted from *Berg & Brown, 1972*. (B) Biased random walk due to decrease or increase in tumbling frequency in presence of attractants and repellents, respectively.

Bacteria detect attractant molecules directly, rather than their metabolites, such as ATP. Thus, a mutant with a defective chemotaxis pathway can still uptake and metabolize a nutrient, but its motility will not respond to that nutrient *(Adler, 1969)*. Additionally, bacteria sense a temporal gradient rather than a spatial one, as their small size (2 μm for *E. coli*) prevents a significant chemical gradient along their length. This temporal gradient is demonstrated when an attractant molecule is enzymatically degraded, altering the bacteria's tumbling frequency *(Brown & Berg, 1974; Macnab & Koshland, 1972)*. Consequently, bacteria possess a distinct chemosensory module to detect chemoeffector molecules in their environment.

1.3 Chemosensory receptors: methyl-accepting chemotaxis proteins

Response to chemoeffectors mediated by specific receptor proteins was postulated in 1969 *(Adler, 1969)*. Subsequently, galactose-binding protein was identified that could regulate chemotaxis *(Hazelbauer & Adler, 1971)*. Research from the late 1960s to early 1970s established that methionine is essential for chemotaxis *(M. S. Springer et al., 1975; Adler & Dahl, 1967; Armstrong, 1972a, 1972b)*. Using tritiated-methyl methionine, a 60-kDa *E. coli* membrane protein was radiolabelled and identified for the first time as crucial for chemotaxis, subsequently named as methyl-accepting chemotaxis protein (MCP) *(Kort et al., 1975)*. Subsequently, through the use of tritiated-methionine, MCPs were identified, including Tsr for serine and repellents, Tar for aspartate and repellents, and Trg for galactose and ribose (Kondoh et al., 1979; Silverman & Simon, 1977; M. S. Springer et al., *1977b*). CheR, essential for chemotaxis, was identified as a methyltransferase and resulted in γ-glutamyl methyl ester in MCPs *(W. R. Springer & Koshland, 1977; Van Der Werf & Koshland, 1977)*. These MCPs have been demonstrated to regulate parallel pathways during chemosensing *(Hazelbauer & Engström, 1980)*. By late 1970s, it was established that methylation of MCPs regulates sensory adaptation in bacterial chemotaxis *(Goy et al., 1978, 1977; M. S. Springer et al., 1977a)*.

Notably, a single MCP can detect various chemicals either directly or through a mediator protein, utilizing the periplasmic ligand-binding domain. The signal generates multiple methylated forms of the receptor MCPs as observed in SDS-PAGE **(Figure 1.4A)** *(Boyd & Simon, 1980; Chelsky & Dahlquist, 1980)*. Multiple methylation of MCPs is implicated in

regulating sensory adaptation to stimuli *(Boyd & Simon, 1980)*. This raises questions about how signalling is regulated in the presence of multiple chemoeffector molecules. It remains unclear how the presence of multiple attractants and repellents, sensed by the same or different MCPs, influences the downstream motility module. The chemosensory signalling module of MCPs connects to the motility module (flagella in *E. coli*) through a phosphotransfer signalling cascade.

1.4 Phosphotransfer signalling cascade by histidine kinase

How is the motility module regulated by the sensory module? By late 1980s, *che* genes responsible for *E. coli* chemotaxis were identified and cloned into protein expression plasmid vectors. In 1987, using γ-^{32}P-ATP, Hess observed autophosphorylation of purified CheA and inferred that protein phosphorylation was involved in chemotaxis *(Hess et al., 1987)*. Subsequent studies showed that CheA phosphorylated CheB (methylesterase), and CheY (response regulator), while CheZ was identified as a phosphatase to CheY *(Hess, Oosawa, et al., 1988; Wylie et al., 1988)*. By sequential proteolytic digestion of ^{32}P-labelled CheA and isolation of phosphorylated peptides by reverse-phase HPLC, which were further digested to individual amino acids and subjected to two-dimensional TLC, histidine residue was identified to be phosphorylated *(Hess, Bourret, et al., 1988)*. CheA was further confirmed to be a Histidine kinase from mutations at the phosphorylation site which also abolished the phosphotransfer activity to downstream CheY *(Hess, Bourret, et al., 1988; Oosawa et al., 1988)*.

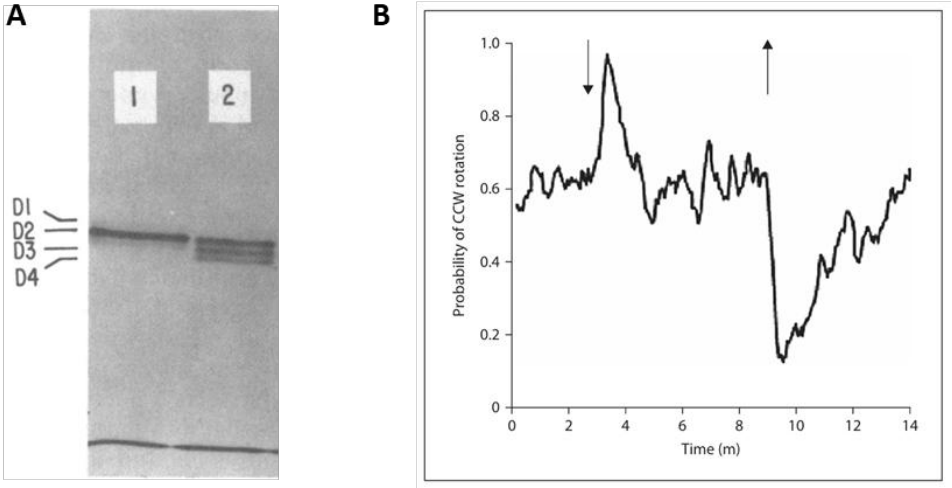


Figure 1.4 Sensory adaptation of chemosensory systems. (A) Observation of methylated Tsr receptor as fast migrating bands in lane 2 in presence of serine as compared to lane 1 (absence of serine). D1-D4 are observed bands of [^{35}S]-methionine labelled Tsr. Adapted from (Boyd & Simon, 1980). (B) Excitation and adaptation in response to stimulus in *B. subtilis*. The arrows

denote addition and subsequent removal of chemoeffector, indicating a transient response to the signal followed by adaptation. Adapted from *Rao & Ordal, 2009*.

Bacterial chemotaxis depends on receptor-mediated changes in phosphorylated proteins, with CheW linking receptors to phosphorylation, and CheY-phosphate acts as the tumble signal *(Borkovich et al., 1989)*. CheA autophosphorylation accelerated in presence of activating signals *(Borkovich & Simon, 1990)* and phosphorylation levels were correlated with the methylation status of the MCPs *(Borkovich et al., 1992)*. The completely demethylated receptor was a potent inhibitor and a poor activator of the kinase, while the fully modified receptor was an excellent activator of the kinase as monitored via phosphorylated CheY levels in *E. coli*. The partially modified receptor functioned effectively as both an inhibitor and an activator. Reversible modification of the MCPs enables the cell to maintain a pool of receptor molecules that can produce a broad range of signalling intensities *(Borkovich et al., 1992)*. In 1992, a ternary protein complex was proposed between receptor MCPs, adaptor protein CheW and histidine kinase CheA as a model of the sensory apparatus from in vitro interaction studies *(Gegner et al., 1992)*. This signalling cascade, characterized by the recognition of a receptor protein linked through a phosphorelay cascade to a regulatory effector protein, is fundamental to two-component signalling pathways *(Bourret & Silversmith, 2010; Bourret et al., 1989)*.

1.5 Sensory adaptation

Sensing chemoeffector gradients involves sensory adaptation, resulting in a phasic response to chemoeffectors, attractants or repellents, that always returns to pre-stimulus levels, regardless of continuous exposure to the chemoeffector **(Figure 1.4B)** *(Rao & Ordal, 2009; Macnab & Koshland, 1972)*. In *E. coli*, phosphorylated regulatory protein CheY (CheY-P) binds to the flagellar motor, causing clockwise rotation of flagellum and cell tumbling, with higher CheY-P concentrations increasing the likelihood of tumbling *(Eisenbach, 1996; Parkinson, 1978)*. Histidine kinase CheA, in a ternary complex with receptor and CheW, is inhibited when attractant binds to receptors, thereby reducing CheY-P levels and increasing the likelihood of a run. At the same time, in presence of repellents, the CheA is activated, and CheY-P levels increase, subsequently increasing the possibility of tumbling *(Borkovich et al., 1989)*. This response is temporary, and cells adapt to the attractant molecules *(Rao et al., 2008; Macnab & Koshland, 1972)*. The pathway with active CheY-P levels dictating tumbling frequency is reset to pre-stimulus levels by phosphatase CheZ *(Hess, Oosawa, et al., 1988)*. The pathway is illustrated in **Figure 1.5**.

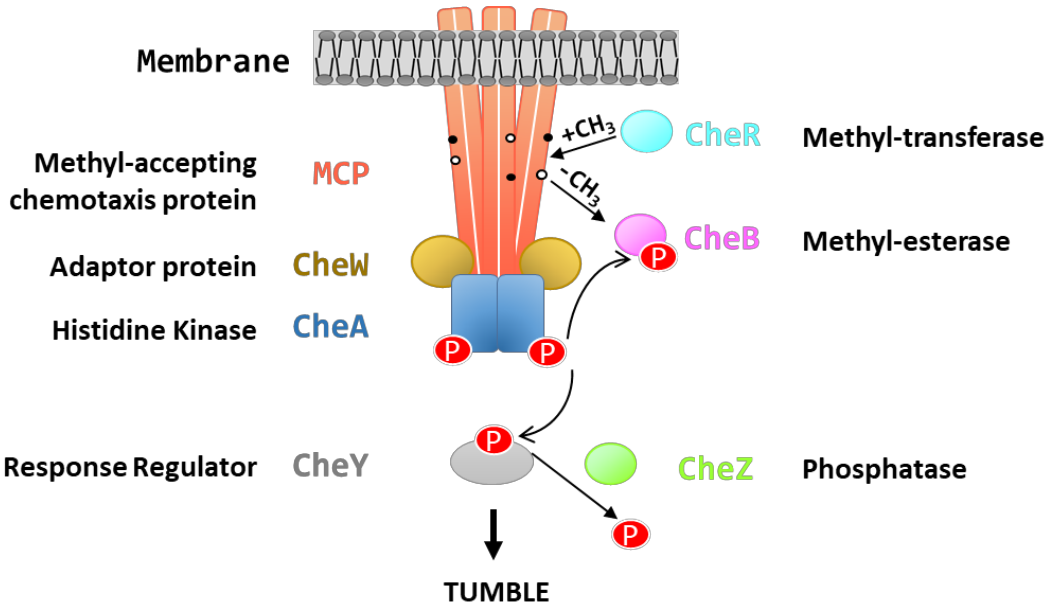


Figure 1.5 Che pathway in *E. coli*. The chemotaxis pathway has membrane-bound MCP linked to the histidine kinase CheA by adaptor protein CheW. CheA undergoes autophosphorylation and transfers phosphate to response regulator CheY and methylesterase CheB. Constitutively active methyltransferase CheR methylates conserved glutamate residues on the receptor. Phosphorylated CheY binds to flagellar motor and results in CCW to CW rotational switch. Constitutively active phosphatase CheZ inactivates CheY-P, while active CheB-P removes methyl groups from the receptor and resets the pathway.

The adaptation is regulated by CheR-mediated methylation and CheB-mediated demethylation of conserved glutamate residues in the receptor, responding to ligand binding or kinase activity *(Kehry et al., 1985; Stock & Koshland, 1978; Kleene et al., 1977; W. R. Springer & Koshland, 1977)*. CheR and CheB-mediated changes in receptor modification status regulate coordinated switching in flagellar rotation **(Figure 1.6)** *(Uchida et al., 2022)*. The methylation levels on the receptor are correlated with presence and absence of attractants and repellents *(Toews et al., 1979)*. Methylation of receptors increases kinase activity of associated CheA while binding of attractants inhibits the kinase activity as observed from reconstituted chemosensory complex from purified proteins from *E. coli (Ninfa et al., 1991)*. When attractants bind, the conformation favours methylation, which reduces affinity to the ligand and counteracts the inhibition due to ligand binding, eventually restoring kinase activity to pre-stimulus levels and enabling adaptation. Cells become less sensitive to higher concentrations of ligand as dissociation constant increases when receptors are methylated *(G. Li & Weis, 2000; Borkovich et al., 1992)*. In presence of repellents or loss of attractants from the receptors, the kinase activity is enhanced, leading to an increase in CheY-P, which results in tumbling. Simultaneously, demethylation of the receptor is regulated through a feedback loop by methylesterase CheB, which is first activated to phosphorylated CheB (CheB-P) by CheA *(Lupas & Stock, 1989)*.

Demethylation favours receptor affinity towards attractants or the removal of repellents by decreasing kinase activity, resulting in adaptation. Thus, the adaptation feedback loops by CheR and CheB are responsive to receptor conformational changes, where active receptors are demethylated by CheB-P and inactive receptors are methylated to active form by CheR, ensuring that receptor always return to pre-stimulus levels after being stimulated by chemoeffector molecules *(Uchida et al., 2022; Rao & Ordal, 2009)*. Unlike *E. coli,* the adaptation in *B. subtilis* is regulated by the CheV system, the CheC/CheD/CheY-P system, and the methylation system *(Rao et al., 2008)*.

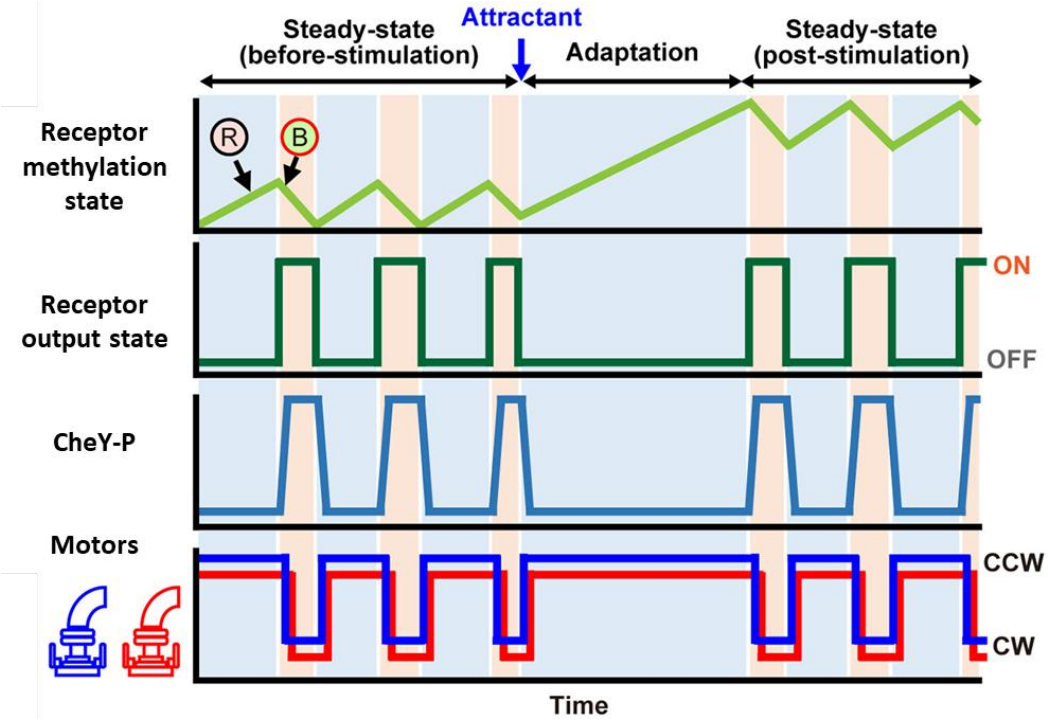


Figure 1.6 Signalling adaptation of chemoreceptors by interplay between methyltransferase 'CheR' and methylesterase 'CheB'. Receptor methylation induces activation of the histidine kinase CheA (represented by the receptor output state in dark green line), thereby stimulating phosphorylation of CheY and CheB. Phosphorylated CheY (CheY-P) interacts with the flagellar motor complex, inducing CW-rotation of flagella. The phosphatase CheZ rapidly dephosphorylates CheY-P, thereby restoring CCW rotation. Active CheB-P gradually demethylates the receptor methylation sites, restoring the system to a steady-state cycle. In presence of attractants, the receptor conformation favours methylation, resulting in a gradual increase in receptor methylation levels, which activates CheA and subsequent CheY phosphorylation. Methylation of the receptor reduces its affinity for the ligand, thereby desensitizing the system to higher concentrations of the attractant and facilitating sensory adaptation. CheZ and CheB-P reset the signalling pathway to its post-stimulus steady state during continued exposure to attractants. Figure adapted from *Uchida et al., 2022*.

E. coli cells compare the stimulus from the past second to that from the past three seconds and respond to the difference *(Block et al., 1982)*. The methylation level of the receptor serves as a chemical memory to decide the favourability of the current swimming direction. A high

methylation level of receptors signifies a recent high attractant environment. In contrast, a low methylation level indicates a recent past exposure to a low concentration of attractant. Repellent memories follow the same principle, with low methylation reflecting a high repellent concentration, while high methylation signifying low repellent levels in the recent past. As the cell swims, it monitors the current chemical environment depending on receptor ligand occupancy, and compares it to the recent past, marked by methylation on receptors. Significant changes in the environment adjust the histidine kinase activity of the chemosensory complex, thereby regulating the likelihood of tumbling *(Blair, 1995)*. The adaptation is precise and robust to variations in biochemical parameters *(Alon et al., 1999, 1999)*. Under strong stimulation, when receptor methylation reaches saturation, the precision adaptation falters *(Krembel et al., 2015; Neumann et al., 2014)*. However, imprecise adaptation may be an evolutionarily advantageous trait, extending cell run length and enhancing performance in static gradients *(Long et al., 2017; Wong-Ng et al., 2016)*. A recent study noted the adaptation of chemosensory diversity in isogenic *E. coli* populations, which enables subsets of a population to concurrently track or respond to chemoeffector molecules, thereby aiding in collective population behavioural decisions *(Moore et al., 2024)*. The outstanding question is how integration of multiple signals takes place to dictate a motility output.

1.6 Gain in signal

The chemotaxis signalling system (CSS) is a highly sophisticated, robust and precise network with a cooperative gain in signal *(Baker et al., 2006; Bourret & Stock, 2002; Bray, 2002)*. There is an amplification of signal, which was observed from the rotational bias of tethered *E. coli* cells on glass slides in presence of attractants like aspartate. It revealed a large gain in chemotactic signalling, whereby occupancy changes in a single receptor elicit a significant response *(Segall et al., 1986)*. The gain was measured *in vivo* as a function of CheA kinase activity via fluorescence resonance energy transfer between phosphorylated CheY and phosphatase CheZ. The gain was ~36-fold at the signalling complex, suggesting one receptor can regulate about three dozen kinases, indicating a functional receptor-kinase network *(Sourjik & Berg, 2002)*. The receptor-kinase network behaved cooperatively with Hill coefficients as high as ~10, suggesting that interactions among receptor-kinase network serve as a general mechanism for signal integration and amplification *(Sourjik & Berg, 2004)*. Signal adaptation by methylation and demethylation of the receptors regulates cooperative kinase behaviour *(G. Li & Weis, 2000)*. Additionally, presence of homologous or heterologous receptor

assemblies influences cooperativity and sensitivity to stimulation *(Bornhorst & Falke, 2003; Lai et al., 2005)*. Cooperation between neighbouring receptors helps reset the signalling status to ground state after stimulation *(M. Li & Hazelbauer, 2005)*. Thus, a network of receptors and kinase molecules, linked by adaptor proteins, results in a cooperative gain in signal during chemotaxis.

1.7 Architecture of chemosensory complex

Chemosensory complexes of receptors with adaptor protein CheW and histidine kinase CheA, localized as membrane-bound polar patches, were initially observed in fixed, sectioned *E. coli* cells by immunogold labelling *(Maddock & Shapiro, 1993)*. Subsequently, in living cells, fluorescently tagged chemotaxis proteins were predominantly found to localize at cell poles *(Sourjik & Berg, 2000)*. Later, receptor arrays at cell poles were observed by cryo-electron tomography of intact *E. coli* cells *(Zhang et al., 2007)*. Receptors are oriented perpendicularly to the inner membrane with sensing domains in the periplasm. Their cytoplasmic ends associate with CheA/CheW proteins, forming a dense layer – baseplate, parallel to the membrane **(Figure 1.7A)** *(Zhang et al., 2007)*. Non-polar, lateral chemosensory clusters were observed at future division sites *(Thiem et al., 2007)*. The packing of receptor clusters showed stimulus-dependent plasticity, where ligand binding can induce slow remodelling of the clusters *(Frank & Vaknin, 2013)*.

The receptors are structured as homodimeric four-helix bundles, which assemble into trimer-of-dimers in the crystallized cytoplasmic domain of the Tsr receptor from *E. coli (Kim et al., 1999)*. These receptor dimers interact at the helical hairpin tip, and the trimer-of-dimers organization is important for receptor function, as shown by amino acid replacement experiments at the trimer-of-dimer interface *(Ames et al., 2002)*. Interestingly, trimer-of-dimers of receptors were also observed through crosslinking experiments even in the absence of CheW and CheA *(Studdert & Parkinson, 2004)*. CheA and CheW stabilize the trimer arrangement of receptor dimers *(Studdert & Parkinson, 2005)*, and it seems that CheW and CheA compete for the same binding site at receptor molecules *(Asinas & Weis, 2006)*. Receptors from evolutionarily distant species, *Thermotoga maritima*, also dimerizes and form anti-parallel, four-helix bundle. However, the dimers are arranged as hedgerows in a crystal lattice **(Figure 1.7B)** *(Park et al., 2006)*. Studies of receptor dimers in lipid nanodiscs show that homodimers can undergo adaptation and transduce transmembrane signals, but trimers of dimers are

required for kinase activation and downstream signalling **(Figure 1.7C)** *(Boldog et al., 2006)*. The core signalling units are composed of two trimer-of-dimers connected by the adaptor protein CheW and the dimeric histidine kinase CheA, maintaining a stoichiometry of 6 receptor dimers to 2 CheW molecules and a dimeric CheA molecule *(M. Li & Hazelbauer, 2011, 2004; Erbse & Falke, 2009)*.

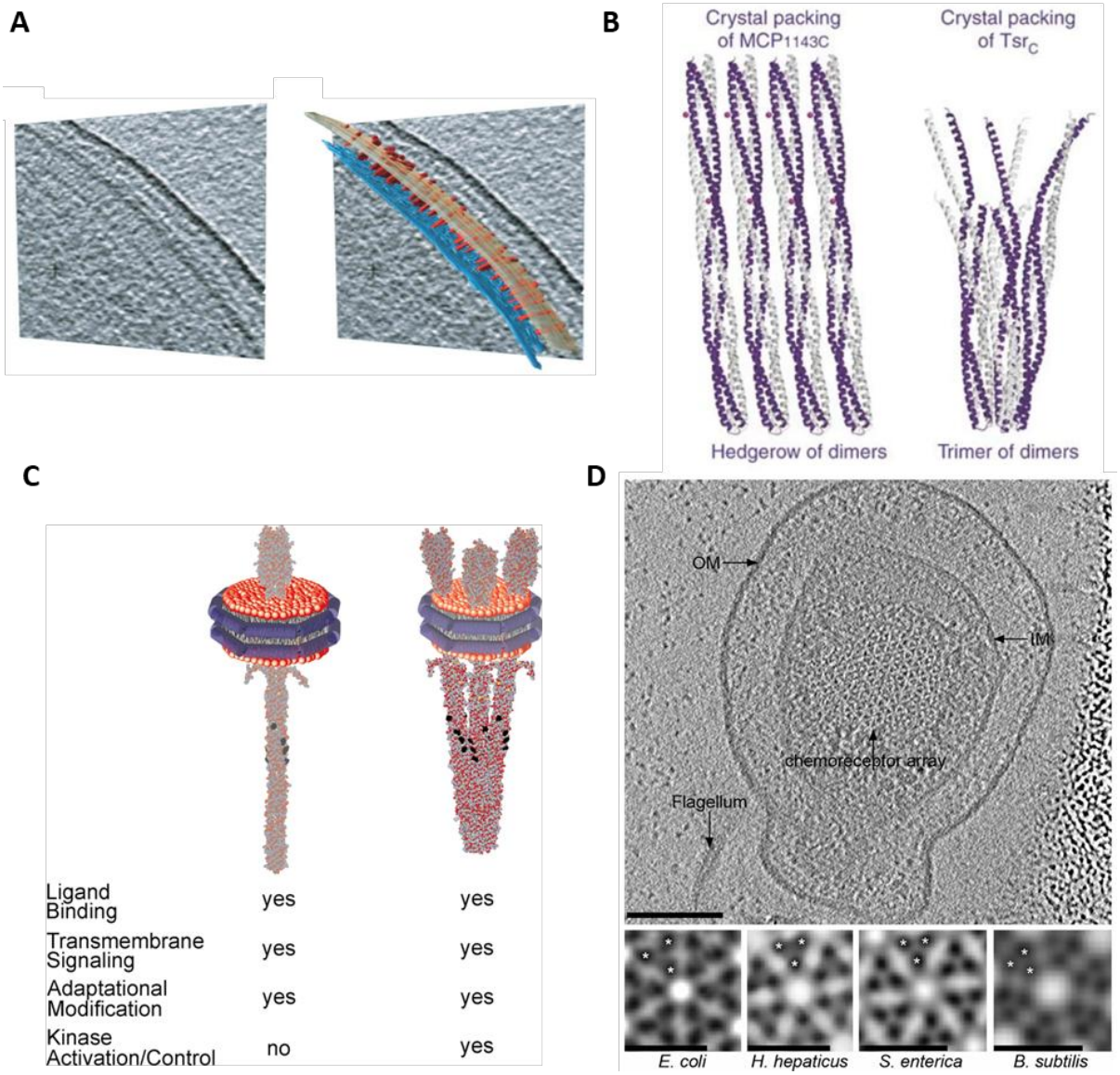


Figure 1.7 Architecture and significance of chemosensory complex. (A) Cryo-tomography of wild-type *E. coli* illustrating the polar receptor array. Receptor arrays, in red, is perpendicular to the inner membrane held by CheA-CheW base-plate in cytoplasm, highlighted in blue. Figure adapted from *Zhang et al., 2007*. (B) Hedgerow and trimer-of-dimer arrangement of dimeric four-helix bundle of cytoplasmic domain from *T. maritima* and *E. coli* MCPs respectively. Figure adapted from *Park et al., 2006*. (C) Functional properties of lipid-nanodisc embedded *E. coli* Tar homodimers and trimer-of-dimers. Figure adapted from *Boldog et al., 2006*. (D) Conserved hexagonal architecture of chemoreceptor arrays as observed by cryo-tomography. Top panel: Tomographic slice of *Salmonella enterica* minicell. OM - outer membrane, IM - inner membrane, Scale bar - 100 nm. Bottom panel: Subtomogram average of

chemoreceptor assays shows hexagonal arrangement of trimer-of-dimers. Individual receptor dimers marked with asterisks, scale bar - 12 nm. Figure adapted from *Briegel et al., 2012*.

The chemosensory array architecture, revealed by subtomogram averaging, shows receptors in a hexagonal packing order connected at the cytoplasmic tip by ordered CheA and CheW **(Figure 1.7D)** *(Briegel et al., 2012, 2009)*. Structures derived from crystallography studies and homology modelling of individual components or macromolecular assemblies, when docked into the electron cryotomography density of native cellular arrays, reveal that receptor trimers form a hexagonal lattice with a "two-facing-two" pattern, connected by a ring of alternating CheA and CheW molecules (**Figure 1.8A)** *(Briegel et al., 2012; Liu et al., 2012)*. This architecture is conserved across bacteria and archaea, with CheA and CheW networks arranging receptor trimers-of-dimers into a rigid, hexagonal pattern spaced at ~12 nm **(Figure 1.7D)** *(Briegel et al., 2012, 2009).* The kinase CheA interacts to the receptor via P5 domain, which is homologous to CheW and is topologically similar to two SH3 domains *(X. Li et al., 2013; Bilwes et al., 1999)*. Similarly, CheW is also composed of two β-barrels, subdomain 1 and subdomain 2, with a hydrophobic interface interacting with receptor *(X. Li et al., 2013)*. Subsequent tomography studies confirmed the universal hexagonal architecture where the cytoplasmic trimer-of-dimer receptor tips are organized within a pseudo-6-fold symmetric ring composed of alternating CheW and CheA-P5 units *(Cassidy et al., 2023; Burt et al., 2020; Cassidy et al., 2020)*. This ring is established through interactions between CheW and CheA-P5 at 'interface 1' – P5 subdomain 1 and CheW subdomain 2, which constitute the core signalling unit *(Natale et al., 2013)*, while 'interface 2' – P5 subdomain 2 and CheW subdomain 1, links these core units to assemble extended arrays **(Figure 1.8B-E)** *(Piñas et al., 2016)*.

The trimer-of-dimers arrangement allows cooperative interactions within receptor dimers *(Lai et al., 2017)*. Moreover, the conserved array architecture, featuring a core signalling unit (CSU) made up of a trimer-of-dimers connected by two CheW monomers and a dimeric CheA forming 'interface 1' between them, and CheA-CheW 'interface 2' linking CSUs into a hexagonal lattice, plays a key role in supporting cooperativity and signal amplification through allosteric interactions within the array *(Piñas et al., 2016; M. Li & Hazelbauer, 2014).* Disruption of array by mutations in CheW abolishes signal amplification while retaining signalling function *(Piñas et al., 2022, 2016; Frank et al., 2016)*. Although the architecture of chemosensory arrays

is well understood, the exact structural mechanism of signal transduction, kinase activation, and cooperative gain in signal in chemosensory arrays remains unclear.

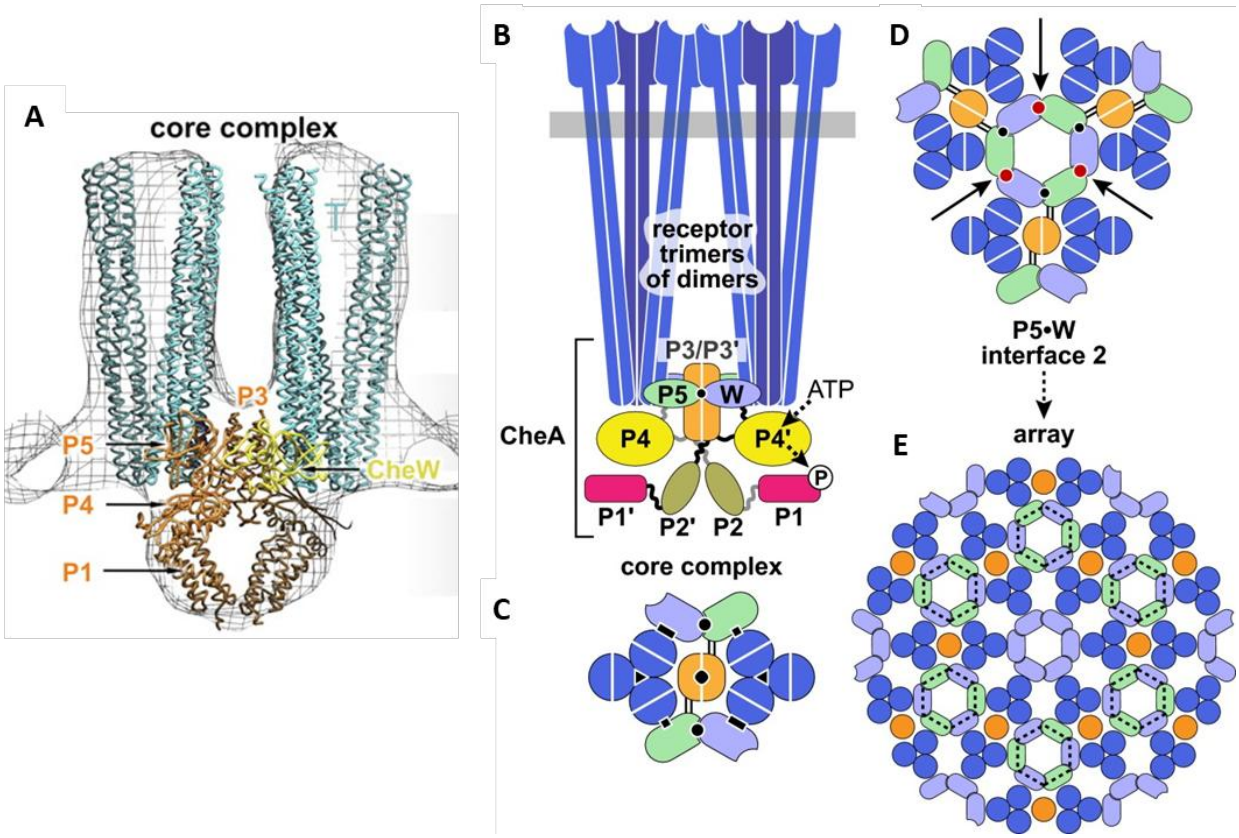


Figure 1.8 Structural organization of chemosensory arrays. (A) Subtomogram average density of chemosensory array from *E. coli* minicells. Density map is fitted with atomic structures from crystallography and homology models as rigid body. A Two-facing-two pattern is observed for the core complex, where two trimer-of-dimers are connected by two CheWs and a dimeric CheA. Figure adapted from *Liu et al., 2012*. (B) Representation of the core signalling complex of a chemosensory array. CheA is composed of five domains – P1 (histidine phosphotransfer, transfers phosphate to CheY and CheB), P2 (CheY and CheB interacting), P3 (dimerization), P4 (ATPase, phosphorylates P1) and P5 (CheW homolog). P5 and CheW interact with each other at receptor tip. (C) Cross-sectional view of the core signalling unit. The interfaces are marked as – trimer-of-dimer (triangles), receptor-CheW (rectangles), receptor-P5 (squares), P3/P3' (diamond), interface 1 by P5 subdomain 1 and CheW subdomain 2 (black circle). (D) Single hexagonal lattice of the array formed by interface 2 between P5 subdomain 2 and CheW subdomain 1 (red circled). (E) An extended chemosensory array formed by an interconnected core complex. Figures B-E are adapted from *Piñas et al., 2016*.

1.8 Diversity in chemosensory systems

In *E. coli*, five chemosensory receptors detect a diverse array of chemical signals that converge into a single chemosensory pathway dictating flagellar rotation *(Parkinson et al., 2015)*. The ligand-binding domain (LBD) of MCPs directly interacts with chemoeffector molecules in the periplasmic space or may associate with ligand-bound periplasmic binding proteins **(Figure**

1.9) *(Stock & Baker, 2009)*. On average, a bacterial genome has 14 chemoreceptor genes, but this varies widely and is not correlated with genome size *(Lacal et al., 2010)*. Bacteria that frequently face stress or adapt to diverse environments typically have more receptor genes *(Bardy et al., 2017)*. Over 50% of all motile bacteria possess multiple chemosensory systems *(Wuichet & Zhulin, 2010)*. Typically, at least one chemosensory pathway directly controls motility, while others likely regulate various programmed cellular processes *(Gumerov et al., 2021; He & Bauer, 2014)*. A systems-level phylogenomics analysis classifies 19 different chemotaxis systems by identifying central and auxiliary components of chemosensory systems *(Wuichet & Zhulin, 2010)*. The chemoreceptors are diversified in terms of topology, localization, and ligand binding domains (LBDs), and over a hundred distinct ligand binding domains are predicted from genomic analysis of MCP sequences (Matilla & Krell, 2017; Á. Ortega et al., 2017). The receptors are also classified based on the number and organization of heptad repeats, resulting in a coiled-coil signalling domain *(Alexander & Zhulin, 2007)*. Although diversity exists in components of chemosensory clusters *(Huang et al., 2019; Wuichet & Zhulin, 2010)*, a universal hexagonal array appears to be conserved in bacteria and archaea *(Briegel et al., 2015, 2009)*.

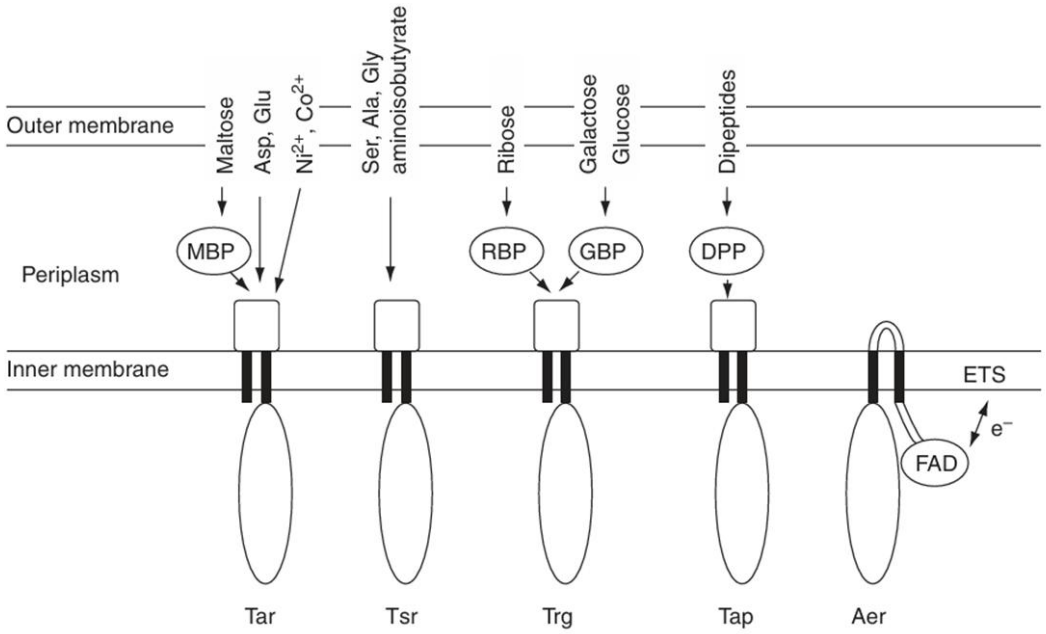


Figure 1.9 Chemoreceptors from *E. coli*. The chemoreceptors (Tar, Tsr, Trg and Tap) sense ligands directly or via periplasmic ligand-binding proteins (MBP: maltose-binding protein, RBP: ribose-binding protein, GBP: galactose-binding protein, DPP: dipeptide-binding protein). 'Aer' has a cytoplasmic sensing domain associated with a flavin cofactor that senses cellular oxidative potential via redox interaction with ETS (Electron Transport Chain) in the membrane. Figure adapted from *Stock & Baker, 2009*.

Chemosensory arrays are diverse in context to protein composition, functional output and cellular localization *(Yang & Briegel, 2020; Mauriello et al., 2018; Á. Ortega et al., 2017)*. A diversity in adaptor proteins exists that forms the baseplate *(Huang et al., 2019)*. For example, CheV, a CheW-CheY chimeric protein *(Fredrick & Helmann, 1994)*, encoded in 60% of all chemotactic prokaryotes *(Wuichet & Zhulin, 2010),* interacts with receptors and CheA and can be phosphorylated by CheA *(Karatan et al., 2001)*. ParP in *V. cholerae* is part of the baseplate that promotes array formation and localization near flagellar poles *(Jones & Armitage, 2015; Yamaichi et al., 2012)*. There is variability in the stoichiometry of baseplate components among chemosensory arrays. In response to environmental stimuli, bacteria can adjust baseplate components to regulate sensory output from these arrays *(Yang & Briegel, 2020)*. In *E. coli* the stoichiometry of the baseplate components CheA to CheW varies between 1:1 and 1:2 *(M. Li & Hazelbauer, 2004)*. The stoichiometry of CheA to CheW to CheV within the baseplate components of *B.* subtilis is 1:1:3, while in cluster II arrays of *V. cholerae* stoichiometry of CheW:CheA:ParP is 35:5.3:1 with four different CheV proteins incorporated at different ratios into the baseplates *(Cannistraro et al., 2011; Yang et al., 2018)*. Additionally, chemoreceptor clustering into arrays is influenced by receptor length, where wild-type and truncated *E. coli* receptors form distinct, length-dependent arrays that function independently *(Herrera Seitz et al., 2014)*. This diversity has functional significance; for example, higher receptor cooperativity may be necessary in species with low kinase levels in chemosensory arrays *(Yang & Briegel, 2020)*, however, structural mechanisms by which array diversity confers functional benefits to bacteria is not explored.

1.9 Diversity in chemosensory arrays

The chemosensory arrays form a conserved hexagonal architecture; however, alternative chemosensory arrays are observed *in vitro* and *in vivo (Yang & Briegel, 2020)*. 'Zippers', or 'micelle-like' architecture, are observed *in vitro* in absence of baseplate components **(Figure 1.10A, B)** *(Briegel, Wong, et al., 2014)*, and 'sandwich' arrays are observed for truncated receptor *in vitro* without transmembrane domain in presence of baseplate components **(Figure 1.10C)** *(Haglin et al., 2017; Briegel, Ladinsky, et al., 2014)*. Such 'sandwich' arrays are observed *in vivo* for cytoplasmic receptors. Cytoplasmic chemoreceptors, approximately 14% of all chemoreceptors *(Collins et al., 2014)*, lacking a transmembrane domain, may inherit a 'sandwich' architecture or receptors sandwiched between baseplate components as observed in *Vibrio cholerae*, *Rhodobacter sphaeroides* and the archaeon *Methanoregula formicica (Briegel*

et al., 2015; Briegel, Ladinsky, et al., 2014). In *Vibrio cholerae,* three distinct chemosensory arrays are observed in the late stationary phase under starvation **(Figure 1.10D)**. The cytoplasmic F9 arrays, in contrast to typical arrays, are formed by two different cytoplasmic receptors varying in length and architecture **(Figure 1.10E)** *(D. R. Ortega et al., 2020; Briegel et al., 2016)*.

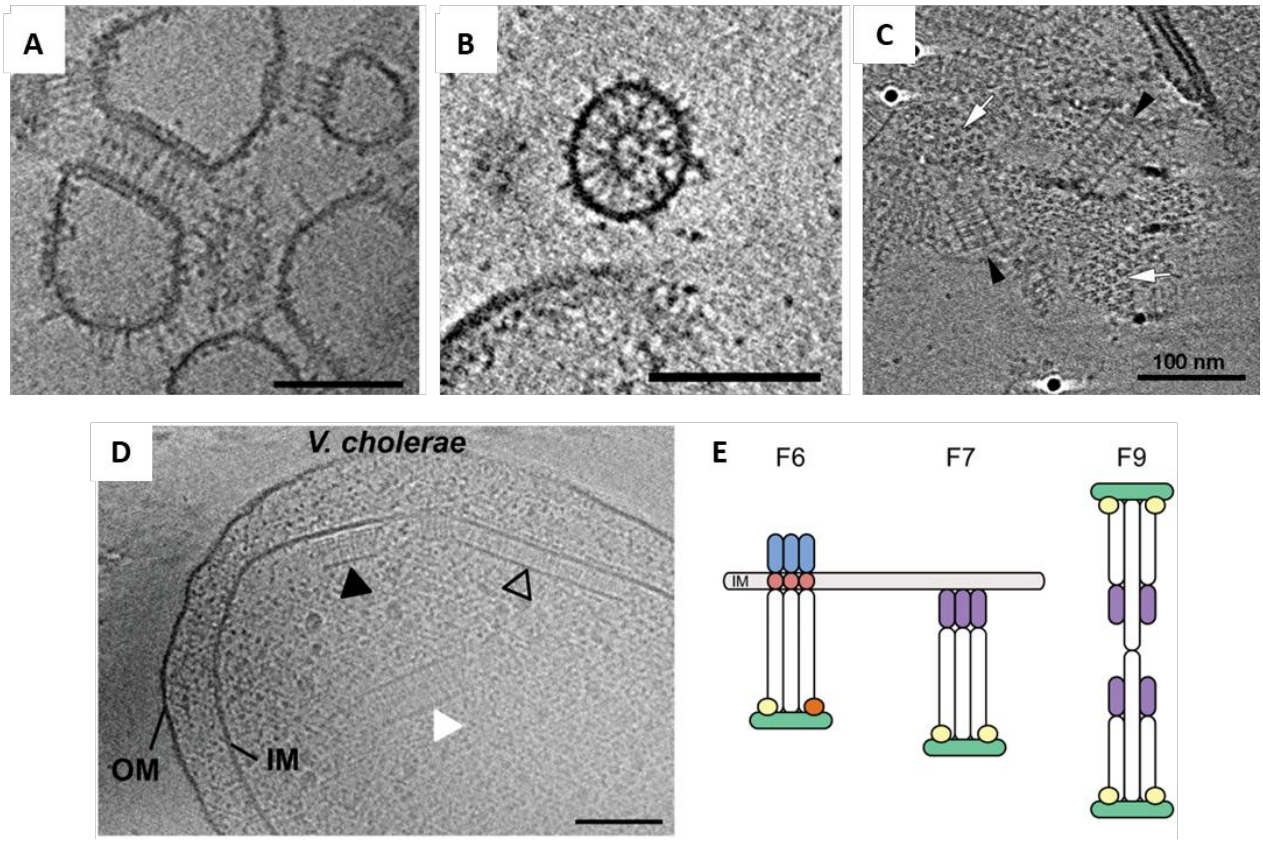


Figure 1.10 Alternative chemosensory arrays. (A) *In vitro'* Zipper-like' and (B) 'Micelle-like' architecture of chemoreceptors in absence of baseplate components. Scale bar 100 nm. Figures adapted from *Briegel, Wong, et al., 2014*. (C) 'Sandwich' architecture of *E. coli* Tar receptors without transmembrane domain in presence of base place components. Figure adapted from *Briegel, Ladinsky, et al., 2014*. (D) and (E) Three distinct chemosensory systems in *V. cholerae* – F6 (empty black triangle) containing chemoreceptors with periplasmic sensing domain (blue) and transmembrane domain (red), F7 (black triangle) with cytoplasmic ligand binding domain (magenta) lacking periplasmic and transmembrane domains, and F9 (white triangle) composed of two different chemoreceptors, one bearing ligand binding domain (magenta) other stabilizing the 'sandwich' architecture. The cytoplasmic domain of the receptors (white) interacts with scaffold proteins CheW (yellow) and/or CheV (orange), and histidine kinase (green). IM: inner membrane, OM: outer membrane. Scale bar: 50 nm. Figure adapted from *D. R. Ortega et al., 2020*.

Alternative array architectures are observed *in vivo* in *Treponema denticola* cells, which exhibit high membrane curvature *(Muok et al., 2020)*. In contrast to hexagonal P6 symmetry arrays, a P2 symmetry architecture of the chemotaxis apparatus is observed, resulting from a linear

organization of CheA and presence of CheW-CheR-like protein in the baseplate **(Figure 1.11A)** *(Muok et al., 2020)*. P2-symmetric array architecture has also been observed in *E. coli* mini cells, in addition to the P6-symmetry architecture **(Figure 1.11B)** *(Burt et al., 2021)*. The physiological reasons behind the existence of two distinct types of array architecture and their significance in signalling mechanisms are yet to be explored.

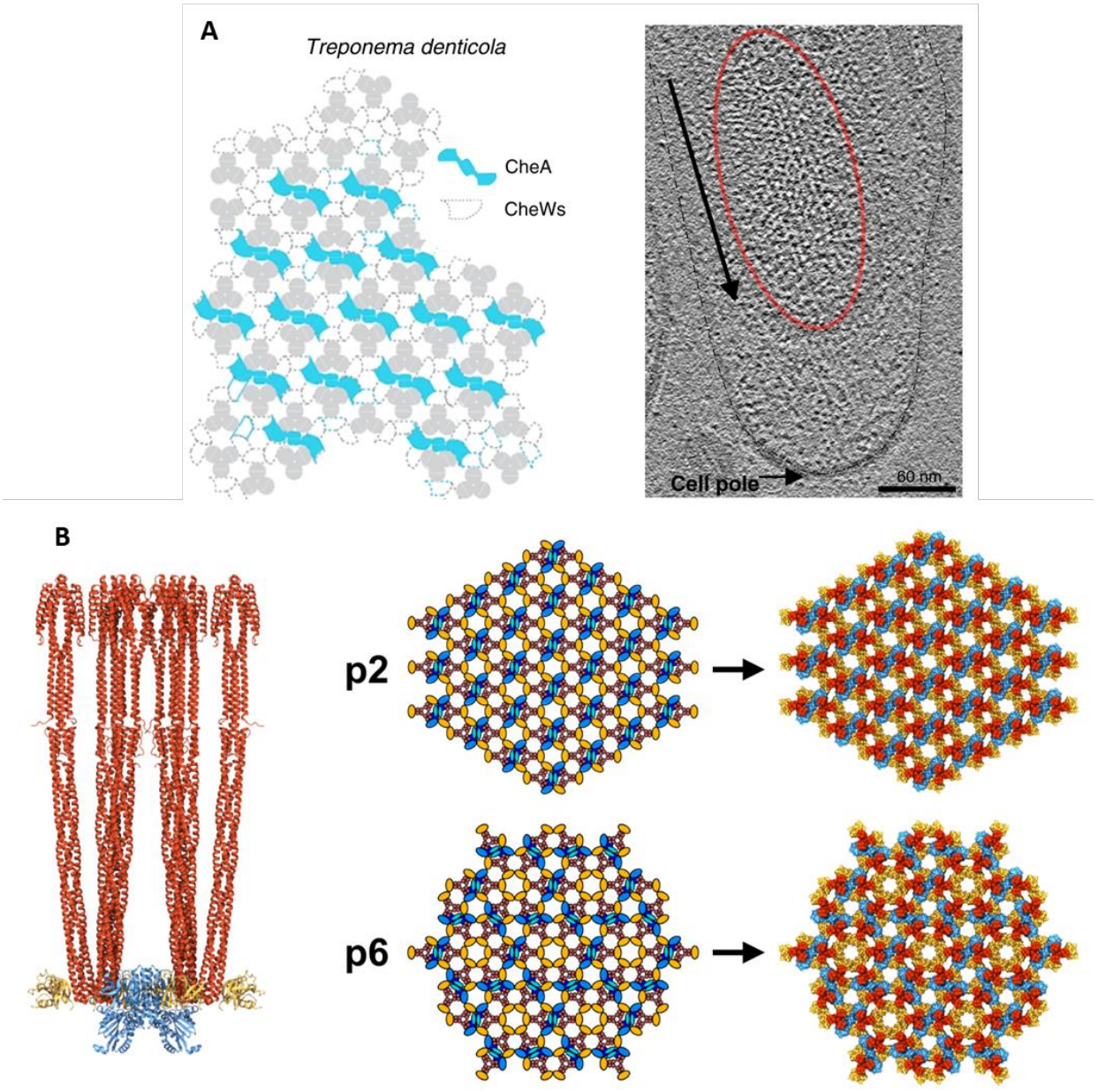


Figure 1.11 Alternative chemosensory arrays *in vivo*. (A) P2 symmetry linear array (inside red circle) observed in *T. denticola* cryo-tomography study. Figure adapted from *Muok et al., 2020*. (B) The core signalling unit (left) from *E. coli* composed of receptors (red), CheW (yellow) and CheA (blue) exhibit P2 and P6 symmetry array organization *in vivo*. Schematic (middle) and all-atom models (right) at baseplate region showing P2 and P6 architecture. Figure adapted from *Burt et al., 2021*.

1.10 Concluding remarks and motivation

Cryogenic electron tomography (CryoET) has been widely used to study bacterial macromolecular chemosensory complexes, which are predominantly membrane-bound. *In vitro* systems with reconstituted chemosensory complexes on lipid nanodiscs and arrays on 2D lipid monolayers, along with *in vivo* studies of lysed bacterial cells, minicells, and native cells, have been used to investigate chemosensory complex architecture **(Figure 1.12)** *(Riechmann & Zhang, 2023; Hadjidemetriou et al., 2022; Qin & Zhang, 2021)*. These studies, along with crystal structures, molecular modelling, and molecular dynamics simulations, revealed the conserved architecture of these arrays, identified the core signalling unit, and elucidated the function of the arrays in amplifying and integrating signals.

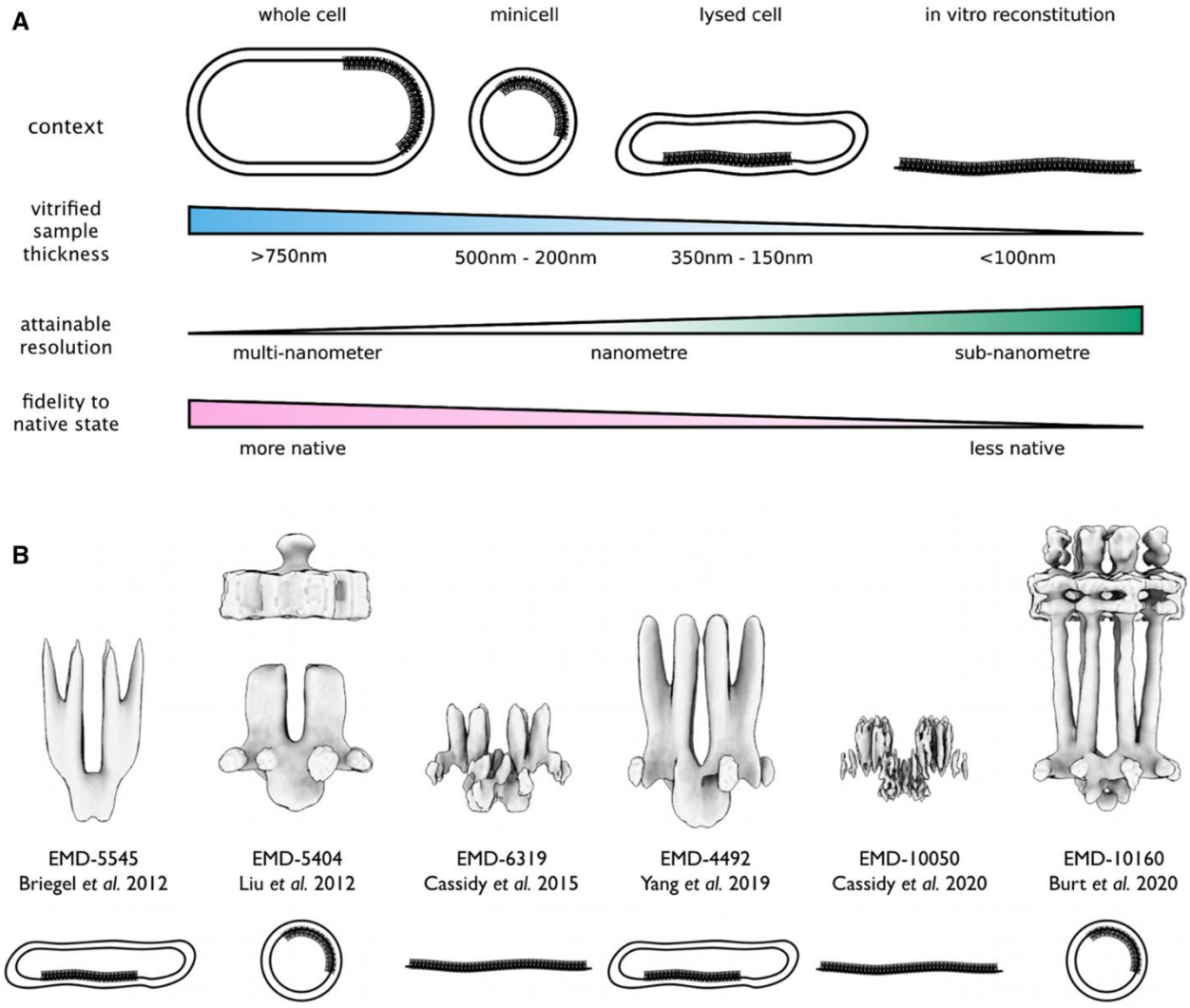


Figure 1.12 Chemosensory arrays resolved using CryoET. (A) Diagram showing inverse co-relation between vitrified sample thickness and attainable resolution, ranging from native whole cells to *in vitro* reconstituted arrays. (B) CSU structures from key studies chronologically from left to right (Adapted from *Hadjidemetriou et al., 2022*).

The chemosensory arrays are highly sensitive across a wide range of chemoeffectors, precisely adapt to chemical gradients, exhibit cooperative signal gain, and result in precise output. However, due to the limited resolution in tomography studies, mechanisms involving signal reception that led to the regulation of kinase activity, methylation adaptation of receptors, and their implications, as well as cooperative signal amplification in chemosensory arrays, are not well understood. The conformational changes in receptors and kinases during the signalling process, as well as the propagation of signals among core signalling units, remain to be elucidated to understand the mechanisms of signal transduction, adaptation, and cooperativity in chemosensory complexes.

To overcome the challenges of limited resolution from tomography studies of membrane-bound arrays **(Figure 1.12)**, structure studies on soluble cytoplasmic chemosensory complexes may provide valuable insights into the mechanisms of signal transduction, adaptation, and cooperativity in chemosensory complexes.

The cytoplasmic Frz chemosensory pathway in Myxococcus xanthus utilises the nucleoid as a scaffold for cluster formation and regulates chemotaxis in the bacterium by modulating the reversal frequency *(Moine et al., 2017; Blackhart & Zusman, 1985)*. The receptor MCP, FrzCD undergoes methylation in the presence of attractants, such as casitone and yeast extract, and demethylation in the presence of repellents, including isoamyl alcohol (IAA), ethanol, and DMSO *(McBride et al., 1992)*. This novel pathway is the only known chemosensory system that uses nucleoid as support for cluster or array formation and is essential for the development cycle of the bacterium *(Bustamante et al., 2004)*. The pathway is homologous to the Che pathway, where FrzCD is the cytoplasmic MCP, FrzE is the histidine kinase, and FrzA and FrzB are adaptor proteins. FrzX and FrzZ serve as response regulators, and FrzF and FrzG are the methyltransferase and methyesterase, respectively **(Figure 1.13)** *(Bustamante et al., 2004; Guzzo et al., 2018)*. Chemotaxis in *M. xanthus* is elaborated in detail in Chapter 2. This chemosensory system is hypothesized to form a core signalling unit, and thereby hexagonal arrays similar to those observed in membrane-bound arrays, using DNA as a scaffold *(Mauriello, 2020)*. The proposed architecture of Frz CSU is elaborated in detail in Chapter 4.

In vitro reconstitution of core signalling unit of Frz pathway and structural studies by single-particle cryoEM may act as model to understand signal transduction mechanisms in chemosensory complexes and may provide novel insights into cytoplasmic chemosensory macromolecular complexes. Frz pathway falls under ACF (Alternate Cellular Function)

classification based on phylogenomics analysis of presence and absence of central and auxiliary components of chemosensory systems *(Gumerov et al., 2021; Wuichet & Zhulin, 2010)*. In contrast to canonical pathways, this pathway is composed of two adaptor proteins and a hybrid histidine kinase in the core signalling unit complex, which will provide insights into the regulation by a diverse signalling system that confers functional benefits to bacterium.

The aim is to reconstitute the minimal repeating unit of the Frz chemosensory complex to obtain a high-resolution structure and elucidate the mechanism of signal transduction in chemosensory systems.

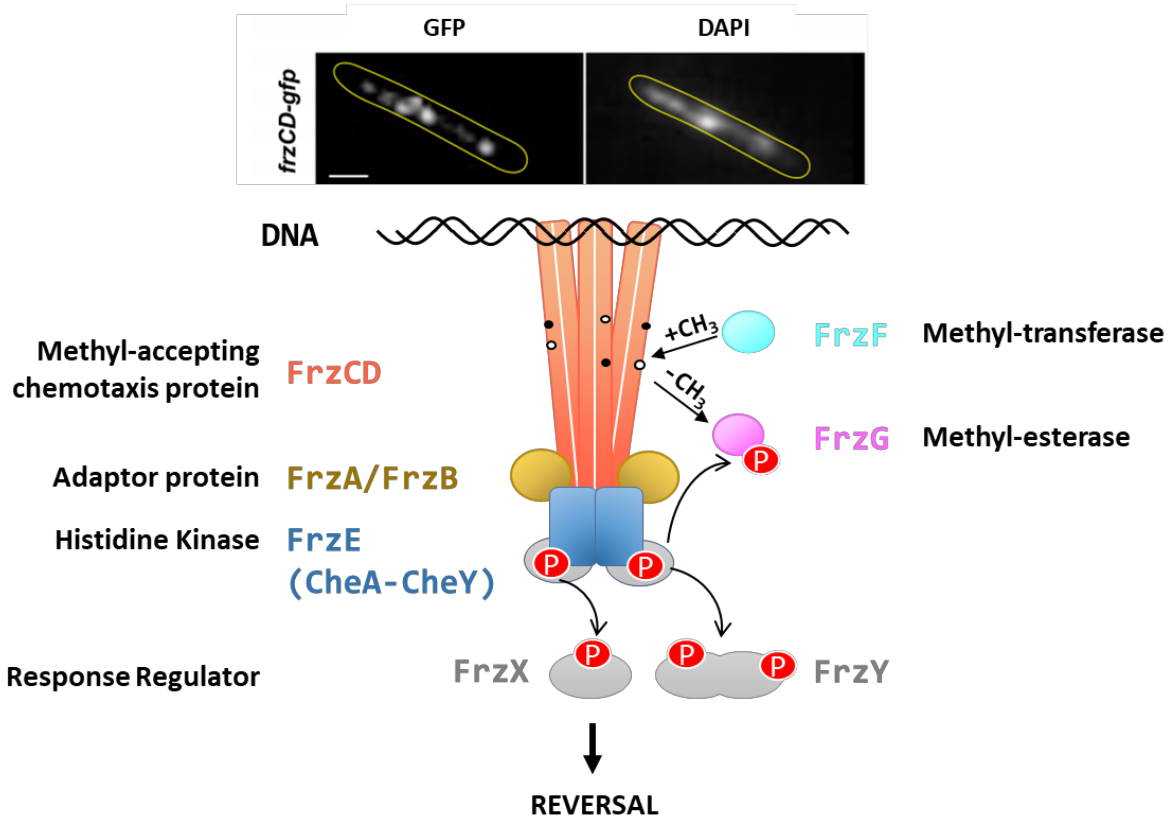


Figure 1.13 Frz pathway in *M. xanthus*. The chemotaxis pathway has cytoplasmic MCP FrzCD that colocalizes with the nucleoid (GFP tagged FrzCD colocalizes with DAPI stained nucleoid). FrzCD interacts with histidine kinase FrzE and adaptor proteins FrzA and FrzB to form the core signalling unit. FrzE undergoes autophosphorylation and transfer phosphate to response regulators FrzX – resulting in cellular reversals, and FrzY. Methyl-esterase FrzG when phosphorylated by FrzE, removed methylation marks on conserved glutamate residues incorporated by constitutively active methyltransferase FrzF. The FrzCD cellular localization figure is adapted from *Moine et al., 2017*.

Objectives:

I. Biochemical characterization of receptor FrzCD

Identification and functional characterization of domains in FrzCD that facilitate oligomerization and cluster formation.

II. Understand the diversity and prevalence of cytoplasmic and membrane-bound MCPs

Identify characterizing features of cytoplasmic MCPs in terms of heptad repeats of the cytoplasmic signalling domain, distribution of HAMP and ligand binding domains.

III. Biochemical characterization of receptor-adaptor complex

Reconstitution of FrzCD-FrzA/B complex, and characterization of the interaction interface to understand the regulation of cluster formation by adaptor proteins.

IV. Structural characterization of receptor-adaptor complex

Determine the structure of receptor-adaptor complexes and identify characteristic features of the complexes that might influence core-signalling unit formation and signal transduction.

1.11 References

1. Adler, J. (1966a). Chemotaxis in Bacteria: Motile *Escherichia coli* migrate in bands that are influenced by oxygen and organic nutrients. *Science*, *153*(3737), 708–716. https://doi.org/10.1126/science.153.3737.708
2. Adler, J. (1966b). Effect of Amino Acids and Oxygen on Chemotaxis in Escherichia coli. *Journal of Bacteriology*, *92*(1), 121–129. https://doi.org/10.1128/jb.92.1.121-129.1966
3. Adler, J. (1969). Chemoreceptors in Bacteria. *Science*, *166*(3913), 1588–1597. https://doi.org/10.1126/science.166.3913.1588
4. Adler, J., & Dahl, M. M. (1967). A Method for Measuring the Motility of Bacteria and for Comparing Random and Non-random Motility. *Journal of General Microbiology*, *46*(2), 161–173. https://doi.org/10.1099/00221287-46-2-161
5. Adler, J., Hazelbauer, G. L., & Dahl, M. M. (1973). Chemotaxis Toward Sugars in Escherichia coli. *Journal of Bacteriology*, *115*(3), 824–847. https://doi.org/10.1128/jb.115.3.824-847.1973
6. Adler, J., & Templeton, B. (1967). The Effect of Environmental Conditions on the Motility of Escherichia coli. *Journal of General Microbiology*, *46*(2), 175–184. https://doi.org/10.1099/00221287-46-2-175
7. Alexander, R. P., & Zhulin, I. B. (2007). Evolutionary genomics reveals conserved structural determinants of signaling and adaptation in microbial chemoreceptors. *Proceedings of the National Academy of Sciences*, *104*(8), 2885–2890. https://doi.org/10.1073/pnas.0609359104
8. Alon, U., Surette, M. G., Barkai, N., & Leibler, S. (1999). Robustness in bacterial chemotaxis. *Nature*, *397*(6715), 168–171. https://doi.org/10.1038/16483
9. Ames, P., Studdert, C. A., Reiser, R. H., & Parkinson, J. S. (2002). Collaborative signaling by mixed chemoreceptor teams in Escherichia coli. *Proceedings of the National Academy of Sciences*, *99*(10), 7060–7065. https://doi.org/10.1073/pnas.092071899
10. Armstrong, J. B. (1972a). An S-adenosylmethionine requirement for chemotaxis in Escherichia coli. *Canadian Journal of Microbiology*, *18*(11), 1695–1701. https://doi.org/10.1139/m72-263
11. Armstrong, J. B. (1972b). Chemotaxis and methionine metabolism in Escherichia coli. *Canadian Journal of Microbiology*, *18*(5), 591–596. https://doi.org/10.1139/m72-093
12. Asinas, A. E., & Weis, R. M. (2006). Competitive and Cooperative Interactions in Receptor Signaling Complexes*. *Journal of Biological Chemistry*, *281*(41), 30512–30523. https://doi.org/10.1074/jbc.M606267200
13. Baker, M. D., Wolanin, P. M., & Stock, J. B. (2006). Systems biology of bacterial chemotaxis. *Current Opinion in Microbiology*, *9*(2), 187–192. https://doi.org/10.1016/j.mib.2006.02.007
14. Bardy, S. L., Briegel, A., Rainville, S., & Krell, T. (2017). Recent Advances and Future Prospects in Bacterial and Archaeal Locomotion and Signal Transduction. *Journal of Bacteriology*, *199*(18), 10.1128/jb.00203-17. https://doi.org/10.1128/jb.00203-17

15. Berg, H. C. (1974). Dynamic properties of bacterial flagellar motors. *Nature*, *249*(5452), 77–79. https://doi.org/10.1038/249077a0

16. Berg, H. C. (1975). Chemotaxis in Bacteria. *Annual Review of Biophysics*, *4*(Volume 4, 1975), 119–136. https://doi.org/10.1146/annurev.bb.04.060175.001003

17. Berg, H. C., & Brown, D. A. (1972). Chemotaxis in Escherichia coli analyzed by Three-dimensional Tracking. *Nature*, *239*(5374), 500–504. https://doi.org/10.1038/239500a0

18. Bilwes, A. M., Alex, L. A., Crane, B. R., & Simon, M. I. (1999). Structure of CheA, a Signal-Transducing Histidine Kinase. *Cell*, *96*(1), 131–141. https://doi.org/10.1016/S0092-8674(00)80966-6

19. Blackhart, B. D., & Zusman, D. R. (1985). "Frizzy" genes of Myxococcus xanthus are involved in control of frequency of reversal of gliding motility. *Proceedings of the National Academy of Sciences*, *82*(24), 8767–8770. https://doi.org/10.1073/pnas.82.24.8767

20. Blair, D. F. (1995). HOW BACTERIA SENSE AND SWIM. *Annual Review of Microbiology*, *49*(Volume 49,), 489–520. https://doi.org/10.1146/annurev.mi.49.100195.002421

21. Block, S. M., Segall, J. E., & Berg, H. C. (1982). Impulse responses in bacterial chemotaxis. *Cell*, *31*(1), 215–226. https://doi.org/10.1016/0092-8674(82)90421-4

22. Boldog, T., Grimme, S., Li, M., Sligar, S. G., & Hazelbauer, G. L. (2006). Nanodiscs separate chemoreceptor oligomeric states and reveal their signaling properties. *Proceedings of the National Academy of Sciences*, *103*(31), 11509–11514. https://doi.org/10.1073/pnas.0604988103

23. Borkovich, K. A., Alex, L. A., & Simon, M. I. (1992). Attenuation of sensory receptor signaling by covalent modification. *Proceedings of the National Academy of Sciences*, *89*(15), 6756–6760. https://doi.org/10.1073/pnas.89.15.6756

24. Borkovich, K. A., Kaplan, N., Hess, J. F., & Simon, M. I. (1989). Transmembrane signal transduction in bacterial chemotaxis involves ligand-dependent activation of phosphate group transfer. *Proceedings of the National Academy of Sciences*, *86*(4), 1208–1212. https://doi.org/10.1073/pnas.86.4.1208

25. Borkovich, K. A., & Simon, M. I. (1990). The dynamics of protein phosphorylation in bacterial chemotaxis. *Cell*, *63*(6), 1339–1348. https://doi.org/10.1016/0092-8674(90)90429-I

26. Bornhorst, J. A., & Falke, J. J. (2003). Quantitative Analysis of Aspartate Receptor Signaling Complex Reveals that the Homogeneous Two-state Model is Inadequate: Development of a Heterogeneous Two-state Model. *Journal of Molecular Biology*, *326*(5), 1597–1614. https://doi.org/10.1016/S0022-2836(03)00026-3

27. Bourret, R. B., Hess, J. F., Borkovich, K. A., Pakula, A. A., & Simon, M. I. (1989). Protein phosphorylation in chemotaxis and two-component regulatory systems of bacteria. *Journal of Biological Chemistry*, *264*(13), 7085–7088. https://doi.org/10.1016/S0021-9258(18)83200-8

28. Bourret, R. B., & Silversmith, R. E. (2010). Two-component signal transduction. *Current Opinion in Microbiology*, *13*(2), 113–115. https://doi.org/10.1016/j.mib.2010.02.003

29. Bourret, R. B., & Stock, A. M. (2002). Molecular Information Processing: Lessons from Bacterial Chemotaxis*. *Journal of Biological Chemistry*, *277*(12), 9625–9628. https://doi.org/10.1074/jbc.R100066200

30. Boyd, A., & Simon, M. I. (1980). Multiple electrophoretic forms of methyl-accepting chemotaxis proteins generated by stimulus-elicited methylation in Escherichia coli. *Journal of Bacteriology*, *143*(2), 809–815. https://doi.org/10.1128/jb.143.2.809-815.1980

31. Bray, D. (2002). Bacterial chemotaxis and the question of gain. *Proceedings of the National Academy of Sciences of the United States of America*, *99*(1), 7–9. https://doi.org/10.1073/pnas.022641699

32. Briegel, A., Ladinsky, M. S., Oikonomou, C., Jones, C. W., Harris, M. J., Fowler, D. J., Chang, Y.-W., Thompson, L. K., Armitage, J. P., & Jensen, G. J. (2014). Structure of bacterial cytoplasmic chemoreceptor arrays and implications for chemotactic signaling. *eLife*, *3*, e02151. https://doi.org/10.7554/eLife.02151

33. Briegel, A., Li, X., Bilwes, A. M., Hughes, K. T., Jensen, G. J., & Crane, B. R. (2012). Bacterial chemoreceptor arrays are hexagonally packed trimers of receptor dimers networked by rings of kinase and coupling proteins. *Proceedings of the National Academy of Sciences of the United States of America*, *109*(10), 3766–3771. https://doi.org/10.1073/pnas.1115719109

34. Briegel, A., Ortega, D. R., Huang, A., Oikonomou, C. M., Gunsalus, R. P., & Jensen, G. J. (2015). Structural conservation of chemotaxis machinery across Archaea and Bacteria. *Environmental Microbiology Reports*, *7*(3), 414–419. https://doi.org/10.1111/1758-2229.12265

35. Briegel, A., Ortega, D. R., Mann, P., Kjær, A., Ringgaard, S., & Jensen, G. J. (2016). Chemotaxis cluster 1 proteins form cytoplasmic arrays in Vibrio cholerae and are stabilized by a double signaling domain receptor DosM. *Proceedings of the National Academy of Sciences*, *113*(37), 10412–10417. https://doi.org/10.1073/pnas.1604693113

36. Briegel, A., Ortega, D. R., Tocheva, E. I., Wuichet, K., Li, Z., Chen, S., Müller, A., Iancu, C. V., Murphy, G. E., Dobro, M. J., Zhulin, I. B., & Jensen, G. J. (2009). Universal architecture of bacterial chemoreceptor arrays. *Proceedings of the National Academy of Sciences*, *106*(40), 17181–17186. https://doi.org/10.1073/pnas.0905181106

37. Briegel, A., Wong, M. L., Hodges, H. L., Oikonomou, C. M., Piasta, K. N., Harris, M. J., Fowler, D. J., Thompson, L. K., Falke, J. J., Kiessling, L. L., & Jensen, G. J. (2014). New insights into bacterial chemoreceptor array structure and assembly from electron cryotomography. *Biochemistry*, *53*(10), 1575–1585. https://doi.org/10.1021/bi5000614

38. Brown, D. A., & Berg, H. C. (1974). Temporal Stimulation of Chemotaxis in Escherichia coli. *Proceedings of the National Academy of Sciences*, *71*(4), 1388–1392. https://doi.org/10.1073/pnas.71.4.1388

39. Burt, A., Cassidy, C. K., Ames, P., Bacia-Verloop, M., Baulard, M., Huard, K., Luthey-Schulten, Z., Desfosses, A., Stansfeld, P. J., Margolin, W., Parkinson, J. S., & Gutsche, I. (2020). Complete structure of the chemosensory array core signalling unit in an E. coli minicell strain. *Nature Communications*, *11*(1), 743. https://doi.org/10.1038/s41467-020-14350-9

40. Burt, A., Cassidy, C. K., Stansfeld, P. J., & Gutsche, I. (2021). Alternative Architecture of the E. coli Chemosensory Array. *Biomolecules*, *11*(4), 495. https://doi.org/10.3390/biom11040495

41. Bustamante, V. H., Martínez-Flores, I., Vlamakis, H. C., & Zusman, D. R. (2004). Analysis of the Frz signal transduction system of Myxococcus xanthus shows the importance of the conserved C-terminal region of the cytoplasmic chemoreceptor FrzCD in sensing signals: Signal sensing by a cytoplasmic MCP. *Molecular Microbiology*, *53*(5), 1501–1513. https://doi.org/10.1111/j.1365-2958.2004.04221.x

42. Cannistraro, V. J., Glekas, G. D., Rao, C. V., & Ordal, G. W. (2011). Cellular Stoichiometry of the Chemotaxis Proteins in Bacillus subtilis. *Journal of Bacteriology*, *193*(13), 3220–3227. https://doi.org/10.1128/jb.01255-10

43. Cassidy, C. K., Himes, B. A., Sun, D., Ma, J., Zhao, G., Parkinson, J. S., Stansfeld, P. J., Luthey-Schulten, Z., & Zhang, P. (2020). Structure and dynamics of the E. coli chemotaxis core signaling complex by cryo-electron tomography and molecular simulations. *Communications Biology*, *3*(1), 24. https://doi.org/10.1038/s42003-019-0748-0

44. Cassidy, C. K., Qin, Z., Frosio, T., Gosink, K., Yang, Z., Sansom, M. S. P., Stansfeld, P. J., Parkinson, J. S., & Zhang, P. (2023). Structure of the native chemotaxis core signaling unit from phage E-protein lysed E. coli cells. *mBio*, *14*(5), e00793-23. https://doi.org/10.1128/mbio.00793-23

45. Chelsky, D., & Dahlquist, F. W. (1980). Structural studies of methyl-accepting chemotaxis proteins of Escherichia coli: Evidence for multiple methylation sites. *Proceedings of the National Academy of Sciences*, *77*(5), 2434–2438. https://doi.org/10.1073/pnas.77.5.2434

46. Collins, K. D., Lacal, J., & Ottemann, K. M. (2014). Internal Sense of Direction: Sensing and Signaling from Cytoplasmic Chemoreceptors. *Microbiology and Molecular Biology Reviews*, *78*(4), 672–684. https://doi.org/10.1128/MMBR.00033-14

47. DePamphilis, M. L., & Adler, J. (1971a). Attachment of Flagellar Basal Bodies to the Cell Envelope: Specific Attachment to the Outer, Lipopolysaccharide Membrane and the Cytoplasmic Membrane. *Journal of Bacteriology*, *105*(1), 396–407. https://doi.org/10.1128/jb.105.1.396-407.1971

48. DePamphilis, M. L., & Adler, J. (1971b). Fine Structure and Isolation of the Hook-Basal Body Complex of Flagella from Escherichia coli and Bacillus subtilis. *Journal of Bacteriology*, *105*(1), 384–395. https://doi.org/10.1128/jb.105.1.384-395.1971

49. Eisenbach, M. (1996). Control of bacterial chemotaxis. *Molecular Microbiology*, *20*(5), 903–910. https://doi.org/10.1111/j.1365-2958.1996.tb02531.x

50. Erbse, A. H., & Falke, J. J. (2009). The Core Signaling Proteins of Bacterial Chemotaxis Assemble To Form an Ultrastable Complex. *Biochemistry*, *48*(29), 6975–6987. https://doi.org/10.1021/bi900641c

51. Frank, V., Piñas, G. E., Cohen, H., Parkinson, J. S., & Vaknin, A. (2016). Networked Chemoreceptors Benefit Bacterial Chemotaxis Performance. *mBio*, *7*(6), 10.1128/mbio.01824-16. https://doi.org/10.1128/mbio.01824-16

52. Frank, V., & Vaknin, A. (2013). Prolonged stimuli alter the bacterial chemosensory clusters. *Molecular Microbiology*, *88*(3), 634–644. https://doi.org/10.1111/mmi.12215

53. Fredrick, K. L., & Helmann, J. D. (1994). Dual chemotaxis signaling pathways in Bacillus subtilis: A sigma D-dependent gene encodes a novel protein with both CheW and CheY homologous domains. *Journal of Bacteriology*, *176*(9), 2727–2735. https://doi.org/10.1128/jb.176.9.2727-2735.1994

54. Gegner, J. A., Graham, D. R., Roth, A. F., & Dahlquist, F. W. (1992). Assembly of an MCP receptor, CheW, and kinase CheA complex in the bacterial chemotaxis signal transduction pathway. *Cell*, *70*(6), 975–982. https://doi.org/10.1016/0092-8674(92)90247-A

55. Goy, M. F., Springer, M. S., & Adler, J. (1977). Sensory transduction in Escherichia coli: Role of a protein methylation reaction in sensory adaptation. *Proceedings of the National Academy of Sciences*, *74*(11), 4964–4968. https://doi.org/10.1073/pnas.74.11.4964

56. Goy, M. F., Springer, M. S., & Adler, J. (1978). Failure of sensory adaptation in bacterial mutants that are defective in a protein methylation reaction. *Cell*, *15*(4), 1231–1240. https://doi.org/10.1016/0092-8674(78)90049-1

57. Gumerov, V. M., Andrianova, E. P., & Zhulin, I. B. (2021). Diversity of bacterial chemosensory systems. *Current Opinion in Microbiology*, *61*, 42–50. https://doi.org/10.1016/j.mib.2021.01.016

58. Guzzo, M., Murray, S. M., Martineau, E., Lhospice, S., Baronian, G., My, L., Zhang, Y., Espinosa, L., Vincentelli, R., Bratton, B. P., Shaevitz, J. W., Molle, V., Howard, M., & Mignot, T. (2018). A gated relaxation oscillator mediated by FrzX controls morphogenetic movements in Myxococcus xanthus. *Nature Microbiology*, *3*(8), 948–959. https://doi.org/10.1038/s41564-018-0203-x

59. Hadjidemetriou, K., Kaur, S., Cassidy, C. K., & Zhang, P. (2022). Mechanisms of E. coli chemotaxis signaling pathways visualized using cryoET and computational approaches. *Biochemical Society Transactions*, *50*(6), 1595–1605. https://doi.org/10.1042/BST20220191

60. Haglin, E. R., Yang, W., Briegel, A., & Thompson, L. K. (2017). His-Tag-Mediated Dimerization of Chemoreceptors Leads to Assembly of Functional Nanoarrays. *Biochemistry*, *56*(44), 5874–5885. https://doi.org/10.1021/acs.biochem.7b00698

61. Hazelbauer, G. L. (2012). Bacterial Chemotaxis: The Early Years of Molecular Studies. *Annual Review of Microbiology*, *66*(Volume 66, 2012), 285–303. https://doi.org/10.1146/annurev-micro-092611-150120

62. Hazelbauer, G. L., & Adler, J. (1971). Role of the Galactose Binding Protein in Chemotaxis of Escherichia coli toward Galactose. *Nature New Biology*, *230*(12), 101–104. https://doi.org/10.1038/newbio230101a0

63. Hazelbauer, G. L., & Engström, P. (1980). Parallel pathways for transduction of chemotactic signals in Escherichia coli. *Nature*, *283*(5742), 98–100. https://doi.org/10.1038/283098a0

64. He, K., & Bauer, C. E. (2014). Chemosensory signaling systems that control bacterial survival. *Trends in Microbiology*, *22*(7), 389–398. https://doi.org/10.1016/j.tim.2014.04.004

65. Herrera Seitz, M. K., Frank, V., Massazza, D. A., Vaknin, A., & Studdert, C. A. (2014). Bacterial chemoreceptors of different length classes signal independently. *Molecular Microbiology*, *93*(4), 814–822. https://doi.org/10.1111/mmi.12700

66. Hess, J. F., Bourret, R. B., & Simon, M. I. (1988). Histidine phosphorylation and phosphoryl group transfer in bacterial chemotaxis. *Nature*, *336*(6195), 139–143. https://doi.org/10.1038/336139a0

67. Hess, J. F., Oosawa, K., Kaplan, N., & Simon, M. I. (1988). Phosphorylation of three proteins in the signaling pathway of bacterial chemotaxis. *Cell*, *53*(1), 79–87. https://doi.org/10.1016/0092-8674(88)90489-8

68. Hess, J. F., Oosawa, K., Matsumura, P., & Simon, M. I. (1987). Protein phosphorylation is involved in bacterial chemotaxis. *Proceedings of the National Academy of Sciences*, *84*(21), 7609–7613. https://doi.org/10.1073/pnas.84.21.7609

69. Huang, Z., Pan, X., Xu, N., & Guo, M. (2019). Bacterial chemotaxis coupling protein: Structure, function and diversity. *Microbiological Research*, *219*, 40–48. https://doi.org/10.1016/j.micres.2018.11.001

70. Jones, C. W., & Armitage, J. P. (2015). Positioning of bacterial chemoreceptors. *Trends in Microbiology*, *23*(5), 247–256. https://doi.org/10.1016/j.tim.2015.03.004

71. Karatan, E., Saulmon, M. M., Bunn, M. W., & Ordal, G. W. (2001). Phosphorylation of the Response Regulator CheV Is Required for Adaptation to Attractants during Bacillus subtilisChemotaxis *. *Journal of Biological Chemistry*, *276*(47), 43618–43626. https://doi.org/10.1074/jbc.M104955200

72. Karmakar, R. (2021). State of the art of bacterial chemotaxis. *Journal of Basic Microbiology*, *61*(5), 366–379. https://doi.org/10.1002/jobm.202000661

73. Keegstra, J. M., Carrara, F., & Stocker, R. (2022). The ecological roles of bacterial chemotaxis. *Nature Reviews Microbiology*, *20*(8), 491–504. https://doi.org/10.1038/s41579-022-00709-w

74. Kehry, M. R., Doak, T. G., & Dahlquist, F. W. (1985). Sensory adaptation in bacterial chemotaxis: Regulation of demethylation. *Journal of Bacteriology*, *163*(3), 983–990. https://doi.org/10.1128/jb.163.3.983-990.1985

75. Kim, K. K., Yokota, H., & Kim, S.-H. (1999). Four-helical-bundle structure of the cytoplasmic domain of a serine chemotaxis receptor. *Nature*, *400*(6746), 787–792. https://doi.org/10.1038/23512

76. Kleene, S. J., Toews, M. L., & Adler, J. (1977). Isolation of glutamic acid methyl ester from an Escherichia coli membrane protein involved in chemotaxis. *Journal of Biological Chemistry*, *252*(10), 3214–3218. https://doi.org/10.1016/S0021-9258(17)40373-5

77. Kondoh, H., Ball, C. B., & Adler, J. (1979). Identification of a methyl-accepting chemotaxis protein for the ribose and galactose chemoreceptors of Escherichia coli. *Proceedings of the National Academy of Sciences*, *76*(1), 260–264. https://doi.org/10.1073/pnas.76.1.260

78. Kort, E. N., Goy, M. F., Larsen, S. H., & Adler, J. (1975). Methylation of a membrane protein involved in bacterial chemotaxis. *Proceedings of the National Academy of Sciences*, *72*(10), 3939–3943. https://doi.org/10.1073/pnas.72.10.3939

79. Krembel, A., Colin, R., & Sourjik, V. (2015). Importance of Multiple Methylation Sites in Escherichia coli Chemotaxis. *PLOS ONE*, *10*(12), e0145582. https://doi.org/10.1371/journal.pone.0145582

80. Lacal, J., García-Fontana, C., Muñoz-Martínez, F., Ramos, J.-L., & Krell, T. (2010). Sensing of environmental signals: Classification of chemoreceptors according to the size of their ligand binding regions: Chemoreceptor diversity. *Environmental Microbiology*, *12*(11), 2873–2884. https://doi.org/10.1111/j.1462-2920.2010.02325.x

81. Lai, R.-Z., Gosink, K. K., & Parkinson, J. S. (2017). Signaling Consequences of Structural Lesions that Alter the Stability of Chemoreceptor Trimers of Dimers. *Journal of Molecular Biology*, *429*(6), 823–835. https://doi.org/10.1016/j.jmb.2017.02.007

82. Lai, R.-Z., Manson, J. M. B., Bormans, A. F., Draheim, R. R., Nguyen, N. T., & Manson, M. D. (2005). Cooperative Signaling among Bacterial Chemoreceptors. *Biochemistry*, *44*(43), 14298–14307. https://doi.org/10.1021/bi050567y

83. Lane, N. (2015). The unseen world: Reflections on Leeuwenhoek (1677) 'Concerning little animals.' *Philosophical Transactions of the Royal Society B: Biological Sciences*, *370*(1666), 20140344. https://doi.org/10.1098/rstb.2014.0344

84. Larsen, S. H., Reader, R. W., Kort, E. N., Tso, W.-W., & Adler, J. (1974). Change in direction of flagellar rotation is the basis of the chemotactic response in Escherichia coli. *Nature*, *249*(5452), 74–77. https://doi.org/10.1038/249074a0

85. Li, G., & Weis, R. M. (2000). Covalent Modification Regulates Ligand Binding to Receptor Complexes in the Chemosensory System of *Escherichia coli*. *Cell*, *100*(3), 357–365. https://doi.org/10.1016/S0092-8674(00)80671-6

86. Li, M., & Hazelbauer, G. L. (2004). Cellular Stoichiometry of the Components of the Chemotaxis Signaling Complex. *Journal of Bacteriology*, *186*(12), 3687–3694. https://doi.org/10.1128/jb.186.12.3687-3694.2004

87. Li, M., & Hazelbauer, G. L. (2005). Adaptational assistance in clusters of bacterial chemoreceptors. *Molecular Microbiology*, *56*(6), 1617–1626. https://doi.org/10.1111/j.1365-2958.2005.04641.x

88. Li, M., & Hazelbauer, G. L. (2011). Core unit of chemotaxis signaling complexes. *Proceedings of the National Academy of Sciences*, *108*(23), 9390–9395. https://doi.org/10.1073/pnas.1104824108

89. Li, M., & Hazelbauer, G. L. (2014). Selective allosteric coupling in core chemotaxis signaling complexes. *Proceedings of the National Academy of Sciences of the United States of America*, *111*(45), 15940–15945. https://doi.org/10.1073/pnas.1415184111

90. Li, X., Fleetwood, A. D., Bayas, C., Bilwes, A. M., Ortega, D. R., Falke, J. J., Zhulin, I. B., & Crane, B. R. (2013). The 3.2 Å Resolution Structure of a Receptor:CheA:CheW Signaling Complex Defines Overlapping Binding Sites and Key Residue Interactions within Bacterial Chemosensory Arrays. *Biochemistry*, *52*(22), 3852–3865. https://doi.org/10.1021/bi400383e

91. Liu, J., Hu, B., Morado, D. R., Jani, S., Manson, M. D., & Margolin, W. (2012). Molecular architecture of chemoreceptor arrays revealed by cryoelectron tomography of Escherichia coli minicells. *Proceedings of the National Academy of Sciences of the*

United States of America, *109*(23), E1481–E1488. https://doi.org/10.1073/pnas.1200781109

92. Long, J., Zucker, S. W., & Emonet, T. (2017). Feedback between motion and sensation provides nonlinear boost in run-and-tumble navigation. *PLOS Computational Biology*, *13*(3), e1005429. https://doi.org/10.1371/journal.pcbi.1005429

93. Lupas, A., & Stock, J. (1989). Phosphorylation of an N-terminal Regulatory Domain Activates the CheB Methylesterase in Bacterial Chemotaxis. *Journal of Biological Chemistry*, *264*(29), 17337–17342. https://doi.org/10.1016/S0021-9258(18)71497-X

94. Macnab, R. M., & Koshland, D. E. (1972). The Gradient-Sensing Mechanism in Bacterial Chemotaxis. *Proceedings of the National Academy of Sciences*, *69*(9), 2509–2512. https://doi.org/10.1073/pnas.69.9.2509

95. Maddock, J. R., & Shapiro, L. (1993). Polar Location of the Chemoreceptor Complex in the Escherichia coli Cell. *Science*, *259*(5102), 1717–1723. https://doi.org/10.1126/science.8456299

96. Matilla, M. A., & Krell, T. (2017). Chemoreceptor-based signal sensing. *Current Opinion in Biotechnology*, *45*, 8–14. https://doi.org/10.1016/j.copbio.2016.11.021

97. Matilla, M. A., & Krell, T. (2018). The effect of bacterial chemotaxis on host infection and pathogenicity. *FEMS Microbiology Reviews*, *42*(1), fux052. https://doi.org/10.1093/femsre/fux052

98. Mauriello, E. M. F. (2020). How an unusual chemosensory system forms arrays on the bacterial nucleoid. *Biochemical Society Transactions*, *48*(2), 347–356. https://doi.org/10.1042/BST20180450

99. Mauriello, E. M. F., Jones, C., Moine, A., & Armitage, J. P. (2018). Cellular Targeting and Segregation of Bacterial Chemosensory Systems. *FEMS Microbiology Reviews*. https://doi.org/10.1093/femsre/fuy015

100. McBride, M. J., Köhler, T., & Zusman, D. R. (1992). Methylation of FrzCD, a methyl-accepting taxis protein of Myxococcus xanthus, is correlated with factors affecting cell behavior. *Journal of Bacteriology*, *174*(13), 4246–4257. https://doi.org/10.1128/jb.174.13.4246-4257.1992

101. Mesibov, R., & Adler, J. (1972). Chemotaxis Toward Amino Acids in Escherichia coli. *Journal of Bacteriology*, *112*(1), 315–326. https://doi.org/10.1128/jb.112.1.315-326.1972

102. Moine, A., Espinosa, L., Martineau, E., Yaikhomba, M., Jazleena, P. J., Byrne, D., Biondi, E. G., Notomista, E., Brilli, M., Molle, V., Gayathri, P., Mignot, T., & Mauriello, E. M. F. (2017). The nucleoid as a scaffold for the assembly of bacterial signaling complexes. *PLOS Genetics*, *13*(11), e1007103. https://doi.org/10.1371/journal.pgen.1007103

103. Moore, J. P., Kamino, K., Kottou, R., Shimizu, T. S., & Emonet, T. (2024). Signal integration and adaptive sensory diversity tuning in *Escherichia coli* chemotaxis. *Cell Systems*, *15*(7), 628-638.e8. https://doi.org/10.1016/j.cels.2024.06.003

104. Muok, A. R., Ortega, D. R., Kurniyati, K., Yang, W., Maschmann, Z. A., Sidi Mabrouk, A., Li, C., Crane, B. R., & Briegel, A. (2020). Atypical chemoreceptor arrays

accommodate high membrane curvature. *Nature Communications*, *11*(1), 5763. https://doi.org/10.1038/s41467-020-19628-6

105. Natale, A. M., Duplantis, J. L., Piasta, K. N., & Falke, J. J. (2013). Structure, Function, and On–Off Switching of a Core Unit Contact between CheA Kinase and CheW Adaptor Protein in the Bacterial Chemosensory Array: A Disulfide Mapping and Mutagenesis Study. *Biochemistry*, *52*(44), 7753–7765. https://doi.org/10.1021/bi401159k

106. Neumann, S., Vladimirov, N., Krembel, A. K., Wingreen, N. S., & Sourjik, V. (2014). Imprecision of Adaptation in Escherichia coli Chemotaxis. *PLOS ONE*, *9*(1), e84904. https://doi.org/10.1371/journal.pone.0084904

107. Ninfa, E. G., Stock, A., Mowbray, S., & Stock, J. (1991). Reconstitution of the bacterial chemotaxis signal transduction system from purified components. *Journal of Biological Chemistry*, *266*(15), 9764–9770. https://doi.org/10.1016/S0021-9258(18)92886-3

108. Oosawa, K., Hess, J. F., & Simon, M. I. (1988). Mutants defective in bacterial chemotaxis show modified protein phosphorylation. *Cell*, *53*(1), 89–96. https://doi.org/10.1016/0092-8674(88)90490-4

109. Ortega, Á., Zhulin, I. B., & Krell, T. (2017). Sensory Repertoire of Bacterial Chemoreceptors. *Microbiology and Molecular Biology Reviews*, *81*(4). https://doi.org/10.1128/MMBR.00033-17

110. Ortega, D. R., Kjær, A., & Briegel, A. (2020). The chemosensory systems of Vibrio cholerae. *Molecular Microbiology*, *114*(3), 367–376. https://doi.org/10.1111/mmi.14520

111. Park, S.-Y., Borbat, P. P., Gonzalez-Bonet, G., Bhatnagar, J., Pollard, A. M., Freed, J. H., Bilwes, A. M., & Crane, B. R. (2006). Reconstruction of the chemotaxis receptor–kinase assembly. *Nature Structural & Molecular Biology*, *13*(5), 400–407. https://doi.org/10.1038/nsmb1085

112. Parkinson, J. S. (1975). Genetics of chemotactic behavior in bacteria. *Cell*, *4*(3), 183–188. https://doi.org/10.1016/0092-8674(75)90166-X

113. Parkinson, J. S. (1976). cheA, cheB, and cheC genes of Escherichia coli and their role in chemotaxis. *Journal of Bacteriology*, *126*(2), 758–770. https://doi.org/10.1128/jb.126.2.758-770.1976

114. Parkinson, J. S. (1978). Complementation analysis and deletion mapping of Escherichia coli mutants defective in chemotaxis. *Journal of Bacteriology*, *135*(1), 45–53. https://doi.org/10.1128/jb.135.1.45-53.1978

115. Parkinson, J. S. (2013). Bacterial Chemotaxis. In S. Maloy & K. Hughes (Eds.), *Brenner's Encyclopedia of Genetics (Second Edition)* (pp. 258–261). Academic Press. https://doi.org/10.1016/B978-0-12-374984-0.00225-4

116. Parkinson, J. S., Hazelbauer, G. L., & Falke, J. J. (2015). Signaling and sensory adaptation in Escherichia coli chemoreceptors: 2015 update. *Trends in Microbiology*, *23*(5), 257–266. https://doi.org/10.1016/j.tim.2015.03.003

117. Piñas, G. E., DeSantis, M. D., Cassidy, C. K., & Parkinson, J. S. (2022). Hexameric rings of the scaffolding protein CheW enhance response sensitivity and cooperativity in *Escherichia coli* chemoreceptor arrays. *Science Signaling*, *15*(718), eabj1737. https://doi.org/10.1126/scisignal.abj1737

118. Piñas, G. E., Frank, V., Vaknin, A., & Parkinson, J. S. (2016). The source of high signal cooperativity in bacterial chemosensory arrays. *Proceedings of the National Academy of Sciences of the United States of America*, *113*(12), 3335–3340. https://doi.org/10.1073/pnas.1600216113

119. Porter, S. L., Wadhams, G. H., & Armitage, J. P. (2011). Signal processing in complex chemotaxis pathways. *Nature Reviews Microbiology*, *9*(3), 153–165. https://doi.org/10.1038/nrmicro2505

120. Qin, Z., & Zhang, P. (2021). Studying bacterial chemosensory array with CryoEM. *Biochemical Society Transactions*, *49*(5), 2081–2089. https://doi.org/10.1042/BST20210080

121. Rao, C. V., Glekas, G. D., & Ordal, G. W. (2008). The three adaptation systems of *Bacillus subtilis* chemotaxis. *Trends in Microbiology*, *16*(10), 480–487. https://doi.org/10.1016/j.tim.2008.07.003

122. Rao, C. V., & Ordal, G. W. (2009). The Molecular Basis of Excitation and Adaptation during Chemotactic Sensory Transduction in Bacteria. In M. Collin & R. Schuch (Eds.), *Contributions to Microbiology* (Vol. 16, pp. 33–64). KARGER. https://doi.org/10.1159/000219372

123. Riechmann, C., & Zhang, P. (2023). Recent structural advances in bacterial chemotaxis signalling. *Current Opinion in Structural Biology*, *79*, 102565. https://doi.org/10.1016/j.sbi.2023.102565

124. Segall, J. E., Block, S. M., & Berg, H. C. (1986). Temporal comparisons in bacterial chemotaxis. *Proceedings of the National Academy of Sciences*, *83*(23), 8987–8991. https://doi.org/10.1073/pnas.83.23.8987

125. Silverman, M., & Simon, M. (1974). Flagellar rotation and the mechanism of bacterial motility. *Nature*, *249*(5452), 73–74. https://doi.org/10.1038/249073a0

126. Silverman, M., & Simon, M. (1977). Chemotaxis in Escherichia coli: Methylation of che gene products. *Proceedings of the National Academy of Sciences*, *74*(8), 3317–3321. https://doi.org/10.1073/pnas.74.8.3317

127. Sourjik, V., & Berg, H. C. (2000). Localization of components of the chemotaxis machinery of Escherichia coli using fluorescent protein fusions. *Molecular Microbiology*, *37*(4), 740–751. https://doi.org/10.1046/j.1365-2958.2000.02044.x

128. Sourjik, V., & Berg, H. C. (2002). Receptor sensitivity in bacterial chemotaxis. *Proceedings of the National Academy of Sciences*, *99*(1), 123–127. https://doi.org/10.1073/pnas.011589998

129. Sourjik, V., & Berg, H. C. (2004). Functional interactions between receptors in bacterial chemotaxis. *Nature*, *428*(6981), 437–441. https://doi.org/10.1038/nature02406

130. Springer, M. S., Goy, M. F., & Adler, J. (1977a). Sensory transduction in Escherichia coli: A requirement for methionine in sensory adaptation. *Proceedings of the National Academy of Sciences*, *74*(1), 183–187. https://doi.org/10.1073/pnas.74.1.183

131. Springer, M. S., Goy, M. F., & Adler, J. (1977b). Sensory transduction in Escherichia coli: Two complementary pathways of information processing that involve methylated proteins. *Proceedings of the National Academy of Sciences*, *74*(8), 3312–3316. https://doi.org/10.1073/pnas.74.8.3312

132. Springer, M. S., Kort, E. N., Larsen, S. H., Ordal, G. W., Reader, R. W., & Adler, J. (1975). Role of methionine in bacterial chemotaxis: Requirement for tumbling and involvement in information processing. *Proceedings of the National Academy of Sciences*, *72*(11), 4640–4644. https://doi.org/10.1073/pnas.72.11.4640

133. Springer, W. R., & Koshland, D. E. (1977). Identification of a protein methyltransferase as the cheR gene product in the bacterial sensing system. *Proceedings of the National Academy of Sciences*, *74*(2), 533–537. https://doi.org/10.1073/pnas.74.2.533

134. Stock, J. B., & Baker, M. D. (2009). Chemotaxis. In M. Schaechter (Ed.), *Encyclopedia of Microbiology (Third Edition)* (pp. 71–78). Academic Press. https://doi.org/10.1016/B978-012373944-5.00068-7

135. Stock, J. B., & Koshland, D. E. (1978). A protein methylesterase involved in bacterial sensing. *Proceedings of the National Academy of Sciences*, *75*(8), 3659–3663. https://doi.org/10.1073/pnas.75.8.3659

136. Studdert, C. A., & Parkinson, J. S. (2004). Crosslinking snapshots of bacterial chemoreceptor squads. *Proceedings of the National Academy of Sciences*, *101*(7), 2117–2122. https://doi.org/10.1073/pnas.0308622100

137. Studdert, C. A., & Parkinson, J. S. (2005). Insights into the organization and dynamics of bacterial chemoreceptor clusters through in vivo crosslinking studies. *Proceedings of the National Academy of Sciences*, *102*(43), 15623–15628. https://doi.org/10.1073/pnas.0506040102

138. Thiem, S., Kentner, D., & Sourjik, V. (2007). Positioning of chemosensory clusters in E. coli and its relation to cell division. *The EMBO Journal*, *26*(6), 1615–1623. https://doi.org/10.1038/sj.emboj.7601610

139. Toews, M. L., Goy, M. F., Springer, M. S., & Adler, J. (1979). Attractants and repellents control demethylation of methylated chemotaxis proteins in Escherichia coli. *Proceedings of the National Academy of Sciences*, *76*(11), 5544–5548. https://doi.org/10.1073/pnas.76.11.5544

140. Tso, W.-W., & Adler, J. (1974). Negative Chemotaxis in Escherichia coli. *Journal of Bacteriology*, *118*(2), 560–576. https://doi.org/10.1128/jb.118.2.560-576.1974

141. Uchida, Y., Hamamoto, T., Che, Y.-S., Takahashi, H., Parkinson, J. S., Ishijima, A., & Fukuoka, H. (2022). The Chemoreceptor Sensory Adaptation System Produces Coordinated Reversals of the Flagellar Motors on an Escherichia coli Cell. *Journal of Bacteriology*, *204*(12), e00278-22. https://doi.org/10.1128/jb.00278-22

142. Van Der Werf, P., & Koshland, D. E. (1977). Identification of a gamma-glutamyl methyl ester in bacterial membrane protein involved in chemotaxis. *Journal of Biological Chemistry*, *252*(8), 2793–2795. https://doi.org/10.1016/S0021-9258(17)40530-8

143. Wadhams, G. H., & Armitage, J. P. (2004). Making sense of it all: Bacterial chemotaxis. *Nature Reviews Molecular Cell Biology*, *5*(12), Article 12. https://doi.org/10.1038/nrm1524

144. Wong-Ng, J., Melbinger, A., Celani, A., & Vergassola, M. (2016). The Role of Adaptation in Bacterial Speed Races. *PLOS Computational Biology*, *12*(6), e1004974. https://doi.org/10.1371/journal.pcbi.1004974

145. Wuichet, K., & Zhulin, I. B. (2010). Origins and Diversification of a Complex Signal Transduction System in Prokaryotes. *Science Signaling*, *3*(128), ra50–ra50. https://doi.org/10.1126/scisignal.2000724

146. Wylie, D., Stock, A., Wong, C.-Y., & Stock, J. (1988). Sensory transduction in bacterial chemotaxis involves phosphotransfer between CHE proteins. *Biochemical and Biophysical Research Communications*, *151*(2), 891–896. https://doi.org/10.1016/S0006-291X(88)80365-6

147. Yamaichi, Y., Bruckner, R., Ringgaard, S., Möll, A., Cameron, D. E., Briegel, A., Jensen, G. J., Davis, B. M., & Waldor, M. K. (2012). A multidomain hub anchors the chromosome segregation and chemotactic machinery to the bacterial pole. *Genes & Development*, *26*(20), 2348–2360. https://doi.org/10.1101/gad.199869.112

148. Yang, W., Alvarado, A., Glatter, T., Ringgaard, S., & Briegel, A. (2018). Baseplate variability of Vibrio cholerae chemoreceptor arrays. *Proceedings of the National Academy of Sciences*, *115*(52), 13365–13370. https://doi.org/10.1073/pnas.1811931115

149. Yang, W., & Briegel, A. (2020). Diversity of Bacterial Chemosensory Arrays. *Trends in Microbiology*, *28*(1), 68–80. https://doi.org/10.1016/j.tim.2019.08.002

150. Zhang, P., Khursigara, C. M., Hartnell, L. M., & Subramaniam, S. (2007). Direct visualization of Escherichia coli chemotaxis receptor arrays using cryo-electron microscopy. *Proceedings of the National Academy of Sciences*, *104*(10), 3777–3781. https://doi.org/10.1073/pnas.0610106104

Chapter 2

Biochemical characterization of cytoplasmic FrzCD chemosensory receptor from *M. xanthus*

Some sections are reprinted from *Jazleena, Das, Guiseppi et al., 2025, mBio*.

(DOI: https://doi.org/10.1128/mbio.00057-25)

2.1 Introduction

M. xanthus is a soil-dwelling, rod-shaped, Gram-negative predatory bacterium. It exhibits complex multicellular behaviour for collective motility, predation, as well as the formation of multicellular biofilms (fruiting bodies) *(Mercier & Mignot, 2016)*. It predates bacteria, yeast, and fungi *(Thiery & Kaimer, 2020)*. The bacteria exhibit gliding motility, a form of motility characterized by smooth movement along the long axis of the cells at the soil- or liquid-air interface, without the use of a flagellum *(Burchard, 1981)*. *Myxococcus* cells move on solid surfaces at a rate of 2-4 μm/min as a coordinated group of swarming cells with characteristic waves (ripples) to invade prey colonies *(Mauriello et al., 2010; Kaiser & Crosby, 1983)*. The bacteria secrete extracellular compounds (antibiotics and digestive enzymes) and kill and consume the biomass. After consumption and starvation, rippling subsides, giving way to a major transition in which large groups form aggregates that mature into spore-filled fruiting bodies **(Figure 2.1)** *(Dinet et al., 2021; Mercier & Mignot, 2016)*. *M. xanthus* use two motility systems – social (S) motility for coordinated group movement mediated by type IV pili at cell poles, and adventurous (A) motility of individual cells by focal adhesion Agl/Glt complexes *(Zhang et al., 2012; Nan & Zusman, 2011; Mauriello et al., 2010; Kaiser, 1979; Hodgkin & Kaiser, 1979)*. The rod-shaped cells have well-defined leading and lagging poles, defining front-rear polarity, and move in the direction of their long axis *(Carreira et al., 2022; Schumacher & Søgaard-Andersen, 2017)*. The cells occasionally swap the leading and lagging poles, resulting in reversals in the direction of movement *(Blackhart & Zusman, 1985)*.

M. xanthus cells regulate the direction of motility by controlling the frequency of polarity reversals similar to tumbling observed in *E. coli* cells **(Figure 2.2)** *(Schumacher & Søgaard-Andersen, 2017; Zhang et al., 2012; McBride et al., 1989)*. The reversals are coordinated to redirect the movements in response to attractants or repellents *(Shi et al., 1993)*. Motility was biased towards nutrient-rich areas, such as yeast extract or casitone, and away from repellents, including short-chain alcohols and DMSO *(Shi et al., 1993)*. The two motility modules, adventurous (A) and social (S), showed selective preferences for firm and soft surfaces, respectively (*Shi & Zusman, 1993)*. The bacteria, in the presence of nutrients, undergo polarity reversals every 10-15 minutes, taking 30-60 seconds for each reversal *(Blackhart & Zusman, 1985)*. The polarity reversals are crucial for the successful development cycle of *M. xanthus* because the aggregation of *M. xanthus* cells into fruiting bodies is dependent on the frequency of reversals *(Bustamante et al., 2004)*.

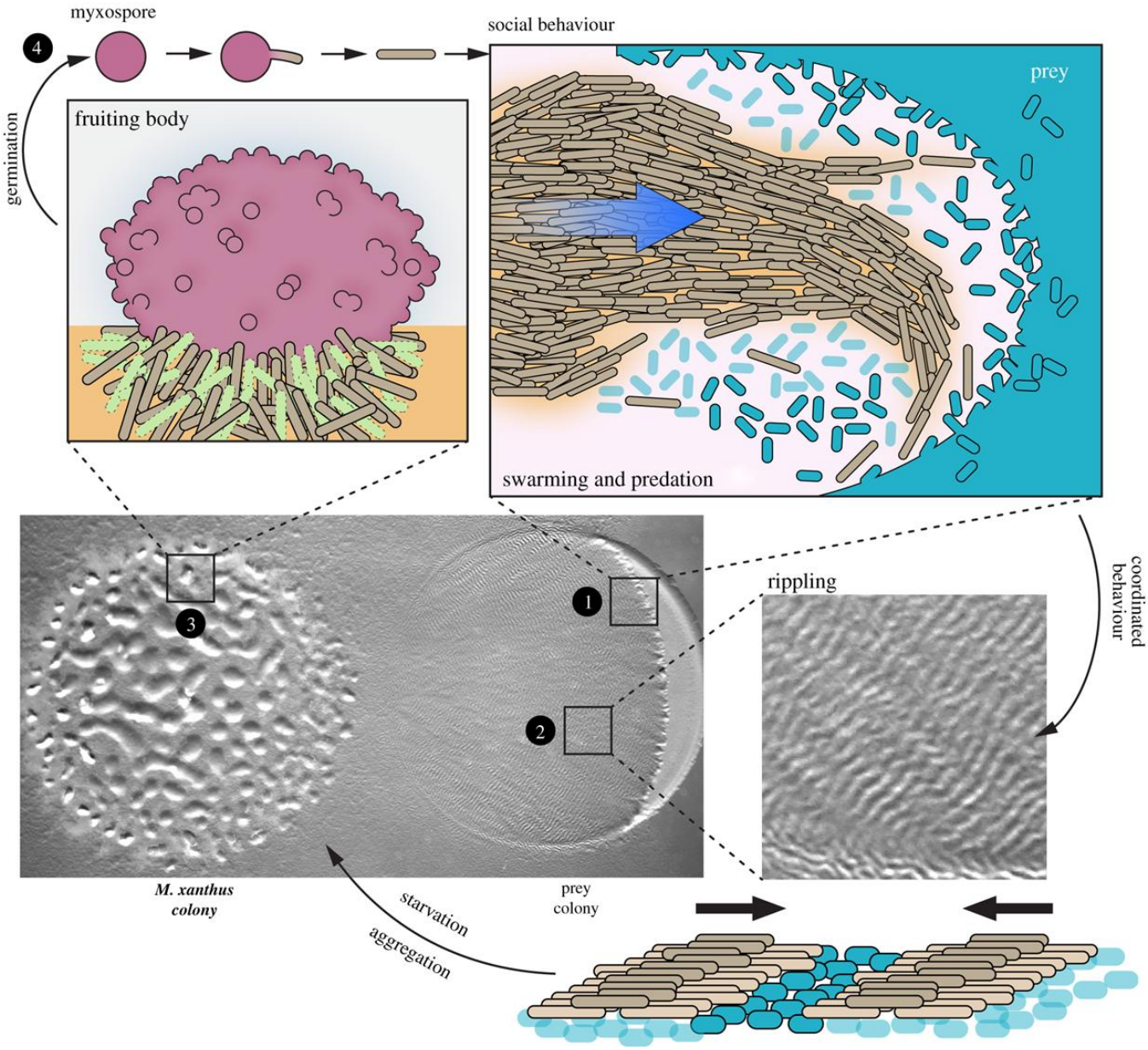


Figure 2.1 Social life cycle of *M. xanthus* involves complex coordinated group behaviour to effectively manage nutrient availability (adapted from *Dinet et al., 2021*). The picture in the middle shows *M. xanthus* colony invading *E. coli* colony. A predation front (1) is observed where *M. xanthus* swarm (cells depicted as light brown colour in the top right cartoon) invades prey colony (cyan cells, lysed cells in light blue colour). Cells move in a coordinated manner, releasing enzymes to lyse prey cells and share the nutrients communally, and characteristic 'rippling' pattern (2) is observed when swarm of cells collides due to opposing direction in polarity reversals (cartoon in bottom right). Fruiting body formation (3) is observed in a nutrient-poor environment, where starving cells aggregate to form multicellular fruiting body (upper left cartoon). The fruiting body contains highly resistant, dormant cells, known as myxospores (dark pink), as well as vegetative cells that form the outer structure, referred to as peripheral rods (light brown). Additionally, cells undergoing programmed cell death (light green) are likely providing nutrients for the sporulation process. Under favourable conditions, dormant myxospores germinate (4), developing into active, vegetative rod-shaped cells (light brown) that can form a new, cooperative community to restart the cycle.

Out of eight chemosensory systems and a total of 21 chemoreceptors in *M. xanthus (Moine et al., 2014)*, the Frz chemosensory system regulates the frequency of polarity reversals in the bacterium *(Blackhart & Zusman, 1985)*. Cells lacking the Frz system exhibit minimal polarity reversals. Hyper-reversal behaviour is observed in cells with a constitutively active Frz system, where cells oscillate back and forth without any net movement *(Blackhart & Zusman, 1985; Bustamante et al., 2004)*. The Frz system was first identified when mutants of *Myxococcus xanthus* incapable of forming fruiting bodies were isolated. These nonfruiting mutants, called "Frizzy", formed frizzy filaments instead of typical fruiting bodies on soft agar *(Zusman, 1982)*. The responsible genes, named *frz* genes after the "frizzy" phenotype, were later identified *(Blackhart & Zusman, 1985)*. Regulation of the polarity reversal frequency is crucial for the coordinated distribution of colonies, the formation of a characteristic 'ripple' pattern, and the development of fruiting bodies *(Sager & Kaiser, 1994; Blackhart & Zusman, 1985)*. During 'rippling' there is an increase in reversal frequency, which decreases during the aggregation stage of fruiting body formation *(Jelsbak & Søgaard-Andersen, 2002; Sager & Kaiser, 1994)*.

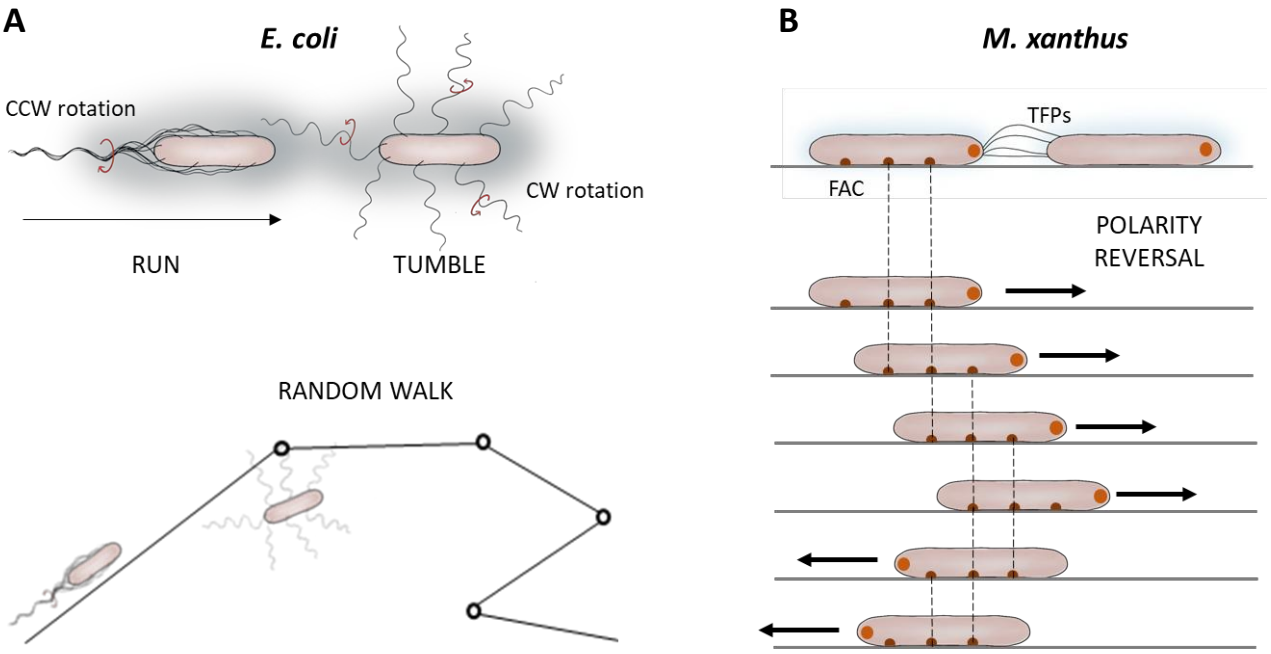


Figure 2.2 Motility in *E. coli* and *M. xanthus*. (A) Run and Tumble in *E. coli,* regulated by counter-clockwise (CCW) rotation and clockwise (CW) rotation of flagella, respectively, give rise to a random walk. (B) Gliding motility in *M. xanthus* is mediated by Type IV pilus (TFP) and focal adhesion complexes (FAC). Cells undergo polarity reversals where the leading pole becomes the new lagging pole, and the direction of motility reverses. The frequency of tumbling in *E. coli* and polarity reversals in *M. xanthus*, in response to environmental cues, dictates the direction of motility towards attractants and away from repellents, respectively.

The Frz chemosensory system (CSS), responsible for regulating motility and, consequently, chemotaxis in *M. xanthus*, is homologous to the Che pathway in *E. coli* **(Figure 2.3)** *(McBride et al., 1989)*. FrzCD, a cytoplasmic methyl-accepting chemotaxis protein, in presence of adaptor protein FrzA (CheW homolog), triggers autophosphorylation of histidine kinase FrzE (CheA homolog) *(Inclán et al., 2008)*. The system has another CheW homolog, FrzB, and two CheY-like response regulators, FrzX and FrzZ *(Bustamante et al., 2004; Guzzo et al., 2018)*. The adaptation of the CSS is mediated by methylation/demethylation of FrzCD by methyltransferase FrzF (CheR homolog), and methylesterase FrzG (CheB homolog) (**Figure 2.3)** *(Astling et al., 2006)*. The cytoplasmic receptor MCP FrzCD undergoes methylation in presence of attractants like casitone, yeast extract and demethylation in presence of repellents like isoamyl alcohol (IAA), ethanol and DMSO *(McBride et al., 1992)*. However, signals that activate the FrzCD pathway are yet to be explored, as the protein lacks any canonical ligand-binding domain.

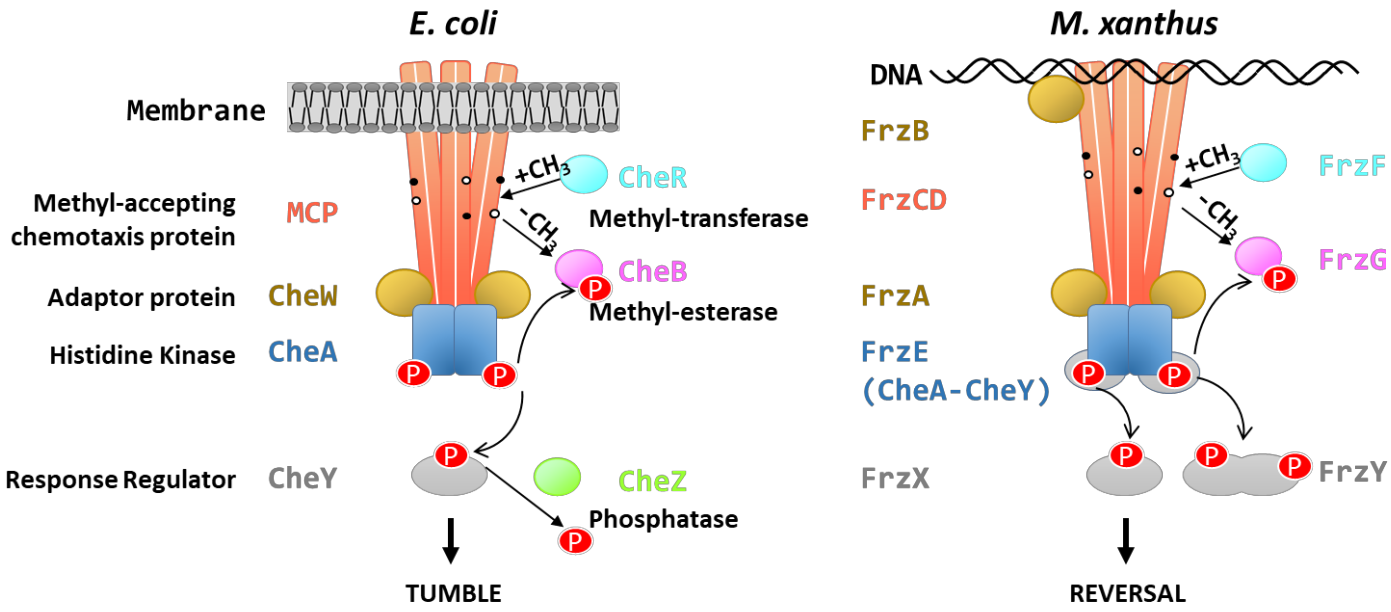


Figure 2.3 Frz chemosensory system of *M. xanthus* is homologous to the Che pathway from *E. coli*. The receptor FrzCD interacts with CheW homolog FrzA and CheA homolog FrzE. FrzB is another CheW homolog of Frz CSS. FrzF and FrzG are homologs of CheR and CheB, respectively. Phosphorylation of CheY homolog FrzX mediates polarity reversals in *M. xanthus* analogous to tumbling in *E. coli*. Proposed organization of Frz CSS using DNA as a scaffold, depicted as homology to Che proteins *(Mauriello, 2020)*.

FrzCD is a novel cytoplasmic MCP that uses nucleoid as a scaffold for the assembly of chemosensory macromolecular complexes, which are observed as multiple clusters along the length of the nucleoid *(Guiseppi et al., 2019; Moine et al., 2017)*. It has a conserved coiled-coil C-terminal methyl-accepting (MA) domain and a positively charged N-terminal region

(residues 1–30), responsible for DNA binding (DB domain) in a sequence-independent manner *(Moine et al., 2017)*. In the absence of the DB domain, the receptor fails to assemble into chemosensory clusters *(Moine et al., 2017)*. Although the architecture of these clusters is not visualized, they exhibit properties of allosteric interactions with cooperative amplification in response to a signal *(Moine et al., 2017)*. Additionally, di-HAMP domains were identified between DB domain and methyl-accepting signalling domain *(MS Thesis, P. J. Jazleena, (Jazleena, 2018; Jazleena, Das, Guiseppi et al., 2025))*. The di-HAMP domains restrict the oligomeric status of FrzCD to a dimer in solution in the absence of DNA *(MS Thesis, P. J. Jazleena, (Jazleena 2018; Jazleena, Das, Guiseppi et al., 2025))*. Here, we initially confirmed the domain boundaries of the FrzCD using multiple sequence alignment followed by homology modelling. The DNA-binding property of the receptor was characterized using electrophoretic mobility shift assay and fluorescence anisotropy. MA domain was found to be essential for the stable formation of higher-order FrzCD–DNA complexes. In this chapter, we investigated the DNA-binding property of FrzCD and its implication in stable cluster formation mediated by the MA domain.

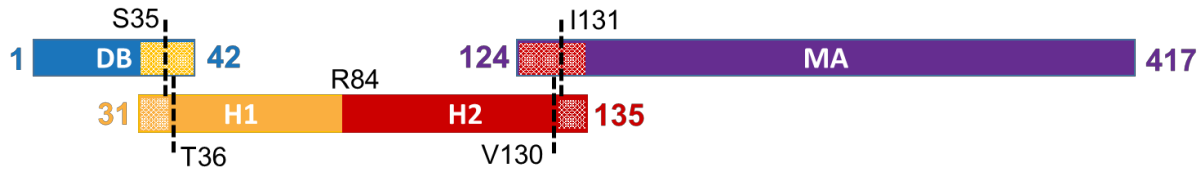
2.2 Materials and Methods

2.2.1 Domain architecture prediction for FrzCD

Secondary structure of FrzCD was predicted using PSIPRED *(Buchan & Jones, 2019)* and JPred 4 *(Drozdetskiy et al., 2015)*. The N-terminal DNA-binding domain sequence FrzCD was aligned against sequences of DB domain sequences from basic leucine zipper (bZIP) families such as 1GU4, Creb1, ATF4, Fos, and Jun using Jalview software (A. M. Waterhouse et al., 2009). A multiple sequence alignment (MSA) was performed for FrzCD against poly-HAMP domains of the Aer2 receptor from *P. aeruginosa (Airola et al., 2010)* using Jalview software *(A. M. Waterhouse et al., 2009)*. Based on the secondary structure prediction as well as MSA, domain boundaries were predicted for FrzCD.

i. **Identification of domain boundaries** from secondary structural prediction using Jpred 4:
- DNA binding (**DB**): 1-30
- HAMP (**H1** and **H2**): 31-135
- Methyl accepting (**MA**, 40H): 136-416

ii. **Modelling of individual domains** as dimers (with 12 residues overlap between domains for superimposition):
- Homology modelling of **DB** (1- 42) against GCN4 (2DGC) in SWISS-MODEL.
- Concatenated **di-HAMP** (31-135) was modelled using H1 and H2 of poly-HAMP AER2 (3LNR) in SWISS-MODEL.
- CCBuilder was used to generate four-helix bundle of two coil-coiled **MA** (124-417) dimers.



iii. **Superimposition** of the domain dimers based on C-α of overlap regions. The domains were joined at residue S34 and S35 between DB and HAMP, and residue V130 and I131 between HAMP and MA to get the final FrzCD model.

Figure 2.4 Workflow for generating a homology model of FrzCD dimer.

2.2.2 Bioinformatics analysis and modelling of FrzCD

FrzCD was dissected into the DNA-binding (DB), di-HAMP (H1 and H2) and methyl-accepting (MA) domains. To obtain a homology model for FrzCD, the approach involved modelling each of these domains separately as dimers with a 12-residue overlap to assemble the model **(Workflow in Figure 2.4)**. Therefore, for DB, residues 1-42 were modelled against

GCN4 (PDB: 2dgc), while the di-HAMP domains (residues 31-135) were modelled against HAMP1 and HAMP2 of Aer2 (PDB: 3lnr) using SWISS-MODEL *(A. Waterhouse et al., 2018)*. The four-helix bundle of MA dimer (residues 124-417) was generated using CCBuilder (Wood & Woolfson, 2018). Dimers of the three domains were superimposed based on C-α overlap regions. Each domain was individually modelled with a 12-residue overlap (equivalent to three alpha-helical turns), and subsequently, superimposition using Cα atoms allowed creation of an entire FrzCD dimer model **(Figure 2.4)**. The domains were joined at residues Ser34 and Ser35 between DB and H1, and residues Val130 and Ile131 between H2 and MA to generate the FrzCD homology model. Recently, a dimer model of FrzCD was generated using AlphaFold2 and ColabFold *(Mirdita et al., 2022; Jumper et al., 2021)*.

2.2.3 Cloning

Restriction-free cloning *(van den Ent & Löwe, 2006)* was used by P. J. Jazleena *(MS Thesis,Jazleena, 2018)* to generate different domain deletion and mutant constructs of FrzCD with a C-terminal His tag in pHis17 backbone (refer to Addgene plasmid #78201 for the vector backbone, obtained from Löwe lab, MRC LMB, Cambridge, UK).

2.2.4 Protein purification

Proteins expressed from pHis17 plasmid were purified by affinity chromatography (HisTrap, GE Life Sciences) and ion-exchange chromatography at 4°C *(MS Thesis, P. J. Jazleena, (Jazleena. 2018; Jazleena, Das, Guiseppi et al., 2025))*. *E. coli* protein expression strain BL21AI was transformed with wild-type and mutant plasmids, and was grown in LB broth supplemented with 100 µg/ml ampicillin at 37°C until OD_{600} reached 0.6. Expression was induced with 0.2% L-arabinose, and cells were incubated at 18°C for 12 hours. Cells were harvested by centrifugation at 4000 × g for 20 minutes and pellets were flash frozen in liquid nitrogen and stored at -80°C until further use. Cell pellets were thawed and resuspended in lysis buffer (200 mM NaCl, 50 mM Tris pH 8, 10% glycerol) and sonicated at 60% amplitude (three cycles of 1 sec ON, 3 sec OFF for 2 min each, with 5 min intervals). The lysate was centrifuged at 35,000 × g for 30 min at 4°C, and the supernatant was loaded onto a 5-ml HisTrap HP column pre-equilibrated with buffer A200 (200 mM NaCl, 50 mM Tris, pH 8.0). Washes with buffer A200, 2% and 5% buffer B200 (200 mM NaCl, 500 mM Imidazole, 50 mM Tris pH 8.0, mixed with A200) were carried out before elution with a step gradient of 10%, 20%, 50% and 100%

of buffer B200 (mixed with A200). EDTA was added to the 5 ml eluted fractions (final concentration of EDTA 1 mM) to prevent protein degradation. Pure protein fractions identified from SDS-PAGE were pooled and dialyzed against A50 (50 mM NaCl, 1 mM EDTA, 50 mM Tris pH 8.0). Ion-exchange chromatography using MonoQ/MonoS 10/100 GL (GE Healthcare) was then performed to remove impurities, including bound DNA. Proteins were loaded with A50 buffer and eluted using a NaCl gradient from 50 mM to 500 mM (0 to 50% A1000, 1000 mM NaCl, 1 mM EDTA, 50 mM Tris pH 8.0) over 20 column volumes. Eluted protein fractions were concentrated with centricons (Vivaspin® 10 kDa or 3 kDa MWCO), aliquoted, flash-frozen, and stored at -80 °C for experiments in Far-UV CD spectroscopy and EMSA experiments.

2.2.5 Circular dichroism spectroscopy

Far-UV CD measurements were carried out on a Jasco J-720 spectropolarimeter. The parameters used for measurements of far-UV CD spectra were as follows: step resolution, 1 nm; scan speed, 100 nm/min; and bandwidth, 1 nm. The concentrations of FrzCD and $FrzCD^{\Delta MA}$ were 2.5 μM and 20 μM, respectively. CAPITO was used to analyze and plot CD data *(Wiedemann et al., 2013)*.

2.2.6 Fluorescence anisotropy

35 bp DNA was 5'-end labelled with 5-(iodoacetamido)fluorescein (5-IAF) using protocol by Zearfoss and Ryder *(Zearfoss & Ryder, 2012)*. The labelling efficiency was around 50%, calculated as a molar ratio of fluorescein to DNA by measuring absorbance at 260 nm for DNA and 490 nm for 5-IAF. The experiment was carried out in Fluoromax-4 (Horiba) and single time-point anisotropy readings were monitored, keeping excitation wavelength at 490 nm, emission wavelength at 516 nm and slit width at 2 nm for both. The sample volume was 200 μL in a quartz cuvette (10 × 2 mm path length) containing 1 μM labelled DNA in 50 mM Tris, pH 8.0, and 50 mM NaCl. It was then titrated with increasing protein concentration, mixed properly by pipetting and waited for 5 mins before taking anisotropy readings. The anisotropy readings were then normalized to zero protein (only labelled DNA) readings and plotted in GraphPad Prism. FrzCD*, a mutant where lysine and arginine (three lysine residues K9, K13 and K18, and two arginine residues R15 and R17) in the DB-domain were replaced by glutamates to disrupt any charge-based interaction, was used as a non-specific binding control.

K_d was calculated for FrzCD and FrzCD$^{\Delta DB}$ fitted to nonlinear regression for one-site specific binding (without non-specific binding component) as well as one-site total and non-specific binding (considering FrzCD* as the non-specific component).

Equations:

- One-Site Specific Binding (Without Non-Specific Component)

$$Y = \frac{B_{max} \cdot X}{K_d + X}$$

X: Concentration of free ligand.

Y: Specific binding

B_{max}: Maximum number of binding sites (same units as Y).

K_d: Equilibrium dissociation constant (same units as X); the concentration at which half-maximum binding occurs

- One-Site Total and Non-Specific Binding

This model fits two data sets simultaneously (Global Fitting): the Total Binding (FrzCD) and the Non-Specific Binding (FrzCD*). Non-specific binding is typically non-saturable and proportional to the ligand concentration.

Total Binding (FrzCD): Y= Specific + Non-Specific

Specific Binding Component: Specific = $\frac{B_{max} \cdot X}{K_d + X}$

X: Concentration of free ligand.

B_{max}: Maximum number of binding sites (same units as Y).

K_d: Equilibrium dissociation constant (same units as X); the concentration at which half-maximum binding occurs

Non-Specific Component: Non-Specific= (NS · X) + (Background)

NS: slope of the nonspecific component (FrzCD*)

Background: The Y-intercept, representing the measured "binding" when no ligand is added (often constrained to zero).

2.2.7 Electrophoretic mobility shift assay (EMSA)

EMSAs were performed for varying lengths of DNA, including 8, 12, 20, and 35 bp, which were custom-synthesised (Sigma and Eurofins) and subsequently annealed. A single-stranded (ss) poly A consisting of 8 bases was also used, and all DNA sequences used for the study are listed in **Table 2.1**. Increasing concentrations of purified proteins, ranging from 0.5 to 50 µM, were incubated with 0.5 to 2 µM of DNA at 25°C for 30 min in a reaction buffer consisting of 50 mM NaCl, 1 mM dithiothreitol, 10% glycerol, and 50 mM Tris, pH 7.4. A higher concentration of DNA, 2 µM, was used for the 8-bp DNA to facilitate visualization on an agarose gel. The samples were mixed with gel loading buffer and loaded on the appropriate percentage agarose gel containing ethidium bromide. 4% agarose gels were used for 8-bp, 12-bp, 20-bp, and 35-bp DNA. Samples with short DNA fragments were run at 80-90 V for 30 minutes in 1x TAE (40 mM Tris-acetate, 1 mM EDTA) buffer, followed by visualization under UV light. The gels were observed for a higher shift in the DNA bands in the presence of increasing protein concentrations.

Table 2.1 List of DNA sequences used for EMSA

DNA length	**Sequence (5’ to 3’)**
8bp_OH	ACTGCAGTC
8bp	ACTGCAGT
ss DNA	AAAAAAAA
12 bp	CTCACTATAGGG
20 bp	TAATACGACTCACTATAGGG
35 bp	GTCACCTGCTCTAGCTAATAGACTGAGCCGAGGTG

2.3 Results

2.3.1 Domain organization of FrzCD consists of a DNA-binding domain, di-HAMP domains and a methyl-accepting domain

Based on the alignment of FrzCD with other MCPs, FrzCD was previously dissected into an N-terminal region of unknown fold (residues 1 to 136) and a C-terminal MA domain (residues 137 to 417) *(Bustamante et al., 2004)*. Subsequently, residues 1 to 31 in the N-terminal region were identified to mediate DNA binding **(Figure 2.5A)** *(Moine et al., 2017)*. The C-terminal domain belonged to the 40H class of MCP cytoplasmic domains **(Figure 2.5B)** *(Moine et al., 2014)*. Secondary structure prediction for the FrzCD sequence suggested that the N-terminal region forms an alpha helix **(Figure 2.5B)**. The leucine zipper domain is a well-known DNA-binding domain that consists of a dimer of helices binding to DNA *(Busch & Sassone-Corsi, 1990)*. Hence, we aligned residues 1-30 with the DNA-binding region of proteins from various families of basic leucine zipper (bZIP) proteins **(Figure 2.5C)**. The presence of a conserved consensus sequence NxxAAxxCR, where x is variable but often a positively charged residue, was identified for FrzCD *(Fujii et al., 2000)*. Therefore, we believe that the DNA-binding features of FrzCD could potentially resemble those of a bZIP family protein.

Based on the characteristic features of MCPs, FrzCD was thought to contain a HAMP domain *(Xu et al., 2007)*, though the domain boundaries were unknown. A secondary structure prediction for FrzCD sequence showed that the majority of the protein sequence consisted of extended helical regions **(Figure 2.5B)**. Circular dichroism spectral analysis of FrzCD confirmed the presence of extended helical regions (~71%, **Figure 2.6A**). At the N-terminal domain, there were two gaps in the helical region **(Figure 2.6B)**, where the residues were predicted to be non-helical. HAMP domain, typically situated between the N-terminal periplasmic and the C-terminal signal transduction domain in an MCP, comprises approximately 50 amino acids, consisting of two helices connected by a loop *(Dunin-Horkawicz & Lupas, 2010)*. Di-HAMP domains were identified by sequence alignment with other poly-HAMP domains between the N-terminal DNA binding domain and C-terminal MA domain *(MS Thesis, P. J. Jazleena (Jazleena, 2018))*. The predicted HAMP domains extend from residues 31 to 83 and 84 to 137, respectively. The second helix AS2 of H1 domain is in tandem with the AS1 of H2 domain **(Figure 2.6B)**. The alignment clearly shows the heptad organization of the amino acid sequence of the helices and conserved motif containing glycine flanking the loop region **(Figure 2.6B)**.

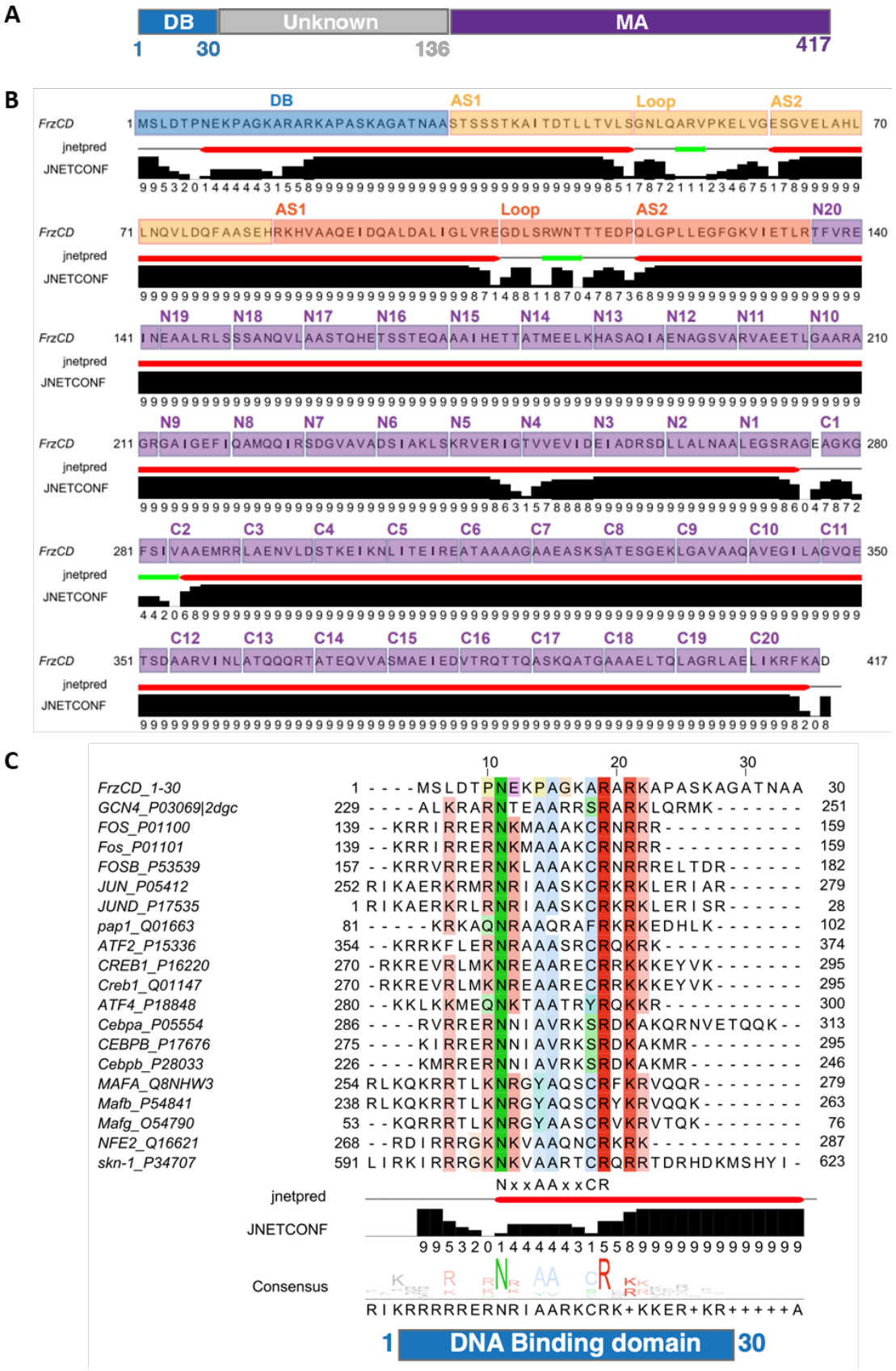


Figure 2.5 FrzCD has an N-terminal DNA-binding domain with conserved positively charged residues. (A) FrzCD comprises an N-terminal DNA-binding (DB) domain (1–30) and a C-terminal methyl-accepting (MA) domain (137–417). Residues 31 to 137 are of unknown fold, as inferred from sequence-based predictions. (B) Secondary structure prediction of FrzCD

using JPred *(Drozdetskiy et al., 2015)*. DB (blue), H1 and H2 (each consisting of AS1, loop and AS2; orange and red), and MA (20 heptads of the N and C-terminal ends labelled as N1-20 and C1-20; purple) domains are marked on the amino acid sequence. Helices and strands are shown as red cylinders and green arrows, respectively. The confidence of secondary structure prediction is indicated by numbers ranging from 0 to 9 (lowest to highest). (C) The DNA-binding domain of FrzCD is similar to bZIP DNA-binding sequences. Sequence alignment of the DB domain with leucine zipper domains reveals a conserved consensus sequence, NxxAAxxCR (where x represents any residue), and positively charged residues (R and K). Secondary structure prediction of the DB domain reveals the presence of a helix similar to those found in basic leucine zipper proteins. The colour scheme as per ClustalX is used for representation in the alignments.

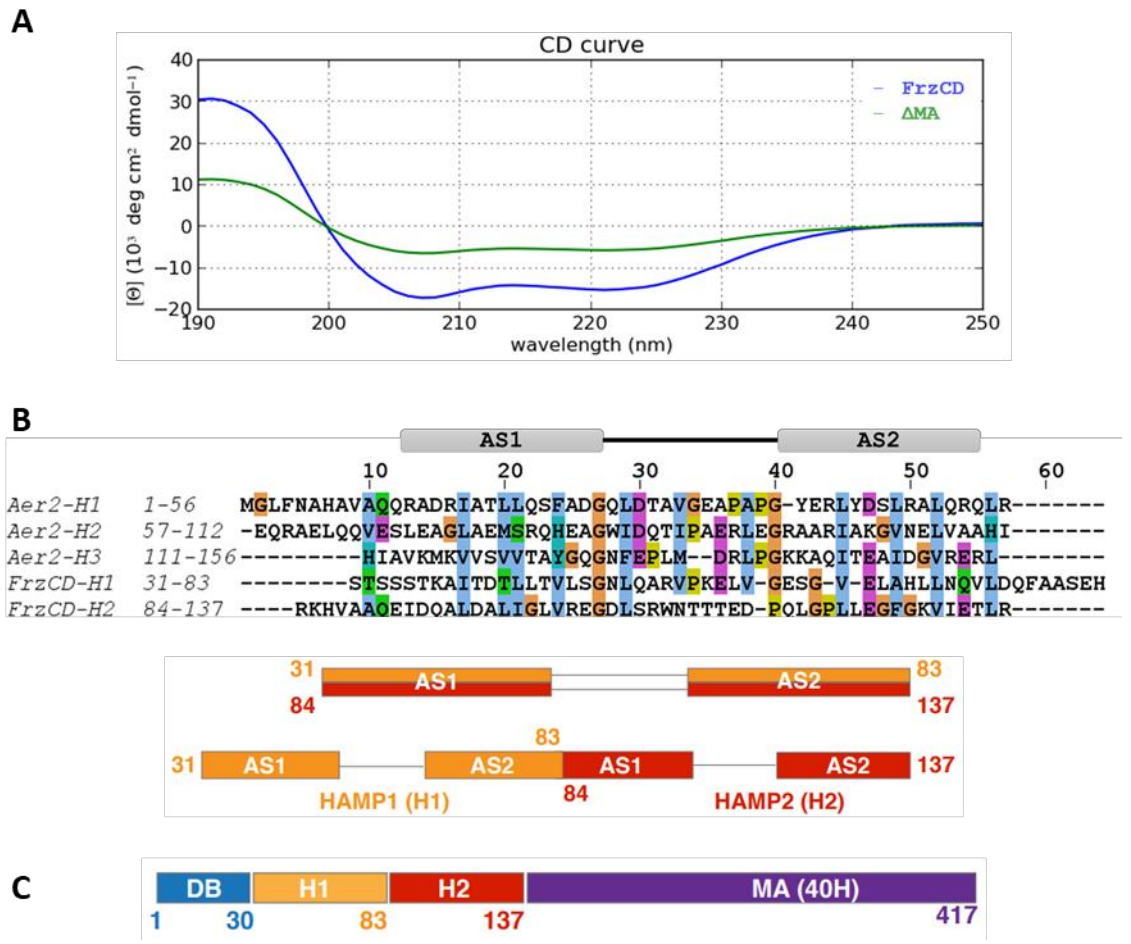


Figure 2.6 Domain architecture of FrzCD. (A) Circular dichroism spectroscopy of FrzCD (blue) and FrzCD$^{\Delta MA}$ (green) shows presence of extended helical regions (71% and 44% helical content, respectively). (B) Sequence alignment of residues 31 to 83 and 84 to 136 of FrzCD with the HAMP domains of the tri-HAMP region from the Aer2 receptor shows the presence of two alpha helices (AS1 and AS2) in each region. We thus renamed regions 31 to 83 and 84 to 136 of FrzCD as HAMP1 (H1) and HAMP2 (H2). The colour scheme as per ClustalX is used for representation in the alignments. (C) Domain architecture of FrzCD: N-terminal DNA binding region (DB: residues 1 to 30) followed by a di-HAMP unit composed of HAMP1 (H1: residues 31 to 83) and HAMP2 (H2: residues 84 to 137) terminating in a long C-terminal coiled-coil signalling domain (MA: 40H, residues 138 to 417).

Interestingly, like the H1 and H2 in the tri-HAMP region of the Aer2 receptor from *P. aeruginosa*, H1 and H2 in FrzCD are connected by a continuous helical linker of around 11 residues *(Airola et al., 2010)*. This differs from the concatenated H2 and H3 seen in Aer2 **(Figure 2.6B)** *(Airola et al., 2010)*. Thus, we concluded that the domain architecture of FrzCD comprised an N-terminal DNA binding region (DB: residues 1 to 30) followed by a tandem di-HAMP unit composed of HAMP1 (H1: residues 31 to 83) and HAMP2 (H2: residues 84 to137) terminating in a long C-terminal coiled-coil signaling domain (MA: 40H, residues 138 to 417) **(Figure 2.6C)**.

2.3.2 Homology model of FrzCD confirms an elongated structure

Once the domains were assigned for the full-length FrzCD, we aimed to obtain a three-dimensional atomic structure by homology modelling **(Figure 2.4)**. The complete model of the dimer was cylindrical with a length of approximately 300 Å and a diameter of approximately 14 Å **(Figure 2.7A-C)**. The AS1 helix of H1 immediately follows the DB domain of FrzCD, and the AS2 helix of H2 precedes the MA domain. The loop connecting the AS1 and AS2 helices of the two HAMP domains projected out from the cylindrical surface formed by the helices **(Figure 2.7B)**. The presence of two concatenated HAMP domains could result in the loops connecting AS1 and AS2 of HAMP domains extending out onto the surface of the protein at varying angles depending on the helix orientation **(Figure 2.7B)**.

Apart from the disordered DB domain, the structure predicted by AlphaFold2 aligned well with our homology model for FrzCD **(Figure 2.7D, E)**. H1 and H2 from FrzCD may also adopt different conformations, similar to H1 and H2 from Aer2 (PDB: 3LNR) *(Airola et al., 2010)*. Various domain-wise deletion constructs were designed based on assigned domain boundaries **(Figure 2.7F)** to characterize the probable function of each domain (**Figure 2.8A, B**) *(Jazleena, 2018; Jazleena, Das, Guiseppi et al., 2025)*.

2.3.3 Standardization of EMSA for small DNA fragments

Increasing concentrations of purified proteins, ranging from 0.5 to 50 μM, were incubated with 0.5 to 2 μM of DNA at 25°C for 30 min in a reaction buffer consisting of 50 mM NaCl, 1 mM dithiothreitol, 10% glycerol, and 50 mM Tris, pH 7.4. A higher concentration of DNA, 2 μM, was used for the 8-bp DNA to facilitate visualization on an agarose gel **(Figure 2.8C-E)**.

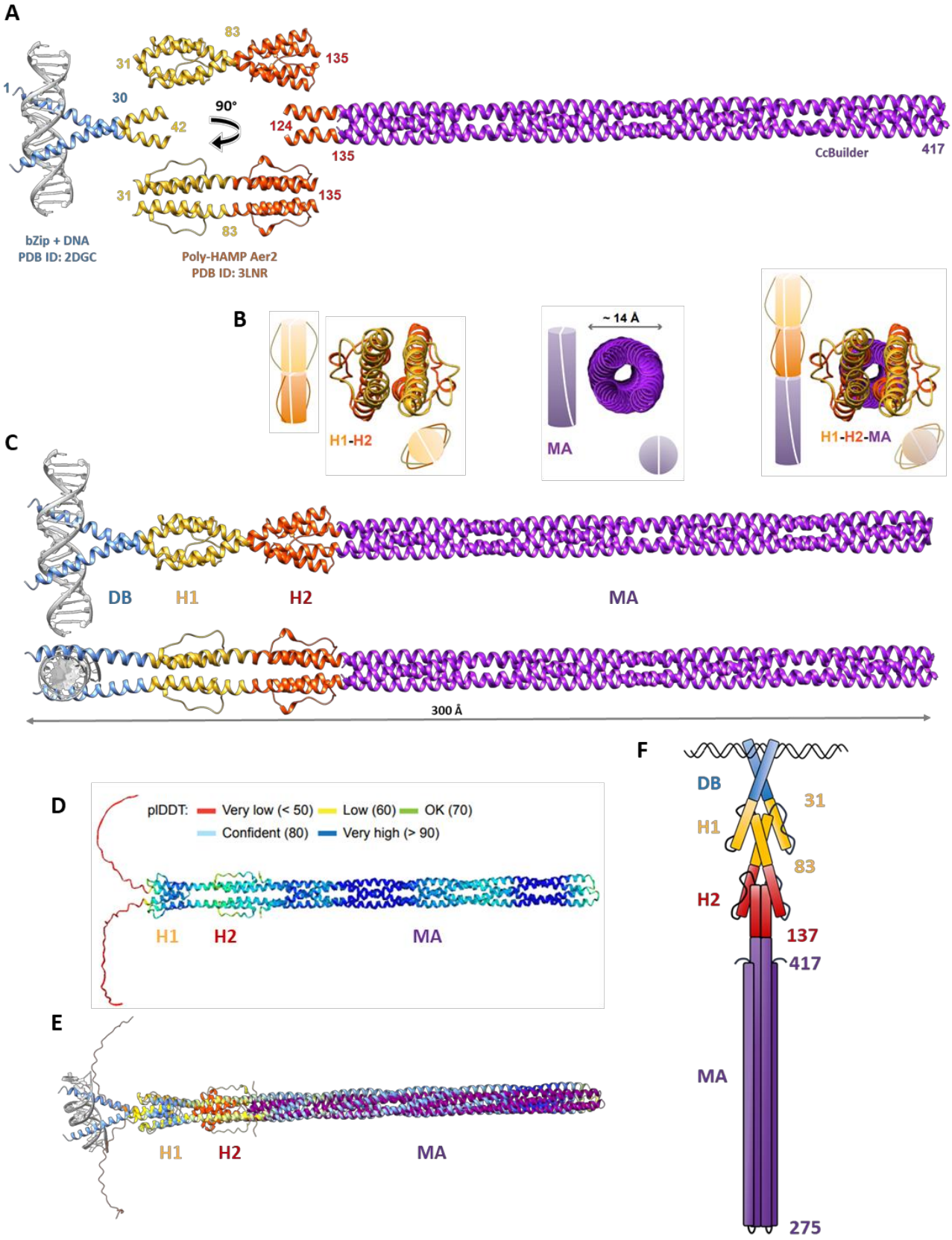


Figure 2.7 Homology model of FrzCD. (A) Schematic representation of strategy employed to generate a homology model of FrzCD where individual domains were modelled separately with an overlap of 12 amino acids for ease of stitching (Figure 2.4). Homology models for the DNA binding and di-HAMP domains were generated using leucine zipper (PDB ID: 2DGC)

and Aer2 (H1 and H2, PDB ID: 3LNR) respectively, in SWISS-MODEL, while the MA domain was modelled using CCBuilder. (B) An end-on view of the dimeric model shows that the loops connecting the AS1 and AS2 helices of H1 and H2 project out from the cylindrical surface formed by the helices. The MA domain subtends a circular view of approximately 14 Å in diameter. The loops connecting AS1 and AS2 of the two HAMP domains may extend out onto the surface at varying angles depending on the relative orientation of the helices. Side and end-on views of the corresponding domains are schematically represented. (C) FrzCD dimer model is an elongated structure of about 300 Å, generated as illustrated in panel A. (D) FrzCD AlphaFold2 model colour-coded according to reliability scored by pLDDT. (E) Superposition of the AlphaFold coordinates of FrzCD dimer (colour-coded according to reliability scored by pLDDT) with homology model (colour-coded according to domains; DB: blue, H1: golden, H2: red, MA: purple). (F) Schematic representation of a FrzCD dimer, as depicted from our structural predictions. AS1 of HAMP1 is continuous with the DB domain, and AS2 of HAMP1 is connected to AS1 of HAMP2 by a short helical linker. AS2 of HAMP2 is continuous with the helix of the MA coiled-coil domain.

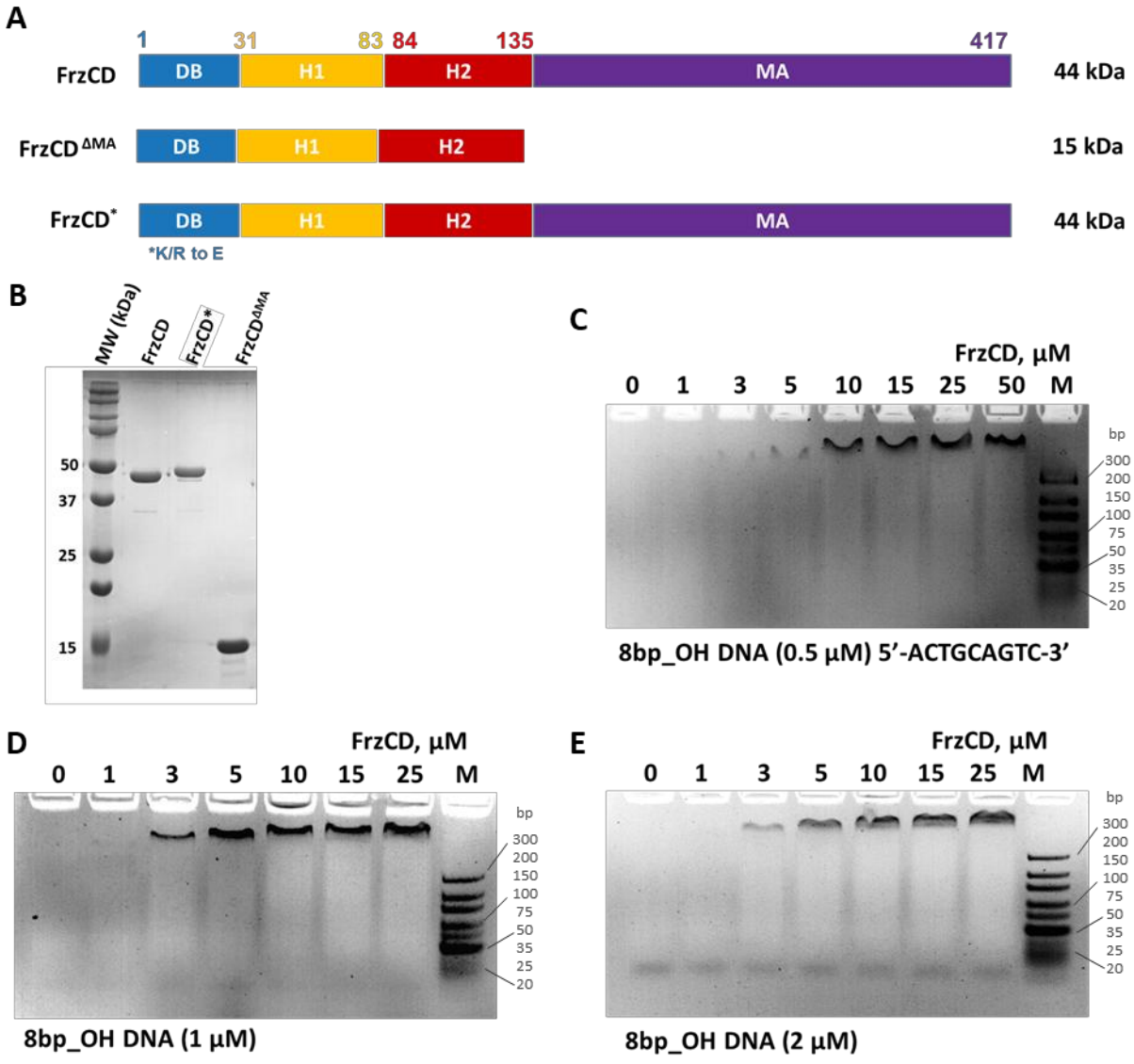


Figure 2.8 Standardization of EMSA for small DNA fragments. (A) Schematic representation of various FrzCD domain deletion and mutant constructs and their corresponding molecular weights. (B) 12% PAGE profile of purified wild-type and mutant FrzCD constructs. Binding of FrzCD to short DNA: (C) 0.5 μM of 8-bp DNA, (D) 1 μM of 8-bp DNA, (E) 2 μM of 8-bp DNA. 4 % agarose gels were used to visualize the shift in 8-bp DNA bound to increasing concentrations of FrzCD. 2 μM of small DNA fragments (8, 12, 20 and 35-bp) were used for further EMSA with wild-type and mutants of FrzCD. M denotes the DNA marker with size ranges as labelled.

2.3.4 DNA-binding properties of FrzCD resemble a leucine zipper domain

Basic leucine zippers are DNA-binding proteins, such as transcription factors that have a basic region, rich in lysine and arginine, which directly interacts with the major groove of DNA. This is followed by a leucine-rich zipper region, which adopts a helical structure and forms a coiled-coil organization in a dimer *(Busch & Sassone-Corsi, 1990; Landschulz et al., 1988)*. A heptad-repeat structural motif (LLF) was identified in the *E. coli* Tsr receptor, which was proposed to act as a leucine zipper and form a methylation-helix cap structure, facilitating HAMP signalling control *(Flack & Parkinson, 2018)*. In the proposed FrzCD domain structure based on homology modelling, the heptads present in the antiparallel helices of the succeeding HAMP domain (H1) can potentially substitute for a protein dimerization function of the leucine zipper, by forming a dimeric coiled-coil structure composed of four helices. The dimeric helices of a leucine zipper that hold on to DNA in a leucine zipper can typically bind to DNA segments as small as 8 bp (prediction based on structural information of DNA-bound complexes of leucine zipper proteins *(Panne et al., 2004)*).

Using EMSA, the DNA-binding properties of FrzCD DNA-binding domain were explored for short DNA fragments. FrzCD bound DNA of lengths as short as 8-bp or 12-bp **(Figure 2.9A, B)**, which is typical of leucine zippers. Interestingly, FrzCD also bound single-stranded DNA (ssDNA) of eight nucleotides **(Figure 2.9C)**, a feature not commonly observed in leucine zippers due to their sequence-specific interaction. This observation indicated that the interaction is predominantly charge-based. The binding of FrzCD$^{\Delta DB}$ to 8-bp and 12-bp DNA was similar to that of FrzCD **(Figure 2.9D, E)**. Sequence alignment of FrzCD DB domain with the leucine zipper DNA binding domain **(Figure 2.5C)** confirmed that the positively charged arginines and lysines are conserved. DNA binding was entirely impaired in FCD* **(Figure 2.9F)**, a mutant where lysine and arginine (three lysine residues K9, K13 and K18, and two arginine residues R15 and R17) in the DB-domain were replaced by glutamates to disrupt any

charge-based interactions. We confirmed that DNA binding by FrzCD was not sequence-specific, as it could bind to segments of DNA with different sequences **(Figures 2.9 and 2.10)**.

The DNA binding region of FrzCD might resembles bZIP DNA binding domain in structural and functional aspects, namely the possible presence of dimeric alpha helices (based on secondary structure prediction; **Figure 2.5B**, and the model; **Figure 2.7**), the requirement of basic residues (mutant construct FrzCD*), and ability to bind short segments of DNA **(Figure 2.9)**. Nonetheless, it is to be noted that the predicted dimeric alpha-helical DNA binding domain might not be accurate because of the presence of proline residues (P6, P10 and P20) in the region, which could act as a helix breaker **(Figure 2.5C)**. However, this might explain the possibility of a predominant charge-based interaction for FrzCD with DNA (which can bind single-stranded DNA and is sequence-independent), compared to bZIP proteins, which interact with the major groove of DNA.

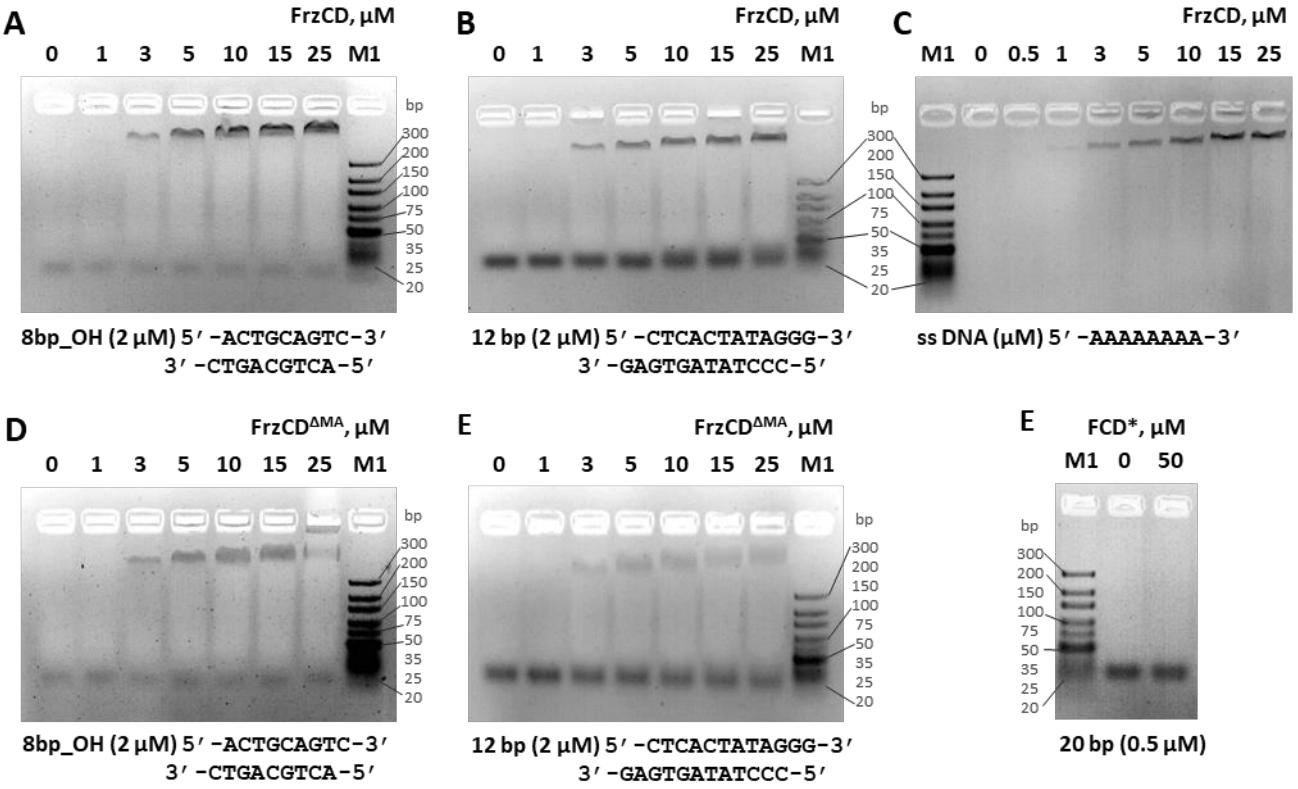
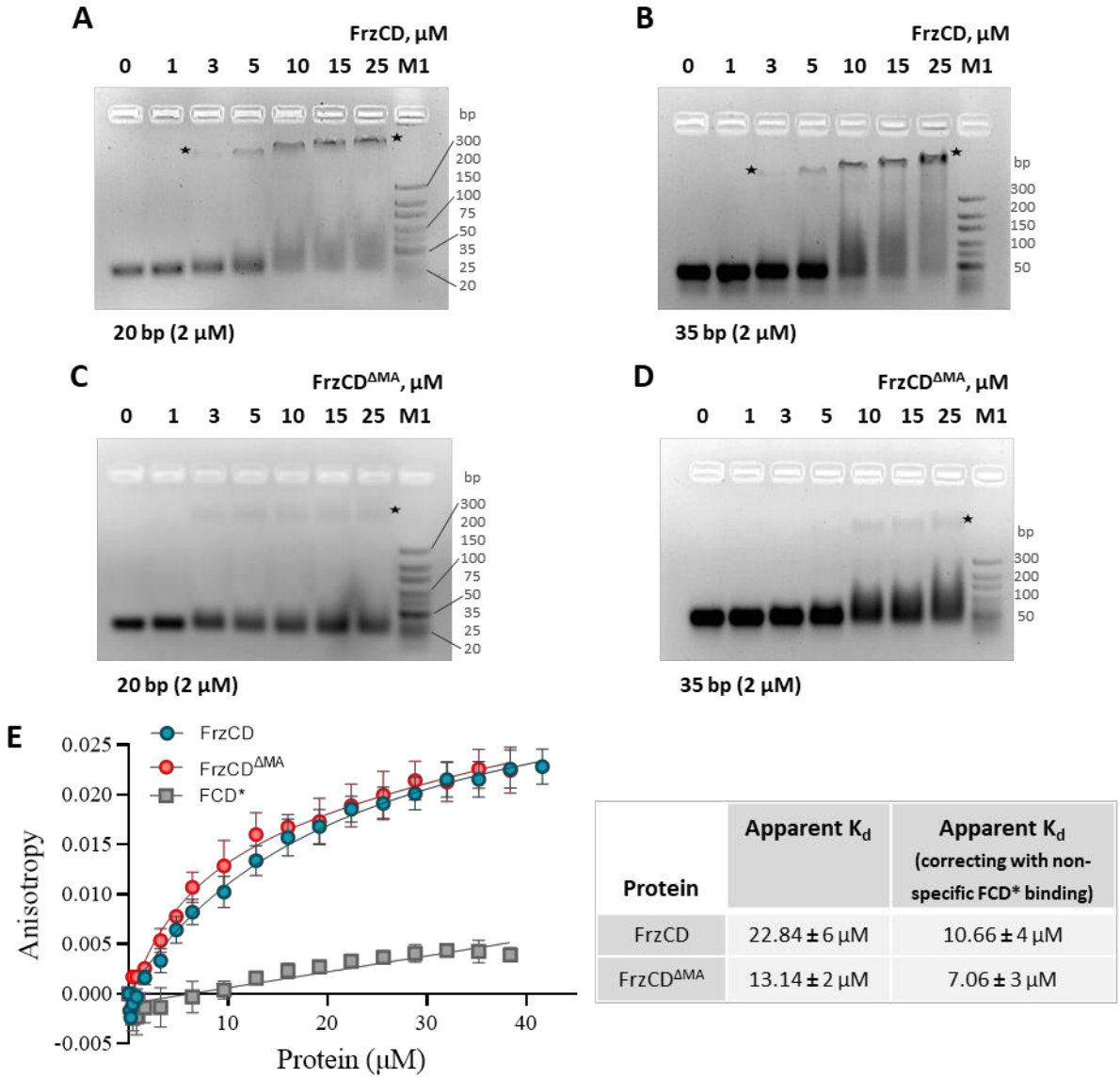


Figure 2.9 FrzCD binds short lengths of double-stranded or single-stranded DNA. Binding of FrzCD to short DNA: (A) 2 µM of 8-bp_OH DNA, (B) 2 µM of 12-bp DNA, and (C) 1 µM of 8-base poly-A ssDNA titrated with increasing FrzCD concentration from 0 to 25 µM. DNA binding of FrzCD$^{\Delta MA}$ mutant construct to: (D) 2 µM 8-bp_OH DNA, and (E) 2 µM 12-bp DNA. (F) FrzCD* mutant does not bind DNA. M1 denotes the DNA marker with size ranges as labelled.



Protein	Apparent K_d	Apparent K_d (correcting with non-specific FCD* binding)
FrzCD	22.84 ± 6 µM	10.66 ± 4 µM
FrzCD$^{\Delta MA}$	13.14 ± 2 µM	7.06 ± 3 µM

Figure 2.10 MA-domain deletion construct does not exhibit a supershift upon binding longer lengths of DNA, unlike wild-type FrzCD. FrzCD binding to: (A) 2 µM of 20-bp DNA, and (B) 2 µM of 35-bp DNA. FrzCD$^{\Delta MA}$ binding to: (C) 2 µM of 20-bp DNA, and (D) 2 µM of 35-bp DNA. '*' denotes supershift of DNA in complex with FrzCD or FrzCD$^{\Delta DB}$. M1 denotes the DNA marker with size ranges as labelled. (E) Fluorescence anisotropy using 35 bp DNA labelled with 5-IAF shows similar binding affinity for FrzCD and FrzCD$^{\Delta MA}$. FCD* was used as a non-specific binding control.

2.3.5 Deletion of MA domain of FrzCD affects supershift in EMSA with longer DNA

Next, we performed EMSA using longer DNA fragments. A higher-order stable shift for 20 bp and 35 bp (marked by '*' for supershifted bands in the figure panels) was observed in EMSA experiments with FrzCD **(Figure 2.10A, B)**. In contrast, FrzCD$^{\Delta DB}$ failed to exhibit stable higher-order shifts for 20 bp and 35 bp DNA **(Figure 2.10C, D),** although the shift pattern for shorter 8-bp and 12-bp DNA is similar to that of the wild-type **(Figure 2.9)**. The absence of a

clear supershift in FrzCD$^{\Delta DB}$ was also evident with longer DNA fragments of 69-bp and 432-bp DNA *(MS Thesis, P. J. Jazleena, (Jazleena, 2018; Jazleena, Das, Guiseppi et al., 2025))*.

Similar stable higher-order shifts were observed for FrzCD constructs either lacking one or both HAMP domains *(MS Thesis, P. J. Jazleena, (Jazleena, 2018; Jazleena, Das, Guiseppi et al., 2025))*. The presence of smeary bands for FrzCD$^{\Delta DB}$ could explain the unstable oligomeric complexes, as only a small population formed stable, higher-order oligomers (faint supershift bands in **Figure 2.10C, D**). The DNA binding event mediated by the DB domain was quantified using fluorescence anisotropy using 35 bp DNA conjugated with 5-(iodoacetamido)-fluorescein (5-IAF). FrzCD* was used as a non-specific binding control **(Figure 2.10E)**. The dissociation constants observed for FrzCD and FrzCDΔDB were found to be similar, at 10.66 μM and 7.06 μM, respectively, indicating a comparable binding affinity for DNA in solution **(Figure 2.10E)**. These observations suggested that the coiled-coil MA domain, despite being far from the actual DNA binding region, facilitated the formation of a stable DNA-protein complex. We concluded that the complex formed in the case of FrzCD$^{\Delta DB}$ was not sufficiently stable to oligomerize further and generate higher-order shifts.

2.4 Discussion

Here, through a combination of structure predictions and careful visual sequence comparison, we identified the domain boundaries of FrzCD **(Figure 2.5-2.7)**. FrzCD has an N-terminal DNA-binding region (DB: residues 1-30) that interacts with DNA in a sequence-independent manner. The DNA-binding architecture of FrzCD resembles a leucine zipper-like mechanism with conserved positively charged amino acids. However, the predicted dimeric alpha-helical DNA-binding domain may be inaccurate due to the presence of proline residues, which can disrupt helices **(Figure 2.5C)**. This suggests that FrzCD, unlike bZIP proteins, likely interacts with DNA primarily through positively charged lysine and arginine residues in the disordered N-terminal region, with a negatively charged phosphate DNA backbone in a sequence-independent manner, and thereby could bind to single-strand DNA **(Figure 2.9C)**. The DB domain is followed by two sequential HAMP domains, H1 and H2, connected by a short helical linker **(Figure 2.6B)**. These domains exhibit conserved non-helical loops that extend beyond the elongated and predominantly helical structure of FrzCD, a characteristic feature of the HAMP domain architecture **(Figure 2.7)**.

A distinct feature of MCPs that contain transmembrane domains is the formation of higher-order assemblies using the membrane as a scaffold *(Briegel et al., 2014; Hazelbauer et al., 2008)*. Higher-order oligomerization is an essential feature for cooperative signal sensing and allosteric activation of downstream signalling in the chemosensory pathway *(Piñas et al., 2016; Sourjik & Armitage, 2010; Sourjik & Berg, 2004)*. In the absence of a transmembrane domain, the cytoplasmic MCP FrzCD is proposed to utilize the nucleoid as a scaffold *(Moine et al., 2017)*. Interestingly, we observed that for smaller DNA fragments, 8-bp and 12-bp DNA, equivalent to the footprint of FrzCD on DNA, FrzCD$^{\Delta DB}$ exhibited stable binding **(Figure 2.9)**. However, smearing was observed for DNA fragments longer than 12-bp, indicative of unstable complex formation **(Figure 2.10C, D)**. While 8-bp DNA is probably the minimal footprint of a dimeric helical structure *(Panne et al., 2004)*, larger DNA fragments might require a stable FrzCD oligomerization for the DNA–FrzCD complex formation. The MA domain may thus be important for the stabilization of FrzCD oligomers on large DNA fragments **(Figure 2.10)**.

Apart from FrzCD$^{\Delta DB}$ and FrzCD*, one or both HAMP domain deleted constructs of FrzCD were generated based on domain boundaries identified from MSA and homology modelling **(Figure 2.5-2.7)**. To characterize the role of HMAP domains, *in vitro* DNA binding and oligomerization assays were carried out *(MS Thesis, P. J. Jazleena (Jazleena, 2018))*.

Simultaneously, *in vivo* studies were performed in collaboration with Dr Emilia Mauriello at CNRS, France. *In vitro* experiments demonstrate that di-HAMP domains restrict FrzCD to a dimeric form in solution and modulates FrzCD affinity for DNA. In contrast, the signalling domain stabilizes higher-order oligomeric assemblies upon DNA binding. Through fluorescence microscopy and analyses of *M. xanthus* social behaviour, the FrzCD HAMP domains were found to influence the formation of Frz clusters on the nucleoid, as well as group motility and development *(Jazleena, Das, Guiseppi et al., 2025)*. A compiled schematic representation of *in vitro* and *in vivo* observations for different FrzCD constructs is illustrated in **Figure 11**.

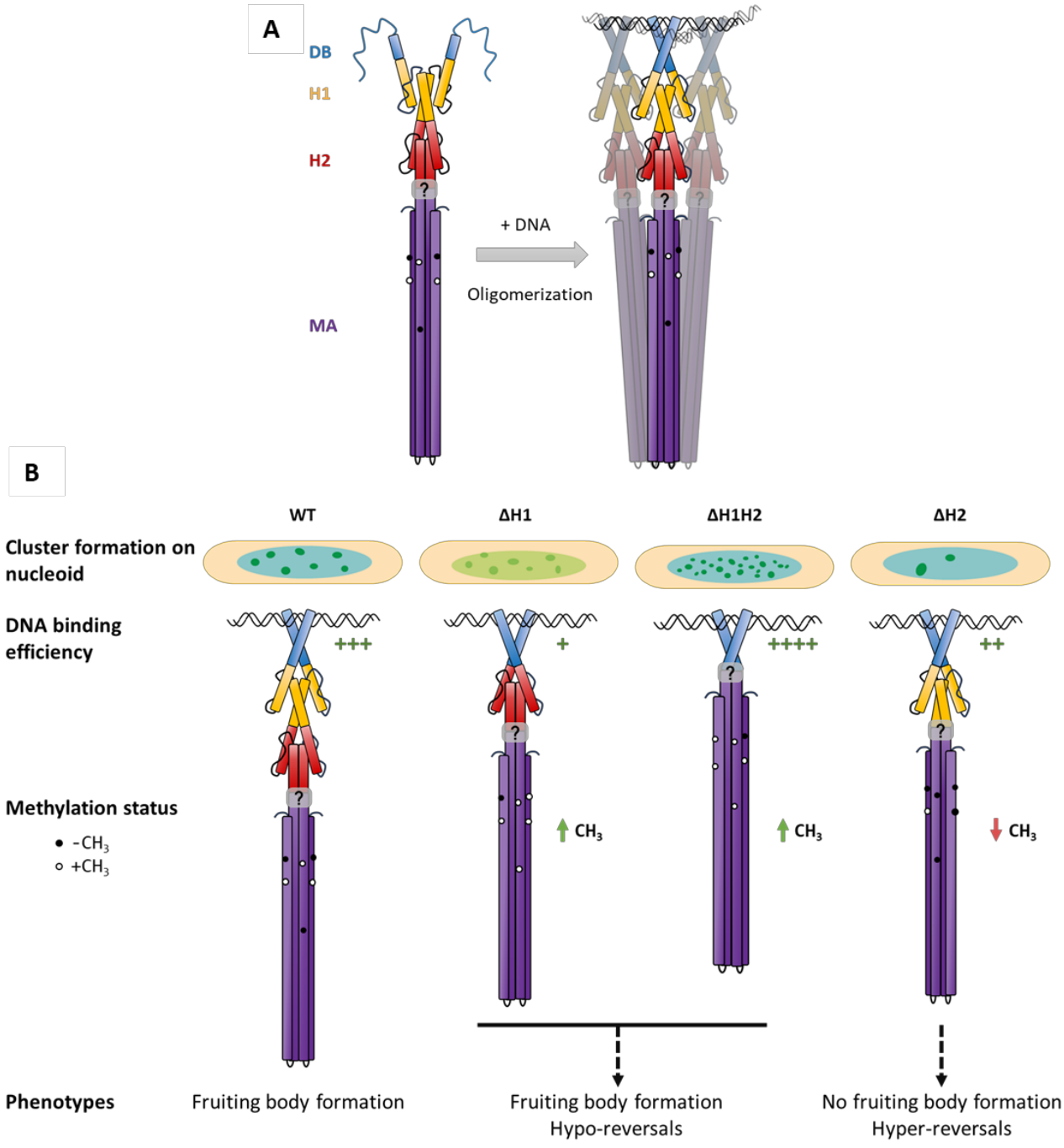


Figure 2.11 Model for the regulation of oligomerization and signalling by HAMP domains. (A) DNA-binding by the positively charged N-terminal region of the FrzCD DB-domain induces conformational changes that are transduced by di-HAMP domains to the MA domain. This conformational change may reorient the MA helices to favour oligomer formation, possibly by axial rotation, allowing the exposure of an interface responsible for oligomerization. (B) Alterations in FrzCD oligomerization and its affinity for DNA, due to the absence of one or both HAMP domains, significantly impact FrzCD cluster formation on the nucleoid. When both HAMP domains H1 and H2 are deleted, the affinity of FrzCD for DNA increases substantially in vitro, which likely accounts for the formation of well-defined and bright, though functionally impaired, nucleoid clusters. Additionally, while the deletion of either H1 or H2 facilitates oligomerization in the absence of DNA, the absence of either HAMP domain reduces the affinity for DNA. This observation might explain the more diffuse clusters seen in FrzCDΔH1 and the reduced number of clusters in FrzCDΔH2 compared to the wild type. The proposed rotation of the HAMP domains, which is transmitted to the methyl-accepting (MA) domain, may affect the accessibility of the methylation sites on the MA domain. Consequently, impaired methylation states lead to defects in reversal frequencies and social behaviours.

Based on the observations, a rotation model of the coiled-coil domain is proposed, which is regulated by DNA binding and the di-HAMP domains. *In vitro* experiments suggested that di-HAMP domains primarily prevents the formation of higher-order oligomers of FrzCD in the absence of DNA *(MS Thesis, P. J. Jazleena (Jazleena, 2018))*. DNA-dependent oligomerization beyond the dimeric state depends on the presence of the MA domain **(Figure 2.10)**. This regulation may be crucial in preventing higher-order oligomerization when freely diffusing FrzCD molecules have not yet encountered the nucleoid in the bacterial cytoplasm. A probable molecular basis for di-HAMP domains restricting the oligomerization state of FrzCD to a dimer in solution can be explained by the following model. Following the initial DNA-binding primarily via the positively charged residues on the FrzCD DB domain, a conformational change might induce the axial rotation of the HAMP helices and, in turn, a reorientation of the MA helices that favours the formation of trimers of dimers **(Figure 2.11A)**. These conformational changes may also lead to a differential exposure of residues that are methylated in the MA domain. The presence of two HAMP domains also influences the DNA-binding ability of FrzCD *(MS Thesis, P. J. Jazleena (Jazleena, 2018))*. Simultaneous deletion of H1 and H2 significantly enhances the affinity of FrzCD for DNA *in vitro*. This behaviour might lead to the formation of well-defined and intense, albeit not fully functional, nucleoid-FrzCDmNG$^{\Delta H1\Delta H2}$ clusters *in vivo* **(Figure 2.11B)**. Conversely, the reduced affinity of FrzCD$^{\Delta H1}$ and FrzCD$^{\Delta H2}$ for DNA might explain the reduced cluster intensity and number, respectively, of these allelic variants *(Jazleena, Das, Guiseppi et al., 2025)*.

The proposed rotation of the FrzCD HAMP domains is consistent with the reported rotation of AS1 and AS2, the molecular mechanism by which HAMP domains mediate the transduction of signals from the sensing to the MA domain of chemoreceptors *(Hulko et al., 2006)*. The model is also coherent with what is reported for other poly-HAMP domains *(Airola et al., 2013)*. In these poly-HAMP domains, molecular movements, including helix rotation, translation, or tilt, facilitate conformational transitions between HAMP conformers that propagate opposing downstream signals. The specific arrangement of two HAMP domains in FrzCD might have evolved to ensure signal transduction when the membrane scaffold is replaced by DNA. The proposed rotation model might also explain the methylation and phenotypic defects observed in the HAMP deletion strains **(Figure 2.11B)**. The di-HAMP domains might allow alternate conformations similar to H1 and H2 of the Aer2 tri-HAMP region, where H1 and H2 conformers result in alternate chemosensory signals. According to this model, the putative rotation of the HAMP domains, transduced to the MA domain, might influence the accessibility of the methylation sites on the MA domain. Impaired methylation states result, in turn, in alterations in reversal frequencies and social behaviours. However, a high signal concentration overrides the impaired methylation states *(Jazleena, Das, Guiseppi et al., 2025)*.

In this chapter, we investigated the DNA-binding property of FrzCD and its implication in stable cluster formation mediated by the MA domain. From *in vivo* and *in vitro* experiments, we observed that the di-HAMP domains of this novel cytoplasmic chemoreceptor could modulate nucleoid array formation in *M. xanthus* and regulate downstream signalling. Furthermore, we propose a model for the regulation of oligomerization and signalling, which brings new insights into the role of HAMP domains and MA domain, not only in signal transduction but also in the plasticity and stability of chemosensory arrays.

2.5 Acknowledgements

I thank Dr. Jaya Sharma for help during standardization of EMSA for small DNA fragments and Dr. Suman Pal for help with CD spectroscopy experiments.

2.6 References

1. Airola, M. V., Sukomon, N., Samanta, D., Borbat, P. P., Freed, J. H., Watts, K. J., & Crane, B. R. (2013). HAMP Domain Conformers That Propagate Opposite Signals in Bacterial Chemoreceptors. *PLoS Biology*, *11*(2), e1001479. https://doi.org/10.1371/journal.pbio.1001479

2. Airola, M. V., Watts, K. J., Bilwes, A. M., & Crane, B. R. (2010). Structure of Concatenated HAMP Domains Provides a Mechanism for Signal Transduction. *Structure*, *18*(4), 436–448. https://doi.org/10.1016/j.str.2010.01.013

3. Astling, D. P., Lee, J. Y., & Zusman, D. R. (2006). Differential effects of chemoreceptor methylation-domain mutations on swarming and development in the social bacterium Myxococcus xanthus. *Molecular Microbiology*, *59*(1), 45–55. https://doi.org/10.1111/j.1365-2958.2005.04926.x

4. Blackhart, B. D., & Zusman, D. R. (1985). "Frizzy" genes of Myxococcus xanthus are involved in control of frequency of reversal of gliding motility. *Proceedings of the National Academy of Sciences*, *82*(24), 8767–8770. https://doi.org/10.1073/pnas.82.24.8767

5. Briegel, A., Wong, M. L., Hodges, H. L., Oikonomou, C. M., Piasta, K. N., Harris, M. J., Fowler, D. J., Thompson, L. K., Falke, J. J., Kiessling, L. L., & Jensen, G. J. (2014). New insights into bacterial chemoreceptor array structure and assembly from electron cryotomography. *Biochemistry*, *53*(10), 1575–1585. https://doi.org/10.1021/bi5000614

6. Buchan, D. W. A., & Jones, D. T. (2019). The PSIPRED Protein Analysis Workbench: 20 years on. *Nucleic Acids Research*, *47*(W1), W402–W407. https://doi.org/10.1093/nar/gkz297

7. Burchard, R. P. (1981). Gliding Motility of Prokaryotes: Ultrastructure, Physiology, and Genetics. *Annual Review of Microbiology*, *35*(Volume 35, 1981), 497–529. https://doi.org/10.1146/annurev.mi.35.100181.002433

8. Busch, S. J., & Sassone-Corsi, P. (1990). Dimers, leucine zippers and DNA-binding domains. *Trends in Genetics: TIG*, *6*(2), 36–40. https://doi.org/10.1016/0168-9525(90)90071-d

9. Bustamante, V. H., Martínez-Flores, I., Vlamakis, H. C., & Zusman, D. R. (2004). Analysis of the Frz signal transduction system of Myxococcus xanthus shows the importance of the conserved C-terminal region of the cytoplasmic chemoreceptor FrzCD in sensing signals: Signal sensing by a cytoplasmic MCP. *Molecular Microbiology*, *53*(5), 1501–1513. https://doi.org/10.1111/j.1365-2958.2004.04221.x

10. Carreira, L. A. M., Szadkowski, D., Müller, F., & Søgaard-Andersen, L. (2022). Spatiotemporal regulation of switching front–rear cell polarity. *Current Opinion in Cell Biology*, *76*, 102076. https://doi.org/10.1016/j.ceb.2022.102076

11. Dinet, C., Michelot, A., Herrou, J., & Mignot, T. (2021). Linking single-cell decisions to collective behaviours in social bacteria. *Philosophical Transactions of the Royal Society B: Biological Sciences*, *376*(1820), 20190755. https://doi.org/10.1098/rstb.2019.0755

12. Drozdetskiy, A., Cole, C., Procter, J., & Barton, G. J. (2015). JPred4: A protein secondary structure prediction server. *Nucleic Acids Research*, *43*(W1), W389-394. https://doi.org/10.1093/nar/gkv332

13. Dunin-Horkawicz, S., & Lupas, A. N. (2010). Comprehensive Analysis of HAMP Domains: Implications for Transmembrane Signal Transduction. *Journal of Molecular Biology*, *397*(5), 1156–1174. https://doi.org/10.1016/j.jmb.2010.02.031

14. Flack, C. E., & Parkinson, J. S. (2018). A zipped-helix cap potentiates HAMP domain control of chemoreceptor signaling. *Proceedings of the National Academy of Sciences*, *115*(15), E3519–E3528. https://doi.org/10.1073/pnas.1721554115

15. Fujii, Y., Shimizu, T., Toda, T., Yanagida, M., & Hakoshima, T. (2000). Structural basis for the diversity of DNA recognition by bZIP transcription factors. *Nature Structural Biology*, *7*(10), 5.

16. Guiseppi, A., Vicente, J. J., Herrou, J., Byrne, D., Barneoud, A., Moine, A., Espinosa, L., Basse, M.-J., Molle, V., Mignot, T., Roche, P., & Mauriello, E. M. F. (2019). A divergent CheW confers plasticity to nucleoid-associated chemosensory arrays. *PLoS Genetics*, *15*(12), e1008533. https://doi.org/10.1371/journal.pgen.1008533

17. Guzzo, M., Murray, S. M., Martineau, E., Lhospice, S., Baronian, G., My, L., Zhang, Y., Espinosa, L., Vincentelli, R., Bratton, B. P., Shaevitz, J. W., Molle, V., Howard, M., & Mignot, T. (2018). A gated relaxation oscillator mediated by FrzX controls morphogenetic movements in Myxococcus xanthus. *Nature Microbiology*, *3*(8), 948–959. https://doi.org/10.1038/s41564-018-0203-x

18. Hazelbauer, G. L., Falke, J. J., & Parkinson, J. S. (2008). Bacterial chemoreceptors: High-performance signaling in networked arrays. *Trends in Biochemical Sciences*, *33*(1), 9–19. https://doi.org/10.1016/j.tibs.2007.09.014

19. Hodgkin, J., & Kaiser, D. (1979). Genetics of gliding motility in Myxococcus xanthus (Myxobacterales): Two gene systems control movement. *Molecular and General Genetics MGG*, *171*(2), 177–191. https://doi.org/10.1007/BF00270004

20. Hulko, M., Berndt, F., Gruber, M., Linder, J. U., Truffault, V., Schultz, A., Martin, J., Schultz, J. E., Lupas, A. N., & Coles, M. (2006). The HAMP Domain Structure Implies Helix Rotation in Transmembrane Signaling. *Cell*, *126*(5), 929–940. https://doi.org/10.1016/j.cell.2006.06.058

21. Inclán, Y. F., Laurent, S., & Zusman, D. R. (2008). The receiver domain of FrzE, a CheA–CheY fusion protein, regulates the CheA histidine kinase activity and downstream signalling to the A- and S-motility systems of Myxococcus xanthus. *Molecular Microbiology*, *68*(5), 1328–1339. https://doi.org/10.1111/j.1365-2958.2008.06238.x

22. Jazleena, P. J. (2018). *Structural and Biochemical Studies of FrzCD, A Cytoplasmic Methyl-accepting Chemosensory Protein (MCP)* [Thesis]. http://dr.iiserpune.ac.in:8080/xmlui/handle/123456789/974

23. Jazleena, P. J., Das, A., Guiseppi, A., Debard, F., Sharma, J., Yaikhomba, M., Mignot, T., Mauriello, E. M. F., & Gayathri, P. (2025). Di-HAMP domains of a cytoplasmic chemoreceptor modulate nucleoid array formation and downstream signaling. *mBio*, *16*(5), e00057-25. https://doi.org/10.1128/mbio.00057-25

24. Jelsbak, L., & Søgaard-Andersen, L. (2002). Pattern formation by a cell surface-associated morphogen in Myxococcus xanthus. *Proceedings of the National Academy of Sciences*, *99*(4), 2032–2037. https://doi.org/10.1073/pnas.042535699

25. Jumper, J., Evans, R., Pritzel, A., Green, T., Figurnov, M., Ronneberger, O., Tunyasuvunakool, K., Bates, R., Žídek, A., Potapenko, A., Bridgland, A., Meyer, C., Kohl, S. A. A., Ballard, A. J., Cowie, A., Romera-Paredes, B., Nikolov, S., Jain, R., Adler, J., … Hassabis, D. (2021). Highly accurate protein structure prediction with AlphaFold. *Nature*, *596*(7873), Article 7873. https://doi.org/10.1038/s41586-021-03819-2

26. Kaiser, D. (1979). Social gliding is correlated with the presence of pili in Myxococcus xanthus. *Proceedings of the National Academy of Sciences*, *76*(11), 5952–5956. https://doi.org/10.1073/pnas.76.11.5952

27. Kaiser, D., & Crosby, C. (1983). Cell movement and its coordination in swarms of myxococcus xanthus. *Cell Motility*, *3*(3), 227–245. https://doi.org/10.1002/cm.970030304

28. Landschulz, W. H., Johnson, P. F., & McKnight, S. L. (1988). The leucine zipper: A hypothetical structure common to a new class of DNA binding proteins. *Science (New York, N.Y.)*, *240*(4860), 1759–1764. https://doi.org/10.1126/science.3289117

29. Mauriello, E. M. F. (2020). How an unusual chemosensory system forms arrays on the bacterial nucleoid. *Biochemical Society Transactions*, *48*(2), 347–356. https://doi.org/10.1042/BST20180450

30. Mauriello, E. M. F., Mignot, T., Yang, Z., & Zusman, D. R. (2010). Gliding Motility Revisited: How Do the Myxobacteria Move without Flagella? *Microbiology and Molecular Biology Reviews : MMBR*, *74*(2), 229–249. https://doi.org/10.1128/MMBR.00043-09

31. McBride, M. J., Köhler, T., & Zusman, D. R. (1992). Methylation of FrzCD, a methyl-accepting taxis protein of Myxococcus xanthus, is correlated with factors affecting cell behavior. *Journal of Bacteriology*, *174*(13), 4246–4257. https://doi.org/10.1128/jb.174.13.4246-4257.1992

32. McBride, M. J., Weinberg, R. A., & Zusman, D. R. (1989). "Frizzy" aggregation genes of the gliding bacterium Myxococcus xanthus show sequence similarities to the chemotaxis genes of enteric bacteria. *Proceedings of the National Academy of Sciences*, *86*(2), 424–428. https://doi.org/10.1073/pnas.86.2.424

33. Mercier, R., & Mignot, T. (2016). Regulations governing the multicellular lifestyle of *Myxococcus xanthus*. *Current Opinion in Microbiology*, *34*, 104–110. https://doi.org/10.1016/j.mib.2016.08.009

34. Mirdita, M., Schütze, K., Moriwaki, Y., Heo, L., Ovchinnikov, S., & Steinegger, M. (2022). ColabFold: Making protein folding accessible to all. *Nature Methods*, *19*(6), Article 6. https://doi.org/10.1038/s41592-022-01488-1

35. Moine, A., Agrebi, R., Espinosa, L., Kirby, J. R., Zusman, D. R., Mignot, T., & Mauriello, E. M. F. (2014). Functional organization of a multimodular bacterial chemosensory apparatus. *PLoS Genetics*, *10*(3), e1004164. https://doi.org/10.1371/journal.pgen.1004164

36. Moine, A., Espinosa, L., Martineau, E., Yaikhomba, M., Jazleena, P. J., Byrne, D., Biondi, E. G., Notomista, E., Brilli, M., Molle, V., Gayathri, P., Mignot, T., & Mauriello, E. M. F. (2017). The nucleoid as a scaffold for the assembly of bacterial signaling complexes. *PLOS Genetics*, *13*(11), e1007103. https://doi.org/10.1371/journal.pgen.1007103

37. Nan, B., & Zusman, D. R. (2011). Uncovering the mystery of gliding motility in the myxobacteria. *Annual Review of Genetics*, *45*, 21–39. https://doi.org/10.1146/annurev-genet-110410-132547

38. Panne, D., Maniatis, T., & Harrison, S. C. (2004). Crystal structure of ATF-2/c-Jun and IRF-3 bound to the interferon-beta enhancer. *The EMBO Journal*, *23*(22), 4384–4393. https://doi.org/10.1038/sj.emboj.7600453

39. Piñas, G. E., Frank, V., Vaknin, A., & Parkinson, J. S. (2016). The source of high signal cooperativity in bacterial chemosensory arrays. *Proceedings of the National Academy of Sciences of the United States of America*, *113*(12), 3335–3340. https://doi.org/10.1073/pnas.1600216113

40. Sager, B., & Kaiser, D. (1994). Intercellular C-signaling and the traveling waves of Myxococcus. *Genes & Development*, *8*(23), 2793–2804. https://doi.org/10.1101/gad.8.23.2793

41. Schumacher, D., & Søgaard-Andersen, L. (2017). Regulation of Cell Polarity in Motility and Cell Division in Myxococcus xanthus. *Annual Review of Microbiology*, *71*, 61–78. https://doi.org/10.1146/annurev-micro-102215-095415

42. Shi, W., Köhler, T., & Zusman, D. R. (1993). Chemotaxis plays a role in the social behaviour of Myxococcus xanthus. *Molecular Microbiology*, *9*(3), 601–611. https://doi.org/10.1111/j.1365-2958.1993.tb01720.x

43. Shi, W., & Zusman, D. R. (1993). The two motility systems of Myxococcus xanthus show different selective advantages on various surfaces. *Proceedings of the National Academy of Sciences*, *90*(8), 3378–3382. https://doi.org/10.1073/pnas.90.8.3378

44. Sourjik, V., & Armitage, J. P. (2010). Spatial organization in bacterial chemotaxis. *The EMBO Journal*, *29*(16), 2724–2733. https://doi.org/10.1038/emboj.2010.178

45. Sourjik, V., & Berg, H. C. (2004). Functional interactions between receptors in bacterial chemotaxis. *Nature*, *428*(6981), 437–441. https://doi.org/10.1038/nature02406

46. Thiery, S., & Kaimer, C. (2020). The Predation Strategy of Myxococcus xanthus. *Frontiers in Microbiology*, *11*. https://doi.org/10.3389/fmicb.2020.00002

47. van den Ent, F., & Löwe, J. (2006). RF cloning: A restriction-free method for inserting target genes into plasmids. *Journal of Biochemical and Biophysical Methods*, *67*(1), 67–74. https://doi.org/10.1016/j.jbbm.2005.12.008

48. Waterhouse, A., Bertoni, M., Bienert, S., Studer, G., Tauriello, G., Gumienny, R., Heer, F. T., de Beer, T. A. P., Rempfer, C., Bordoli, L., Lepore, R., & Schwede, T. (2018). SWISS-MODEL: Homology modelling of protein structures and complexes. *Nucleic Acids Research*, *46*(W1), W296–W303. https://doi.org/10.1093/nar/gky427

49. Waterhouse, A. M., Procter, J. B., Martin, D. M. A., Clamp, M., & Barton, G. J. (2009). Jalview Version 2—A multiple sequence alignment editor and analysis workbench. *Bioinformatics*, *25*(9), 1189–1191. https://doi.org/10.1093/bioinformatics/btp033

50. Wiedemann, C., Bellstedt, P., & Görlach, M. (2013). CAPITO--a web server-based analysis and plotting tool for circular dichroism data. *Bioinformatics (Oxford, England)*, *29*(14), 1750–1757. https://doi.org/10.1093/bioinformatics/btt278

51. Wood, C. W., & Woolfson, D. N. (2018). CCBuilder 2.0: Powerful and accessible coiled-coil modeling. *Protein Science: A Publication of the Protein Society*, *27*(1), 103–111. https://doi.org/10.1002/pro.3279

52. Xu, Q., Black, W. P., Mauriello, E. M. F., Zusman, D. R., & Yang, Z. (2007). Chemotaxis mediated by NarX-FrzCD chimeras and nonadapting repellent responses in Myxococcus xanthus. *Molecular Microbiology*, *66*(6), 1370–1381. https://doi.org/10.1111/j.1365-2958.2007.05996.x

53. Zearfoss, N. R., & Ryder, S. P. (2012). End-labeling oligonucleotides with chemical tags after synthesis. *Methods in Molecular Biology (Clifton, N.J.)*, *941*, 181–193. https://doi.org/10.1007/978-1-62703-113-4_14

54. Zhang, Y., Ducret, A., Shaevitz, J., & Mignot, T. (2012). From individual cell motility to collective behaviors: Insights from a prokaryote, Myxococcus xanthus. *FEMS Microbiology Reviews*, *36*(1), 149–164. https://doi.org/10.1111/j.1574-6976.2011.00307.x

55. Zusman, D. R. (1982). "Frizzy" mutants: A new class of aggregation-defective developmental mutants of Myxococcus xanthus. *Journal of Bacteriology*, *150*(3), 1430–1437. https://doi.org/10.1128/jb.150.3.1430-1437.1982

Chapter 3

Diversity of HAMP and ligand-binding domains in different MCP heptad classes

(This work was done along with Dr Jaya Sharma)

3.1 Introduction

Bacteria constantly monitor and adapt to different environmental and intracellular stimuli for survival. The stimulus-response mechanisms are primarily governed by three pathways based on domain organization and complexity. One-component and two-component signalling pathways mediate stimulus-induced gene expressions *(Stock et al., 2000; Ulrich et al., 2005)*, while the chemosensory signalling pathway primarily regulates motility behaviour *(Porter et al., 2011; Wadhams & Armitage, 2004)*. Chemosensory systems are non-canonical two-component systems that have evolved to include additional modules, providing new functions in ligand identification, increased sensitivity, and response regulation *(Gumerov et al., 2021; Watts et al., 2019)*. The core of these systems is formed by an array of ternary complexes composed of chemoreceptors (called methyl-accepting chemotaxis proteins (MCPs)), adaptor protein (CheW in *E. coli*) and histidine kinase (CheA in *E. coli*) *(Briegel et al., 2015, 2014)*. Chemoreceptor MCPs detect various stimuli and relay signals to histidine kinases, which regulate the phosphorelay cascade and define the resulting motility response.

Chemotaxis in *E. coli* is extensively studied and is mediated by five MCPs that regulate a single chemosensory cascade *(Parkinson et al., 2015)*. However, complex chemosensory systems have been identified in other bacteria through genomic analysis *(Lacal et al., 2010; Wuichet & Zhulin, 2010)*. Bacteria, on average, possess 14 MCP genes per genome *(Lacal et al., 2010)*. The number of MCPs is independent of genome size but was correlated with the bacterial lifestyle and metabolic diversity *(Bardy et al., 2017; Lacal et al., 2010)*. Bacteria that sustain themselves in multiple environments have nearly five times more MCPs than bacteria that are specific to a single ecological niche *(Alexandre et al., 2004)*. In archaea, strains lacking MCPs tend to have smaller genome sizes compared to those that possess MCPs *(Cha et al., 2022)*. Additionally, many genomes encode multiple chemosensory pathways that serve diverse functions beyond motility regulation *(Cha et al., 2022; Gumerov et al., 2021)*. Typically, at least one chemosensory pathway directly dictates motility, while others likely regulate various programmed cellular processes *(Gumerov et al., 2021; He & Bauer, 2014)*. These complex chemosensory networks have organism-specific functions, such as virulence in *P. aeruginosa* or in the developmental life cycle of *M. xanthus (Munar-Palmer et al., 2024; Zusman et al., 2007)*. In fact, systems-level phylogenomic analyses have classified chemosensory pathways into 19 distinct classes based on the identification of central and auxiliary components *(Wuichet & Zhulin, 2010)*. Flagellar motility is regulated by 17 of these classes (F1–F17), type IV pilus-

based motility by class TFP, and alternative cellular functions, such as the regulation of second messenger levels, by class ACF *(Wuichet & Zhulin, 2010)*.

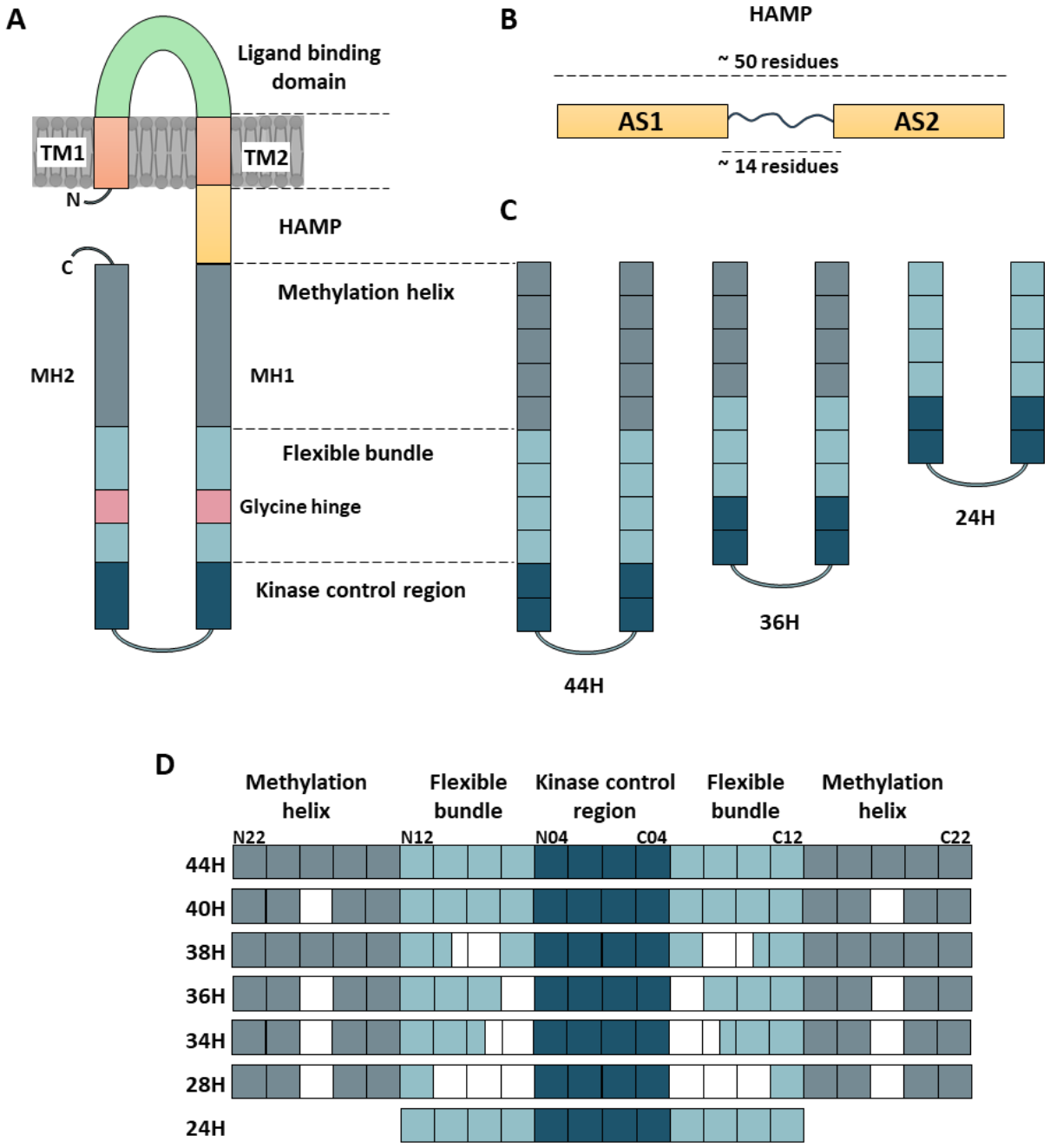


Figure 3.1 Domains and features of a methyl-accepting chemotaxis protein. (A) Topology of a typical membrane-bound MCP with a periplasmic LBD linked by a HAMP domain to a cytoplasmic signalling domain. The signalling MA domain is composed of methylation helices, a flexible region and a kinase control region. TM stands for transmembrane helix, and MH stands for methylation helix. (B) Schematic representation of the HAMP domain. (C) Examples of heptad classes of MCPs based on the number of heptads in the MA domain. Each box represents two heptads. (D) Major heptad classes of MCPs *(Alexander & Zhulin, 2007)*. The heptads are numbered from N22 at the N-terminus to N01-C01 at the centre of the kinase control region and up to C22 in the C-terminal arm. Each box represents two heptads, and gaps are represented as white boxes.

A canonical MCP has an input periplasmic ligand binding domain (LBD) that identifies the stimuli and transmits to a conserved histidine kinase interacting output domain (called kinase control module) at cytoplasmic signalling tip mediated by an input-output coupling HAMP (histidine kinase, adenylyl cyclase, MCP, and phosphatase domain) **(Figure 3.1A, B)** *(Bi & Lai, 2014; Aravind & Ponting, 1999)*. Although the signalling coiled-coil domain is conserved across all MCPs for interaction with the kinase and adaptor protein *(Alexander & Zhulin, 2007)*, there is a large diversity in protein topology and LBDs *(Ortega et al., 2017; Salah Ud-Din & Roujeinikova, 2017; Lacal et al., 2010)*. MCPs are classified into four different topologies based on the presence of transmembrane domains and localization of LBDs *(Wuichet et al., 2007)*. Class I (Ia and Ib) and Class II MCPs harbour a transmembrane (TM) domain with a periplasmic or a cytoplasmic LBD, respectively. Class III (IIIm and IIIc) include MCPs with 1 – 8 TM helices, while Class IV (IVa and IVb) lacks any TM helices and is soluble *(Salah Ud-Din & Roujeinikova, 2017)*. The transmembrane topology, with extracellular LBD is the predominant class in bacteria and archaea, while cytoplasmic MCPs are more common in archaea *(Lacal et al., 2010)*.

The functional regulation of an MCP is determined by chemoeffector binding to the LBD. There is an enormous sequence divergence across different LBD families. Nonetheless, the same LBD class can recognize different chemoeffectors, and conversely, the same chemoeffector molecule is recognized by different LBDs *(Matilla et al., 2025, 2022; Ortega et al., 2017)*. This is due to the rapid evolution of LBDs, where the same ligand is recognized by domains with huge sequence divergence *(Gavira et al., 2020)*. The sensory input for MCP is mediated by the direct interaction of chemoeffector molecules with the LBD *(Machuca et al., 2016; Milburn et al., 1991)*, or sometimes indirectly through a chemoeffector-binding protein that interacts with the LBD *(Liu et al., 2015; Kossmann et al., 1988)*. Some of the LBDs have cofactors, such as heme or flavin adenine dinucleotide (FAD), that help monitor oxygen and redox status in the cell *(Hou et al., 2000; Bibikov et al., 1997; Rebbapragada et al., 1997)*. The diversity in LBDs dictates the adaptability and survival of bacteria in different environments.

The HAMP domain acts as a signal relay module between the input LBD and output signalling domains. It is around 50 residues containing two α-helices (AS1 and AS2) linked by a flexible connector of around 14 residues, which dimerizes to form a parallel four-helix bundle **(Figure 3.1B)** *(Dunin-Horkawicz & Lupas, 2010; Hulko et al., 2006; Butler & Falke, 1998)*. The AS1

and AS2 have a characteristic coiled-coil heptad repeat where the hydrophobic residues at positions ‘a’ and ‘d’ point inward to form the core *(Hulko et al., 2006)*. The flexible loop connecting AS1 and AS2 has two conserved hydrophobic residues that interact and stabilize the helix core *(Ames et al., 2014)*. The HAMP domain undergoes conformational changes, similar to a piston, diagonal scissoring, and helical rotation, which are not mutually exclusive, to transduce the signal to the output domain *(Gushchin & Gordeliy, 2018)*. Structural studies have revealed two distinct HAMP conformations, characterized by different helical registers, rotation, and crossing angles, which dictate opposite downstream signals in bacterial chemotaxis *(Airola et al., 2013)*.

Additionally, the HAMP domain in *E. coli* can sense intracellular pH *(Umemura et al., 2002)*. Sequence identity among HAMP domains is low *(Dunin-Horkawicz & Lupas, 2010; Appleman & Stewart, 2003)*. However, they can be exchanged between various MCPs without affecting their signalling role *(Ames et al., 2014)*. Moreover, MCPs may harbour more than one HAMP module (poly-HAMP) *(Dunin-Horkawicz & Lupas, 2010)*, such as five HAMP domains in the Aer2 receptor from *P. aeruginosa* and di-HAMP domains in the cytoplasmic MCP FrzCD from *M. xanthus (Airola et al., 2013; Jazleena, Das, Guiseppi et al., 2025)*.

The output signalling domain is a long, dimeric, four-helix bundle that interacts with histidine kinase and an adaptor protein to form hexagonal chemosensory arrays *(Briegel et al., 2015, 2014)*. It is formed by two antiparallel coiled-coils having a methylation helix region and a conserved kinase control module *(Park et al., 2006; Kim et al., 1999)*. A glycine hinge is present between the methylation helix region and the kinase control module that allows flexibility to avoid clashes during array formation **(Figure 3.1A)** *(Akkaladevi et al., 2018)*. Methylation of conserved glutamate residues in the methylation helix acts as a sensory adaptation mechanism for the bacterium *(Uchida et al., 2022; Rao et al., 2008)*. Additionally, the signalling domain can sense changes in osmolarity through alterations in the packing of the coiled-coils, as well as small diffusible ligands like ethanol and short-chain alcohols *(Tohidifar et al., 2020; Vaknin & Berg, 2006)*.

MCPs are classified based on the number of heptad repeats present in the coiled-coil methyl-accepting (MA) signalling domain, ranging from 24H to 44H as the major classes **(Figure 3.1C, D)** *(Alexander & Zhulin, 2007)*. Additionally, experiments demonstrate that wild-type and truncated *E. coli* receptors (lower heptad repeats) form distinct, length-dependent arrays that function independently *(Herrera Seitz et al., 2014)*. The underlying mechanism to respond

to sensory inputs is shared across different evolved pathways. It involves the identification of the stimulus, the transduction of stimulus information, and the elicitation of an appropriate response through gene expression or behavioural changes. Evolved diversity is observed to sense, adapt and fine-tune the CSSs for optimal survival *(Cha et al., 2022; Yang & Briegel, 2020; Gumerov et al., 2021; Huang et al., 2019; Mauriello et al., 2018; Wuichet & Zhulin, 2010; Wuichet et al., 2007)*.

In the context of MCPs, diversity and modularity are observed in – (i) sensor LBDs, (ii) the molecular topology in terms of harbouring TM helices and LBDs, (iii) the presence of HAMP domains, and (iv) the number of heptad repeats in coiled-coil signalling domains *(Matilla et al., 2025, 2022; Ortega et al., 2017; Salah Ud-Din & Roujeinikova, 2017; Dunin-Horkawicz & Lupas, 2010; Lacal et al., 2010; Alexander & Zhulin, 2007)*. Here, we looked into the diversity, distribution and prevalence of HAMP and ligand-binding domains in different MCP heptad classes. The aim of this analysis, in context to FrzCD, was to look into – (i) occurrences of multiple HAMP and the significance of the observation of di-HAMP domains in FrzCD, and ii) to identify the LBD in FrzCD based on LBD trends in other MCPs. We investigated whether there exists an evolutionary bias in the distribution of MCP heptad classes relative to (i) membrane-bound (M) and cytoplasmic (Cy) MCPs, (ii) the presence or absence of single or multiple HAMP domains, and (iii) LBDs.

Our analysis of 5,156 methyl-accepting chemotaxis protein (MCP) sequences reveals diversity in their domain architecture, specifically across ligand-binding domains (LBDs), HAMP domains, and coiled-coil signalling domain lengths. Major heptad classes identified were 44H, 40H, 38H, and 36H. Approximately 90% of MCPs analyzed were membrane-bound (M-MCPs). Besides the major classes, membrane-bound MCPs predominantly featured higher heptad counts (above 44H), while shorter classes (less than 36H) were more prevalent in cytoplasmic MCPs. The HAMP domain was present in 78% of all MCPs, predominantly as a single domain (67%). Notably, about 72% of Cy-MCPs lacked HAMP domains. Poly-HAMP domains were identified, and their topology, as concatenated or separated, was investigated. Predominantly, poly-HAMPs were found to be concatenated. We also looked into the LBDs in the MCPs. Certain LBDs exhibited a clear preference for either M-MCPs or Cy-MCPs. However, no correlation was found between MCP heptad classes, HAMP domain presence (single, di-, or poly), or specific LBD types.

3.2 Methods

3.2.1 Data Source

MCP IDs were obtained from the Representative Proteomics 15 (RP15) dataset of PFAM 33.1 database *(Finn et al., 2014)*. PF00015 was used as a query, which corresponds to the conserved MCP signalling domain. Sequences were retrieved from UniProt (https://www.uniprot.org/id-mapping/), and the SMART database was used to annotate features such as TM helices and LBDs in the retrieved sequences *(Letunic & Bork, 2018)* **(Figure 3.2)**. Databases between April 2020 and July 2021 were used to carry out this analysis.

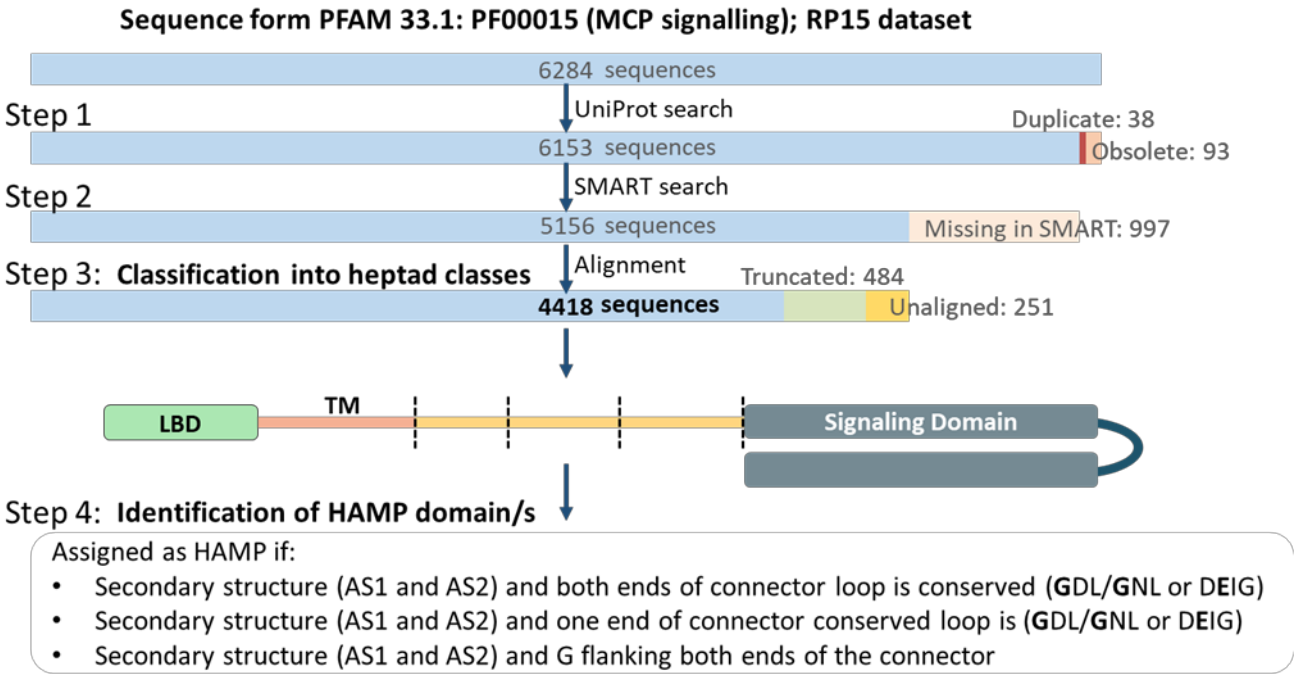


Figure 3.2 Schematic representation of the workflow for the classification of MCPs and identification of the HAMP domain. MCP heptad classes and identified from sequence alignment and HAMP domains were identified based on alignment and secondary structure prediction (Figure 3.3).

3.2.2 Classification of MCPs into heptad classes

Jalview was used to visualize and analyze the sequences *(Waterhouse et al., 2009)*. To classify MCPs into different heptad classes, multiple sequence alignment was performed using ClustalO and Mafft with default parameters in Jalview *(Waterhouse et al., 2009)*. The N02-C02 region of the signalling domain (kinase control module) was highly conserved and used as a reference segment to align sequences **(Figure 3.3A)**. MCPs were classified into different

heptad classes based on their alignment with reference sequences (a subset of sequences was chosen as reference sequences from *Alexander & Zhulin, 2007*). The MiST2 database was also used to cross-check the classification of some sequences into heptad classes *(Ulrich & Zhulin, 2010)*. The workflow is illustrated in **Figure 3.2**.

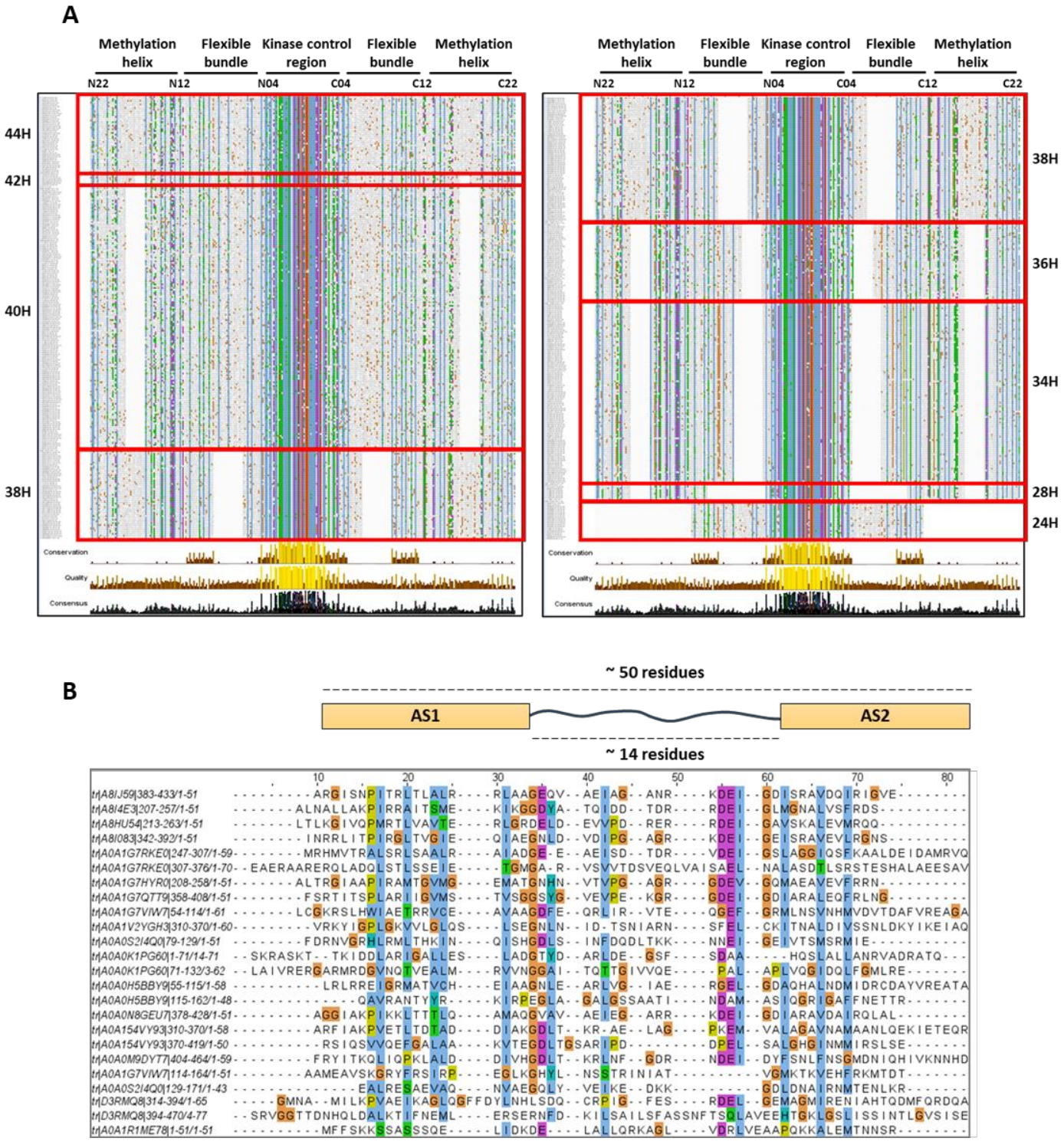


Figure 3.3 Representative alignment showing classification of MCPs into heptad classes (A) and identification of HAMP domains (B). MCP heptad classes are highlighted based on the number of heptads in the coiled-coil MA domain (Alexander & Zhulin, 2007). The colour

scheme, as per ClustalX in Jalview *(Waterhouse et al., 2009)*, is used to represent the alignments.

3.2.3 Identification of HAMP domains

HAMP domain identification using SMART is reported to identify less than 30% of HAMP homologs *(Elliott et al., 2009)*. Hence, sequences were investigated in Jalview for the identification of HAMP domains (this part of the analysis was carried out by Dr. Jaya Sharma). The sequence upstream of the signalling coiled-coil domain was checked for the HAMP domain based on alignment with reference sequences from *(Dunin-Horkawicz & Lupas, 2010; Parkinson, 2010)* and JPred secondary structure prediction in Jalview *(Waterhouse et al., 2009)*. For membrane-bound MCPs, sequences between TM helices and the start of coiled-coil heptad were investigated (50 to 80 residues at a time) for the presence of HAMP domains **(Figure 3.3B)**. The workflow for identification of HAMP domains is illustrated in **Figure 3.2**.

3.3 Results and Discussion

3.3.1 Prevalence of different MCP heptad classes in membrane-bound and cytoplasmic MCPs

We analyzed 5,156 sequences and classified them into different MCP classes based on the heptad repeats of the MA signalling region (a representative alignment of the sequences is shown in **Figure 3.3A**). 40H (40 heptad repeats in the MA domain) is the most prevalent class, accounting for 23% of MCPs, followed by 44H, 38H, and 36H, which account for 20%, 16%, and 14% of MCPs, respectively. These four classes are the most prevalent MCP classes, accounting for 73% of all MCPs. 14% of the MCP sequences in our analysis are unaligned or have a truncated MA signalling domain, which cannot be reliably classified into a heptad class. The remaining 13% MCPs comprise eight other classes, including four higher-heptad-repeat MCP classes (64H, 58H, 52H, and 48H) and four lower-heptad-repeat MCP classes (34H, 30H, 28H, and 24H) **(Figure 3.4A)**.

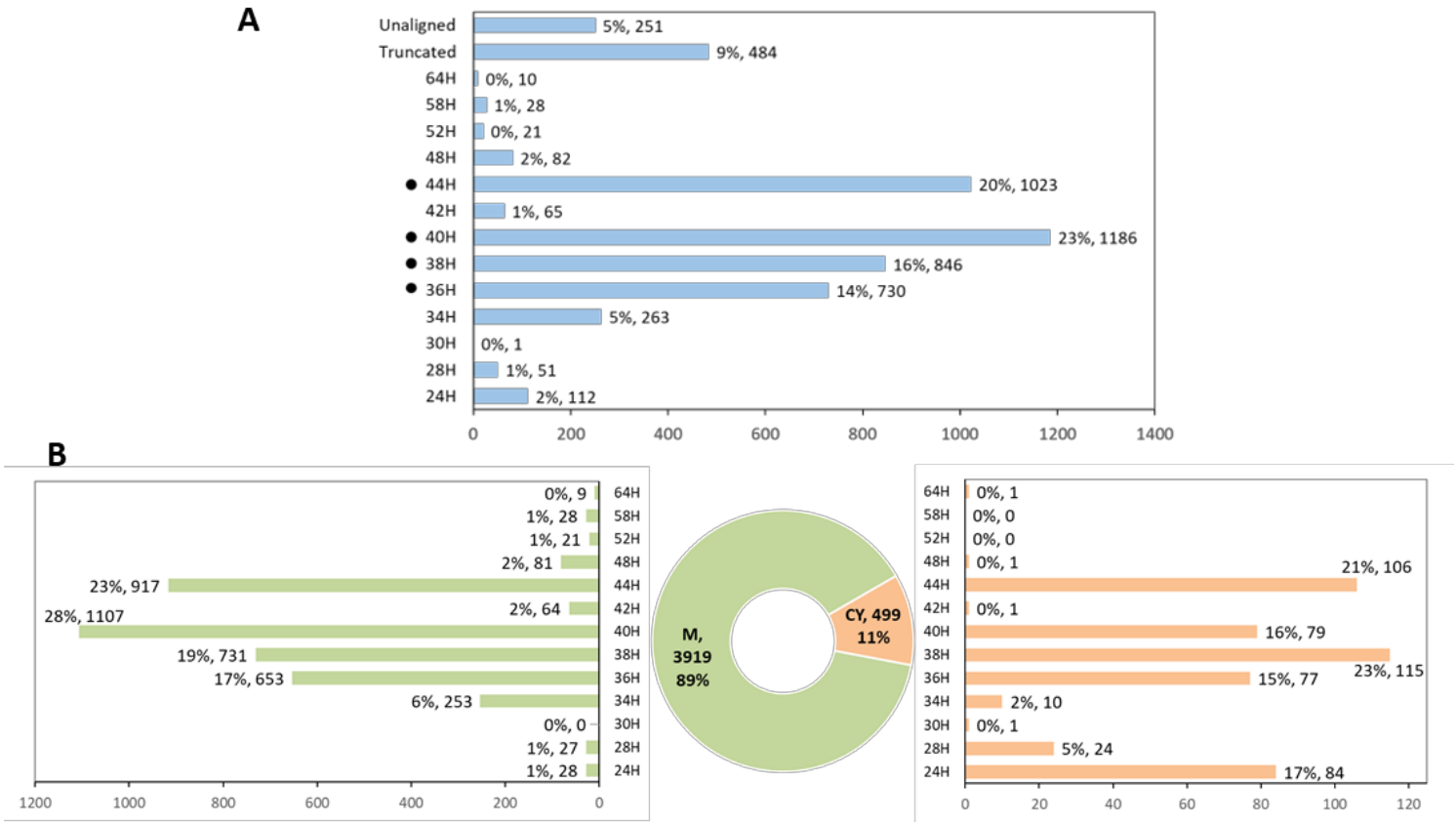


Figure 3.4 Classification of MCPs into different classes. (A) Plot showing the distribution of proteins in different MCP classes. The major MCP classes, 44H, 40H, 38H, and 36H, are highlighted with a black circle. (B) Plot showing distribution of MCP classes in membrane-bound (M, 89%) and cytoplasmic (Cy, 11%) MCPs. Major MCP classes are evenly distributed between M-MCPs (green) and Cy-MCPs (orange), while MCPs with lower heptad repeats, i.e.,

28H and 24H, are predominant in Cy-MCPs and MCP classes with higher heptad repeats are comparatively predominant in M-MCPs. Absolute numbers and percentages are mentioned for each bar.

Next, we examined the prevalence of membrane-bound MCPs (M-MCPs) and cytoplasmic MCPs (Cy-MCPs). We observed that 89% of the MCPs are membrane-bound (**Figure 3.4B)**. These MCPs belong to either class I, II, or III topology, while 11% of MCPs are cytoplasmic, having a class IV topology *(Wuichet et al., 2007)*. We then looked into the distribution of the MCP heptad classes across M-MCP and Cy-MCPs **(Figure 3.4B)**. The prevalent heptad classes (44H, 40H, 38H and 36H) accounted for 87% of M-MCPS and 75% of Cy-MCPs. Notably, 44H and 36H are almost evenly distributed between the two groups, while 40H and 38H dominate M-MCPs and Cy-MCPs, respectively. Interestingly, MCP classes with lower heptad repeats, less than 36H, are more prevalent in cytoplasmic MCPs (23% of C-MCPs and 8% of M-MCPs). In contrast, higher heptad-repeat MCPs, above 44H, are observed for membrane-bound MCPs (4% of M-MCPs). There is a significant abundance of 24H MCP class (17%) observed for Cy-MCPs compared to M-MCPs.

3.3.2 HAMP domain is predominantly present in membrane-bound MCPs

HAMP domain was identified for the MCPs based on sequence alignment and secondary structure prediction of the protein region N-terminally adjacent to the MA domain. We looked into the distribution of HAMP domains in individual MCPs. The HAMP domain is conventionally known to couple signals from the input domain to the output domain across TM domain for class I topology MCPs *(Hulko et al., 2006)*. Poly-HAMP MCPs are also reported, such as the cytoplasmic Aer2 chemoreceptor from *P. aeruginosa*, which has five HAMP domains *(Watts et al., 2011; Airola et al., 2010)*.

We observed that the majority of MCPs (approximately 78%) have HAMP domains, ranging from single HAMP MCPs to as many as 13 HAMP MCPs **(Figure 3.5B)**. These MCPs mostly have a single HAMP domain (67%), followed by di-HAMP domains (7%). Next, we analyzed whether there was a preference for HAMP domains in M-MCPs compared to Cy-MCPs. We found that 85% of M-MCPs have a HAMP domain compared to only 28% for Cy-MCPs **(Figure 3.5C)**. Additionally, poly-HAMP MCPs are identified in both M- and Cy-MCPS (12% of M-MCPs and 8% of C-MCPs). In the case of Cy-MCPs, the prevalence of the HAMP domain is reported for class IVa topology chemoreceptors with long N-terminal domains with an LBD,

which might couple signal transduction similar to M-MCPs *(Dunin-Horkawicz & Lupas, 2010; Salah Ud-Din & Roujeinikova, 2017; Watts et al., 2011)*.

Structural studies revealed two different HAMP conformers present in the tri-HAMP domain of the Cy-MCP Aer2 receptor from *P. aeruginosa*, with distinct helical registers, rotations, and crossing angles that dictate opposite downstream signals in bacterial chemotaxis *(Airola et al., 2013)*. However, poly-HAMP in Cy-MCPs might play additional roles. Apart from signalling, the tri-HAMP region in cytoplasmic Aer2 MCP controls the cellular localization of receptors in *P. aeruginosa (Anaya et al., 2022)*, while the di-HAMP domains of cytoplasmic MCP FrzCD modulates array formation on the nucleoid of *M. xanthus (Jazleena, Das, Guiseppi et al., 2025)*. Additionally, no correlation was observed between the MCP heptad classes and the number of HAMP domains present in the MCPs **(Figure 3.6)**.

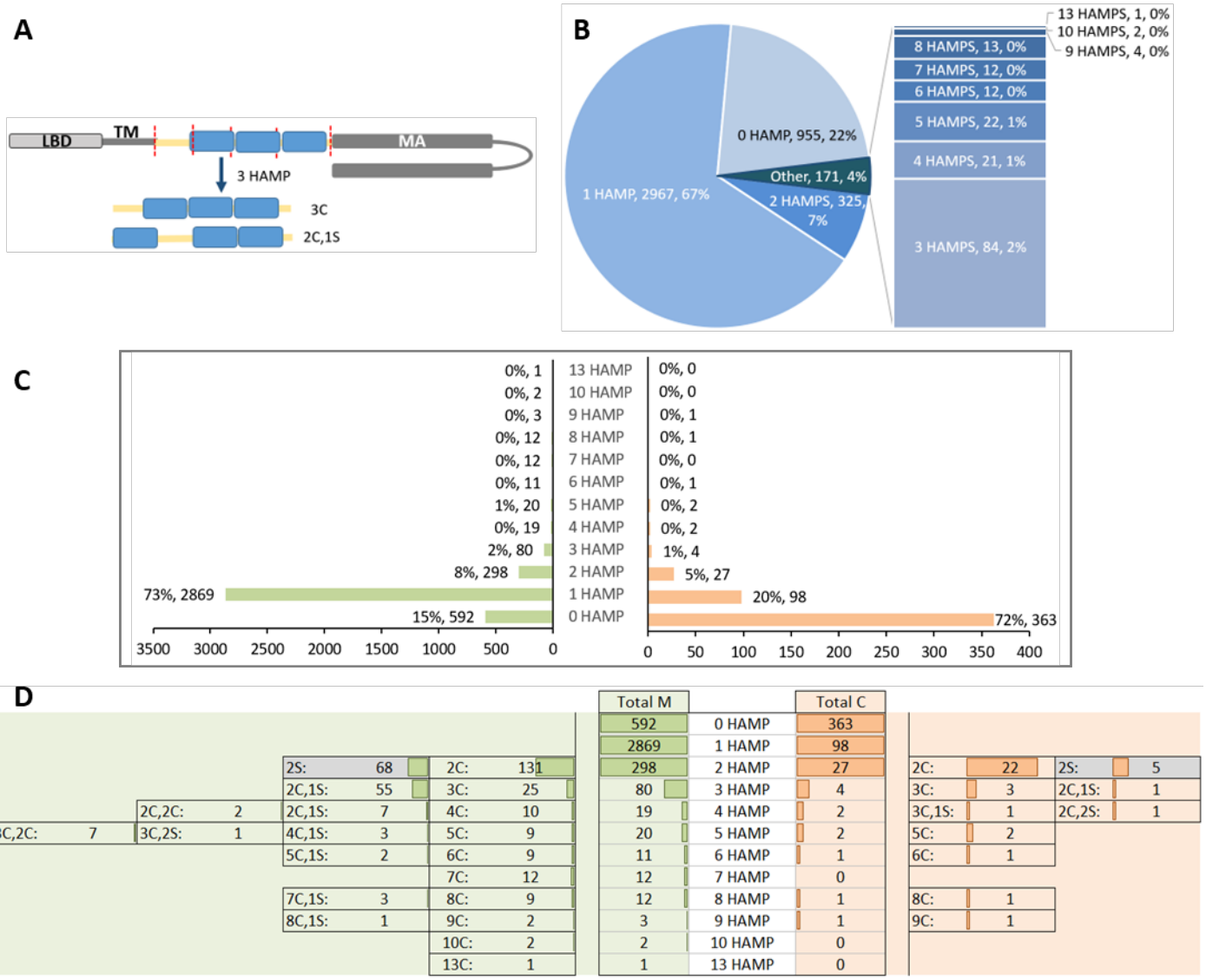


Figure 3.5 Prevalence and distribution of HAMP domains. (A) Schematic illustration of the identification of poly-HAMP MCPs and classification based on localization. It is observed that

poly-HAMP domains are found adjacent or concatenated (denoted as 'C') or might be separated from one another (>80 residues, denoted as S). The schematic shows that if three HAMP domains are identified in an MCP, they might be concatenated, represented as 3C, or if one is separated, it is defined as 2C,1S. (B) Plot showing distribution of MCPs according to the number of HAMP domains: 78% of MCPs have a HAMP domain, and the majority have a single HAMP domain (67%). Poly-HAMP MCPs account for 22% of MCPs, with a majority of 2-HAMP MCPs. Absolute numbers and percentages are mentioned in the plot. (C) Distribution of MCPs according to the number of HAMP domains present in Cy-MCPs and M-MCPs. It is observed that the majority of M-MCPs (85%) possess a HAMP domain, compared to Cy-MCPs (approximately 28%). Absolute numbers and percentages are mentioned for each bar. (D) Distribution of Poly-HAMP MCPs as concatenated (C) or Separated (S). The notation in figure here is denoted by combination of C and S. For example, a protein with 5 HAMP domains has the following possibilities: 5 concatenated (5C), four concatenated HAMP and one separated (4C,1S), three concatenated and two separated (3C,2S) or three concatenated and after separation rest two HAMPs are concatenated (3C,2C). M-MCPs are green, Cy-MCPS are orange and grey denotes absence of concatenated HAMPs in poly-HAMP MCPs. Absolute numbers are mentioned along with a bar representing the fraction of total (Total M-MCPs: 3919 and Total Cy-MCPs: 499).

A

HAMP classes	MCP heptad class																																				
	24H			28H			30H			34H			36H			38H			40H			42H			44H			48H			64H			
	#	%H	%TH	#	%H	%TH	#	%H	%TH	#	%H	%TH	#	%H	%TH	#	%H	%TH	#	%H	%TH	#	%H	%TH	#	%H	%TH	#	%H	%TH	#	%H	%TH	
0 HAMP	82	98%	23%	24	100%	7%	1	100%	0%	6	60%	2%	8	10%	2%	89	77%	24%	62	78%	17%	1	100%	0%	89	82%	24%	1	100%	0%							363
1 HAMP	2	2%	2%										44	57%	44%	23	20%	23%	14	18%	14%				14	13%	14%				1	100%	1%				98
2 HAMP										1	10%	4%	19	25%	70%	2	2%	7%	3	4%	11%				2	2%	7%										27
3 HAMP										1	10%	25%	1	1%	25%	1	1%	25%							1	1%	25%										4
4 HAMP													2	3%	100%																						2
5 HAMP													2	3%	100%																						2
6 HAMP													1	1%	100%																						1
8 HAMP										1	10%	100%																									1
9 HAMP										1	10%	100%																									1
	84			24			1			10			77			115			79			1			106			1			1						499

5 10 20 50 100

B

HAMP classes	MCP heptad class																																				
	24H			28H			34H			36H			38H			40H			42H			44H			48H			52H			58H			64H			
	#	%H	%TH	#	%H	%TH	#	%H	%TH	#	%H	%TH	#	%H	%TH	#	%H	%TH	#	%H	%TH	#	%H	%TH	#	%H	%TH	#	%H	%TH	#	%H	%TH	#	%H	%TH	
0 HAMP	21	75%	4%	8	30%	1%	12	5%	2%	132	20%	22%	52	7%	9%	134	12%	23%	3	5%	1%	205	22%	35%	17	21%	3%				5	18%	1%	3	33%	1%	592
1 HAMP	7	25%	0%	8	30%	0%	192	76%	7%	219	34%	8%	653	89%	23%	924	83%	32%	61	95%	2%	693	76%	24%	64	79%	2%	20	95%	1%	23	82%	1%	5	56%	0%	2869
2 HAMP				11	41%	4%	18	7%	6%	193	30%	65%	19	3%	6%	45	4%	15%				10	1%	3%				1	5%	0%				1	11%	0%	298
3 HAMP							10	4%	13%	57	9%	71%	5	1%	6%	2	0%	3%				6	1%	8%													80
4 HAMP							3	1%	16%	11	2%	58%	1	0%	5%	1	0%	5%				3	0%	16%													19
5 HAMP							9	4%	45%	10	2%	50%																									20
6 HAMP										11	2%	100%																									11
7 HAMP							3	1%	25%	9	1%	75%																									12
8 HAMP							2	1%	17%	9	1%	75%	1	0%	8%																						12
9 HAMP							1	0%	33%	2	0%	67%																									3
10 HAMP							2	1%	100%																												2
13 HAMP							1	0%	100%																												1
	28			27			253			653			731			1107			64			917			81			21			28			9			3919

10 20 100 200 500 1000

- absolute number of sequences
%H – percentage of sequences that belong to a particular HAMP class
%TH – percentage of sequences where HAMP domain/s were identified

Figure 3.6 Distribution of HAMP domains in different MCP heptad classes. Presence of single, di- or poly-HAMP domain harbouring MCPs in (A) Cy-MCPs heptad classes, and (B) M-MCP heptad classes. '#' denotes the absolute number of sequences, '%H' denotes the percentage of sequences that belong to a particular HAMP class (for example, 1 HAMP, 2 HAMP and so on), and '%TH' denotes the percentage of sequences where HAMP domain/s

were identified for a heptad class. Boxes are coloured according to the absolute number of sequences represented by the key.

3.3.3 Poly-HAMP MCPs mostly have concatenated HAMP domains

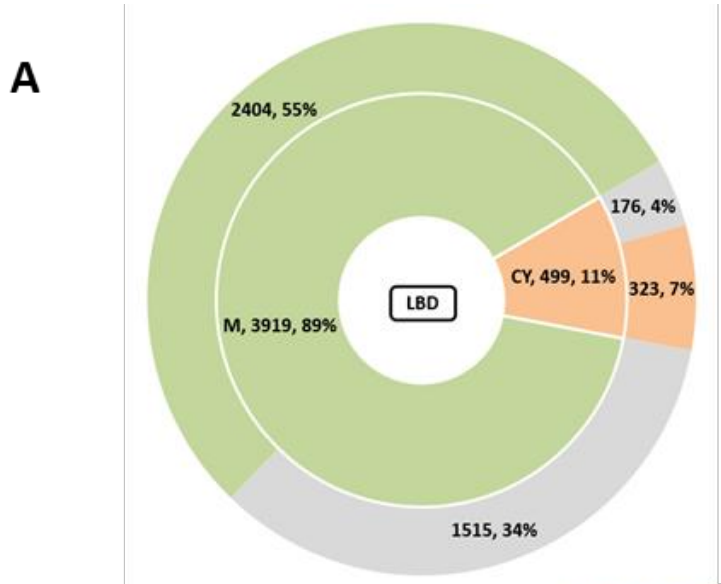
A poly-HAMP MCP might have the HAMP domains in tandem (concatenated) or separated by a stretch with LBD. For example, the *P. aeruginosa* Aer2 chemoreceptor consists of three N-terminal concatenated HAMP domains, followed by a PAS LBD and two additional concatenated HAMP domains, which are linked to the C-terminal MA domain *(Watts et al., 2011)*. Poly-HAMP MCPs (more than one HAMP domain) accounted for around 11% of MCPs in our analysis **(Figure 3.5B)**.

We examined the topological distribution of poly-HAMP domains, considering their arrangement as either concatenated or separated **(Figure 3.5A)**. The distribution of poly-HAMP MCPs between M-MCPs and Cy-MCPs is listed in **Figure 3.5D,** where 'C' stands for concatenated HAMPs and 'S' stands for separated HAMPs. It is observed that MCPs with five HAMP domains have the following architecture: '5C' - five concatenated HAMPs, '4C,1S' - four concatenated C-terminal HAMP linked to the MA domain and one separated HAMP, '3C,2S' - three concatenated and two separated HAMP domains with gaps, and '3C,2C' – three concatenated HAMPs followed by a gap and then two concatenated HAMPs. The gap length considered is greater than 80 residues. It is observed that apart from di-HAMP MCPs (where the two HAMP domains are separated, i.e. 15% of poly-HAMP M-MCPs and 13% of poly-HAMP Cy-MCPs), all other poly-HAMP MCPs have at least 2 HAMP domains concatenated, which increases all the way to 10 or 13 HAMP MCPs where all the HAMP domains are concatenated. The structure of the N-terminal three concatenated HAMP domains provided insight into the presence of two different HAMP conformers responsible for antagonistic signalling outputs *(Airola et al., 2013)*. However, the functional advantage of concatenated HAMP domains over single HAMP domains is not well understood.

3.3.4 Not all MCPS possess an exclusive LBD

SMART database was used to identify the LBDs present in the MCPs in our analysis. At least one LBD was identified in 62% of the MCPs, which included 55% of M-MCPs and only 7% of Cy-MCPs **(Figure 3.7A)**. More than 70 different LBD types were identified across 40 distinct families and 18 Pfam clans, as listed in **Table 3.1**. Cache-like domain (39% of MCPs),

4HB_MCP (31% of MCPs), and PAS (11% of MCPs) are the three most abundant LBD clans, accounting for 81% of MCPs with known LBDs. CZB accounts for 5% while PBP, Protoglobin, NIT and PilJ account for 2% of MCPs **(Figure 3.7C)**. A detailed distribution of MCPs with different LBDs is listed in **Table 3.1.**



B

M	LBD	CY
963	4HB_MCP	0
62	PilJ	0
34	DUF3365	0
3	Ammonium_transp	0
1	Cupin	0
1	Gx_transp	0
5	GPCR_A	0
2	GBD	0
1	2heme_cytochrom	0
1	Band_7	0
1	AI-2E_transport	0
1	DUF442	0
1	DUF745	0
1	FRB_dom	0
1192	Cache-like	17
60	NIT	2
39	Hemerythrin	2
22	PilZ	8
3	GAF	2
1	P-loop_NTPase	1
2	Beta_prppeller	1
2	E-set	1
19	HNOX-like	10
65	PBP	34
194	PAS	130
80	CZB	75
1	Protoglobin	63
0	4Fe-4S	2
0	PhoU	1
0	PocR	3
0	FIST	2
0	FIST_C	2
0	Fe_hyd_lg_C	1
2756		358

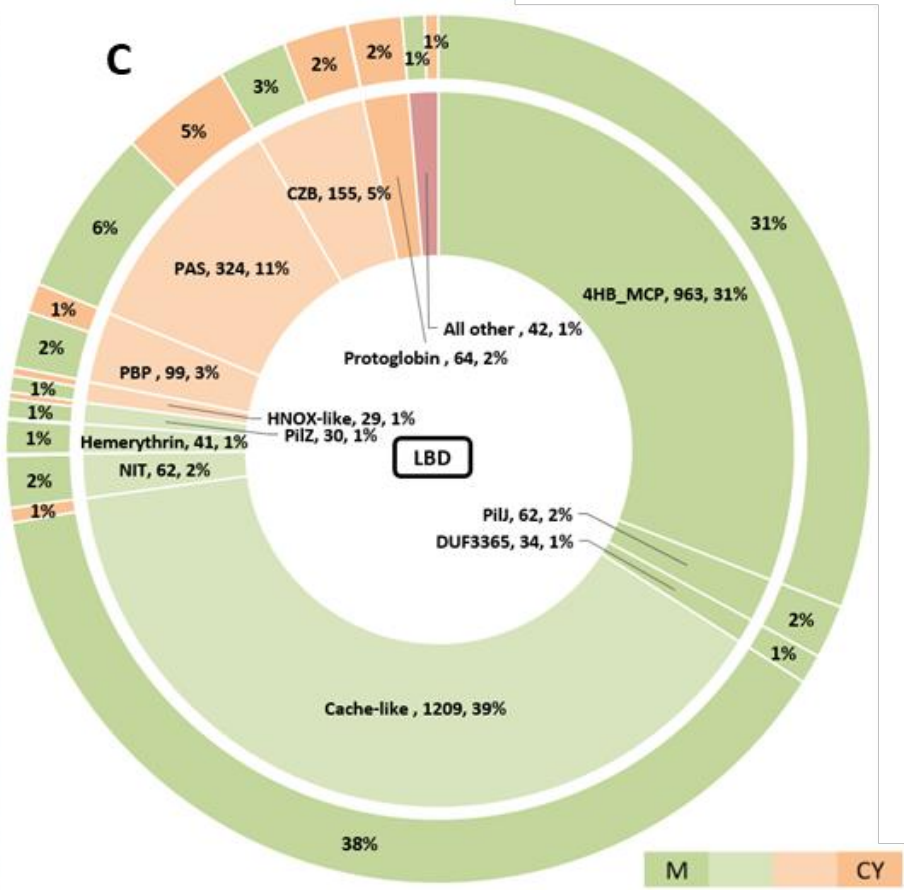


Figure 3.7 Distribution of LBDs across MCPs. (A) Plot showing the presence of one or more LBDs as identified by the SMART server *(Letunic & Bork, 2018)*. SAMRT identified one or more LBDs in 62% of MCPs. M-MCPs are green, Cy-MCPS are orange and grey denotes the absence of any LBD. (B) Diversity of LBDs between cytoplasmic and membrane-bound

MCPS. Shades of green indicate the prevalence of the domain in M-MCPs, while shades of orange indicate abundance in Cy-MCPs. The absolute numbers are listed in the table. (C) Plot showing the prevalence of the most abundant LBDs and their distribution between Cy-MCPs (orange) vs M-MCPs (green). Cache-like domain (39%) and 4HB_MCP (31%) are the predominant LBDs in MCPs, followed by PAS (11%).

3.3.5 LBDs are either membrane-bound or cytoplasmic depending on the diffusion and intracellular accessibility features of the ligand

The presence of different LBDs was identified separately for M-MCPs and Cy-MCPs. Interestingly, certain LBDs were exclusively present in either M-MCPs or Cy-MCPs while others were either prevalent in M-MCPs or Cy-MCPs **(Figure 3.7B)**. Domains like 4HB_MCP, PilJ, DUF3365, GPCR_A, Ammonium_transp, GBD and a few others are extensively found in M-MCPs, while Protoglobin, 4Fe-4S, PhoU and Fist are present only in Cy-MCPs. Besides, Cache-like, NIT, and Hemerythrin are prevalent in M-MCPs, while PAS, CZB, PBP, and HNOX-like are more prevalent in Cy-MCPs. **Figure 3.7B** lists the abundance of LBDs according to their distribution in M-MCPs and Cy-MCPs. The availability of ligands present in cytoplasm and periplasm might explain this asymmetric distribution of LBDs. LBD diversity is also closely associated with ecological habitats *(Cha et al., 2022; Alexandre et al., 2004)*. Additionally, a single domain can detect a wide range of ligands. For example, dCache primarily senses amino acids, purines, sugars, inorganic ions, polyamines and many other molecules *(Matilla et al., 2022)*. Similarly, the PAS domain acts as a universal intracellular sensor, correlating with its high prevalence among cytoplasmic MCPs. It can sense gas molecules, the redox state, aromatic amino acids, among others *(Matilla et al., 2022)*. Furthermore, some LBDs are very specific, such as the nitrate and nitrite sensor domain, NIT *(Shu et al., 2003)*. Predicting the ligand stimulus for a particular LBD remains challenging due to low sequence similarity among family members that bind the same ligand *(Matilla & Krell, 2024)*. Sensory LBDs undergo rapid evolution, which enables them to recognize the same ligand despite substantial sequence divergence *(Gavira et al., 2020)*.

Next, we looked into the distribution of LBDs in the context of different MCP heptad classes. There was an absence of correlation for the preference of LBDs to specific MCP classes **(Figure 3.8).** A similar analysis was carried out with respect to the number of HAMP domains in MCPs and the LBD present, however, no correlation was observed.

Table 3.1 Prevalence and distribution of LBDs between Cy-MCPs and M-MCPs.

Clan	Family		Cytoplasmic	Membrane
4HB_MCP (CL0457)	4HB_MCP_1	PF12729	0	581
	CHASE3	PF05227	0	44
	HBM	PF16591	0	101
	TarH	PF02203	0	237
Cache-like (CL0165)	dCache and sCache	PF08269	13	1185
		PF02743		
		PF14827		
		PF17201		
		PF17200		
		PF17203		
		PF17202		
		PF09984		
	Diacid_rec	PF05651	3	0
	GAPES1	PF17155	0	3
	YkuI_C	PF10388	1	0
	CHASE8	PF17152	0	4
PAS (CL0183)	PAS	PF00989	130	194
		PF00989		
		PF13596		
		PF08447		
		PF08448		
		PF13188		
		PF13426		
GAF (CL0161)	GAF	PF01590	2	3
		PF13185		
Protoglobin (CL0090)	Globin	PF00042	1	0
	Protoglobin	PF11563	62	1
PBP (CL0144)	Peripla_BP	PF00532	13	8
		PF13377		
		PF13407		
		PF13433		
		PF13458		
		PF01094		
PBP (CL0177)	NMT1	PF09084	3	3
	DctP	PF03480	0	2
	SBP_bac_3	PF00497	11	0
	SBP_bac_5	PF00496	3	48
	Phosphonate-bd	PF12974	4	4
4Fe-4S (CL0344)	Fer4	PF00037	1	0
		PF13237		
		PF12837		
		PF12838		
	FeS	PF04060	1	0
P-loop_NTPase (CL0023)	AAA	PF00004	1	1
	Pfam:ABC_tran	PF00005		
Cupin (CL0029)	cNMP_binding	PF00027	0	1
Gx_transp (CL0315)	5TM-5TMR_LYT	PF07694	0	1
GPCR_A (CL0129)	7TMR-DISM_7TM	PF07695	0	5
GBD (CL0202)	7TMR-DISMED2	PF07696	0	2
HNOX-like (CL0210)	HNOB	PF07700	10	19
2heme_cytochrom (CL0328)	Ni_hydr_CYTB	PF01292	0	1
Beta_prppeller (CL0186)	Reg_prop	PF07494	1	2
E-set (CL0159)	Y_Y_Y	PF07495	1	2
PhoU (CL0297)	PhoU	PF01895	1	0
No assigned clan	CZB	PF13682	75	80
	Hemerythrin	PF01814	2	39
	Pfam:NIT	PF08376	2	60
	Pfam:PilJ	PF13675	0	62
	Pfam:PilZ	PF07238	8	22
	Pfam:PocR	PF10114	3	0
	Pfam:Band_7	PF01145	0	1
	Pfam:FIST	PF08945	2	0
	Pfam:FIST_C	PF10442	2	0
	Pfam:AI-2E_transport	PF01594	0	1
	Pfam:Ammonium_transp	PF00909	0	3
	Pfam:DUF3365	PF11845	0	34
	Pfam:DUF442	PF04273	0	1
	Pfam:DUF745	PF05335	0	1
	Pfam:Fe_hyd_lg_C	PF02906	1	0
	Pfam:FRB_dom	PF08771	0	1

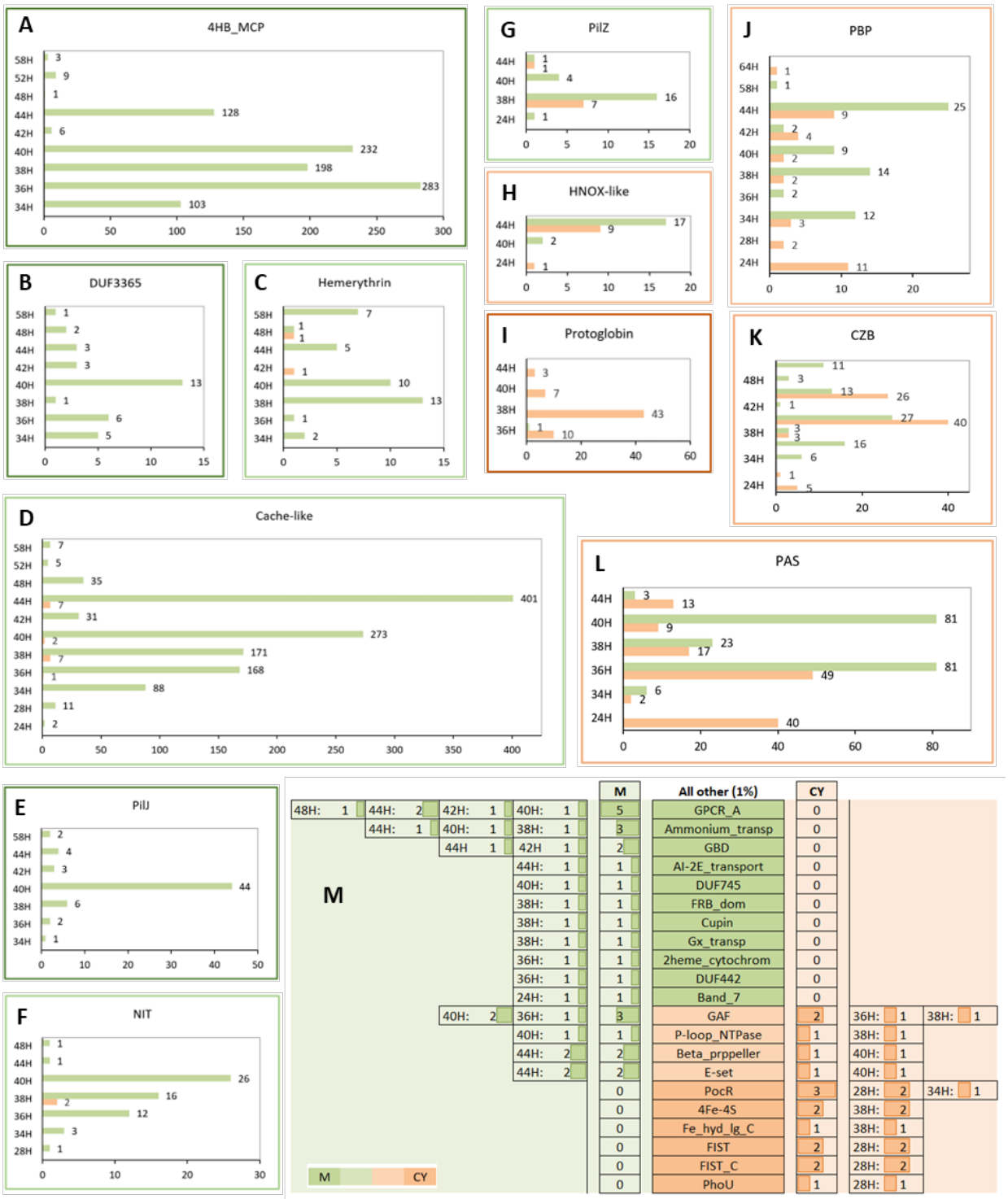


Figure 3.8 Distribution of LBDs across different MCP classes. No correlation was observed between the distribution of LBDs and MCP classes. However, the LBDs can be grouped according to their prevalence between M-MCPs and Cy-MCPs. Domains like 4HB_MCP (A), DUF3365 (B), PilJ (E), GPCR_A, Ammonium_transp, GBD, Al-2E_transport, DUF745, FRB_dom, Cupin, Gx_transp, 2heme_cytochrom, DUF442, and Band_7(M) are exclusively observed in M-MCPs. LBDs like Hemerythrin (C), Cache-like (D), NIT (F), PilZ (G) are predominantly observed in M-MCPs, while HNOX-like (H), PBP (J), CZB (K), PAS (L), GAF, P-loop_NTPase, Beta-propeller, E-set (M) are predominantly observed in Cy-MCPs. Domains like Protoglobin (I), PocR, 4Fe-4S, Fe_hyd_Ig_C, FIST, FIST_C, PhoU (M) are exclusively observed in Cy-MCPs.

3.4 Conclusions

This analysis highlights the diversity of MCPs in terms of sensory LBDs, the presence of single, di-, or poly-HAMP domains, and the number of heptads in the coiled-coil signalling domain. We classified 5,156 sequences into MCP heptad classes, where 44H, 40H, 38H, and 36H MCP classes represent the major categories identified in our study. The majority of MCPs (approximately 90%) are membrane-bound. Subsequently, we examined the distribution of MCP heptad classes within Cy-MCPs and M-MCPs and observed that, besides the predominant classes, MCP classes with fewer heptads, such as 28H and 24H, are more common in cytoplasmic MCPs. Conversely, MCP classes with higher heptad counts are comparatively predominant in membrane-bound MCPs.

We identified HAMP domains within the MCP sequences and categorized them based on the number of HAMP domains present, noting whether, for poly-HAMP arrangements, the HAMP domains were concatenated or separated. The HAMP domain was present in the majority of MCPs (78%), predominantly as a single HAMP domain (67%). Cytoplasmic MCPs largely lack HAMP domains, with around 72% lacking them, and the remaining tend to contain a single HAMP domain. This likely indicates that a single HAMP domain is sufficient to serve as an input-output coupling domain in M-MCPs. In contrast, poly-HAMP regions may have additional roles, such as the tri-HAMP region in cytoplasmic Aer2 MCPs, which regulate the cellular localization of receptors in *P. aeruginosa (Anaya et al., 2022)*. Similarly, the di-HAMP domains in the cytoplasmic MCP FrzCD influences array formation on the nucleoid in *M. xanthus (Jazleena, Das, Guiseppi et al., 2025)*. Poly-HAMP arrangements were predominantly found to be concatenated, although their significance is not well understood. They have been observed to be present in opposing conformers in the Aer2 receptor *(Airola et al., 2013)*. We failed to identify other MCPs with an architecture and DB domain similar to FrzCD (a DB sequence of b-Zip proteins: NxxAAxxCR, where x is a variable but often positively charged residue). This emphasizes the novel nature of cytoplasmic MCP FrzCD.

We further identified LBDs within the MCP sequences and evaluated their prevalence in Cy-MCPs and M-MCPs. The most abundant LBD families were Cache-like domains (39% of MCPs), 4HB_MCP (31%), and PAS domains (11%), collectively accounting for 81% of LBDs identified in our analysis. We observed that certain LBDs were preferred in either M-MCPs or Cy-MCPs, with some LBD types being predominantly present in one group. No correlation was found between MCP heptad classes and the presence of single, di-, or poly-HAMP

domains, nor with specific LBD types. We believe FrzCD can detect intracellular signals, such as changes in osmolality or small, diffusible molecules like short-chain alcohols. Changes in osmolarity is reported to alter the packing of the coiled-coils of *E. coli* MCPs, and ethanol molecules are reported to bind to the coiled-coil of transmembrane chemoreceptor McpB MCPs in *B. subtilis (Tohidifar et al., 2020; Vaknin & Berg, 2006)*. Although the fundamental hexagonal architecture of chemosensory arrays is conserved, it is less explored how diversities in terms of poly-HAMP domains and MCP heptad classes influence array architecture and signal transduction.

3.5 References

1. Airola, M. V., Sukomon, N., Samanta, D., Borbat, P. P., Freed, J. H., Watts, K. J., & Crane, B. R. (2013). HAMP Domain Conformers That Propagate Opposite Signals in Bacterial Chemoreceptors. *PLOS Biology*, *11*(2), e1001479. https://doi.org/10.1371/journal.pbio.1001479

2. Airola, M. V., Watts, K. J., Bilwes, A. M., & Crane, B. R. (2010). Structure of Concatenated HAMP Domains Provides a Mechanism for Signal Transduction. *Structure*, *18*(4), 436–448. https://doi.org/10.1016/j.str.2010.01.013

3. Akkaladevi, N., Bunyak, F., Stalla, D., White, T. A., & Hazelbauer, G. L. (2018). Flexible Hinges in Bacterial Chemoreceptors. *Journal of Bacteriology*, *200*(5), 10.1128/jb.00593-17. https://doi.org/10.1128/jb.00593-17

4. Alexander, R. P., & Zhulin, I. B. (2007). Evolutionary genomics reveals conserved structural determinants of signaling and adaptation in microbial chemoreceptors. *Proceedings of the National Academy of Sciences*, *104*(8), 2885–2890. https://doi.org/10.1073/pnas.0609359104

5. Alexandre, G., Greer-Phillips, S., & Zhulin, I. B. (2004). Ecological role of energy taxis in microorganisms. *FEMS Microbiology Reviews*, *28*(1), 113–126. https://doi.org/10.1016/j.femsre.2003.10.003

6. Ames, P., Zhou, Q., & Parkinson, J. S. (2014). HAMP domain structural determinants for signalling and sensory adaptation in Tsr, the Escherichia coli serine chemoreceptor. *Molecular Microbiology*, *91*(5), 875–886. https://doi.org/10.1111/mmi.12443

7. Anaya, S., Orillard, E., Greer-Phillips, S. E., & Watts, K. J. (2022). New Roles for HAMP Domains: The Tri-HAMP Region of Pseudomonas aeruginosa Aer2 Controls Receptor Signaling and Cellular Localization. *Journal of Bacteriology*, *204*(9), e00225-22. https://doi.org/10.1128/jb.00225-22

8. Appleman, J. A., & Stewart, V. (2003). Mutational Analysis of a Conserved Signal-Transducing Element: The HAMP Linker of the Escherichia coli Nitrate Sensor NarX. *Journal of Bacteriology*, *185*(1), 89–97. https://doi.org/10.1128/jb.185.1.89-97.2003

9. Aravind, L., & Ponting, C. P. (1999). The cytoplasmic helical linker domain of receptor histidine kinase and methyl-accepting proteins is common to many prokaryotic signalling proteins. *FEMS Microbiology Letters*, *176*(1), 111–116. https://doi.org/10.1111/j.1574-6968.1999.tb13650.x

10. Bardy, S. L., Briegel, A., Rainville, S., & Krell, T. (2017). Recent Advances and Future Prospects in Bacterial and Archaeal Locomotion and Signal Transduction. *Journal of Bacteriology*, *199*(18), 10.1128/jb.00203-17. https://doi.org/10.1128/jb.00203-17

11. Bi, S., & Lai, L. (2014). Bacterial chemoreceptors and chemoeffectors. *Cellular and Molecular Life Sciences: CMLS*, *72*(4), 691–708. https://doi.org/10.1007/s00018-014-1770-5

12. Bibikov, S. I., Biran, R., Rudd, K. E., & Parkinson, J. S. (1997). A signal transducer for aerotaxis in Escherichia coli. *Journal of Bacteriology*, *179*(12), 4075–4079. https://doi.org/10.1128/jb.179.12.4075-4079.1997

13. Briegel, A., Ladinsky, M. S., Oikonomou, C., Jones, C. W., Harris, M. J., Fowler, D. J., Chang, Y.-W., Thompson, L. K., Armitage, J. P., & Jensen, G. J. (2014). Structure of bacterial cytoplasmic chemoreceptor arrays and implications for chemotactic signaling. *eLife*, *3*, e02151. https://doi.org/10.7554/eLife.02151

14. Briegel, A., Ortega, D. R., Huang, A., Oikonomou, C. M., Gunsalus, R. P., & Jensen, G. J. (2015). Structural conservation of chemotaxis machinery across Archaea and Bacteria. *Environmental Microbiology Reports*, *7*(3), 414–419. https://doi.org/10.1111/1758-2229.12265

15. Butler, S. L., & Falke, J. J. (1998). Cysteine and disulfide scanning reveals two amphiphilic helices in the linker region of the aspartate chemoreceptor. *Biochemistry*, *37*(30), 10746–10756. https://doi.org/10.1021/bi980607g

16. Cha, G., Liu, Y., Yang, Q., Bai, L., Cheng, L., & Fan, W. (2022). Comparative Genomic Insights into Chemoreceptor Diversity and Habitat Adaptation of Archaea. *Applied and Environmental Microbiology*, *88*(22), e0157422. https://doi.org/10.1128/aem.01574-22

17. Dunin-Horkawicz, S., & Lupas, A. N. (2010). Comprehensive Analysis of HAMP Domains: Implications for Transmembrane Signal Transduction. *Journal of Molecular Biology*, *397*(5), 1156–1174. https://doi.org/10.1016/j.jmb.2010.02.031

18. Elliott, K. T., Zhulin, I. B., Stuckey, J. A., & DiRita, V. J. (2009). Conserved Residues in the HAMP Domain Define a New Family of Proposed Bipartite Energy Taxis Receptors. *Journal of Bacteriology*, *191*(1), 375–387. https://doi.org/10.1128/JB.00578-08

19. Finn, R. D., Bateman, A., Clements, J., Coggill, P., Eberhardt, R. Y., Eddy, S. R., Heger, A., Hetherington, K., Holm, L., Mistry, J., Sonnhammer, E. L. L., Tate, J., & Punta, M. (2014). Pfam: The protein families database. *Nucleic Acids Research*, *42*(D1), D222–D230. https://doi.org/10.1093/nar/gkt1223

20. Gavira, J. A., Gumerov, V. M., Rico-Jiménez, M., Petukh, M., Upadhyay, A. A., Ortega, A., Matilla, M. A., Zhulin, I. B., & Krell, T. (2020). How Bacterial Chemoreceptors Evolve Novel Ligand Specificities. *mBio*, *11*(1), 10.1128/mbio.03066-19. https://doi.org/10.1128/mbio.03066-19

21. Gumerov, V. M., Andrianova, E. P., & Zhulin, I. B. (2021). Diversity of bacterial chemosensory systems. *Current Opinion in Microbiology*, *61*, 42–50. https://doi.org/10.1016/j.mib.2021.01.016

22. Gushchin, I., & Gordeliy, V. (2018). Transmembrane Signal Transduction in Two-Component Systems: Piston, Scissoring, or Helical Rotation? *BioEssays: News and Reviews in Molecular, Cellular and Developmental Biology*, *40*(2). https://doi.org/10.1002/bies.201700197

23. He, K., & Bauer, C. E. (2014). Chemosensory signaling systems that control bacterial survival. *Trends in Microbiology*, *22*(7), 389–398. https://doi.org/10.1016/j.tim.2014.04.004

24. Herrera Seitz, M. K., Frank, V., Massazza, D. A., Vaknin, A., & Studdert, C. A. (2014). Bacterial chemoreceptors of different length classes signal independently. *Molecular Microbiology*, *93*(4), 814–822. https://doi.org/10.1111/mmi.12700

25. Hou, S., Larsen, R. W., Boudko, D., Riley, C. W., Karatan, E., Zimmer, M., Ordal, G. W., & Alam, M. (2000). Myoglobin-like aerotaxis transducers in Archaea and Bacteria. *Nature*, *403*(6769), 540–544. https://doi.org/10.1038/35000570

26. Huang, Z., Pan, X., Xu, N., & Guo, M. (2019). Bacterial chemotaxis coupling protein: Structure, function and diversity. *Microbiological Research*, *219*, 40–48. https://doi.org/10.1016/j.micres.2018.11.001

27. Hulko, M., Berndt, F., Gruber, M., Linder, J. U., Truffault, V., Schultz, A., Martin, J., Schultz, J. E., Lupas, A. N., & Coles, M. (2006). The HAMP Domain Structure Implies Helix Rotation in Transmembrane Signaling. *Cell*, *126*(5), 929–940. https://doi.org/10.1016/j.cell.2006.06.058

28. Jazleena, P. J., Das, A., Guiseppi, A., Debard, F., Sharma, J., Yaikhomba, M., Mignot, T., Mauriello, E. M. F., & Gayathri, P. (2025). Di-HAMP domains of a cytoplasmic chemoreceptor modulate nucleoid array formation and downstream signaling. *mBio*, *16*(5), e00057-25. https://doi.org/10.1128/mbio.00057-25

29. Kim, K. K., Yokota, H., & Kim, S.-H. (1999). Four-helical-bundle structure of the cytoplasmic domain of a serine chemotaxis receptor. *Nature*, *400*(6746), 787–792. https://doi.org/10.1038/23512

30. Kossmann, M., Wolff, C., & Manson, M. D. (1988). Maltose chemoreceptor of Escherichia coli: Interaction of maltose-binding protein and the tar signal transducer. *Journal of Bacteriology*, *170*(10), 4516–4521. https://doi.org/10.1128/jb.170.10.4516-4521.1988

31. Lacal, J., García-Fontana, C., Muñoz-Martínez, F., Ramos, J.-L., & Krell, T. (2010). Sensing of environmental signals: Classification of chemoreceptors according to the size of their ligand binding regions. *Environmental Microbiology*, *12*(11), 2873–2884. https://doi.org/10.1111/j.1462-2920.2010.02325.x

32. Letunic, I., & Bork, P. (2018). 20 years of the SMART protein domain annotation resource. *Nucleic Acids Research*, *46*(D1), D493–D496. https://doi.org/10.1093/nar/gkx922

33. Liu, Y. C., Machuca, M. A., Beckham, S. A., Gunzburg, M. J., & Roujeinikova, A. (2015). Structural basis for amino-acid recognition and transmembrane signalling by tandem Per–Arnt–Sim (tandem PAS) chemoreceptor sensory domains. *Acta Crystallographica Section D: Biological Crystallography*, *71*(10), 2127–2136. https://doi.org/10.1107/S139900471501384X

34. Matilla, M. A., Gavira, J. A., Monteagudo-Cascales, E., Zhulin, I. B., & Krell, T. (2025). Structural and functional diversity of sensor domains in bacterial transmembrane receptors. *Trends in Microbiology*, *33*(7), 796–809. https://doi.org/10.1016/j.tim.2025.02.019

35. Matilla, M. A., & Krell, T. (2024). Bacterial amino acid chemotaxis: A widespread strategy with multiple physiological and ecological roles. *Journal of Bacteriology*, *206*(10), e00300-24. https://doi.org/10.1128/jb.00300-24

36. Matilla, M. A., Velando, F., Martín-Mora, D., Monteagudo-Cascales, E., & Krell, T. (2022). A catalogue of signal molecules that interact with sensor kinases, chemoreceptors and transcriptional regulators. *FEMS Microbiology Reviews*, *46*(1), fuab043. https://doi.org/10.1093/femsre/fuab043

37. Mauriello, E. M. F., Jones, C., Moine, A., & Armitage, J. P. (2018). Cellular Targeting and Segregation of Bacterial Chemosensory Systems. *FEMS Microbiology Reviews*. https://doi.org/10.1093/femsre/fuy015

38. Munar-Palmer, M., Santamaría-Hernando, S., Liedtke, J., Ortega, D. R., López-Torrejón, G., Rodríguez-Herva, J. J., Briegel, A., & López-Solanilla, E. (2024). Chemosensory systems interact to shape relevant traits for bacterial plant pathogenesis. *mBio*, *15*(7), e00871-24. https://doi.org/10.1128/mbio.00871-24

39. Ortega, Á., Zhulin, I. B., & Krell, T. (2017). Sensory Repertoire of Bacterial Chemoreceptors. *Microbiology and Molecular Biology Reviews*, *81*(4). https://doi.org/10.1128/MMBR.00033-17

40. Park, S.-Y., Borbat, P. P., Gonzalez-Bonet, G., Bhatnagar, J., Pollard, A. M., Freed, J. H., Bilwes, A. M., & Crane, B. R. (2006). Reconstruction of the chemotaxis receptor–kinase assembly. *Nature Structural & Molecular Biology*, *13*(5), 400–407. https://doi.org/10.1038/nsmb1085

41. Parkinson, J. S. (2010). Signaling mechanisms of HAMP domains in chemoreceptors and sensor kinases. *Annual Review of Microbiology*, *64*, 101–122. https://doi.org/10.1146/annurev.micro.112408.134215

42. Parkinson, J. S., Hazelbauer, G. L., & Falke, J. J. (2015). Signaling and sensory adaptation in Escherichia coli chemoreceptors: 2015 update. *Trends in Microbiology*, *23*(5), 257–266. https://doi.org/10.1016/j.tim.2015.03.003

43. Porter, S. L., Wadhams, G. H., & Armitage, J. P. (2011). Signal processing in complex chemotaxis pathways. *Nature Reviews Microbiology*, *9*(3), 153–165. https://doi.org/10.1038/nrmicro2505

44. Rao, C. V., Glekas, G. D., & Ordal, G. W. (2008). The three adaptation systems of *Bacillus subtilis* chemotaxis. *Trends in Microbiology*, *16*(10), 480–487. https://doi.org/10.1016/j.tim.2008.07.003

45. Rebbapragada, A., Johnson, M. S., Harding, G. P., Zuccarelli, A. J., Fletcher, H. M., Zhulin, I. B., & Taylor, B. L. (1997). The Aer protein and the serine chemoreceptor Tsr independently sense intracellular energy levels and transduce oxygen, redox, and energy signals for Escherichia coli behavior. *Proceedings of the National Academy of Sciences*, *94*(20), 10541–10546. https://doi.org/10.1073/pnas.94.20.10541

46. Salah Ud-Din, A. I. M., & Roujeinikova, A. (2017). Methyl-accepting chemotaxis proteins: A core sensing element in prokaryotes and archaea. *Cellular and Molecular Life Sciences: CMLS*, *74*(18), 3293–3303. https://doi.org/10.1007/s00018-017-2514-0

47. Shu, C. J., Ulrich, L. E., & Zhulin, I. B. (2003). The NIT domain: A predicted nitrate-responsive module in bacterial sensory receptors. *Trends in Biochemical Sciences*, *28*(3), 121–124. https://doi.org/10.1016/S0968-0004(03)00032-X

48. Stock, A. M., Robinson, V. L., & Goudreau, P. N. (2000). Two-Component Signal Transduction. *Annual Review of Biochemistry*, *69*(Volume 69, 2000), 183–215. https://doi.org/10.1146/annurev.biochem.69.1.183

49. Tohidifar, P., Bodhankar, G. A., Pei, S., Cassidy, C. K., Walukiewicz, H. E., Ordal, G. W., Stansfeld, P. J., & Rao, C. V. (2020). The Unconventional Cytoplasmic Sensing Mechanism for Ethanol Chemotaxis in Bacillus subtilis. *mBio*, *11*(5). https://doi.org/10.1128/mBio.02177-20

50. Uchida, Y., Hamamoto, T., Che, Y.-S., Takahashi, H., Parkinson, J. S., Ishijima, A., & Fukuoka, H. (2022). The Chemoreceptor Sensory Adaptation System Produces Coordinated Reversals of the Flagellar Motors on an Escherichia coli Cell. *Journal of Bacteriology*, *204*(12), e00278-22. https://doi.org/10.1128/jb.00278-22

51. Ulrich, L. E., Koonin, E. V., & Zhulin, I. B. (2005). One-component systems dominate signal transduction in prokaryotes. *Trends in Microbiology*, *13*(2), 52–56. https://doi.org/10.1016/j.tim.2004.12.006

52. Ulrich, L. E., & Zhulin, I. B. (2010). The MiST2 database: A comprehensive genomics resource on microbial signal transduction. *Nucleic Acids Research*, *38*(Database issue), D401-407. https://doi.org/10.1093/nar/gkp940

53. Umemura, T., Matsumoto, Y., Ohnishi, K., Homma, M., & Kawagishi, I. (2002). Sensing of Cytoplasmic pH by Bacterial Chemoreceptors Involves the Linker Region That Connects the Membrane-spanning and the Signal-modulating Helices*. *Journal of Biological Chemistry*, *277*(2), 1593–1598. https://doi.org/10.1074/jbc.M109930200

54. Vaknin, A., & Berg, H. C. (2006). Osmotic stress mechanically perturbs chemoreceptors in Escherichia coli. *Proceedings of the National Academy of Sciences*, *103*(3), 592–596. https://doi.org/10.1073/pnas.0510047103

55. Wadhams, G. H., & Armitage, J. P. (2004). Making sense of it all: Bacterial chemotaxis. *Nature Reviews Molecular Cell Biology*, *5*(12), Article 12. https://doi.org/10.1038/nrm1524

56. Waterhouse, A. M., Procter, J. B., Martin, D. M. A., Clamp, M., & Barton, G. J. (2009). Jalview Version 2—A multiple sequence alignment editor and analysis workbench. *Bioinformatics (Oxford, England)*, *25*(9), 1189–1191. https://doi.org/10.1093/bioinformatics/btp033

57. Watts, K. J., Taylor, B. L., & Johnson, M. S. (2011). PAS/poly-HAMP signalling in Aer-2, a soluble haem-based sensor. *Molecular Microbiology*, *79*(3), 686–699. https://doi.org/10.1111/j.1365-2958.2010.07477.x

58. Watts, K. J., Vaknin, A., Fuqua, C., & Kazmierczak, B. I. (2019). New Twists and Turns in Bacterial Locomotion and Signal Transduction. *Journal of Bacteriology*, *201*(20), 10.1128/jb.00439-19. https://doi.org/10.1128/jb.00439-19

59. Wuichet, K., Alexander, R. P., & Zhulin, I. B. (2007). Comparative Genomic and Protein Sequence Analyses of a Complex System Controlling Bacterial Chemotaxis. *Methods in Enzymology*, *422*, 1–31. https://doi.org/10.1016/S0076-6879(06)22001-9

60. Wuichet, K., & Zhulin, I. B. (2010). Origins and Diversification of a Complex Signal Transduction System in Prokaryotes. *Science Signaling*, *3*(128), ra50–ra50. https://doi.org/10.1126/scisignal.2000724

61. Yang, W., & Briegel, A. (2020). Diversity of Bacterial Chemosensory Arrays. *Trends in Microbiology*, *28*(1), 68–80. https://doi.org/10.1016/j.tim.2019.08.002

62. Zusman, D. R., Scott, A. E., Yang, Z., & Kirby, J. R. (2007). Chemosensory pathways, motility and development in Myxococcus xanthus. *Nature Reviews Microbiology*, *5*(11), 862–872. https://doi.org/10.1038/nrmicro1770

Chapter 4

Regulation of cytoplasmic chemosensory cluster formation by adaptor proteins

4.1 Introduction

Chemotaxis, in motile bacteria, enables temporal sensing of environmental cues to track spatial gradients of chemoeffector molecules and navigate to favourable environments *(Porter et al., 2011; Wadhams & Armitage, 2004)*. Chemotaxis aids in biological processes like biofilm formation, quorum sensing, cell adhesion, symbiotic association with plants as well as pathogenesis in hosts *(Keegstra et al., 2022; Karmakar, 2021)*. Chemoeffector molecules, attractants and repellents, are sensed by chemosensory systems (CSSs) that regulate motility modules via a phosphorelay signalling cascade *(Falke et al., 1997)*. CSSs are composed of chemoreceptors, also called methyl-accepting chemotaxis proteins (MCPs), that are linked to histidine kinases by adaptor proteins. Adaptor or scaffold proteins mediate crucial connections between MCPs and kinases during signal transduction *(Piñas et al., 2016)*.

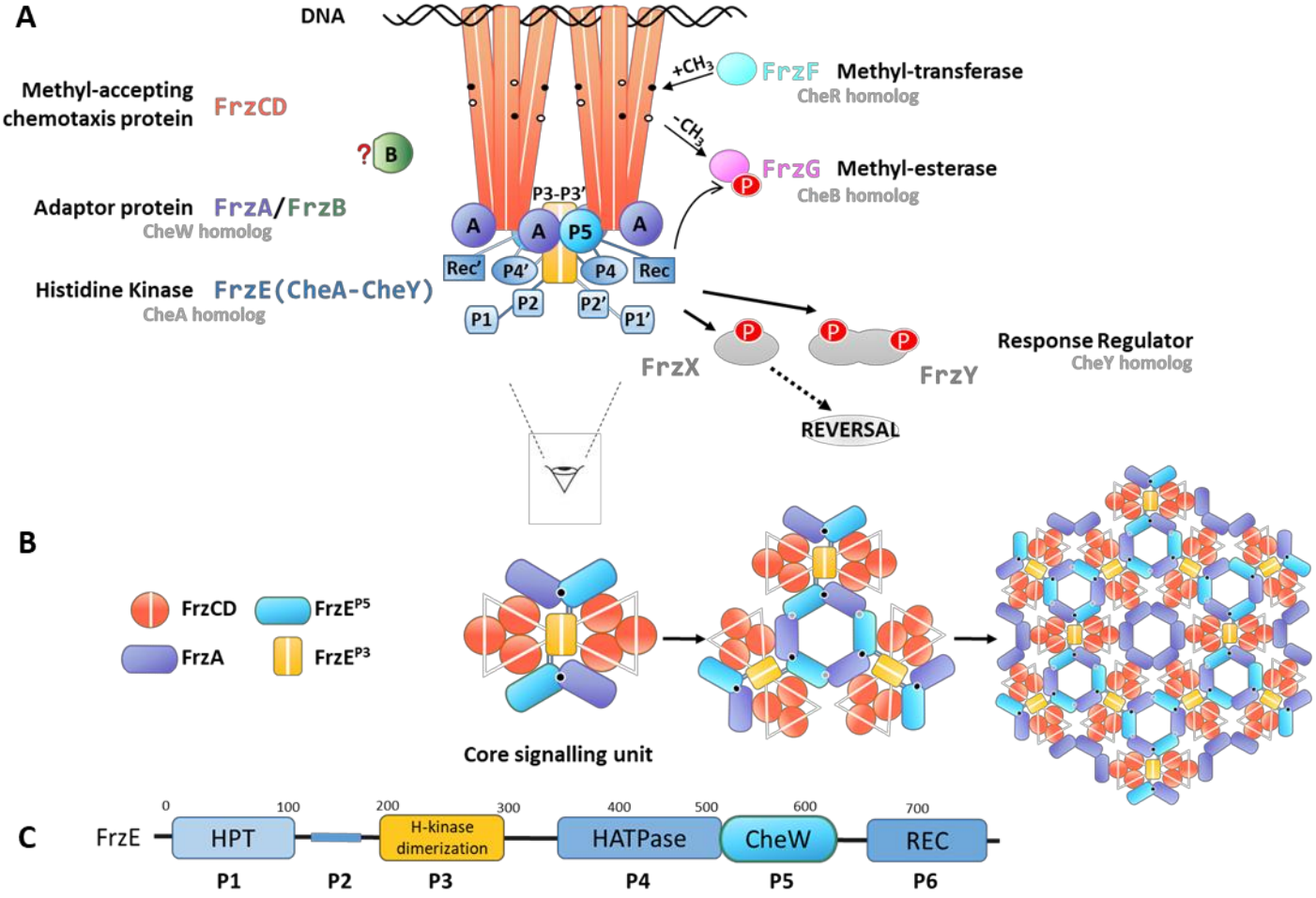


Figure 4.1 ***M. xanthus*** **Frz chemosensory system.** (A) The proteins of Frz CSS are homologous to Che CSS from *E. coli*. The receptor FrzCD interacts with CheW homolog FrzA and CheA homolog FrzE. FrzB is another CheW homolog of Frz CSS. FrzF and FrzG are homologs of CheR and CheB, respectively. Phosphorylation of CheY homolog FrzX mediates polarity reversals in the bacterium. Proposed organization of Frz CSS using DNA as a scaffold depicted as homology to Che proteins *(Mauriello, 2020; Guiseppi et al., 2019)*. (B)

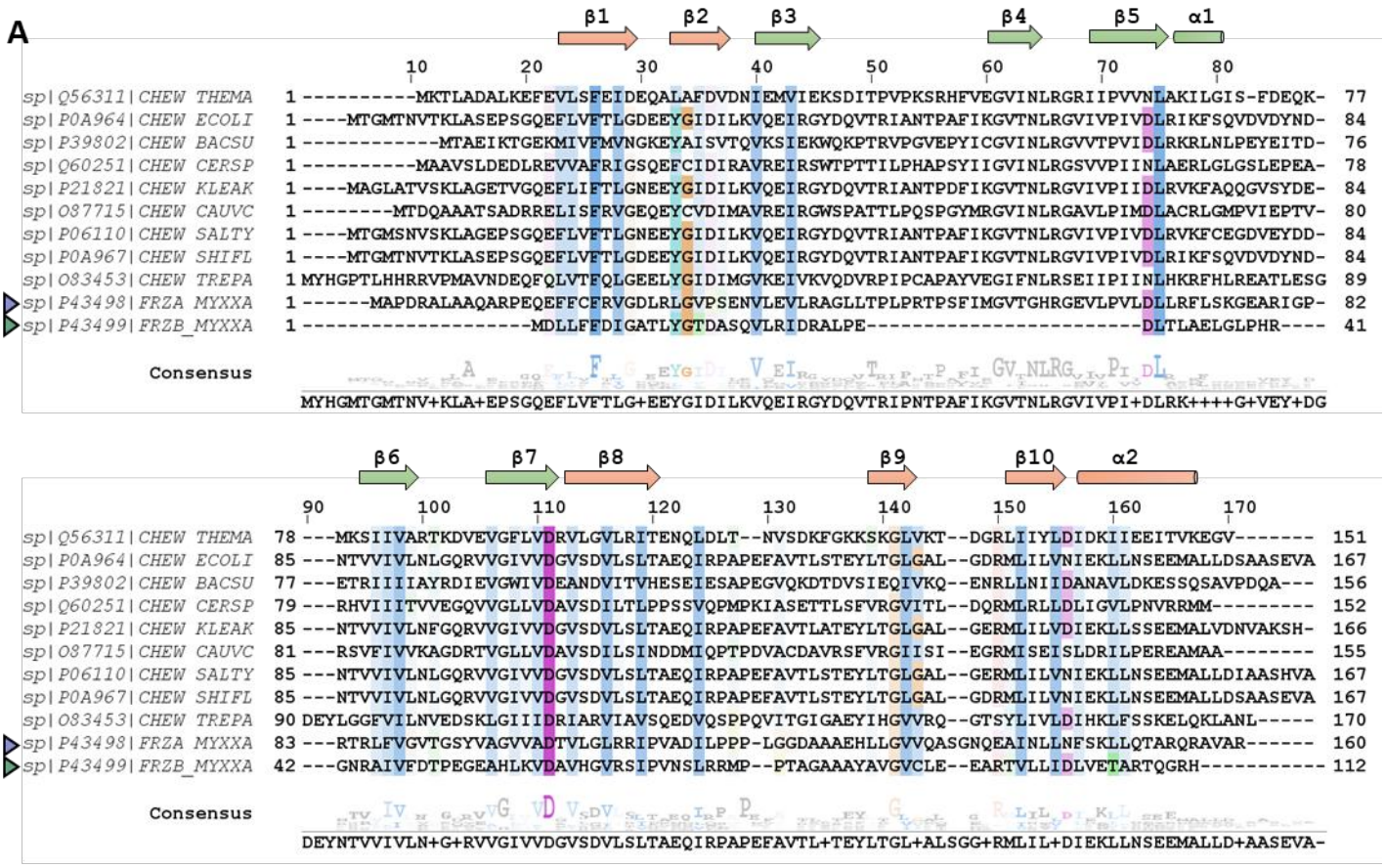
Architecture of assembly of FrzCD CSU depicted as homology to Che proteins *(Guiseppi et al., 2019; Mauriello, 2020)*. Trimer of dimers of FrzCD interacts with dimeric FrzE and FrzA at 'interface 1' (black circle). Interactions between FrzE-P5 and FrzA at 'interface 2' results in a hexagonal architecture that extend to form arrays. (C) Domains of histidine kinase FrzE. FrzE is a hybrid histidine kinase with an additional Rec domain *(Acuña et al., 1995)*.

Signal transduction pathways in prokaryotes and eukaryotes are mediated by interactions of adaptor proteins with input receptors and output kinases *(Shaw & Filbert, 2009; Bhattacharyya et al., 2006)*. The adaptor proteins, although arguably play a simple role of tethering target protein partners, regulate pathways by allosteric control over their partners to fine-tune outputs *(Piñas et al., 2016; Good et al., 2011)*. CSSs are organized as large hexagonal arrays, where the core signalling unit (CSU) is formed by receptor trimer-of-dimers connected by two adaptor proteins and a dimeric histidine kinase, called CheW and CheA respectively in *E. coli (Briegel et al., 2009)*. This architecture is conserved across bacteria and archaea, with CheA and CheW networks arranging receptor trimers-of-dimers into a rigid, hexagonal pattern spaced at ~12 nm **(Figure 4.1)** *(Briegel et al., 2015, 2009)*.

The kinase CheA interacts with receptor via P5 domain, structurally homologous to CheW domain, and is topologically similar to two SH3 domains from eukaryotic adaptor proteins *(X. Li et al., 2013; Bilwes et al., 1999)*. The cytoplasmic trimer-of-dimer receptor tips are organized within a pseudo-6-fold symmetric ring composed of alternating CheW and CheA-P5 units. CheW is composed of two subdomains, each having five β-strands. Subdomain 1 is formed by β1, β2 and β8- β10, while subdomain 2 is formed by β3- β7 **(Figure 4.2A)** *(Y. Li et al., 2007; Park et al., 2006; Griswold et al., 2002; Griswold & Dahlquist, 2002)*. β3 and β4 of subdomain 1 of CheA-P5 interact with β4 and β5 of CheW subdomain 2 to form 'interface 1' of the core signalling unit (CSU). CSUs are joined at 'interface 2' by subdomain 2 of CheA-P5 and subdomain 1 of CheW to assemble into extended arrays **(Figure 4.1)** *(X. Li et al., 2013; Natale et al., 2013)*.

The receptor cytoplasmic tip interacts with CheA-P5 or CheW at a hydrophobic groove between subdomain 1 and subdomain 2 *(X. Li et al., 2013)*. The trimer-of-dimers arrangement allows cooperative interactions within receptor dimers *(Lai et al., 2017)*. Moreover, the conserved array architecture, featuring a core signalling unit (CSU) made up of a trimer-of-dimers connected by two CheW monomers and a dimeric CheA forming 'interface 1' between them, and CheA-CheW 'interface 2' linking CSUs into a hexagonal lattice, plays a key role in supporting cooperativity and signal amplification through allosteric interactions within the

array *(Piñas et al., 2016; M. Li & Hazelbauer, 2014)*. Disruption of array by mutations in CheW abolishes signal amplification while retaining signalling function *(Frank et al., 2016; Piñas et al., 2016)*. Moreover, homo-hexameric CheW rings are observed as part of arrays that augment cooperativity between CSUs and enhance sensitivity of arrays to chemoeffectors *(Piñas et al., 2022; Cassidy et al., 2020; Yang et al., 2018; Cassidy et al., 2015)*.



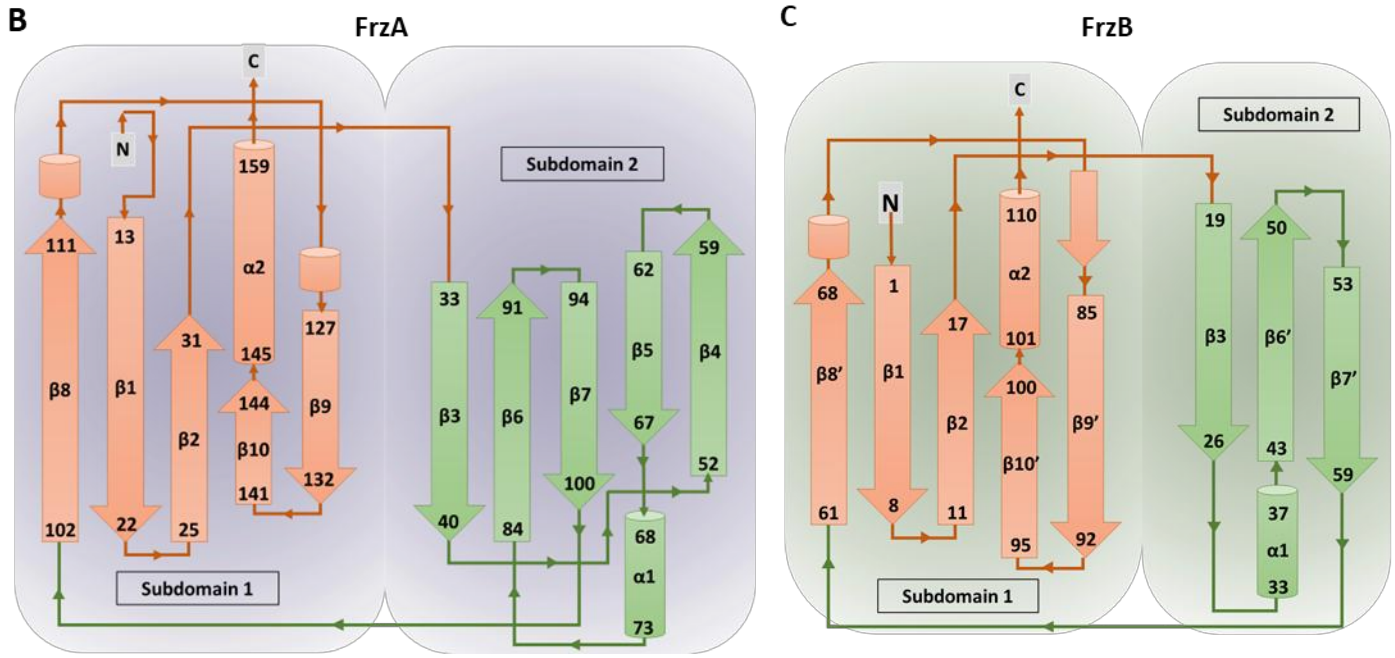


Figure 4.2 FrzB lacks β4 and β5 in subdomain 2 *(Guiseppi et al., 2019)***.** Adaptor proteins are homologous to the SH3 domain and are composed of two β-barrels, subdomain 1 and subdomain 2, each containing five β-strands. (A) Alignment of FrzA and FrzB with annotated CheW sequences from other bacteria. The colour scheme, as per ClustalX in Jalview at 30% identity, is used to represent the alignment *(Waterhouse et al., 2009)*. (B) Topology diagram highlights the arrangement of secondary structures of FrzA and FrzB. FrzB lacks β4 and β5 in subdomain 2.

The majority of bacterial CSSs have MCPs with transmembrane domains (~86%) *(Collins et al., 2014)*. However, there are cytoplasmic MCPs that lack the transmembrane domain *(Mauriello et al., 2018; Wuichet et al., 2007)*. Such cytoplasmic clusters are thought to sense intracellular signals *(Porter et al., 2011, 2008)*. Cytoplasmic CSSs can form arrays of two mirroring layers where the MCPs are sandwiched between CheA-CheW layers *(Briegel et al., 2016, 2014)*. However, cytoplasmic Frz CSS from the gliding bacterium *Myxococcus xanthus* forms clusters on the nucleoid *(Moine et al., 2017)*. The Frz pathway regulates the frequency of polarity reversals in the bacterium, thereby dictating the direction of movement in response to environmental cues *(Blackhart & Zusman, 1985)*. Motility regulation is essential for the multistage development cycle of the bacterium, leading to the formation of fruiting bodies under unfavourable growth conditions *(Dinet et al., 2021)*.

The Frz CSU is composed of cytoplasmic MCP (FrzCD), histidine kinase (FrzE) and adaptor proteins (FrzA and FrzB) *(Bustamante et al., 2004)*. In absence of FrzCD, FrzE and FrzA, cells have significantly reduced reversal frequencies and cannot respond to the activator isoamyl alcohol (IAA). Although absence of FrzB results in a similar phenotype, the cells respond to IAA with an increase in reversal frequencies *(Guzzo et al., 2015; Bustamante et al., 2004)*. FrzCD interacts with DNA via its positively charged N-terminal region in a sequence-independent manner and forms clusters on the nucleoid with FrzE and FrzA *(Guiseppi et al., 2019; Moine et al., 2017)*. Although the architecture of these clusters is not visualized, they exhibit properties of allosteric interactions with cooperative amplification in response to a signal *(Moine et al., 2017)*. Analogous to membrane-bound CSSs, Frz CSS may form hexagonal assemblies by using the nucleoid as a scaffold **(Figure 4.1)** *(Mauriello, 2020)*.

Between the two adaptor proteins in this system, FrzA is essential for cluster formation and signal transduction, while FrzB may act as a stabilizing factor *(Mauriello, 2020; Guiseppi et al., 2019)*. In contrast to FrzA, the absence of FrzB in *M. xanthus* resembles the wild-type phenotype in presence of IAA and is therefore proposed to act upstream of FrzCD in the signal

transduction pathway *(Guiseppi et al., 2019)*. FrzB is a divergent CheW and lacks β4 and β5 of subdomain 2 essential for 'interface 1' interaction with FrzE-P5 **(Figure 4.2)**. Thus, FrzB, in presence of FrzCD failed to initiate autophosphorylation of FrzE *in vitro*. Interestingly, incorporating the two missing β-strands in FrzB from FrzA restores interaction with FrzE *(Guiseppi et al., 2019)*. In absence of FrzB, instead of multiple distinct clusters on the nucleoid, Frz clusters mostly collapse into a single large cluster *(Guiseppi et al., 2019)*. It is proposed that FrzCD in presence of FrzE and FrzA forms clusters on the nucleoid whose size is determined either by stabilizing role of FrzB as central hexa-CheW rings of the cluster, or by inhibiting cluster networks due to absence of interaction with FrzE *(Mauriello, 2020)*.

Our study reveals the regulatory role of two adaptor proteins associated with this CSS in mediating the organization of assemblies into multiple clusters on the nucleoid. Electron density from cryoEM shows interaction of FrzA at the signalling tip of FrzCD (elaborated in Chapter 5). We show that the receptor-adaptor complexes are dynamic assemblies. In the two adaptor CSS, both adaptors were found to interact at the same interface on the receptor. We identified key residues that mediate hydrophobic and anchoring salt-bridge interactions between the receptor and adaptors. However, differences in the characteristics of the adaptor proteins might lead to different functions. We observed that FrzB, a non-canonical adaptor protein, forms a less stable complex with FrzCD. Additionally, FrzB does not interact with histidine kinase to form CSU *(Guiseppi et al., 2019)*. We hypothesize that FrzA, with its higher affinity for FrzCD, has a competitive advantage in forming stable CSUs and mediates the propagation of arrays. Arrays are inhibited by FrzB-FrzCD interactions that cannot form CSU, thereby regulating the size of clusters on the nucleoid and promoting the formation of multiple clusters, as observed in an *in vivo* study *(Guiseppi et al., 2019)*. Our study provides new insights into how differences in characteristics between homologous proteins in the same CSS may have distinct roles in fine-tuning CSS assemblies into clusters.

4.2 Materials and Methods

4.2.1 Cloning

Restriction free cloning *(van den Ent & Löwe, 2006)* was used to generate constructs of FrzCD with C-terminal Strep-tag and FrzA/FrzB with N-terminal hexa-Histidine tag in pHis17 plasmid **(Figure 4.3A)** (refer to Addgene plasmid #78201 for the vector backbone, obtained from Löwe lab, MRC LMB, Cambridge, UK). *Escherichia coli* DH-5α and NEB Turbo cells (New England Biolabs) were used for cloning. FrzCD gene was cloned with C-term Strep-tag from pFCD-H6 *(Jazleena, Das, Guiseppi et al. 2025; Moine et al., 2017)*, and amp^R cassette was replaced with kanamycin resistance gene using specific primers (pHis17^{KanR}, **Table 4.1 and 4.2**). FrzA and FrzB was cloned from pGEX vector *(Guiseppi et al., 2019)* with N-terminal hexa-Histidine tag in pHis17^{AmpR}. Subsequently, different constructs of FrzCD, FrzA, and FrzB were generated using restriction-free cloning. A detailed list of clones and primers is mentioned in **Tables 4.1 and 4.2**.

Table 4.1 Plasmids used in this study.

Plasmid	Insert	Source
FrzCD	pHis17 with *frzCD* having C-term Strep tag, containing KanR cassette	This study
FrzCD$^{\Delta DB}$	pHis17 with $frzCD^{\Delta DB}$ having C-term Strep tag, containing KanR cassette	This study
FrzCD$^{\Delta DBH2}$	pHis17 with $frzCD^{\Delta DH2B}$ having C-term Strep tag, containing KanR cassette	This study
FrzCD $^{\Delta 261\text{-}267_\Delta 286\text{-}292}$	pHis17 with $frzCD^{\Delta 261\text{-}267_\Delta 286\text{-}292}$ having C-term Strep tag, containing KanR cassette	This study
FrzCD$^{E255A\text{-}D258A}$	pHis17 with $frzCD^{E255A\text{-}D258A}$ having C-term Strep tag, containing KanR cassette	This study
FrzCD$^{D258A\text{-}D261A}$	pHis17 with $frzCD^{D258A\text{-}D261A}$ having C-term Strep tag, containing KanR cassette	This study
FrzCD^{L265D_L269D}	pHis17 with $frzCD^{L265D_L269D}$ having C-term Strep tag, containing KanR cassette	This study

FrzCD$^{\Delta H1}$	pHis17 with *frzCD$^{\Delta H1}$* having C-term Strep tag, containing KanR cassette	This study
FrzCD$^{\Delta H2}$	pHis17 with *frzCD$^{\Delta H2}$* having C-term Strep tag, containing KanR cassette	This study
FrzCD$^{\Delta H1H2}$	pHis17 with *frzCD$^{\Delta H1H2}$* having C-term Strep tag, containing KanR cassette	This study
FrzA	pHis17 with *frzA* having N-term hexa-His tag	This study
FrzA^{R39A}	pHis17 with *frzA^{R39A}* having N-term hexa-His tag	This study
FrzA^{R85A}	pHis17 with *frzA^{R85A}* having N-term hexa-His tag	This study
FrzB	pHis17 with *frzB* having N-term hexa-His tag	This study
FrzB^{R25A}	pHis17 with *frzB^{R25A}* having N-term hexa-His tag	This study
FrzB^{R44A}	pHis17 with *frzB^{R44A}* having N-term hexa-His tag	This study

Table 4.2 Primers used for restriction-free cloning.

Primer	Sequence (5' to 3')
pHisKan-F	GCTAAAGTTGTTAAAGACTTTAAATTGCCGCGCGGCAGCCACATG
pHisK-R	GTATATATGAGTAAACTTGGTCTGACAGTTAGAAAAACTCATCGAGCATC
T7-R	GCTAGTTATTGCTCAGCGG
FrzCD$^{\Delta DB}$-F	AAGAAGGAGATATACATATGTCGACCTCTTCCTCCACCAA
FrzCD $^{\Delta 261\text{-}267_\Delta 286\text{-}292}$-F	AGCCGCGCGGGTGAGGCCGGCAAGGGCTTCTCCATCGTCGCGGAGAACGTCCTGGACTCCAC
FrzCD $^{\Delta 261\text{-}267_\Delta 286\text{-}292}$-R	GCCCTTGCCGGCCTCACCCGCGCGGCTGCCTTCCAGCGCGGAGCGGTCCGCGATCTCGTC
FCD$^{E255/D258A}$-F	TGGAGGTCATCGACGCCATCGCGGCCCGCTCCGACCTGCT
FCD^{D258A_D261A}-F	AGGTCATCGACGAGATCGCGGCCCGCTCCGCCCTGCTGGCGCTGAACGCG
FCD^{D258A}-F	TCATCGACGAGATCGCGGCCCGCTCCGACCTGCTGGCGCT
FrzCD^{L265D_L269D}-F	CCGCGCGGCTGCCTTCGTCCGCCGCGTTGTCCGCCAGCAGGTCGGA
FrzCD$^{\Delta H1}$-F	GGCGCCACGAACGCGGCGTCGCGCAAGCATGTGGCGGCG
FrzCD$^{\Delta H2}$-F	CAGTTCGCGGCCTCCGAGCACGTGCGGGAGATCAACGAG
FrzCD$^{\Delta H1H2}$-F	GGCGCCACGAACGCGGCGTCGGTGCGGGAGATCAACGAG

FrzA-F	GAGATATAATGCACCACCACCACCACCATATGGCTCCGGACCGCGCC TTGGCCGCC
FrzA-R	TAATGATGATGATGATGATGGGATCCTCACCGCGCCACCGCCCGCTG CCGTGCCGTC
$FrzA^{R39A}$-F	TGCTCGAAGTGCTTGCGGCCGGTCTGCTCA
$FrzA^{R85A}$-F	AGGCCCGCATCGGCCCGCGCACCGCGCTGTTCGTCGGCGTCACGGGC A
FrzB-F	AAGGAGATATAATGCGTCACCACCACCACCACCATATGGACCTCCTC TTCTTCGACATCG
FrzB-R	CTTTTAATGATGATGATGATGGGATCCTCAGTGCCTTCCTTGAGT CCTTGCGGT
$FrzB^{R25A}$	TGCTGCGCATCGACGCGGCGCTGCCGGAGGA
$FrzB^{R44A}$	CACCGAGGCAACGCGGCCATCGTCTTCGA

4.2.2 Purification of receptor-adaptor complex

E. coli expression strains such as BL21-AI, BL21-DE3, and T7 Express (BL21 derivative) were used for co-transformation and heterologous expression of receptor and adaptor proteins simultaneously. Co-transformed cells of FrzCD (C-Term Strep-tagged in $pHis17^{KanR}$), and FrzA or FrzB plasmids (N-terminal hexa-Histidine tagged in $pHis17^{AmpR}$) were grown overnight at 37°C in LB agar plates under double antibiotic pressure (100 µg/mL ampicillin and 50 µg/mL kanamycin). Patches of colonies were used to inoculate primary cultures, which were subsequently seeded into secondary cultures, both supplemented with 100 µg/mL ampicillin and 50 µg/mL kanamycin. Induction was performed at an OD_{600} of 0.6–0.8 using 0.2% (w/v) L-arabinose for BL21-AI or 0.5 mM IPTG for BL21-DE3 and T7 Express strains, followed by overnight incubation at 18°C. Cells were harvested by centrifugation at 4000 × g for 20 minutes and pellets were flash frozen in liquid nitrogen and stored at -80°C until further use. Cell pellets were thawed and resuspended in lysis buffer containing 200 mM NaCl, 50 mM HEPES buffer (pH 7.5), 20 mM imidazole, and 10% glycerol. Cell lysis was performed by sonication at 60% amplitude using three cycles of 1 second on and 3 seconds off for 2 minutes each, with 5-minute intervals between cycles. Lysates were clarified by centrifugation at 35,000 × g for 45 minutes at 4 °C. For FrzCD-FrzA complex purification, tandem pull-down using HisTrapFF (Cytiva) and StrepTrapXT or StrepTrapHP (Cytiva) followed by size exclusion chromatography (Figure 2A). The supernatant was loaded onto a 5 mL HisTrapFF column pre-equilibrated with chilled buffer A (200 mM NaCl, 50 mM HEPES, pH 7.5, 20 mM imidazole) at 4 °C. Wash procedures involved six column volume rinses with buffer A, and

with 2% and 5% of buffer B (200 mM NaCl, 500 mM imidazole, 50 mM HEPES [pH 7.5]). Elution was performed via stepwise gradient with increasing concentrations of buffer B (10%, 20%, 50%, and 100%). Subsequently, eluted fractions were checked on SDS-PAGE for FrzCD-FrzA bands and pooled. Next, the pooled fractions were loaded onto either a 5 mL StrepTrapXT or StrepTrapHP column, pre-equilibrated with buffer A at 4°C. Wash procedure involved six to eight column volume rinses with buffer A followed by elution with either 50 mM d-biotin (StrepTrapXT) or 2.5 mM d-desthiobiotin (StrepTrapHP) in 50 mM HEPES [pH 7.5], 200 mM NaCl and 20 mM Imidazole. Eluted fractions were checked on SDS-PAGE for FrzCD-FrzA bands and then pooled and concentrated to approximately 1 mL using a centrifugal filter (Amicon Ultra-15, 10 kDa, Millipore). Size exclusion chromatography was performed in either Superdex200 Increase 10/300 GL (Cytiva) or ENrich SEC650 10 x 300 (BioRad) column pre-equilibrated with buffer C (50 mM HEPES [pH 7.5], 50 mM NaCl) at 4 °C. Eluted fractions were analyzed by SDS-PAGE to verify the co-elution of FrzCD and FrzA bands. Subsequently, those fractions were pooled, concentrated using a centrifugal filter, aliquoted, flash-frozen, and stored at −80 °C for cryoEM experiments. Same steps were followed to purify FrzCD$^{\Delta DB}$-FrzA and FrzCD$^{\Delta DBH2}$-FrzA complex for cryoEM experiments.

FrzCD-FrzB complex was purified by affinity pull-down using HisTrapFF from lysate of co-transformed cells. Purified protein complexes are shown in **Figure 4.4D,** and purification steps are illustrated in **Figure 4.4**. FrzCD$^{\Delta H1H2}$ (with C-term Strep-tag) and FrzCD$^{\Delta 261\text{-}267_\Delta 286\text{-}292}$ (with C-term hexa-His tag) were purified by affinity chromatography using StrepTrapXT and HisTrapFF columns, respectively, followed by anion exchange chromatography using MonoQ 4.6/100 PE (Cytiva) at 50 mM HEPES (pH 7.5) and NaCl gradient from 50 mM NaCl to 500 mM NaCl. Protein concentration was estimated using absorbance at 280 nm and using bicinchoninic acid (BCA) protein assay.

4.2.3 Mass photometry of purified receptor-adaptor complexes

Mass photometry was carried out in Refeyn TwoMP at the Biophysics facility, Department of Biochemistry, University of Cambridge. The coverslips were rinsed with isopropanol and Mili-Q and dried using a dry nitrogen source before use. Final concentration of 0.05 to 0.2 μM of sample was used in buffer C (50 mM HEPES [pH 7.5], 50 mM NaCl) and movies were captured in regular view. Standard plot for mass estimation was crosschecked using BSA (66 kDa) and IgG (150 kDa) before mass estimation was carried out for FrzCD-FrzA, FrzCD$^{\Delta DB}$-FrzA and FrzCD$^{\Delta DBH2}$-FrzA complexes.

4.2.4 Pull-down assays

Different constructs of FrzCD were co-transformed with FrzA/FrzB. Protein expression was carried out in the above-mentioned conditions. Receptor-adaptor complex formation (of FrzCD and FrzA/FrzB) was checked by one-step affinity pull-downs either via HisTrap or StrepTrap columns, followed by SDS-PAGE of eluted fractions. For HisTrap pull-downs, a wash of 6 column volumes of 10% buffer B was carried out before elution with 100% buffer B.

4.2.5 Electrophoretic mobility shift assay

The protocol as mentioned in **Chapter 2** was followed.

4.2.6 *In vitro* competition assay

Purified FrzCD-FrzA complex (2 µl of 9 µg/µl) was mixed with increasing concentration of $FrzCD^{\Delta H1H2}$ (1 µl, 2 µl, 4 µl and 8 µl of 4.5 µg/µl protein) in buffer D (50 mM HEPES [pH 7.5], 200 mM NaCl). Final volume of each reaction was adjusted to 50 µl using buffer D (Input sample in Figure 5 F). 25 µl of each reaction was added to 20 µl of Ni-NTA Agarose (Qiagen) slurry, pre-equilibrated with buffer D. Additionally, 175 µl of buffer D was added to facilitate mixing during incubation. Reactions were incubated at 4°C for 1 hour and vortexed gently a few times during incubation. Next, the reactions were spun at 1000 × g for 30 secs at 4°C. The supernatant was collected as flow flow-through sample **(Figure 4.14F)**. Protein bound to beads was rinsed with 200 µL buffer D, followed by centrifugation at 1000 × g for 30 seconds at 4°C to collect the supernatant as wash fraction. Finally, the samples were incubated for 30 seconds with 200 µL elution buffer (50 mM HEPES [pH 7.5], 200 mM NaCl, and 500 mM Imidazole), followed by centrifugation to collect the supernatant as elution fractions **(Figure 4.14F)**. Next, trichloroacetic acid (TCA) precipitation was performed on all fractions (flow-through, wash, and elution). 80 µL of 50% TCA was added to the fractions, and the samples were spun at 20,000 × g for 20 minutes at 4°C. The supernatant of the fractions was discarded, and 200 µl of acetone was added. The fractions were then incubated at 4°C for 30 mins, followed by centrifugation at 20,000 × g for 20 mins at 4°C. After discarding the supernatants, the pellet of the samples was dried at 45°C on an Eppendorf Thermomixer. The pellet of the fractions was resuspended in 1x TGS buffer (25 mM Tris, 192 mM glycine, 0.1% w/v SDS, pH 8.3) and checked on SDS-PAGE **(Figure 4.14G).**

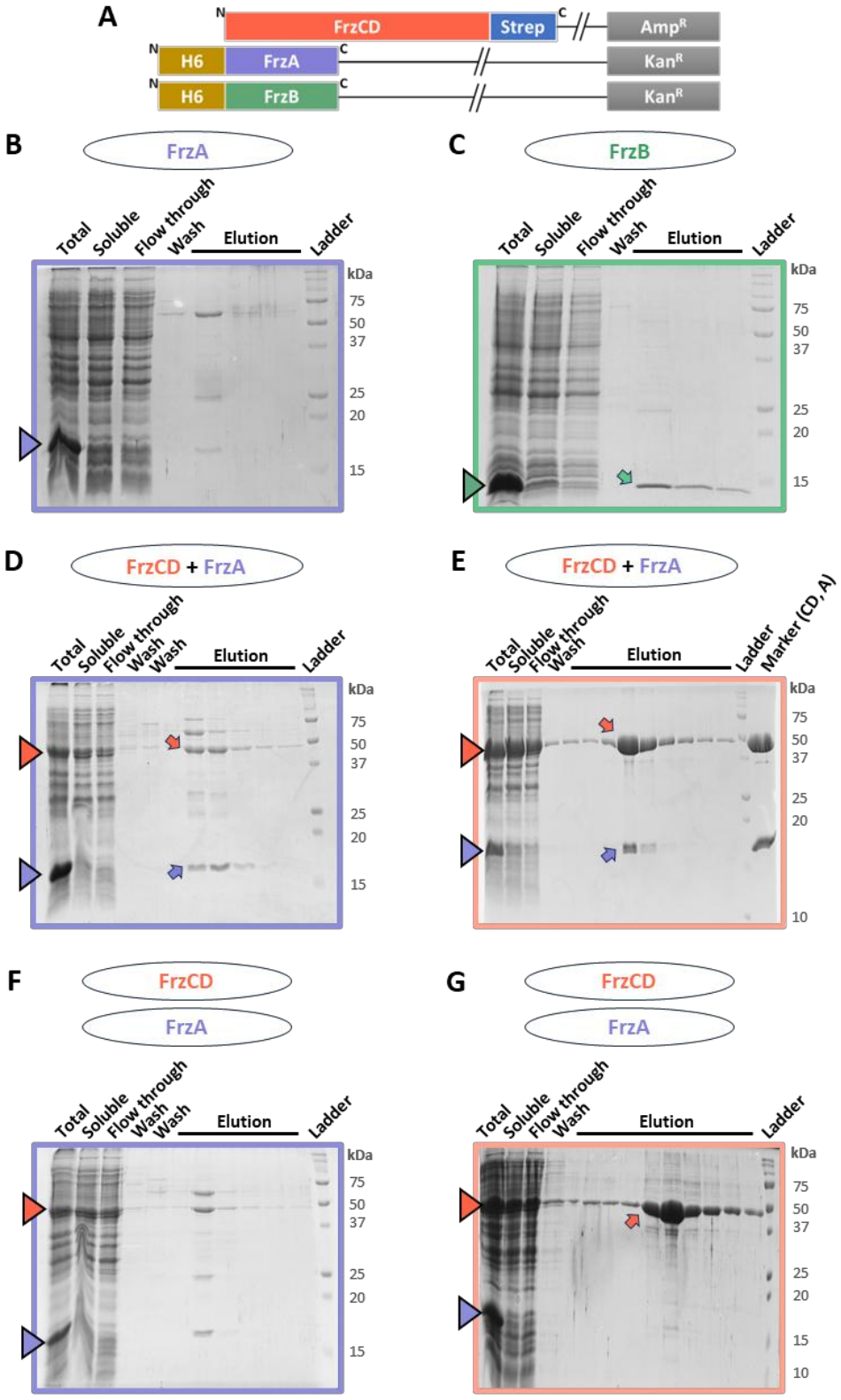


Figure 4.3 Standardization of receptor-adaptor complex formation. (A) Schematic representation of plasmid constructs used for reconstitution of receptor-adaptor complex. NiNTA affinity chromatography of His-tagged FrzA (B), and His-tagged FrzB (C). Pull-down from mixed lysates individually expressing FrzCD and FrzA by His-tagged FrzA (D), and Strep-tagged FrzCD (E). Pull-down from lysates of co-transformed cells with both FrzA and FrzCD plasmids by FrzA (F) and FrzCD (G). Colour of the border of the gels denotes the protein by which the pull-down was carried out.

4.3 Results

4.3.1 Adaptor protein FrzA forms a stable complex with FrzCD

FrzA was insoluble during heterologous expression in *E. coli* cells, while FrzB was partially soluble during heterologous expression **(Figure 4.3B, C)**. However, co-transforming cells with plasmids containing FrzCD and FrzA, harbouring kanamycin and ampicillin resistance genes respectively, yielded a soluble FrzCD-FrzA complex when grown under double antibiotic pressure **(Figure 4.3D, E)**. Surprisingly, a mixture of lysed cells, from individual expression of either FrzA or FrzCD, did not yield soluble FrzA to form a FrzCD-FrzA complex **(Figure 4.3F, G)**. Hence, FrzA is probably misfolded without stabilizing interactions with FrzCD during expression.

We used a strategy of tandem pull-down via hexa-histidine tag on FrzA and a Strep-tag on FrzCD to isolate a stoichiometric complex of FrzCD and FrzA. This was followed by size exclusion chromatography (SEC) to purify stable FrzCD-FrzA complex **(Figure 4.4A)**. FrzB formed a soluble complex with FrzCD in co-transformed cells **(Figure 4.4B)**. Notably, under similar conditions of expression and purification, FrzCD-FrzB complex was not as stable as the FrzCD-FrzA complex. We observed that the majority of FrzB dissociated from the complex during subsequent purification steps of affinity tag pull-down and/or size exclusion chromatography **(Figures 4.4B and 4.5)**. Purified FrzCD-FrzA/FrzB complexes came bound with DNA fragments from the cell, but could still bind to additional free DNA fragments as observed in the mobility shift assay **(Figure 4.4C)**. FrzCD and FrzA co-eluted in size exclusion chromatography, while the majority of FrzB dissociated from FrzCD-FrzB complex, and eluted as a separate peak during SEC **(Figure 4.5)**. Thus, FrzCD-FrzA complex was observed to be more stable and, unlike FrzCD-FrzB, did not dissociate during tandem pull-down and size exclusion chromatography. Estimated mass of different FrzCD constructs in complex with FrzA corresponded to a dimeric receptor molecule with a deviation of around ±18 kDa corresponding to the molecular weight of FrzA **(Figure 4.6)**.

4.3.2 FrzA interacts at the signalling tip of dimeric FrzCD

Since FrzCD and FrzA form a stable complex, cryo-electron microscopy was used to understand the architecture of the complex. We solved structures of $FrzCD^{\Delta DB}$ and $FrzCD^{\Delta DBH2}$ in complex with FrzA. Structural characterization of receptor-adaptor complex is elaborated in

Chapter 5. FrzA interacted at the signalling tip of coiled-coil MA domain of dimeric FrzCD. Next, we characterized the interacting interface of FrzCD-FrzA complex.

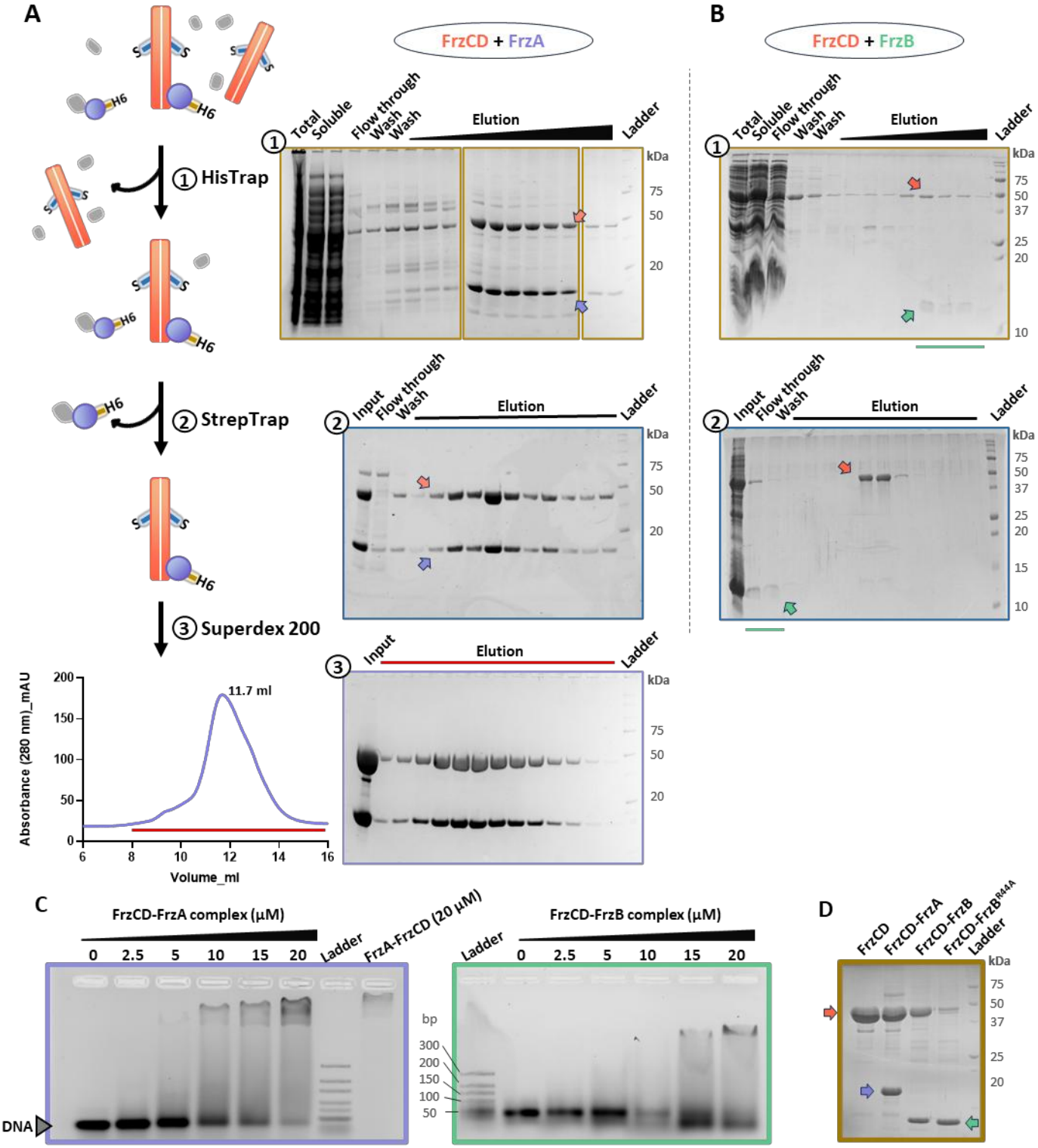


Figure 4.4 Purification strategy for receptor-adaptor complex. (A) Reconstitution of FrzCD-FrzA complex from heterologous expression in *E. coli* cells co-transformed with FrzCD and FrzA plasmid harbouring kanamycin and ampicillin resistance genes, respectively. Tandem pull-down with His-tagged FrzA (1) and Strep-tagged FrzCD (2), followed by size exclusion chromatography (3), yielded a stable FrzCD-FrzA complex. 'H6' denotes hexa-

histidine tagged and 'S' denotes Strep-tagged protein. Orange and violet arrows denote FrzCD (45 kDa) and FrzA (18 kDa), respectively. (B) Co-transformed *E. coli* cells with Strep-tagged FrzCD and His-tagged FrzB, harbouring kanamycin and ampicillin resistance genes, respectively, yielded a FrzCD-FrzB complex (1). However, the complex is less stable and dissociates in subsequent pull-down (2). Orange and green arrow denotes FrzCD (45 kDa) and FrzB (13 kDa), respectively. Green line denotes fractions where FrzB is present. (C) FrzCD-FrzA complex comes bound to DNA (left gel, last lane) as observed in agarose gel stained with EtBr. Receptor adaptor complex shows binding to additional DNA fragments in mobility shift assay (Left gel: FrzCD-FrzA complex; Right gel: FrzCD-FrzB complex). 2µM 35-bp DNA fragment was used. Grey triangle denotes unbound DNA. (D) SDS-PAGE showing pull-down of FrzCD by FrzA and FrzB. FrzB interface mutant (R44A) failed to pull down FrzCD efficiently compared to wild type FrzB. Orange, violet and green arrow denotes FrzCD, FrzA and FrzB, respectively.

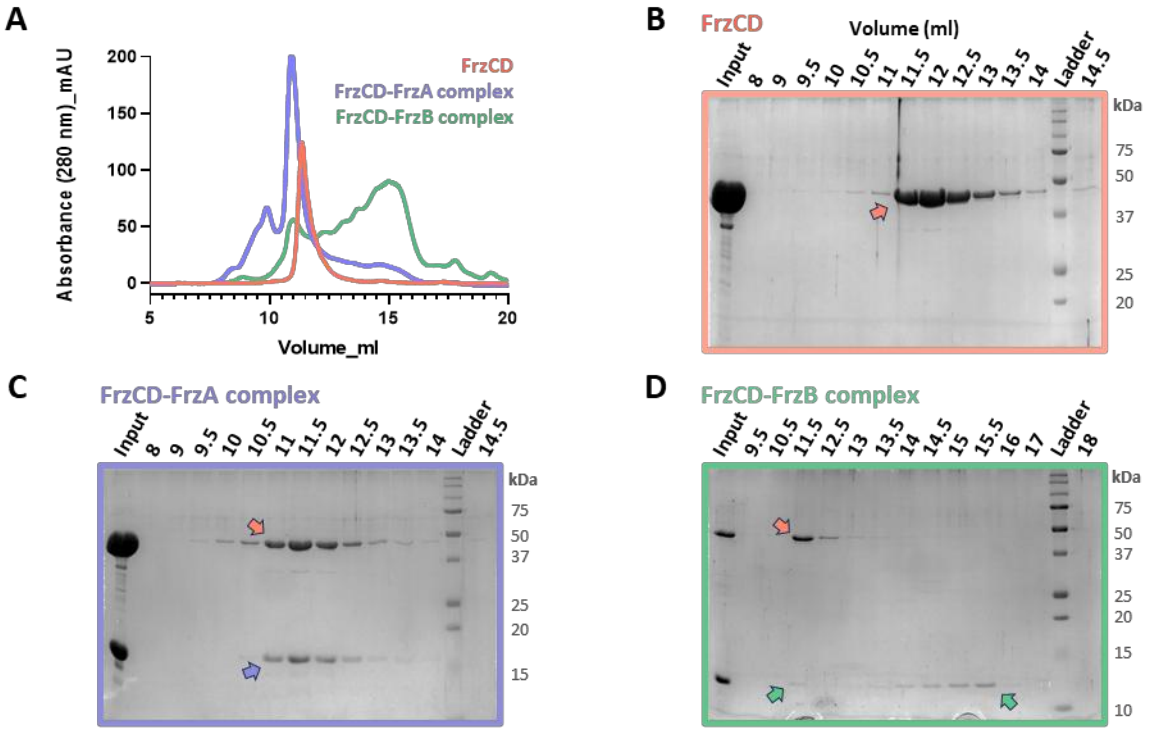


Figure 4.5 FrzCD-FrzA forms a more stable complex than FrzCD-FrzB. (A) Size exclusion chromatography elution profiles in ENrich SEC 650 column of FrzCD (orange), FrzCD-FrzA complex (violet), and FrzCD-FrzB complex (green). Corresponding elution fractions of FrzCD (B), FrzCD-FrzA complex (C), and FrzCD-FrzB complex (D) are checked in SDS-PAGE. Orange, violet and green arrow denotes FrzCD, FrzA and FrzB, respectively.

4.3.3 FrzA and FrzB interact at same interface on FrzCD

We used AlphaFold3 generated models to identify interface interactions important for receptor-adaptor complexes **(**elaborated in **Figure 4.7)**. The interface was validated by heterologous co-transformations of interface mutants of either FrzCD or FrzA/FrzB, followed by pull-down assays to verify stable complex formation. Initially, to confirm the interaction region in FrzCD, we deleted a heptad pair of the coiled-coil, residues 261-267 at the N-terminal arm (N02) and

residues 286-292 at the C-terminal arm (C02) bearing the interacting interface, residues D261 to A267 **(Figures 4.7 and 4.8A, B)**. Strep-tagged FrzCD$^{\Delta 261\text{-}267_\Delta 286\text{-}292}$ failed to interact with FrzA as well as FrzB compared to wild type FrzCD **(Figure 4.8C-F)**. Conversely, during His-tagged pull-downs by adaptor proteins, FrzA was observed to be insoluble and partially soluble FrzB did not pull down FrzCD$^{\Delta 261\text{-}267_\Delta 286\text{-}292}$ **(Figure 4.8G, H)**. FrzCD$^{\Delta 261\text{-}267_\Delta 286\text{-}292}$ formed a stable dimer and showed DNA binding in mobility shift assay **(Figure 4.9)**. FrzA and FrzB interact at overlapping interfaces on FrzCD, and the differences in residues probably result in differential binding affinities **(Figure 4.10A)**.

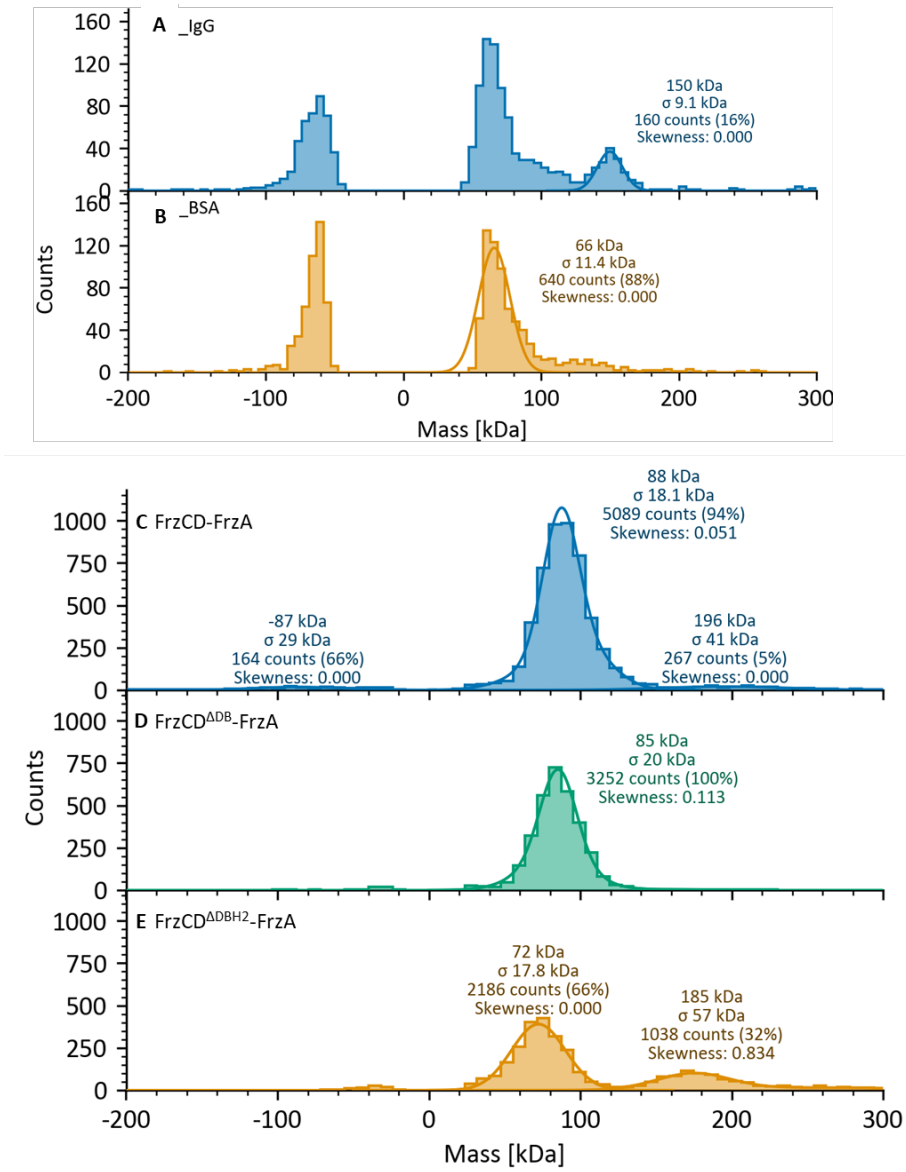
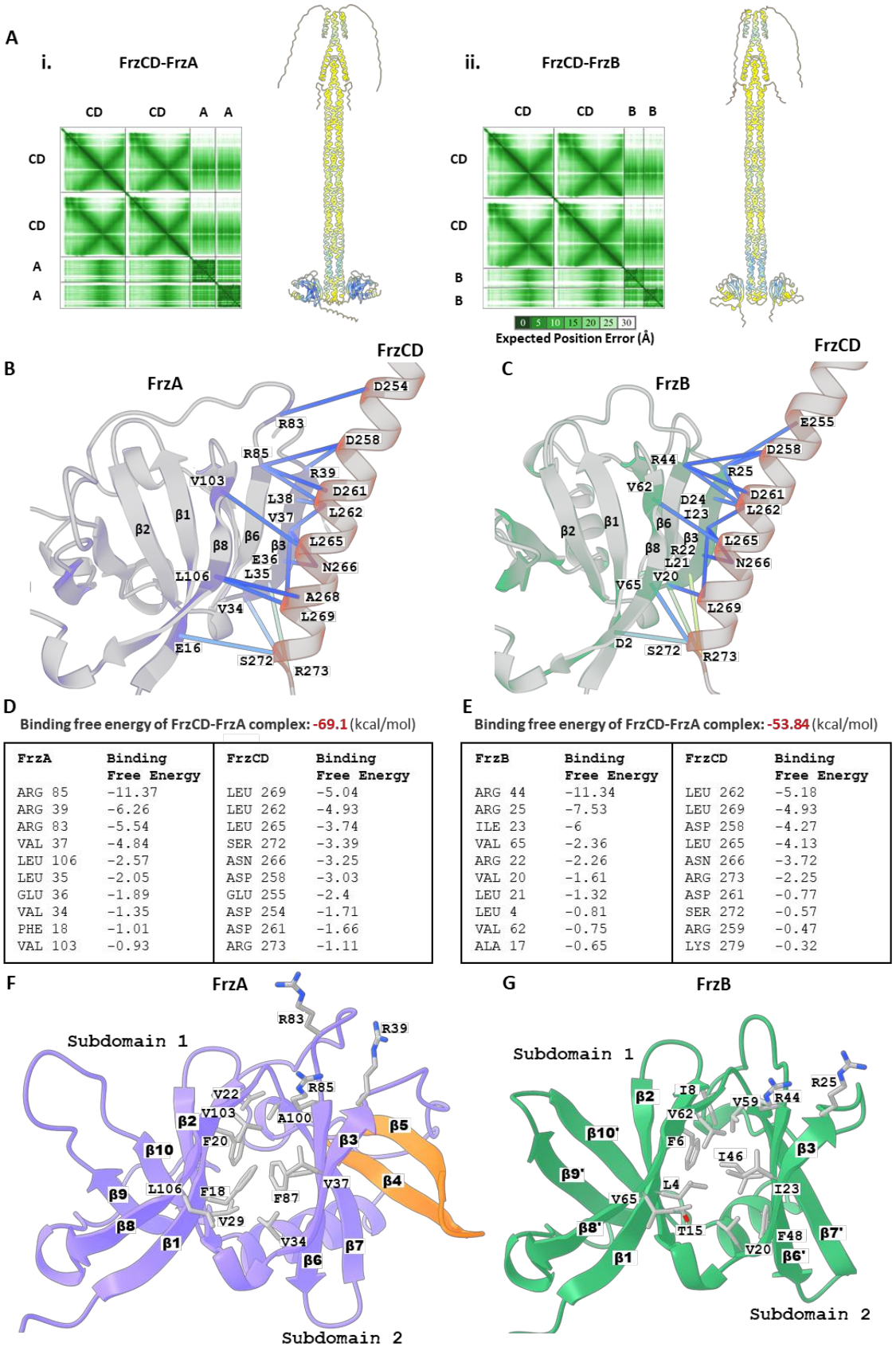


Figure 4.6 Mass estimation of receptor adaptor complexes. (A) IgG (150 kDa), (B) BSA (66 kDa) were used as controls before estimation of (C) FrzCD-FrzA, (D) FrzCD$^{\Delta DB}$-FrzA and (E) FrzCD$^{\Delta DBH2}$-FrzA complexes. FrzA is 18 kDa, monomeric FrzCD is 44.7 kDa, FrzCD$^{\Delta DB}$ is 42 kDa and FrzCD$^{\Delta DBH2}$ is 36 kDa.



FrzA	Binding Free Energy	FrzCD	Binding Free Energy
ARG 85	-11.37	LEU 269	-5.04
ARG 39	-6.26	LEU 262	-4.93
ARG 83	-5.54	LEU 265	-3.74
VAL 37	-4.84	SER 272	-3.39
LEU 106	-2.57	ASN 266	-3.25
LEU 35	-2.05	ASP 258	-3.03
GLU 36	-1.89	GLU 255	-2.4
VAL 34	-1.35	ASP 254	-1.71
PHE 18	-1.01	ASP 261	-1.66
VAL 103	-0.93	ARG 273	-1.11

FrzB	Binding Free Energy	FrzCD	Binding Free Energy
ARG 44	-11.34	LEU 262	-5.18
ARG 25	-7.53	LEU 269	-4.93
ILE 23	-6	ASP 258	-4.27
VAL 65	-2.36	LEU 265	-4.13
ARG 22	-2.26	ASN 266	-3.72
VAL 20	-1.61	ARG 273	-2.25
LEU 21	-1.32	ASP 261	-0.77
LEU 4	-0.81	SER 272	-0.57
VAL 62	-0.75	ARG 259	-0.47
ALA 17	-0.65	LYS 279	-0.32

Figure 4.7 Interface of receptor-adaptor complex from AlphaFold3 predicted models. (A) AlphaFold3 predicted models of: (i) FrzCD-FrzA complex (ipTM = 0.63, pTM = 0.61), and (ii) FrzCD-FrzB complex (ipTM = 0.61, pTM = 0.58). Interface residues within a 4 Å main

chain cutoff distance in FrzCD-FrzA/FrzB predicted models are shown according to the PAE score (B and C). Blue to yellow lines denote low to high PAE score in predicted structures. Binding free energy of FrzCD-FrzA/FrzB predicted models calculated in HawkDock server (MM/GBSA method) *(Zhang et al., 2025)*. Interface residues along with binding free energy are tabulated for FrzCD-FrzA/FrzB models (D and E). Residues of FrzA and FrzB at the hydrophobic groove between two β-barrels that form the interface for FrzCD interaction are shown (F and G). FrzB lacks β4 and β5 in subdomain 2, highlighted in orange in FrzA.

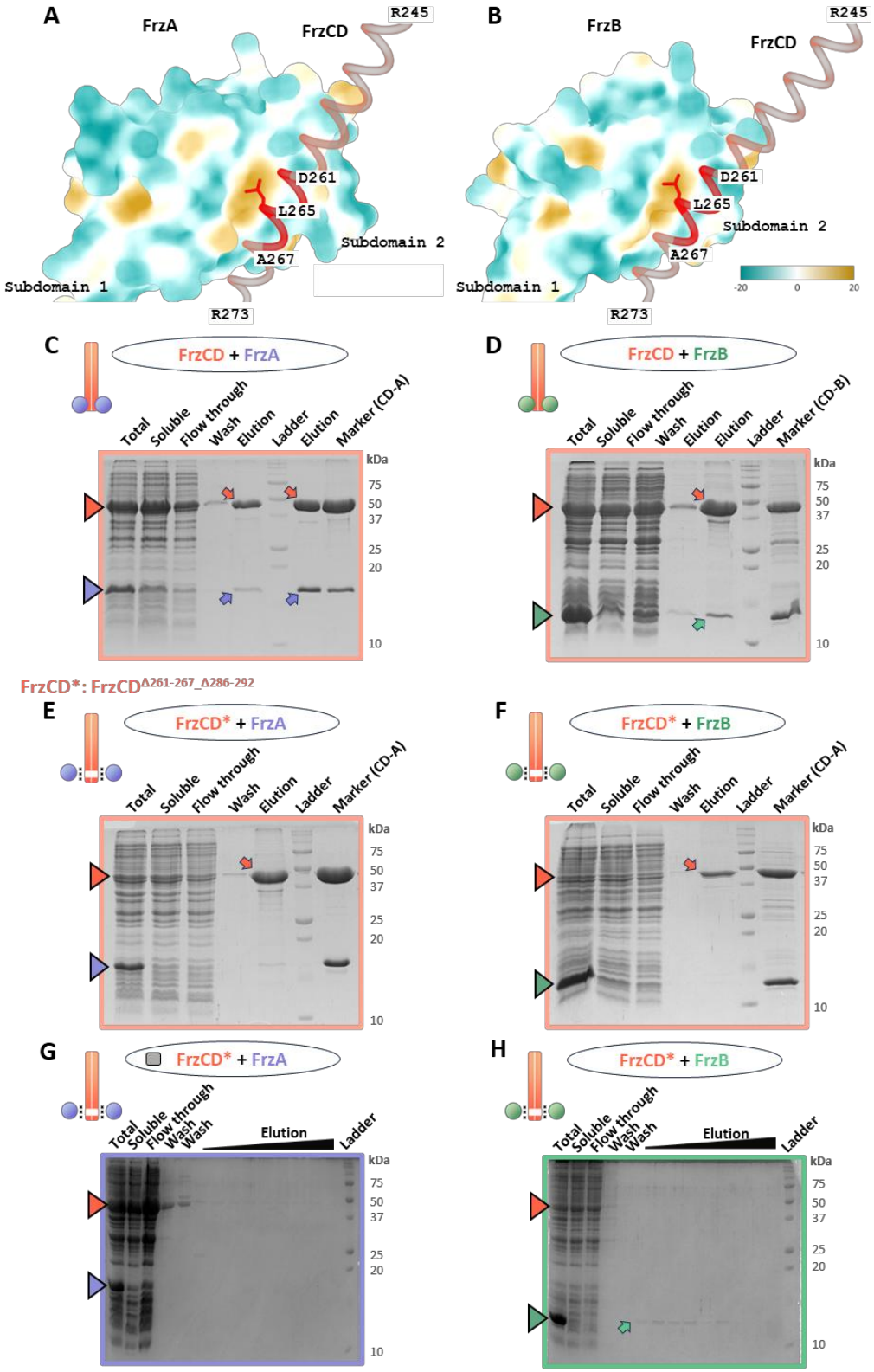


Figure 4.8 FrzA and FrzB interact at the signalling tip of FrzCD. Heptad D261-A267 interacts with the hydrophobic groove of FrzA and FrzB (A and B). Pull-down of FrzA (C), and FrzB (D) by FrzCD from cells co-transformed with both plasmids shows receptor-adaptor complex formation. FrzCD$^{\Delta 261\text{-}267_\Delta 286\text{-}292}$ (FrzCD*) failed to pull down FrzA (E), and FrzB (F) from co-transformed cells. Similarly, FrzA and FrzB failed to pull down FrzCD* in co-transformed cells (G and H). Orange, violet and green triangle denotes FrzCD (45 kDa), FrzA (18 kDa) and FrzB (13 kDa) in the total fraction, respectively, while arrows represent proteins in the pull-down fraction. Colour of the border of the gels denotes the protein by which the pull-down was carried out.

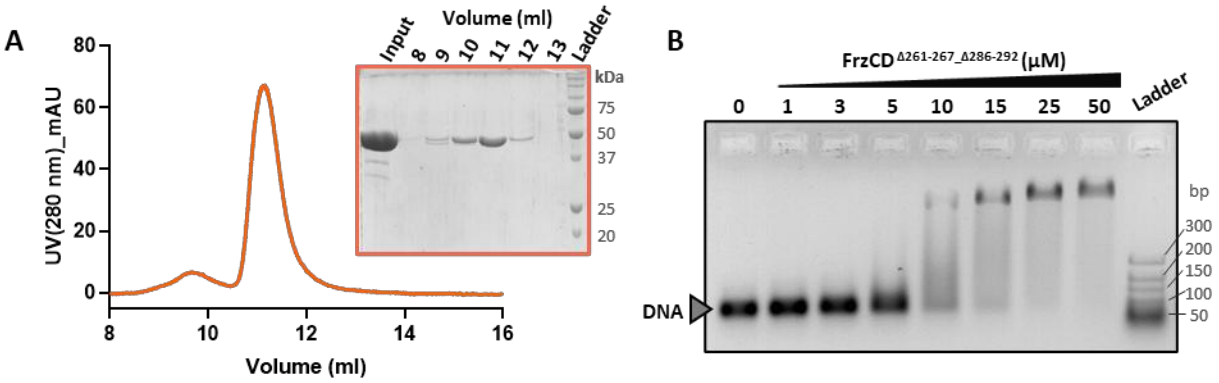


Figure 4.9 FrzCD$^{\Delta 261\text{-}267_\Delta 286\text{-}292}$ (FrzCD*) formed a stable dimer and shows DNA binding in mobility shift assay. (A) Size exclusion chromatography of FrzCD$^{\Delta 261\text{-}267_\Delta 286\text{-}292}$ (FrzCD*). (H) Mobility shift assay of FrzCD* with 1μM 54 bp DNA fragment. Grey triangle denotes unbound DNA.

4.3.4 Hydrophobic and salt-bridge interactions mediate receptor-adaptor complexes

The predicted AlphaFold3 model reveals the presence of a conserved hydrophobic groove in FrzA and FrzB that interacts with a hydrophobic surface on the signalling tip of FrzCD **(Figures 4.10B, C)**. However, the predicted binding free energy of FrzCD-FrzA complex formation (-69.1 kcal/mol) was lower than that of FrzCD-FrzB complex (-53.84 kcal/mol) (calculated in HawkDock server *(Zhang et al., 2025)*). We noticed that leucine 265 and leucine 269 of FrzCD fit into the hydrophobic groove of FrzA and FrzB **(Figure 4.10B, C)**. Mutating leucine to aspartate, FrzCD^{L265D_L269D}, failed to pull down FrzA and FrzB **(Figure 4.10D, E)**.

Additionally, we observed salt-bridge interactions in the predicted FrzCD-FrzA/FrzB models. The interactions are between – (i) R85 of FrzA with D258 and D261 of FrzCD, (ii) R39 of FrzA with E255 and/or D258 of FrzCD, and (iii) R83 of FrzA with D254 of FrzCD **(Figures 4.11A)**. Here, positively charged arginine residues formed likely salt bridge interactions with negatively charged aspartate and glutamate residues on heptad (N03), N-terminal to the hydrophobic groove interacting heptad (N02) of FrzCD **(Figure 4.10A)**.

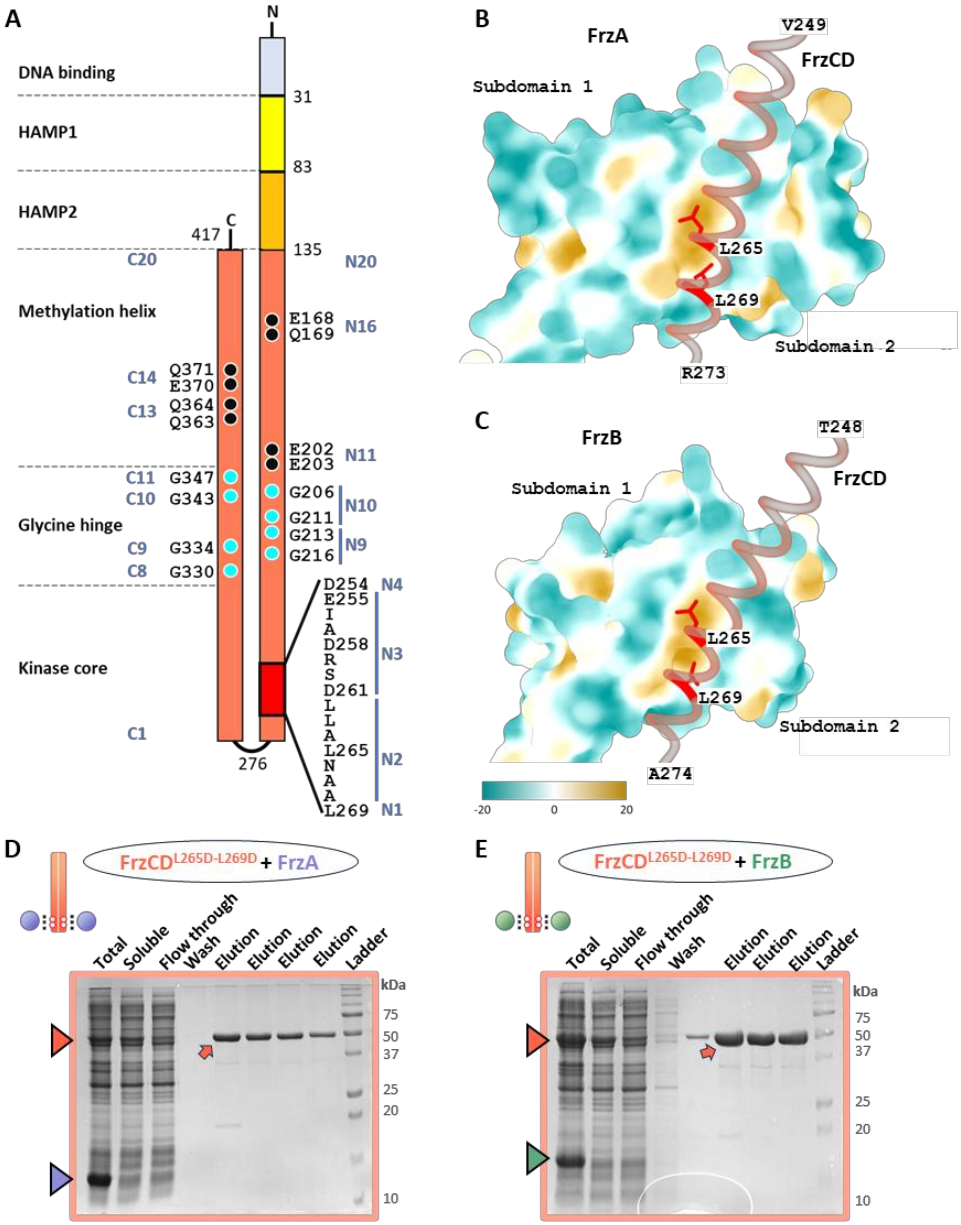


Figure 4.10 Hydrophobic interactions at receptor-adaptor interaction interface. (A) Schematic representation of domains of FrzCD. Aspartate and glutamate residues important for methylation-dependent adaptation are highlighted in black circles *(Astling et al., 2006).* Glycine residues responsible for flexibility of the coil-coil domain are highlighted in cyan. Red square at the signalling tip corresponds to interface residues. Corresponding location of residues in heptads are labelled in blue. Interaction of leucine 265 and leucine 269 of FrzCD with hydrophobic groove of FrzA (B), and FrzB (C). Surface of FrzA and FrzB is coloured by hydrophobicity. Pull-down of FrzA (D), and FrzB (E) by FrzCD$^{L265D\text{-}L269D}$ from cells co-transformed with both plasmids shows receptor-adaptor complex formation. Orange, violet and green triangle denotes FrzCD (45 kDa), FrzA (18 kDa) and FrzB (13 kDa) in total fraction, respectively, while arrows represent proteins in the pull-down fraction.

We checked the importance of salt bridge pairs, one at a time, by co-transforming mutants of FrzCD (FrzCD^{E255A_D258A}, FrzCD^{D258A_D261A} and FrzCD^{D258A}) and FrzA (FrzA^{R39A} and FrzA^{R85A}), with their respective wild-type partner, followed by pull-down by Strep-tagged

FrzCD mutant. Simultaneous mutation of residues E255 and D258 of FrzCD, as well as residues D258 and D261 of FrzCD, abolishes complex formation **(Figure 4.11B, C)**. Mutation of R39 of FrzA, however, did not break the interaction, and pull-down of FrzA^{R39A} by FrzCD was similar to wild-type FrzCD **(Figure 4.11D, 4.8C)**. Complex formation was absent when R85 of FrzA was mutated, suggesting that the interaction between R85 of FrzA and D258 of FrzCD is primary to anchoring FrzA to FrzCD **(Figure 4.11E)**. Subsequently, FrzCD^{D258A} did not pull down FrzA, confirming that salt-bridge interaction, in addition to hydrophobic interactions, is essential for stable FrzCD-FrzA complex formation **(Figure 4.11E, F)**. Similarly, FrzCD-FrzB complex has two salt-bridge pairs – (i) between R44 of FrzB with D258 and D261 of FrzCD, and (ii) R25 of FrzA with E255 and D258 of FrzCD, and both interactions are important for complex formation. Breaking of either of the salt-bridges inhibits FrzCD-FrzB complex formation **(Figure 4.12)**.

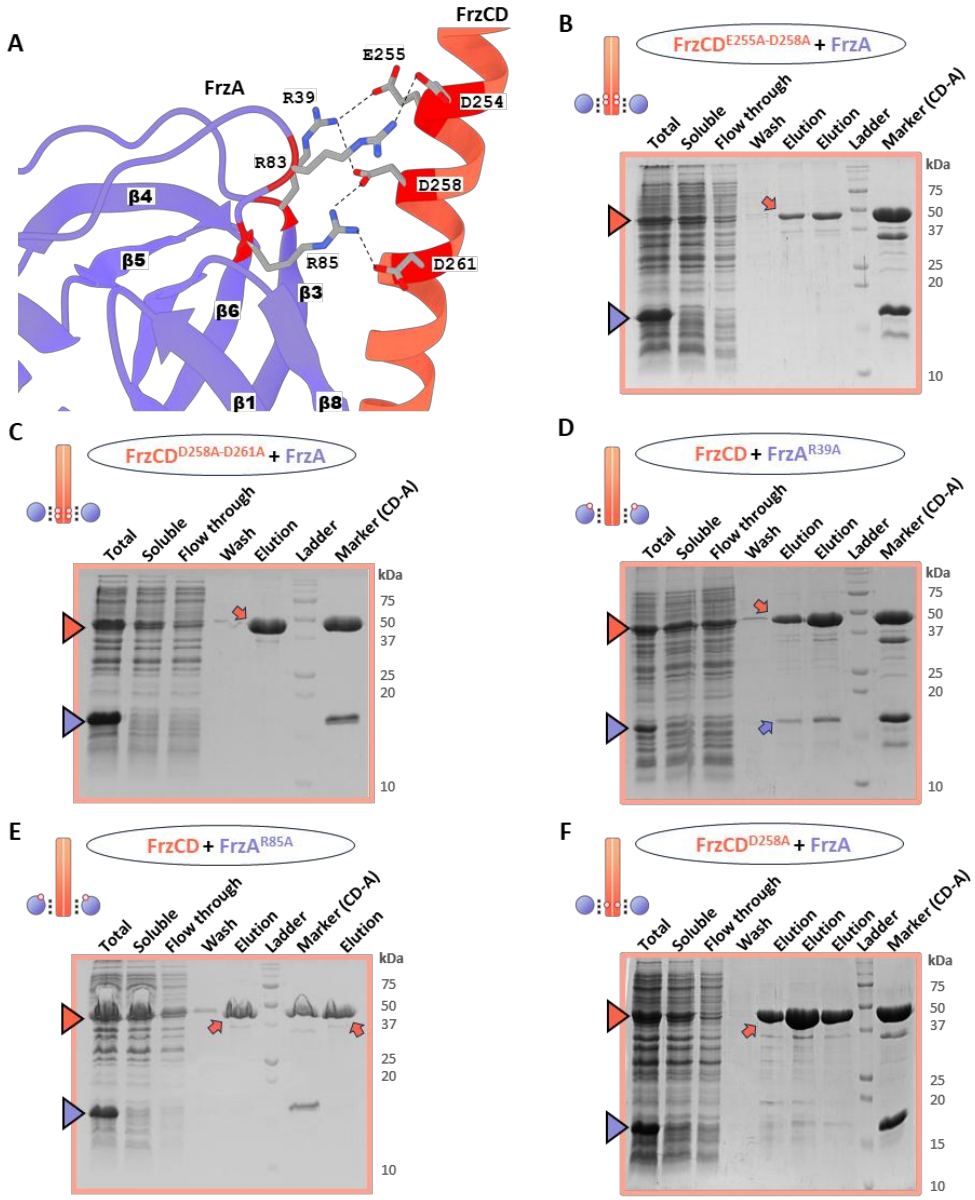


Figure 4.11 Salt-bridge interactions between FrzCD and FrzA. (A) Diagram showing probable salt-bridge interactions between FrzA and FrzCD. (B) FrzCD-FrzA complex formation was lost when E255 and D258 of FrzCD were mutated, as observed in pull-down by FrzCD$^{E255A-D258A}$ in co-transformed cells. Similarly, complex formation was lost when E258 and D261 of FrzCD were mutated (C). Pull-downs by FrzCD from co-transformed cells show interaction with FrzA harbouring arginine 39 to alanine mutation (D). The interaction is lost when either arginine 85 of FrzA is mutated to alanine (E) and aspartate 258 of FrzCD is mutated to alanine (F). Orange and violet triangle denotes FrzCD (45 kDa) and FrzA (18 kDa) in the total fraction, while arrows represent proteins in the pull-down fractions.

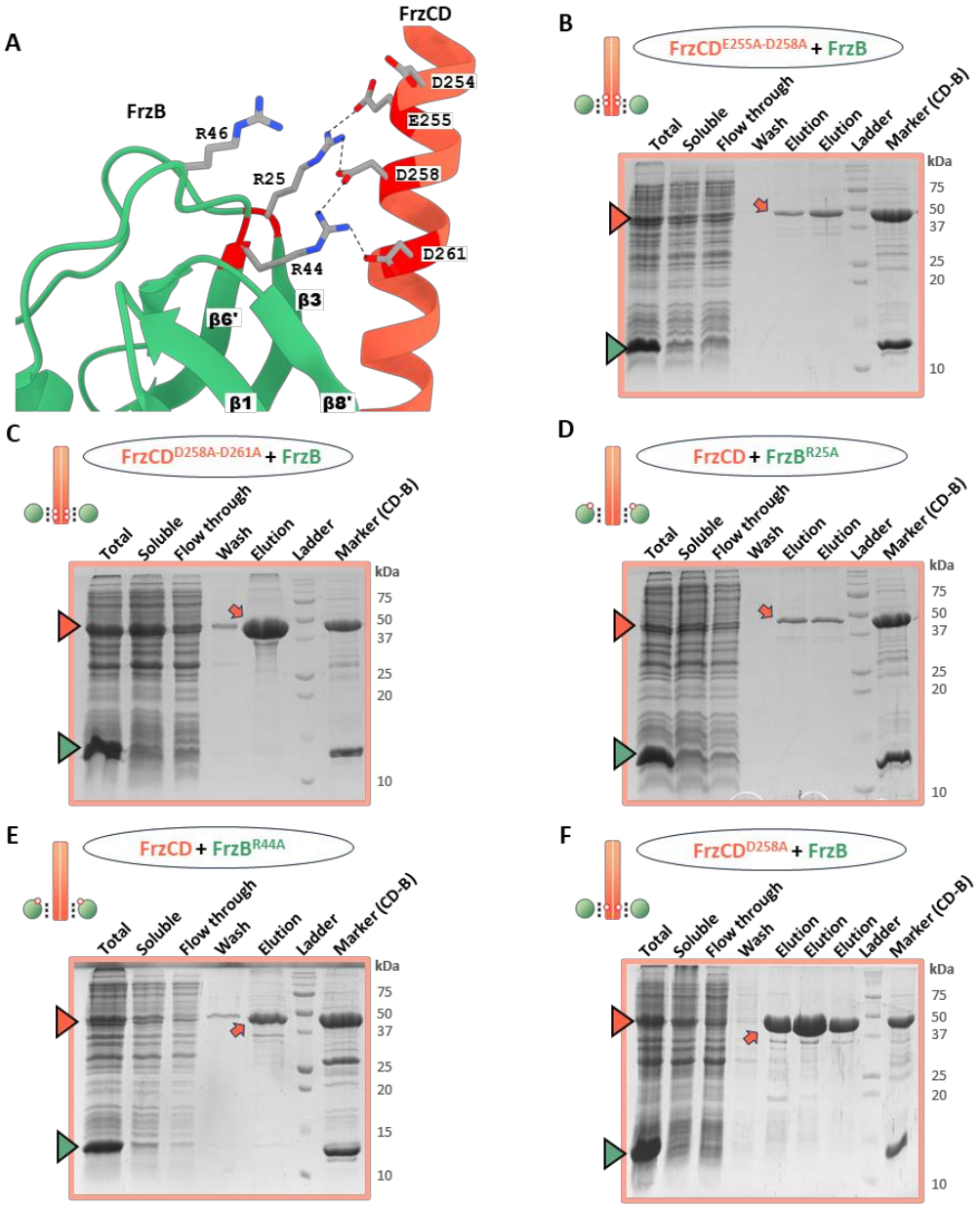


Figure 4.12 Salt-bridge interactions between FrzCD and FrzB. (A) Diagram showing probable salt-bridge interactions between FrzB and FrzCD. (B) FrzCD$^{E255A-D258A}$ and (C) FrzCD$^{D258A-D261A}$ failed to pull-down FrzB. FrzCD-FrzB complex formation is inhibited by arginine 25 or arginine 44 mutation to alanine in FrzB (D and E). (F) Aspartate 258 to alanine mutation on FrzCD also breaks the interaction. Orange and green triangle denotes FrzCD (45 kDa) and FrzB (13 kDa) in the total fraction, respectively, while arrows represent proteins in the pull-down fractions.

4.3.5 Receptor-adaptor complex is a dynamic assembly

We checked the plasticity of receptor-adaptor complexes *in vitro*. Since the di-HAMP domains regulate signalling output of Frz pathway *(Jazleena, Das, Guiseppi et al., 2025)*, we checked whether interaction with adaptor protein FrzA was influenced by di-HAMP domains. FrzCD was observed to form a stable complex with different Frz signalling states in HAMP1, HAMP2, or both HAMP-deleted FrzCD (FrzCDΔH1, FrzCDΔH2, and FrzCD$^{\Delta H1H2}$) **(Figure 4.13)**.

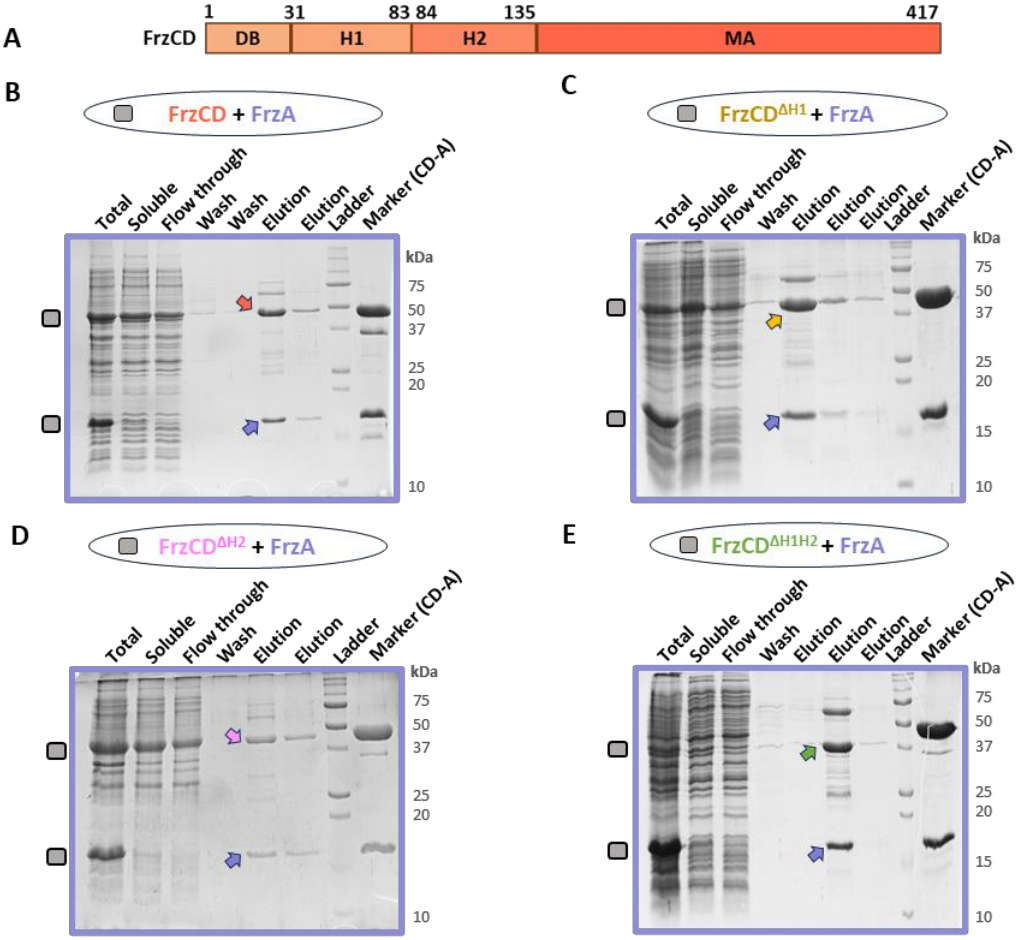


Figure 4.13 FrzA interacts with different Frz signalling states dictated by HAMP domain. (A) Domain architecture of FrzCD. Pull down of FrzCD (B), FrzCD$^{\Delta H1}$ (C), FrzCD$^{\Delta H2}$ (D), and FrzCD$^{\Delta H1H2}$ (E) by FrzA from co-transformed cells (grey square). Orange, yellow, pink, green and violet arrows denote FrzCD (45 kDa), FrzCD$^{\Delta H1}$ (39 kDa), FrzCD$^{\Delta H2}$ (39 kDa), FrzCD$^{\Delta H1H2}$ (33 kDa) and FrzA (18 kDa) respectively.

We used competition pull-down assays, where co-transformed *E. coli* cells with a HAMP domain-deleted FrzCD-FrzA complex were mixed with cells expressing wild-type FrzCD. We observed that wild-type FrzCD is pulled down by a soluble, preformed FrzA-FrzCD$^{\Delta H1H2}$ complex **(Figure 4.14A)**. Likewise, FrzCD$^{\Delta H1H2}$ was pulled down by preformed soluble FrzA-FrzCD complex, suggesting the dynamic nature of the receptor-adaptor complex **(Figure 4.14B)**. This could be due to lateral interactions between FrzCD dimers and truncated

FrzCD$^{\Delta H1H2}$ dimers, or interactions between FrzA and FrzCD. FrzCD^{D258A}, an interface mutant between FrzCD-FrzA, did not interact with preformed FrzA-FrzCD$^{\Delta H1H2}$, confirming that the interaction was mediated by soluble FrzA, which is part of the preformed FrzA-FrzCD$^{\Delta H1H2}$ complex **(Figure 4.14C)**. Furthermore, competition pull-down assays with FrzCD$^{\Delta H1}$ and FrzCD$^{\Delta H2}$ confirmed the dynamic nature of the receptor-adaptor assembly **(Figure 4.14D, E)**.

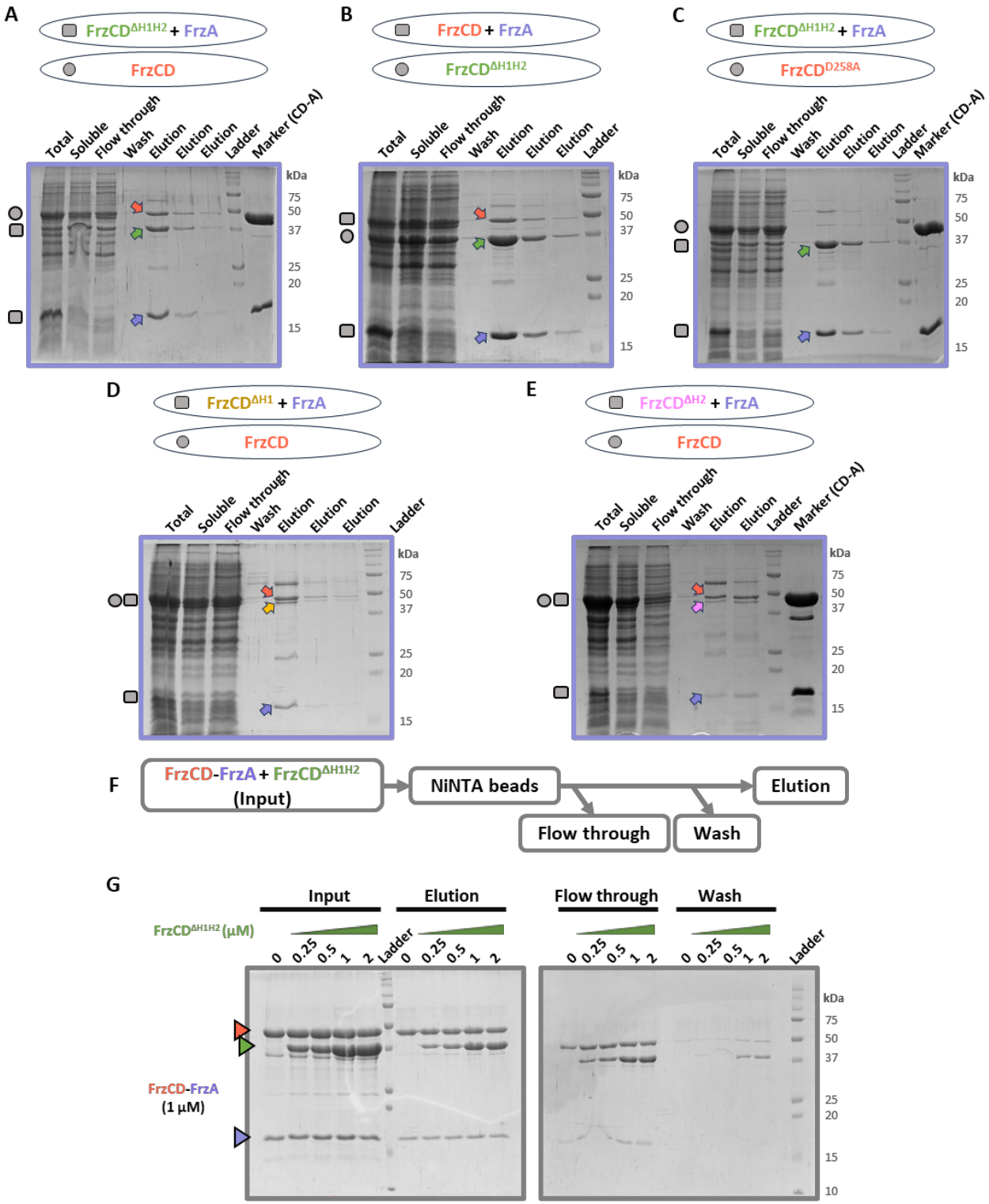


Figure 4.14 Receptor-adaptor complex is a dynamic assembly. (A) Pull-down of FrzCD$^{\Delta H1H2}$ and FrzCD by FrzA from mixed lysates of co-transformed FrzCD$^{\Delta H1H2}$ with FrzA (grey square) and separately expressed FrzCD (grey circle). (B) Pull-down of FrzCD$^{\Delta H1H2}$ and FrzCD by FrzA from mixed lysates of co-transformed FrzCD with FrzA (grey square) and separately expressed FrzCD$^{\Delta H1H2}$ (grey circle). (C) Pull-down of FrzCD$^{\Delta H1H2}$ alone by FrzA from mixed lysates of co-transformed FrzCD$^{\Delta H1H2}$ with FrzA (grey square) and separately expressed FrzCD^{D258A} (grey circle). Orange, violet and green arrows denote FrzCD (45 kDa), FrzA (18 kDa) and FrzCD$^{\Delta H1H2}$ (33 kDa) in pull-down fractions. (D) Pull-down of FrzCD$^{\Delta H1}$ and FrzCD by FrzA from mixed lysates of co-transformed FrzCD$^{\Delta H1}$ with FrzA (grey square) and separately expressed FrzCD (grey circle). (E) Pull-down of FrzCD$^{\Delta H2}$ and FrzCD by FrzA from mixed lysates of co-transformed FrzCD$^{\Delta H2}$ with FrzA (grey square) and separately expressed FrzCD (grey circle). Orange, yellow and pink arrows denote FrzCD (45 kDa), FrzCD$^{\Delta H1}$ (39 kDa), and FrzCD$^{\Delta H2}$ (39 kDa), respectively. (F) Diagram showing steps of in-vitro competition assay of purified FrzCD-FrzA complex with FrzCDΔH1H2. (G) An *in vitro* competition assay shows the elution of FrzCDΔH1H2 and FrzCD in complex with FrzA as a dynamic assembly. Orange, violet and green triangle denotes FrzCD (45 kDa), FrzA (18 kDa) and FrzCD$^{\Delta H1H2}$ (33 kDa). Colour of the border of the gels denotes the protein by which the pull-down was carried out.

Since FrzA forms a soluble complex in presence of stabilizing interactions with FrzCD during expression, we believe that wild-type or HAMP domains deleted FrzCD can interact with FrzA and replace the receptor molecules in preformed assemblies. We tested this *in vitro* by competing FrzCD$^{\Delta H1H2}$ with a preformed complex of FrzCD-FrzA and observed that FrzCD$^{\Delta H1H2}$ was incorporated into the assemblies **(Figure 4.14F, G)**. This dynamic nature highlights the plasticity that exists in the receptor-adaptor complexes.

4.4 Discussion

Phylogenomics analysis showed diversity in the components of chemotaxis signalling pathways. In addition to the central components of signalling pathways, auxiliary components were identified as part of chemosensory signalling pathways *(Wuichet & Zhulin, 2010)*. Over half of all motile bacteria possess multiple chemosensory systems *(Wuichet & Zhulin, 2010)*. Typically, at least one CSS directly controls motility, while others likely regulate various programmed cellular processes *(Gumerov et al., 2021; He & Bauer, 2014)*. The Frz system is one of the eight CCSs in *M. xanthus* and is responsible for regulating motility in the bacterium *(Moine et al., 2014)*. A diversity in adaptor proteins exists that forms the baseplate *(Huang et al., 2019)*. For example, CheV, a CheW-CheY chimeric protein *(Fredrick & Helmann, 1994)*, which is encoded in 60% of all chemotactic prokaryotes *(Wuichet & Zhulin, 2010)*, interacts with receptors and CheA and can be phosphorylated by CheA *(Karatan et al., 2001)*. The emergence of multiple adaptor proteins in an organism is believed to be part of different chemotaxis cluster assemblies that respond to different environmental stimuli *(Huang et al., 2019)*. Additionally, multiple adaptor proteins can regulate a single chemotaxis signalling pathway, and bacteria could adjust baseplate components in response to environmental stimuli to regulate sensory output from chemosensory arrays *(Yang & Briegel, 2020; Yang et al., 2018; Cannistraro et al., 2011)*. CSS with multiple adaptor proteins fall into three categories: (i) only one coupling protein is essential for chemotaxis, while others are dispensable or conditional; (ii) two coupling proteins coexist redundantly, so deleting either reduces but does not eliminate chemotaxis; (iii) two proteins coexist non-redundantly, each contributing uniquely to the pathway *(Huang et al., 2019)*. In *M. xanthus*, FrzA is paramount for cluster formation and signal transduction, while FrzB, a non-canonical adaptor lacking β4 and β5 in subdomain 2, may act as a stabilizing factor regulating the size of clusters on the nucleoid *(Guiseppi et al., 2019; Mauriello, 2020)*.

Here, we looked into the characteristics of FrzA and FrzB, which enable them to carry out their distinct roles to ensure proper cluster formation on nucleoid and thereby signal transduction in regulating motility and development of the bacterium. We purified complexes of FrzA and FrzB with FrzCD. FrzCD-FrzA complex was observed to be more stable than FrzCD-FrzB **(Figures 4.4 and 4.5)**. The structural characterization of the receptor-adaptor complex is elaborated in detail in **Chapter 5**. We identified the interaction interface on the receptor helix for binding to the adaptor. FrzA binds at the signalling tip of the coiled-coil domain of FrzCD. Two FrzA

molecules interact on dimeric FrzCD at the signalling tip. We validated the interface by identifying key residues that mediate hydrophobic interactions (leucine 265 and 269 of FrzCD) and salt bridge interactions (aspartate 285 of FrzCD with arginine 85 of FrzA) **(Figures 4.10 and 4.11)**. AlphaFold3 also predicts the same interface for the FrzCD-FrzB complex. We validated the interface and identified the key residues. Apart from hydrophobic interactions, two salt bridges are essential for complex formation (aspartate 258 and 261 of FrzCD with arginine 44 of FrzB, and glutamate 255 together with aspartate 258 of FrzCD interacts with arginine 39 of FrzB) **(Figures 4.10 and 4.12)**.

Although both adaptor proteins have a conserved hydrophobic groove between subdomain 1 and subdomain 2 that interacts with the same receptor interface on FrzCD, the interface residues on the adaptor proteins differ **(Figure 4.7)**. The salt bridge interactions are mediated by residues that lie on the heptad N-terminal to the interface heptad on FrzCD and anchor the adaptor protein at the signalling tips **(Figure 4.10A)**. The predicted binding free energy of FrzCD-FrzA complex formation (-69.1 kcal/mol) is lower than FrzCD-FrzB complex (-53.84 kcal/mol). Two salt-bridge interaction pairs are essential for FrzCD-FrzB complex formation, as opposed to one anchoring interaction FrzCD-FrzA complex. Apart from the essential R85-D258 interaction for FrzA and FrzCD, we noticed additional possible salt bridges in the predicted model. These include R85 of FrzA with D261 of FrzCD, R39 of FrzA with E255 or D258 of FrzCD and R83 in the loop connecting β6 and β7 of FrzA with D254 of FrzCD **(Figure 4.11A)**. FrzB, which lacks β4 and β5 in subdomain 2, harbours R46 analogous to R83 of FrzA, in the loop connecting β6' and β7' of FrzB, but is predicted to be far from the interacting interface with FrzCD **(Figure 4.12A)**. Apart from differences in interface residues at the hydrophobic groove, which might influence the stability of receptor-adaptor complexes, FrzCD-FrzA, in contrast to the FrzCD-FrzB complex, might have secondary salt-bridge interactions besides the primary anchoring $FrzCD^{D258}$-$FrzA^{R85}$ interaction, resulting in a more stable complex. This was evident during tandem pull-downs of the complexes from co-transformed cells as well as in SEC. FrzCD and FrzA co-eluted in SEC, but FrzB dissociated and eluted as a separate peak, suggesting that the FrzCD-FrzB complex is not as stable as the FrzCD-FrzA complex **(Figure 4.6)**.

FrzA was only soluble in co-transformed cells with FrzCD, implying that stable interactions during expression are important for soluble FrzA-FrzCD complex formation **(Figure 4.4)**. This was true when FrzA was co-transformed with HAMP-deleted constructs of FrzCD (ΔH1, ΔH2

and ΔH1H2). This implies that the interacting interface of the coiled-coil domain is compatible with alternate signalling states of FrzCD imparted by the di-HAMP domains *(Jazleena, Das, Guiseppi et al., 2025)*. However, the binding efficiency of FrzA with these constructs was not explored. We observed that the receptor-adaptor complex is a dynamic assembly. FrzCD can interact with the preformed complex of FrzA with either one (H1/H2) or both HAMP-deleted FrzCD and vice versa. This dynamic nature is mediated by interactions with FrzA, which is part of preformed soluble complex **(Figure 4.14)**. Together, the flexibility of the FrzCD (at glycine hinge) and the dynamic process of assembly with adaptors may be crucial for facilitating and regulating the plasticity of clusters on the nucleoid.

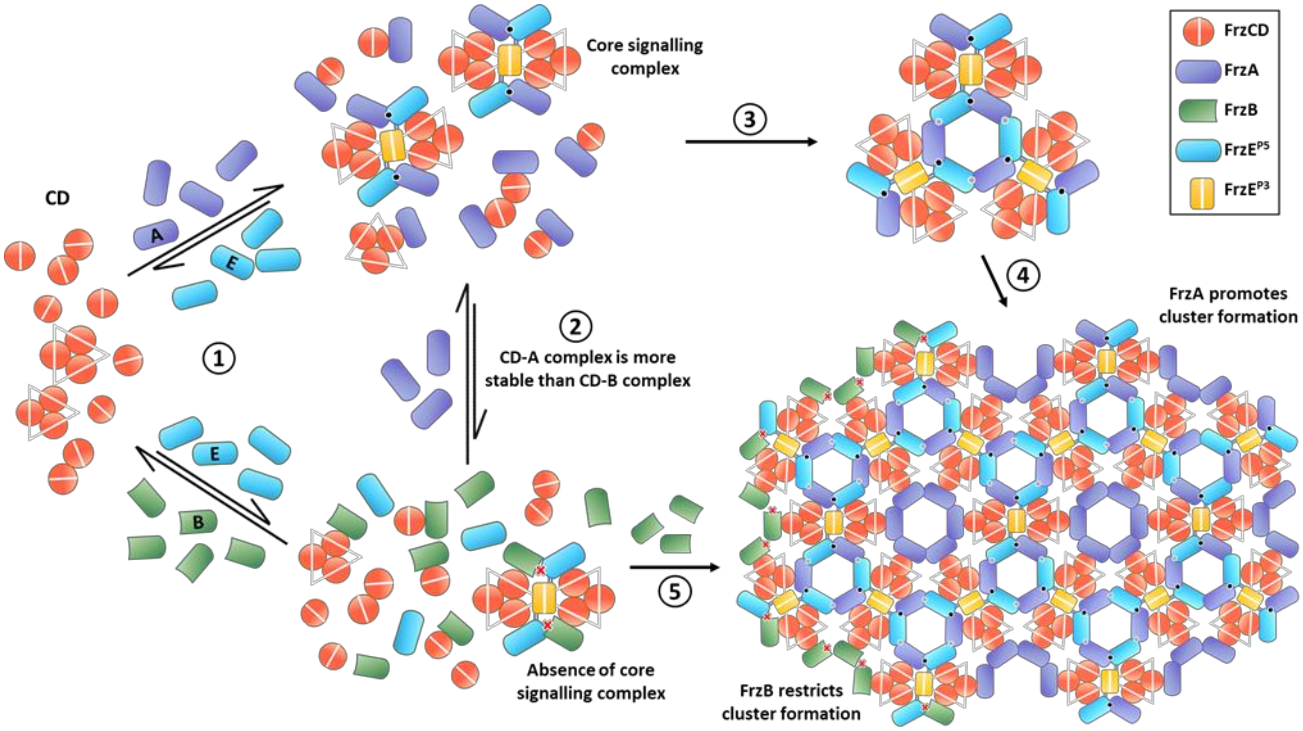


Figure 4.15 Mechanism of regulation of chemosensory array formation by FrzA and FrzB. FrzA and FrzB interact with receptor FrzCD and histidine kinase FrzE (1). FrzB lacks β4 and β5 in subdomain 2, which mediates interaction with FrzE-P5 at interface 1 *(Guiseppi et al., 2019)*, and fails to form a core signalling complex. Additionally, FrzCD-FrzB complex is observed to be less stable than FrzCD-FrzA complex. Thus, formation of a core signalling complex between FrzCD, FrzA and FrzE is possibly preferred (2). The core signalling complexes assemble into a hexagonal architecture (3) via interaction at interface 1 (black circle) and interface 2 (grey circle), which extend into an array (4). Presence of FrzA, which stably interacts with FrzCD and FrzE-P5 at interface 1, promotes array formation. However, binding of FrzB to FrzCD, possibly favoured by lower local FrzA concentration, fails to interact with FrzE and restricts array extension, thereby regulating the array size on the nucleoid (5).

Furthermore, we propose a model on how FrzB, a non-canonical adaptor protein, together with FrzA, regulate array formation on the nucleoid. FrzA interacts with receptor FrzCD to form

stable complexes and, in the presence of histidine kinase FrzE, forms core signalling units via interactions at interface 1. FrzB lacks β4 and β5 in subdomain 2, responsible for interaction with FrzE-P5 at interface 1, and hence, could not form CSU *(Guiseppi et al., 2019; Mauriello, 2020)*. Since the FrzCD-FrzB complex is observed to be less stable than FrzCD-FrzA complex, the formation of the core signalling complex between FrzCD, FrzA and FrzE is possibly preferred. The core signalling complexes assemble into a hexagonal architecture via interaction at interface 2, which extends into an array **(Figure 4.15).** Since both adaptor proteins have the same binding interface on FrzCD, it is the property of the interacting interface of FrzA and FrzB with FrzCD that provides competitive regulation for array propagation. FrzA, which stably interacts with FrzCD and FrzE-P5 at interface 1, promotes CSU formation and array propagation. However, binding of FrzB to FrzCD, possibly favoured by lower local FrzA concentration, fails to interact with FrzE and restricts array extension, thereby regulating the array size on the nucleoid and promoting multiple clusters.

In conclusion, this study provides new insights into the regulatory role of adaptor proteins from a novel cytoplasmic CSS in the formation of multiple clusters on the nucleoid. The distinct characteristics of two adaptors in this CSS bring division of labour in mediating multiple cluster formation on the nucleoid. One promotes array formation while the other inhibits it. The difference in stability of receptor-adaptor assemblies, a property of the interfaces of the adaptors, adds new dimensions to understanding how adaptor proteins can fine-tune regulatory networks. This provides insight into how CSS with multiple homologous components can have different roles in fine-tuning signalling outputs.

4.5 Acknowledgements

I thank Tiyasa Bain for cloning FrzCD HAMP deleted constructs with a C-terminal Strep tag into the pHis17 vector. I appreciate her assistance during the purification and pull-downs of certain batches of receptor-adaptor complexes.

4.6 References

1. Acuña, G., Shi, W., Trudeau, K., & Zusman, D. R. (1995). The 'CheA' and 'CheY' domains of Myxococcus xanthus FrzE function independently in vitro as an autokinase and a phosphate acceptor, respectively. *FEBS Letters*, *358*(1), 31–33. https://doi.org/10.1016/0014-5793(94)01389-I

2. Astling, D. P., Lee, J. Y., & Zusman, D. R. (2006). Differential effects of chemoreceptor methylation-domain mutations on swarming and development in the social bacterium Myxococcus xanthus. *Molecular Microbiology*, *59*(1), 45–55. https://doi.org/10.1111/j.1365-2958.2005.04926.x

3. Bhattacharyya, R. P., Reményi, A., Yeh, B. J., & Lim, W. A. (2006). Domains, Motifs, and Scaffolds: The Role of Modular Interactions in the Evolution and Wiring of Cell Signaling Circuits. *Annual Review of Biochemistry*, *75*(Volume 75, 2006), 655–680. https://doi.org/10.1146/annurev.biochem.75.103004.142710

4. Bilwes, A. M., Alex, L. A., Crane, B. R., & Simon, M. I. (1999). Structure of CheA, a Signal-Transducing Histidine Kinase. *Cell*, *96*(1), 131–141. https://doi.org/10.1016/S0092-8674(00)80966-6

5. Blackhart, B. D., & Zusman, D. R. (1985). "Frizzy" genes of Myxococcus xanthus are involved in control of frequency of reversal of gliding motility. *Proceedings of the National Academy of Sciences*, *82*(24), 8767–8770. https://doi.org/10.1073/pnas.82.24.8767

6. Briegel, A., Ladinsky, M. S., Oikonomou, C., Jones, C. W., Harris, M. J., Fowler, D. J., Chang, Y.-W., Thompson, L. K., Armitage, J. P., & Jensen, G. J. (2014). Structure of bacterial cytoplasmic chemoreceptor arrays and implications for chemotactic signaling. *eLife*, *3*, e02151. https://doi.org/10.7554/eLife.02151

7. Briegel, A., Ortega, D. R., Huang, A. N., Oikonomou, C. M., Gunsalus, R. P., & Jensen, G. J. (2015). Structural conservation of chemotaxis machinery across Archaea and Bacteria. *Environmental Microbiology Reports*, *7*(3), 414–419. https://doi.org/10.1111/1758-2229.12265

8. Briegel, A., Ortega, D. R., Mann, P., Kjær, A., Ringgaard, S., & Jensen, G. J. (2016). Chemotaxis cluster 1 proteins form cytoplasmic arrays in Vibrio cholerae and are stabilized by a double signaling domain receptor DosM. *Proceedings of the National Academy of Sciences*, *113*(37), 10412–10417. https://doi.org/10.1073/pnas.1604693113

9. Briegel, A., Ortega, D. R., Tocheva, E. I., Wuichet, K., Li, Z., Chen, S., Müller, A., Iancu, C. V., Murphy, G. E., Dobro, M. J., Zhulin, I. B., & Jensen, G. J. (2009). Universal architecture of bacterial chemoreceptor arrays. *Proceedings of the National Academy of Sciences*, *106*(40), 17181–17186. https://doi.org/10.1073/pnas.0905181106

10. Bustamante, V. H., Martínez-Flores, I., Vlamakis, H. C., & Zusman, D. R. (2004). Analysis of the Frz signal transduction system of Myxococcus xanthus shows the importance of the conserved C-terminal region of the cytoplasmic chemoreceptor FrzCD in sensing signals. *Molecular Microbiology*, *53*(5), 1501–1513. https://doi.org/10.1111/j.1365-2958.2004.04221.x

11. Cannistraro, V. J., Glekas, G. D., Rao, C. V., & Ordal, G. W. (2011). Cellular Stoichiometry of the Chemotaxis Proteins in Bacillus subtilis. *Journal of Bacteriology*, *193*(13), 3220–3227. https://doi.org/10.1128/jb.01255-10

12. Cassidy, C. K., Himes, B. A., Alvarez, F. J., Ma, J., Zhao, G., Perilla, J. R., Schulten, K., & Zhang, P. (2015). CryoEM and computer simulations reveal a novel kinase conformational switch in bacterial chemotaxis signaling. *eLife*, *4*, e08419. https://doi.org/10.7554/eLife.08419

13. Cassidy, C. K., Himes, B. A., Sun, D., Ma, J., Zhao, G., Parkinson, J. S., Stansfeld, P. J., Luthey-Schulten, Z., & Zhang, P. (2020). Structure and dynamics of the E. coli chemotaxis core signaling complex by cryo-electron tomography and molecular simulations. *Communications Biology*, *3*(1), 24. https://doi.org/10.1038/s42003-019-0748-0

14. Collins, K. D., Lacal, J., & Ottemann, K. M. (2014). Internal Sense of Direction: Sensing and Signaling from Cytoplasmic Chemoreceptors. *Microbiology and Molecular Biology Reviews*, *78*(4), 672–684. https://doi.org/10.1128/mmbr.00033-14

15. Dinet, C., Michelot, A., Herrou, J., & Mignot, T. (2021). Linking single-cell decisions to collective behaviours in social bacteria. *Philosophical Transactions of the Royal Society B: Biological Sciences*, *376*(1820), 20190755. https://doi.org/10.1098/rstb.2019.0755

16. Falke, J. J., Bass, R. B., Butler, S. L., Chervitz, S. A., & Danielson, M. A. (1997). THE TWO-COMPONENT SIGNALING PATHWAY OF BACTERIAL CHEMOTAXIS: A Molecular View of Signal Transduction by Receptors, Kinases, and Adaptation Enzymes. *Annual Review of Cell and Developmental Biology*, *13*, 457–512. https://doi.org/10.1146/annurev.cellbio.13.1.457

17. Frank, V., Piñas, G. E., Cohen, H., Parkinson, J. S., & Vaknin, A. (2016). Networked Chemoreceptors Benefit Bacterial Chemotaxis Performance. *mBio*, *7*(6), 10.1128/mbio.01824-16. https://doi.org/10.1128/mbio.01824-16

18. Fredrick, K. L., & Helmann, J. D. (1994). Dual chemotaxis signaling pathways in Bacillus subtilis: A sigma D-dependent gene encodes a novel protein with both CheW and CheY homologous domains. *Journal of Bacteriology*, *176*(9), 2727–2735. https://doi.org/10.1128/jb.176.9.2727-2735.1994

19. Good, M. C., Zalatan, J. G., & Lim, W. A. (2011). Scaffold Proteins: Hubs for Controlling the Flow of Cellular Information. *Science*, *332*(6030), 680–686. https://doi.org/10.1126/science.1198701

20. Griswold, I. J., & Dahlquist, F. W. (2002). The dynamic behavior of CheW from *Thermotoga maritima* in solution, as determined by nuclear magnetic resonance: Implications for potential protein–protein interaction sites. *Biophysical Chemistry*, *101–102*, 359–373. https://doi.org/10.1016/S0301-4622(02)00157-6

21. Griswold, I. J., Zhou, H., Matison, M., Swanson, R. V., McIntosh, L. P., Simon, M. I., & Dahlquist, F. W. (2002). The solution structure and interactions of CheW from Thermotoga maritima. *Nature Structural Biology*, *9*(2), 121–125. https://doi.org/10.1038/nsb753

22. Guiseppi, A., Vicente, J. J., Herrou, J., Byrne, D., Barneoud, A., Moine, A., Espinosa, L., Basse, M.-J., Molle, V., Mignot, T., Roche, P., & Mauriello, E. M. F. (2019). A divergent CheW confers plasticity to nucleoid-associated chemosensory arrays. *PLOS Genetics*, *15*(12), e1008533. https://doi.org/10.1371/journal.pgen.1008533

23. Gumerov, V. M., Andrianova, E. P., & Zhulin, I. B. (2021). Diversity of bacterial chemosensory systems. *Current Opinion in Microbiology*, *61*, 42–50. https://doi.org/10.1016/j.mib.2021.01.016

24. Guzzo, M., Agrebi, R., Espinosa, L., Baronian, G., Molle, V., Mauriello, E. M. F., Brochier-Armanet, C., & Mignot, T. (2015). Evolution and Design Governing Signal Precision and Amplification in a Bacterial Chemosensory Pathway. *PLOS Genetics*, *11*(8), e1005460. https://doi.org/10.1371/journal.pgen.1005460

25. He, K., & Bauer, C. E. (2014). Chemosensory signaling systems that control bacterial survival. *Trends in Microbiology*, *22*(7), 389–398. https://doi.org/10.1016/j.tim.2014.04.004

26. Huang, Z., Pan, X., Xu, N., & Guo, M. (2019). Bacterial chemotaxis coupling protein: Structure, function and diversity. *Microbiological Research*, *219*, 40–48. https://doi.org/10.1016/j.micres.2018.11.001

27. Jazleena, P. J., Das, A., Guiseppi, A., Debard, F., Sharma, J., Yaikhomba, M., Mignot, T., Mauriello, E. M. F., & Gayathri, P. (2025). Di-HAMP domains of a cytoplasmic chemoreceptor modulate nucleoid array formation and downstream signaling. *mBio*, *16*(5), e00057-25. https://doi.org/10.1128/mbio.00057-25

28. Karatan, E., Saulmon, M. M., Bunn, M. W., & Ordal, G. W. (2001). Phosphorylation of the Response Regulator CheV Is Required for Adaptation to Attractants during Bacillus subtilisChemotaxis *. *Journal of Biological Chemistry*, *276*(47), 43618–43626. https://doi.org/10.1074/jbc.M104955200

29. Karmakar, R. (2021). State of the art of bacterial chemotaxis. *Journal of Basic Microbiology*, *61*(5), 366–379. https://doi.org/10.1002/jobm.202000661

30. Keegstra, J. M., Carrara, F., & Stocker, R. (2022). The ecological roles of bacterial chemotaxis. *Nature Reviews Microbiology*, *20*(8), 491–504. https://doi.org/10.1038/s41579-022-00709-w

31. Lai, R.-Z., Gosink, K. K., & Parkinson, J. S. (2017). Signaling Consequences of Structural Lesions that Alter the Stability of Chemoreceptor Trimers of Dimers. *Journal of Molecular Biology*, *429*(6), 823–835. https://doi.org/10.1016/j.jmb.2017.02.007

32. Li, M., & Hazelbauer, G. L. (2014). Selective allosteric coupling in core chemotaxis signaling complexes. *Proceedings of the National Academy of Sciences*, *111*(45), 15940–15945. https://doi.org/10.1073/pnas.1415184111

33. Li, X., Fleetwood, A. D., Bayas, C., Bilwes, A. M., Ortega, D. R., Falke, J. J., Zhulin, I. B., & Crane, B. R. (2013). The 3.2 Å Resolution Structure of a Receptor:CheA:CheW Signaling Complex Defines Overlapping Binding Sites and Key Residue Interactions within Bacterial Chemosensory Arrays. *Biochemistry*, *52*(22), 3852–3865. https://doi.org/10.1021/bi400383e

34. Li, Y., Hu, Y., Fu, W., Xia, B., & Jin, C. (2007). Solution structure of the bacterial chemotaxis adaptor protein CheW from *Escherichia coli*. *Biochemical and Biophysical Research Communications*, *360*(4), 863–867. https://doi.org/10.1016/j.bbrc.2007.06.146

35. Mauriello, E. M. F. (2020). How an unusual chemosensory system forms arrays on the bacterial nucleoid. *Biochemical Society Transactions*, *48*(2), 347–356. https://doi.org/10.1042/BST20180450

36. Mauriello, E. M. F., Jones, C., Moine, A., & Armitage, J. P. (2018). Cellular targeting and segregation of bacterial chemosensory systems. *FEMS Microbiology Reviews*, *42*(4), 462–476. https://doi.org/10.1093/femsre/fuy015

37. Moine, A., Agrebi, R., Espinosa, L., Kirby, J. R., Zusman, D. R., Mignot, T., & Mauriello, E. M. F. (2014). Functional Organization of a Multimodular Bacterial Chemosensory Apparatus. *PLOS Genetics*, *10*(3), e1004164. https://doi.org/10.1371/journal.pgen.1004164

38. Moine, A., Espinosa, L., Martineau, E., Yaikhomba, M., Jazleena, P. J., Byrne, D., Biondi, E. G., Notomista, E., Brilli, M., Molle, V., Gayathri, P., Mignot, T., & Mauriello, E. M. F. (2017). The nucleoid as a scaffold for the assembly of bacterial signaling complexes. *PLOS Genetics*, *13*(11), e1007103. https://doi.org/10.1371/journal.pgen.1007103

39. Natale, A. M., Duplantis, J. L., Piasta, K. N., & Falke, J. J. (2013). Structure, Function, and On–Off Switching of a Core Unit Contact between CheA Kinase and CheW Adaptor Protein in the Bacterial Chemosensory Array: A Disulfide Mapping and Mutagenesis Study. *Biochemistry*, *52*(44), 7753–7765. https://doi.org/10.1021/bi401159k

40. Park, S.-Y., Borbat, P. P., Gonzalez-Bonet, G., Bhatnagar, J., Pollard, A. M., Freed, J. H., Bilwes, A. M., & Crane, B. R. (2006). Reconstruction of the chemotaxis receptor–kinase assembly. *Nature Structural & Molecular Biology*, *13*(5), 400–407. https://doi.org/10.1038/nsmb1085

41. Piñas, G. E., DeSantis, M. D., Cassidy, C. K., & Parkinson, J. S. (2022). Hexameric rings of the scaffolding protein CheW enhance response sensitivity and cooperativity in Escherichia coli chemoreceptor arrays. *Science Signaling*, *15*(718), eabj1737. https://doi.org/10.1126/scisignal.abj1737

42. Piñas, G. E., Frank, V., Vaknin, A., & Parkinson, J. S. (2016). The source of high signal cooperativity in bacterial chemosensory arrays. *Proceedings of the National Academy of Sciences*, *113*(12), 3335–3340. https://doi.org/10.1073/pnas.1600216113

43. Porter, S. L., Wadhams, G. H., & Armitage, J. P. (2008). *Rhodobacter sphaeroides*: Complexity in chemotactic signalling. *Trends in Microbiology*, *16*(6), 251–260. https://doi.org/10.1016/j.tim.2008.02.006

44. Porter, S. L., Wadhams, G. H., & Armitage, J. P. (2011). Signal processing in complex chemotaxis pathways. *Nature Reviews Microbiology*, *9*(3), 153–165. https://doi.org/10.1038/nrmicro2505

45. Shaw, A. S., & Filbert, E. L. (2009). Scaffold proteins and immune-cell signalling. *Nature Reviews Immunology*, *9*(1), 47–56. https://doi.org/10.1038/nri2473

46. van den Ent, F., & Löwe, J. (2006). RF cloning: A restriction-free method for inserting target genes into plasmids. *Journal of Biochemical and Biophysical Methods*, *67*(1), 67–74. https://doi.org/10.1016/j.jbbm.2005.12.008

47. Wadhams, G. H., & Armitage, J. P. (2004). Making sense of it all: Bacterial chemotaxis. *Nature Reviews Molecular Cell Biology*, *5*(12), Article 12. https://doi.org/10.1038/nrm1524

48. Waterhouse, A. M., Procter, J. B., Martin, D. M. A., Clamp, M., & Barton, G. J. (2009). Jalview Version 2—A multiple sequence alignment editor and analysis workbench. *Bioinformatics*, *25*(9), 1189–1191. https://doi.org/10.1093/bioinformatics/btp033

49. Wuichet, K., Alexander, R. P., & Zhulin, I. B. (2007). Comparative Genomic and Protein Sequence Analyses of a Complex System Controlling Bacterial Chemotaxis. In *Methods in Enzymology* (Vol. 422, pp. 3–31). Elsevier. https://doi.org/10.1016/S0076-6879(06)22001-9

50. Wuichet, K., & Zhulin, I. B. (2010). Origins and Diversification of a Complex Signal Transduction System in Prokaryotes. *Science Signaling*, *3*(128), ra50–ra50. https://doi.org/10.1126/scisignal.2000724

51. Yang, W., Alvarado, A., Glatter, T., Ringgaard, S., & Briegel, A. (2018). Baseplate variability of Vibrio cholerae chemoreceptor arrays. *Proceedings of the National Academy of Sciences*, *115*(52), 13365–13370. https://doi.org/10.1073/pnas.1811931115

52. Yang, W., & Briegel, A. (2020). Diversity of Bacterial Chemosensory Arrays. *Trends in Microbiology*, *28*(1), 68–80. https://doi.org/10.1016/j.tim.2019.08.002

53. Zhang, X., Jiang, L., Weng, G., Shen, C., Zhang, O., Liu, M., Zhang, C., Gu, S., Wang, J., Wang, X., Du, H., Zhang, H., Zhang, K., Wang, E., & Hou, T. (2025). HawkDock version 2: An updated web server to predict and analyze the structures of protein–protein complexes. *Nucleic Acids Research*, *53*(W1), W306–W315. https://doi.org/10.1093/nar/gkaf379

Chapter 5

Structure of receptor-adaptor complex suggests presence of an asymmetric interface at the signalling tip

5.1 Introduction

Chemosensory signalling in motile bacteria biases motility modules in response to environmental cues, facilitating the exploration of favourable environments *(Hazelbauer, 2012; Wadhams & Armitage, 2004)*. The signalling mechanism is conserved throughout bacterial and archaeal kingdoms *(Gumerov et al., 2021; Wuichet & Zhulin, 2010)*. The receptor called MCP (methyl-accepting chemotaxis protein), in complex with adaptor protein and histidine kinase, forms the core signalling unit (CSU) *(M. Li & Hazelbauer, 2011)*. MCPs orient perpendicularly to the inner membrane with sensing domains in the periplasm, while their cytoplasmic ends associate with CheA/CheW proteins, forming a dense layer parallel to the membrane *(Zhang et al., 2007)*. The core signalling units are composed of two trimer-of-dimers connected by the adaptor protein CheW and the dimeric histidine kinase CheA, maintaining a stoichiometry of 6 receptor dimers to 2 CheW molecules and a dimeric CheA molecule (**Figure 5.1A, B**) *(M. Li & Hazelbauer, 2011; Erbse & Falke, 2009; M. Li & Hazelbauer, 2004)*. The CSUs are arranged as hexagonal arrays, which are conserved in bacteria and archaea for membrane-bound and cytoplasmic chemosensory arrays *(Briegel et al., 2015; Briegel, Ladinsky, et al., 2014; Briegel et al., 2009)*. The architecture and diversity of chemosensory arrays are elaborated in detail in Chapter 1.

A canonical MCP has a transmembrane (TM) domain that is continuous with a periplasmic ligand-binding domain and a cytoplasmic HAMP domain, which acts as an input-output coupling module for cytoplasmic coiled-coil methyl-accepting signalling domain *(Bi & Lai, 2014; Aravind & Ponting, 1999)*. The input-output coupling domain is referred to as HAMP due to its presence in histidine kinase, adenylyl cyclase, MCP, and phosphatase domains *(Aravind & Ponting, 1999)*. A 'Gearbox model' was initially proposed as a mechanism of signal transduction by HAMP domain, where helices rotate by ±26° changing the packing of the helices from a canonical *'knobs into holes'* packing to an *x-da* packing and vice versa (**Figure 5.1C**) *(Hulko et al., 2006)*. Subsequently, alternate HAMP conformations were observed in the crystal structure of the poly-HAMP domain of the Aer2 receptor from *P. aeruginosa (Airola et al., 2010)*. This poly-HAMP unit features a helical insert separating HAMP 1 and HAMP 2, while HAMP 2 and HAMP 3 share a continuous helix, forming a concatenated di-HAMP. Notably, HAMP 1 and HAMP 3 adopt similar conformations, whereas HAMP 2 displays a distinct conformation (**Figure 5.1D**) *(Airola et al., 2010)*. The two different HAMP conformers mediate alternate signalling in the MCPs *(Airola et al., 2013)*. HAMP domain in *E. coli*

histidine kinase NarQ, upon ligand binding, undergoes lever-like motions and converts the piston-like motions from TM helices into downstream helical rotations *(Gushchin et al., 2017)*. Recently, Alphafold2 has been used to capture conformational variability of the HAMP domain, which includes rotations, shifts, displacements, and tilts of helices *(Winski et al., 2023)*. Crystal structure of cytoplasmic MA region of MCP from *T. maritima* in complex with CheW and CheA kinase regulatory (P4-P5) module highlights that CheA-P5 and CheW interact through a conserved hydrophobic interface to form pseudo 6-fold symmetric rings *(X. Li et al., 2013; Briegel et al., 2012)*. However, the mechanism by which the HAMP domain mediates structural changes in the cytoplasmic coiled-coil MA domain has not been captured.

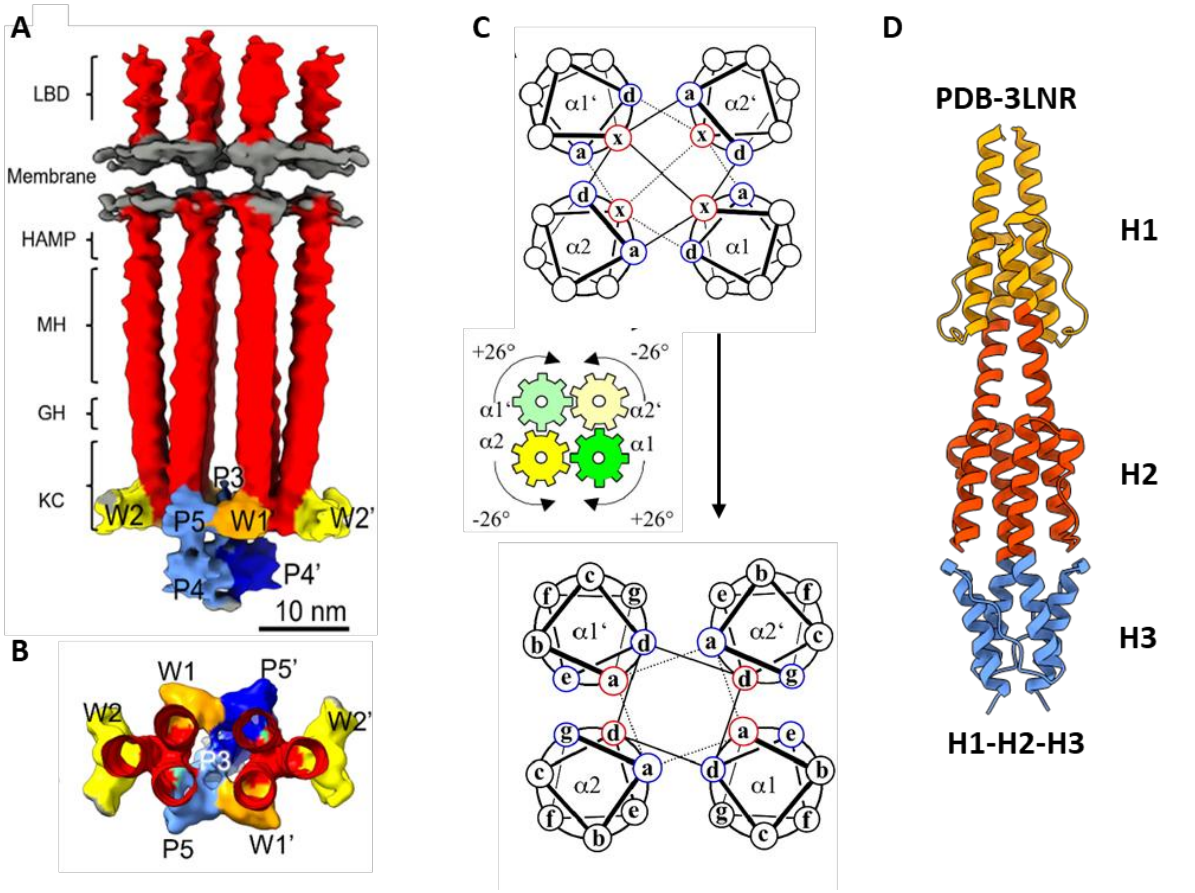


Figure 5.1 Core signalling unit of chemosensory array and regulation of signal transduction by HAMP domain in MCPs. (A) CryoET sub-tomogram averaging of CSU of native chemosensory arrays from lysed *E. coli* cells at an overall resolution of 12 Å *(adapted from Cassidy et al., 2023)*. MCP dimer is red, CheA dimer is light/dark blue, and CheW is yellow/orange. The P3-dimerisation, P4-ATPase, and P5-CheW homolog domains of CheA are labelled. Regions of MCP are labelled: LBD- ligand binding domain, HAMP domain, MH-Methylation helix, GH- glycine hinge and KC- kinase control region. (B) A top view of the CSU, from the glycine hinge to the baseplate, is shown. (C) Schematic representation of HAMP conformations in complementary x-da packing (top) versus knobs-into-holes packing (bottom). The two conformations are interconvertible by ±26° rotation of helices *(adapted from Hulko et al., 2006)*. (D) Tri-HAMP region of Aer2 receptor from *P. aeruginosa*, where H1 and H3 are in similar conformations, while H2 adopt a different conformation, PDB: 3LNR *(Airola et al., 2010)*.

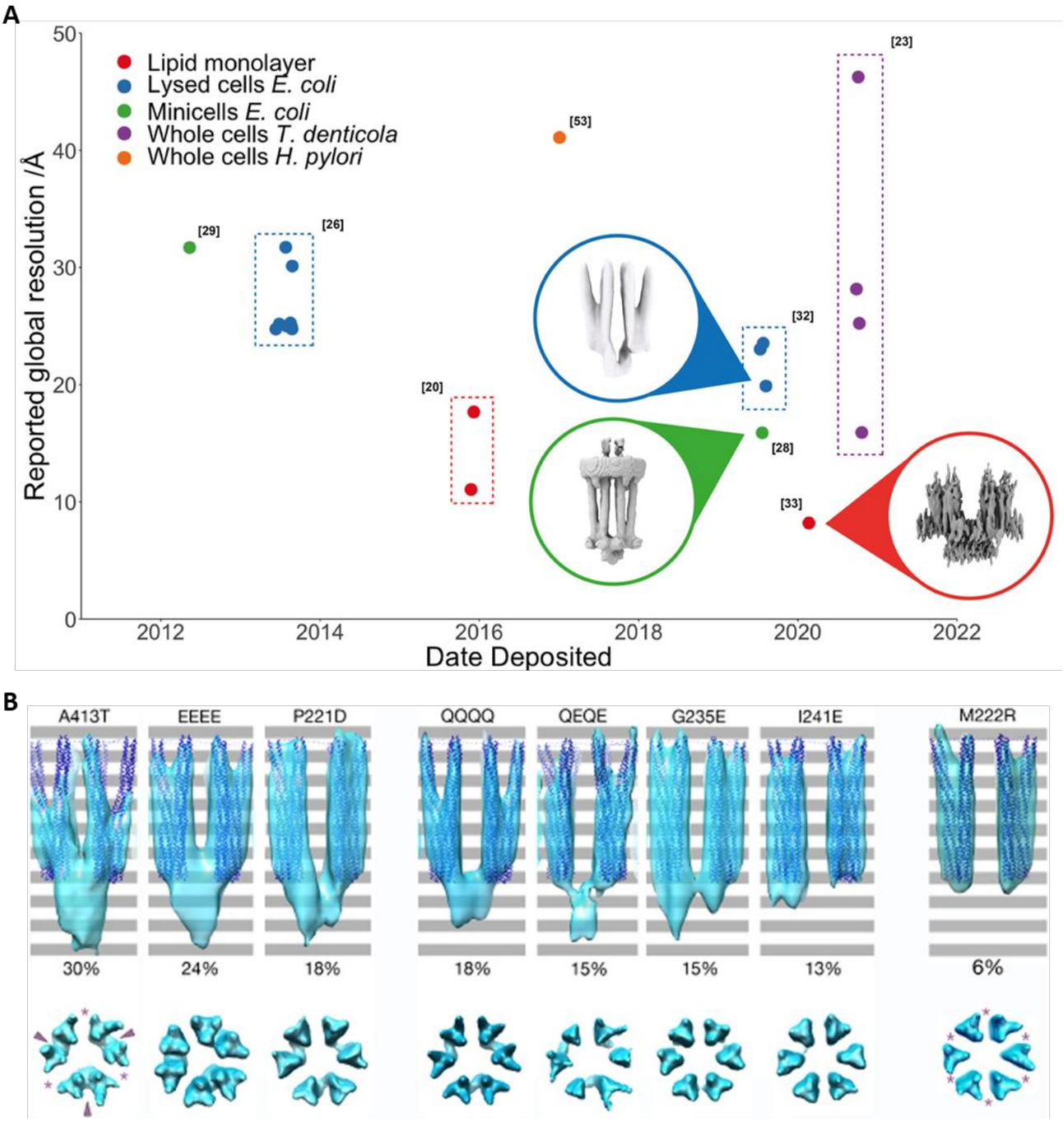


Figure 5.2 Cryo-electron tomography studies of chemosensory arrays. (A) Plot showing reported global resolution Cryo-ET maps of chemosensory arrays using different strategies (lipid monolayer, lysed cells, minicells and native cells) *(Adapted from Riechmann & Zhang, 2023)*. Publications in the figure are as follows: [20] Cassidy et al., 2015, [23] Muok, Ortega, et al., 2020, [26] Briegel et al., 2013, [28] Burt et al., 2020, [29] Liu et al., 2012, [32] Yang et al., 2019, [33] Cassidy et al., 2020, and [53] Qin et al., 2017. (B) CSU of *E. coli* Tsr receptor harbouring different substitutions shows varied 'keel' electron density. The QEQE receptor represents the wild-type, while the EEEE and QQQQ variants mimic fully unmethylated or methylated forms of the receptor *(adapted from Briegel et al., 2013)*.

Cryo-electron tomography has been widely used to study bacterial chemosensory macromolecular complexes **(Figure 5.2A)** *(Riechmann & Zhang, 2023; Hadjidemetriou et al.,*

2022; Qin & Zhang, 2021). *In vitro* systems with reconstituted complexes on lipid nanodiscs and 2D lipid monolayers, along with *in vivo* studies of lysed cells, minicells, and native bacteria, have elucidated their architecture *(Hadjidemetriou et al., 2022; Qin & Zhang, 2021)*. These, combined with crystal structures and molecular modelling, revealed a conserved array architecture, identified the core signalling unit, and explained how these arrays amplify and integrate signals. Studies have been carried out with receptors harbouring different combinations of 'Q' and 'E' residues at the methylation sites to understand different signalling architecture of CSUs. Chemosensory array was reconstituted on lipid monolayer with receptors harbouring combinations of 'Q' and 'E' residues at the methylation sites, suggesting that stability of CSUs varied from highest with 'QQQQ' substitution (kinase-ON) to lowest with 'EEEE' substitution (kinase-OFF) of methylation sites (Cassidy et al., 2015, 2020). *In vivo* studies suggested that the array remained ordered in different signalling states *(Briegel et al., 2013)*. Additionally, a 'keel' density was observed in CSU, which varied across different signalling states and was more mobile for kinase-ON states (**Figure 5.2B**) *(Muok, Briegel, et al., 2020; Briegel et al., 2013)*. CSU from kinase-OFF (EEEE substitution) and kinase-ON (QQQQ substitution) of Tsr receptor from lysed *E. coli* cells showed a transition from a compact conformation in kinase-OFF to an expanded conformation in kinase-ON density using molecular dynamics flexible fitting *(Yang et al., 2019)*. These studies highlighted possible changes in CSU of chemosensory arrays that regulates downstream signalling. However, due to the limited resolution in tomographic studies **(Figure 5.2A)**, the mechanisms involved in signal detection that regulate kinase activity, methylation adaptation of receptors, and their implications, as well as cooperative signal amplification within chemosensory arrays, are not yet fully understood.

Since the Frz chemosensory pathway forms a soluble cytoplasmic chemosensory cluster, structural studies of *in vitro* reconstituted core signalling units may serve as a model to understand signal transduction mechanisms in chemosensory complexes. Here, we reconstituted receptor-adaptor complex (FrzCD-FrzA) and used single-particle CryoEM to understand its architecture. Our structural data on the complex confirmed the presence of N-terminal di-HAMP domains, which is continuous with the MA domain. HAMP1 domain of di-HAMP exhibits high flexibility, likely due to the presence of a helical linker between HAMP1 and HAMP2. The receptor has a curvature induced by the glycine hinge, which creates an asymmetric interface at the signalling tip. We observed that FrzA binding is biased in occupying

the concave interface, as indicated by a more pronounced density of FrzA at this site. FrzA showed a rotational shift along the FrzCD longitudinal axis in the absence of HAMP2 domain.

Based on our observations, we propose a model in which asymmetry at the signalling tip of dimeric FrzCD, induced by curvature, may result in a preferred binding interface for FrzA at the concave side. The convex interface might support binding of histidine kinase FrzE in cytoplasm or support oligomerization on nucleoid to form clusters. This is the first structural report of a chemoreceptor with HAMP and MA domains in complex with an adaptor protein, at a resolution of 6.13 Å. The structure provided new insights into the possible role of the curvature of a dimeric receptor, due to the glycine hinge, in creating an asymmetric interface for the binding of an adaptor, histidine kinase or support oligomerization. The study highlights that soluble FrzCD-FrzA complex may serve as a promising first step towards reconstituting a cytoplasmic chemosensory complex to understand the mechanism of signal transduction in chemosensory clusters.

5.2 Materials and Methods

5.2.1 CryoEM Sample Preparation and Data Acquisition

FrzCD-FrzA samples were diluted to 1 mg/mL in a final buffer composition of 50 mM HEPES (pH 7.5), 50 mM NaCl, and applied to Quantifoil Cu 300 R1.2/1.3 grids. DNA fragments (14-bp, 25-bp, and higher) were tested as scaffolds for the FrzCD-FrzA complex at a final concentration of 50 μM. They were individually mixed with the complex (diluted at 1 mg/mL) and incubated on ice. Samples were also prepared at a concentration of 5 mg/ml in the presence of 8 mM CHAPSO (added just before plunge freezing). Grids were glow-discharged in a PELCO easiGLOW glow discharge unit equipped with an oil pump (TED PELLA Inc., USA) using the following conditions: 25 mA, 0.38 mBar, 1 min. Samples were frozen using a Vitrobot Mark IV at the following conditions: 3 second blot time, -5 blot force, and blotted once. Grids were screened on Talos Arctica, and data collection was performed on Talos Arctica and Titan Krios in the Department of Biochemistry, University of Cambridge, with the parameters listed in **Table 5.1**. Short DNA fragments used as scaffolds are: E3 (14-bp): 5'-CGGTAATTACATGG-3' and A (25-bp): 5'-CCAGGGTATGCAAATTATTAAGGGC-3'.

FrzCD$^{\Delta DB}$-FrzA were diluted to 1 mg/mL in a final buffer composition of 50 mM HEPES (pH 7.5), 50 mM NaCl, and applied to Quantifoil Cu 300 R1.2/1.3 grids. Grids were glow-discharged and frozen on grids as described above. Grids were screened on Talos Arctica, and data collection was performed on Talos Arctica and Titan Krios in the Department of Biochemistry, University of Cambridge, with the parameters listed in **Table 5.1**.

FrzCD$^{\Delta DBH2}$-FrzA samples were diluted to 1 mg/mL at a final buffer composition of 50 mM HEPES (pH 7.5), 50 mM NaCl and applied on Quantifoil Cu 300 1.2/1.3 grids. Glow discharge was performed in Quorum GLOQUBEplus using the following conditions: 20 mA, 45 sec for negative surface, and 20 mA, 120 sec for positive surface. Samples were frozen using a Vitrobot Mark IV under the following conditions: 2.5 second blot time, 4 blot force, and blotted once. Grids were screened, and data were collected on a Glacios 2 in the Cryo TEM Pune BioCluster facility. Data were automatically collected using EPU software (Thermo Fisher) with parameters given in **Table 5.1**.

Table 5.1 CryoEM samples and data collection parameters.

Sample	$FrzCD^{\Delta DB}$-FrzA (CHAPSO)	FrzCD-FrzA (CHAPSO)	$FrzCD^{\Delta DB}$-FrzA	$FrzCD^{\Delta DBH2}$-FrzA
Microscope	Talos Arctica	Talos Arctica	Titan Krios	Glacios 2
Detector and mode	Falcon 3 linear	Falcon 3 linear	Falcon 4i counting	Falcon 4i fast
Magnification	73,000x	73,000x	165,000x	165,000x
Pixel Size, Å/pixel	1.37	1.37	0.729	0.71
Voltage (kV)	200	200	300	200
Flux on detector (e^-/pix/sec)	67.35	92.23	6.1	6.41
Total Dose, $e^-/Å^2$	55.94	45.33	50.39	30
Defocus Range (µM)	-3.3, -3.0, -2.7, -2.4, -2.1, -1.8	-3.3, -3.0, -2.7, -2.4, -2.1, -1.8	-1.8, -1.6, -1.4, -1.2, -1.0, -0.8, -0.6	-0.6, -0.8, -1.0, -1.2, -1.4, -1.8, -2.2

5.2.2 CryoEM data processing and modelling

Datasets were processed in CryoSPARC v4.7 *(Punjani et al., 2017)*. Patch motion correction and patch CTF correction were performed on $FrzCD^{\Delta DB}$-FrzA micrographs, followed by manual curation of micrographs after a CTF fit cutoff of 5 Å was applied. Denoised micrographs were used for blob picker, followed by 2D classification of extracted particles. Selected 2D classes were used to generate templates for subsequent particle picking. Multiple rounds of template-based particle picking were carried out. Next, several rounds of 2D classification were performed on the extracted particles, where junk particles were separated in each round of 2D classification. Ab-initio models were generated for good 2D classes as well as junk classes. Heterogeneous refinement was carried out between the generated models followed by refinement steps. Detailed steps of the workflow are illustrated in **Figure 5.4**.

$FrzCD^{\Delta DBH2}$-FrzA dataset, collected in .eer format movies, was divided into 60 fractions (0.5 e^-/frame). Micrographs were processed using the steps outlined above. A detailed workflow is illustrated in **Figure 5.5**.

AlphaFold3 *(Abramson et al., 2024; Jumper et al., 2021)* generated models **(Figure 5.3)** were used to fit in the electron density using iMODFIT at a resolution of 8 Å *(Lopéz-Blanco & Chacón, 2013)*. Visualization of maps, models, and figures was made using Chimera and ChimeraX *(Meng et al., 2023; Pettersen et al., 2004)*. Both the AlphaFold3-generated model and the flexible-fitted iMODFIT model were superimposed and individually fitted into the CryoEM density map to calculate the RMSD of individual chains and domains, as shown in **Figures 5.9 and 5.10**. The axes of the models were determined in ChimeraX using the entire structure (selected atoms/centroids and mass weighting) of the FrzCD$^{\Delta DB}$-FrzA AlphaFold3 predicted model. For the flexible, fitted model in the density, which has a curved structure, an axis was drawn by selecting atoms from HAMP1 to the glycine hinge. The angle between these two axes was calculated to quantify the bend in the flexible fitted model.

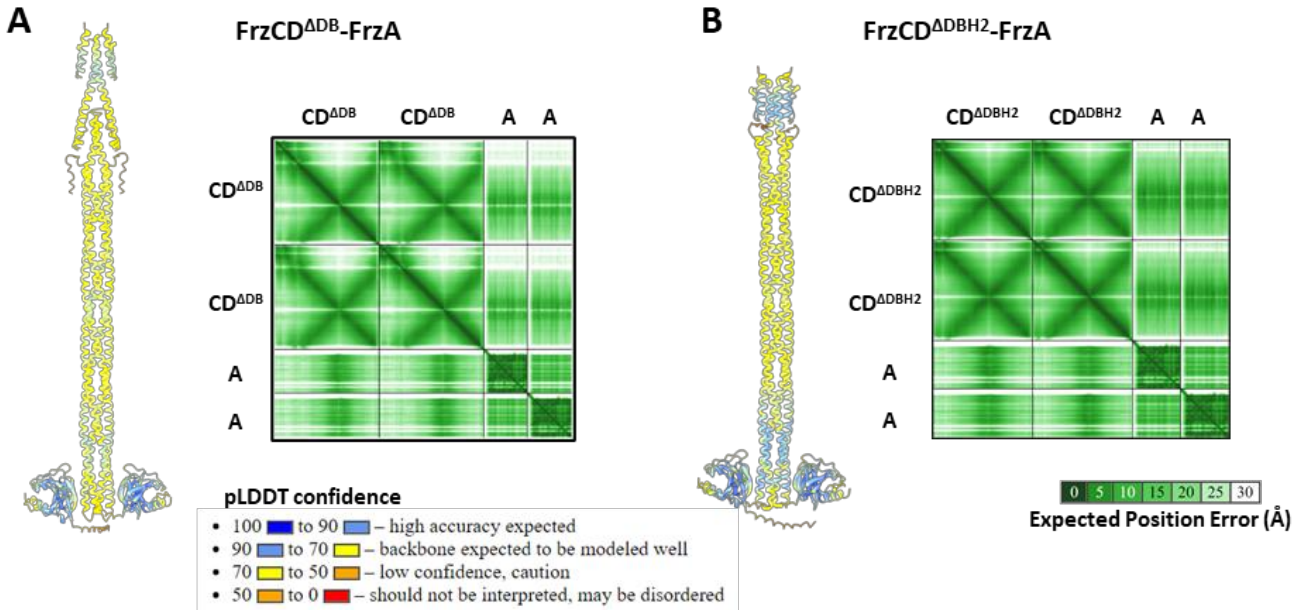
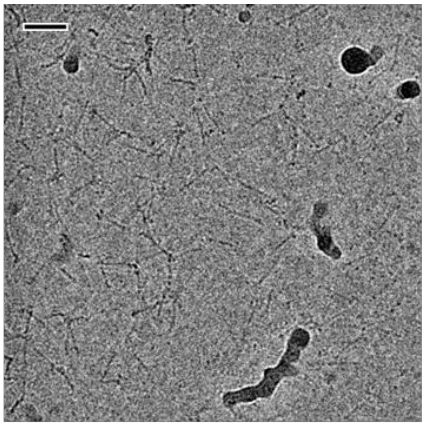


Figure 5.3 AlphaFold3 predicted models of: (A) FrzCD$^{\Delta DB}$-FrzA complex (ipTM = 0.6, pTM = 0.59), and (B) FrzCD$^{\Delta DBH2}$-FrzA complex (ipTM = 0.66, pTM = 0.65).



11,163 movies (.tiff format)

Patch Motion Correction
(saved result in 16-bit floating point)

Patch CTF estimation

Micrograph Junk Detector

Curate exposure (10,590 micrographs)
(Manual curation and CTF fit cutoff of 5 Å)

Micrograph Denoiser

↓

Blob picker
(Elliptical blob, Max. diameter 260 Å, Min. diameter 100 Å)

Inspect Picks

Micrograph Junk Detector

Extract Micrographs
(Box size 700 pix, Fourier crop to 350 pix)

2D classification
(Full iteration: 2, online-EM iterations: 40, Batchsize per class: 400)

Select 2D

Template Picker (Particle Diameter: 280 Å)

× 2

↓

Select 2D

Template Picker
(Particle Diameter: 280 Å,
Min. Separation Distance: 0.2 diameters)
(picked parallelly from CTF corrected as well as CTF corrected denoised micrographs)

↓

Inspect Picks
Micrograph Junk Detector
Extract Micrographs
(Box size 700 pix, Fourier crop to 350 pix)

2D classification
(Full iteration: 2, online-EM iterations: 40, Batchsize per class: 400)

Select 2D

Remove Duplicates
(791,647 particles)

2D classification
(Full iteration: 2, online-EM iterations: 40, Batchsize per class: 400)
Select 2D

× 2

252,207 particles | **487,303 junk particles**

Extract Micrographs
(Box size 700 pix, Fourier crop to 512 pix)

Extract Micrographs
(Box size 700 pix, Fourier crop to 512 pix)

Ab-Initio (245,758)
(**2 classes**, No. of initial iterations: 300, No. of final iterations: 500)

Ab-Initio
(4 Junk classes)

Hetero Refinement
(6 classes)

Best model (200,586 particles)

Ab-initio
(**2 classes**, No. of initial iterations: 300, No. of final iterations: 500, **Class similarity: 0**)

Hetero Refinement

Best model (145,432 particles)

NU- Refine, C1

Global CTF Refinement

NU-Refine, C1
(145,432 particles)

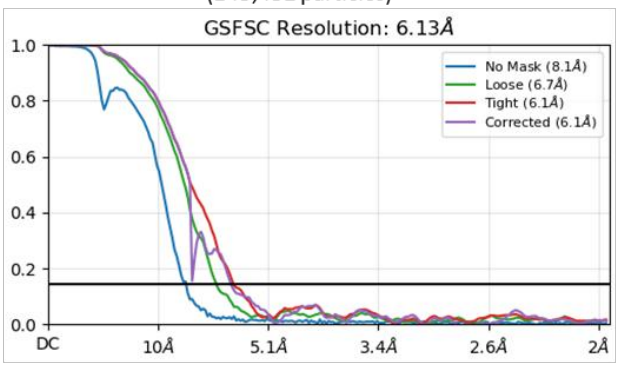
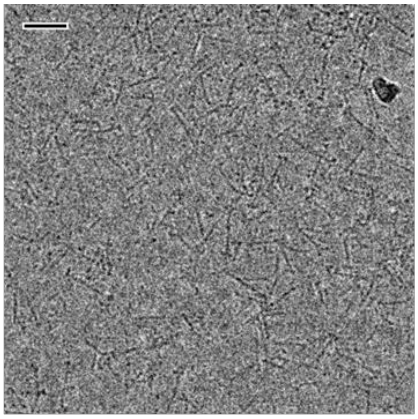


Figure 5.4 Workflow for processing of dataset of FrzCD$^{\Delta DB}$-FrzA complex in CryoSPARC. Scale bar 300 Å.



37,465 movies (.eer format)
(EER no. of fractions: 60, 0.5 e^-/frame,
EER Unsampling factor: 2)

Patch Motion Correction
(saved result in 16-bit floating point)

Patch CTF estimation
(36,316 exposures)

Micrograph Junk Detector

Curate exposure (28,246micrographs)
(Manual curation and CTF fit cutoff of 5 Å)

Micrograph Denoiser

Blob picker
(Elliptical blob, Max. diameter 260 Å, Min. diameter 100 Å)

Inspect Picks

Micrograph Junk Detector

Extract Micrographs
(Box size 1260 pix, Fourier crop to 630 pix)

2D classification
(Full iteration: 2, online-EM iterations: 40, Batchsize per class: 400)

Select 2D

Template Picker (Particle Diameter: 250 Å)

Select 2D

Template Picker
(Particle Diameter: 250 Å,
Min. Separation Distance: 0.2 diameters)
(picked parallelly from CTF corrected as well as CTF corrected denoised micrographs)

Inspect Picks
Micrograph Junk Detector
Extract Micrographs
(Box size 1296 pix, Fourier crop to 432 pix)

2D classification
(Full iteration: 2, online-EM iterations: 40, Batchsize per class: 400)

Select 2D

Remove Duplicates
(1,975,817 particles)

2D classification
(Full iteration: 2, online-EM iterations: 40, Batchsize per class: 400)
Select 2D
× 4

765,578 particles

652,085 junk particles

Extract Micrographs
(Box size 1260 pix, Fourier crop to 630 pix)

Extract Micrographs
(Box size 1260 pix, Fourier crop to 630 pix)

Ab-Initio (753,779 particles)
(**2 classes**, No. of initial iterations: 300, No. of final iterations: 500)

Ab-Initio
(6 Junk classes)

Hetero Refinement
(6 classes)

Best model (294,839 particles)

NU- Refine, C1

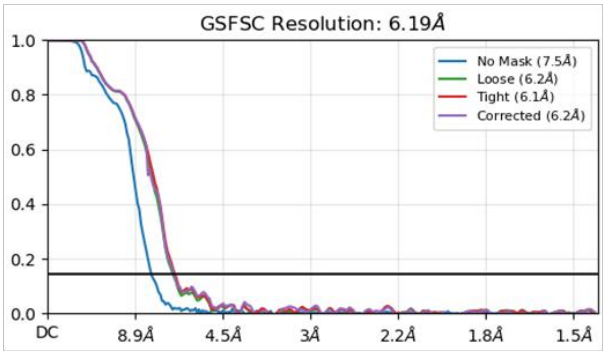


Figure 5.5 Workflow for processing of dataset of FrzCD$^{\Delta DBH2}$-FrzA complex in CryoSPARC. Scale bar 300 Å.

5.3 Results

5.3.1 CryoEM trials and observation

FrzCD has an N-terminal DNA binding domain followed by di-HAMP domains and C-terminal coiled-coil MA domain *(Jazleena, Das, Guiseppi et al., 2025)*. To determine the atomic structure of FrzCD and confirm the presence of di-HAMP domains, extensive crystallization trials were initially carried out for receptor FrzCD and FrzCD$^{\Delta MA}$ (containing DB and the di-HAMP domains) with different DNA fragments. Later crystallization trials were carried out of receptor-adaptor complexes (FrzCD$^{\Delta DBH1H2}$-FrzA, CD$^{\Delta DBH2}$-FrzA), where the crystals diffracted to a resolution of ~ 8 Å *(MS thesis, Tiyasa Bain (Bain, 2025))*.

Next, we used cryo-electron microscopy to understand the architecture of the complex. Molecules of FrzCD-FrzA complex were observed to be clumped during screening trials in presence and absence of CHAPSO (a zwitter-ionic detergent that broadens the particle orientation distributions *(Chen et al., 2019)*), making them suboptimal for single-particle cryoEM **(Figure 5.6A)**. Although purified FrzCD-FrzA comes bound with DNA fragments, it could still bind to additional free DNA fragments **(Chapter 4, Figure 4.4C)**. We attempted to optimize sample preparation in the presence of DNA fragments as a scaffold. We observed clumping of samples during screening **(Figure 5.6B).** This was probably due to sequence independent DNA binding property of FrzCD, which oligomerizes in presence of DNA, leading to a heterogeneous sample *(Jazleena, Das, Guiseppi et al., 2025)*. Subsequently, FrzCD$^{\Delta DB}$-FrzA complex (FrzCD without DNA binding domain) was used for CryoEM studies, which exhibited a more favourable particle distribution **(Figure 5.6C)**.

Since the di-HAMP domains modulate the downstream signalling of the Frz pathway *(Jazleena, Das, Guiseppi et al., 2025)*, we carried out CryoEM studies with a HAMP2-deleted construct of FrzCD in complex with FrzA (FrzCD$^{\Delta DBH2}$-FrzA) to understand the different signalling states of the receptor.

Interestingly, we observed atypical *in vitro* ‘star-like’ clusters and ‘triangle-like’ clusters for FrzCD$^{\Delta DB}$-FrzA and FrzCD-FrzA complexes, respectively, in presence of CHAPSO **(Figure 5.7)**. Such architecture is possibly mediated by interactions among FrzA **(Figure 5.7)**. However, the relevance of such architecture in chemotactic signalling remains to be explored.

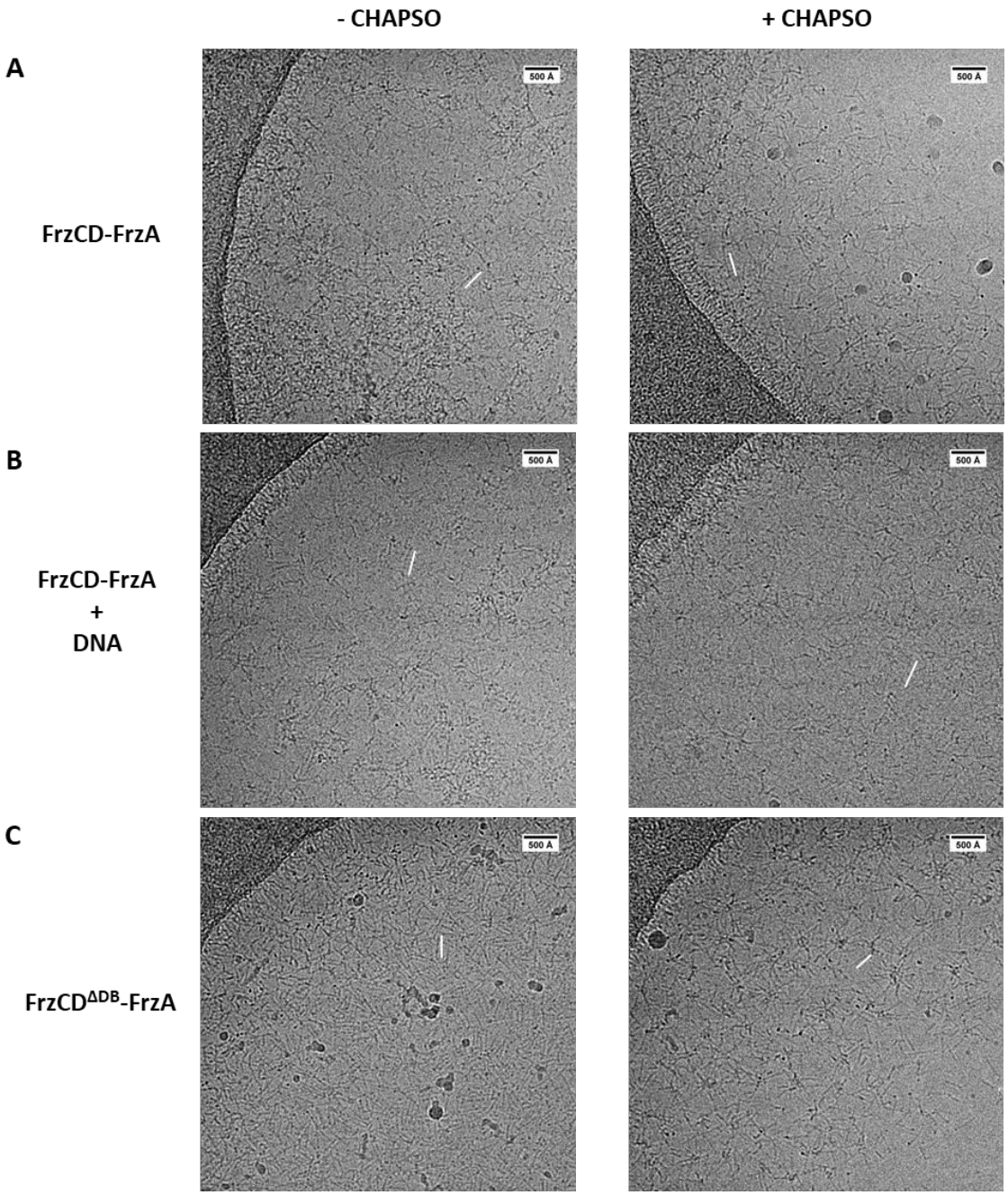


Figure 5.6 Representative CryoEM micrographs of receptor-adaptor complexes. (A) FrzCD-FrzA complex, (B) FrzCD-FrzA complex in presence of 25 bp DNA, and (C) FrzCD$^{\Delta DB}$-FrzA complex. Scale bar at top right corner: 300 Å. FrzCD particle is highlighted as white lines in the micrographs.

5.3.2 Structure of receptor-adaptor complexes

2D classes and electron density map of FrzCD$^{\Delta DB}$-FrzA confirm the presence of di-HAMP domains of dimeric-FrzCD is continuous to a C-terminal coiled-coil signalling domain. Two FrzA molecules interact with dimeric FrzCD at the signalling tip **(Figure 5.8A and 5.9)**. FrzCD$^{\Delta DBH2}$-FrzA density confirms a similar architecture but lacks the expected N-terminal

HAMP1 domain in the density **(Figure 5.8B)**. The structures of FrzCD$^{\Delta DB}$-FrzA and FrzCD$^{\Delta DBH2}$-FrzA complexes were solved to resolutions of 6.13 Å and 6.19 Å, respectively **(Figures 5.4, 5.5 and 5.8)**. Due to the resolution limitations of the CryoEM map to about 6 Å, we used a model generated from AlphaFold3 prediction of FrzCD$^{\Delta DB}$-FrzA complex to fit into the density. Although the predicted model has low ipTM (0.6) and pTM (0.59) scores **(Figure 5.3)**, it supports the experimental density map where FrzA molecules interact at the signalling tip of dimeric FrzCD **(Figure 5.8 and 5.9)**.

The structure of receptor FrzCD$^{\Delta DB}$ features an N-terminal HAMP1 domain, which is poorly resolved. The HAMP2 domain is continuous with the methylation helix, followed by the glycine hinge and kinase control region. Notably, we observed a curvature of the coiled-coil MA domain in both the FrzCD$^{\Delta DB}$-FrzA and FrzCD$^{\Delta DBH2}$-FrzA complexes **(Figure 5.8A and 5.9)**. Additionally, the electron density of the adaptor protein was more pronounced on the concave surface (FrzA) compared to the convex surface (FrzA') of FrzCD, with the blue triangle indicating the concave interface and the yellow triangle marking the convex interface in **Figures 5.8A, B and 5.11**.

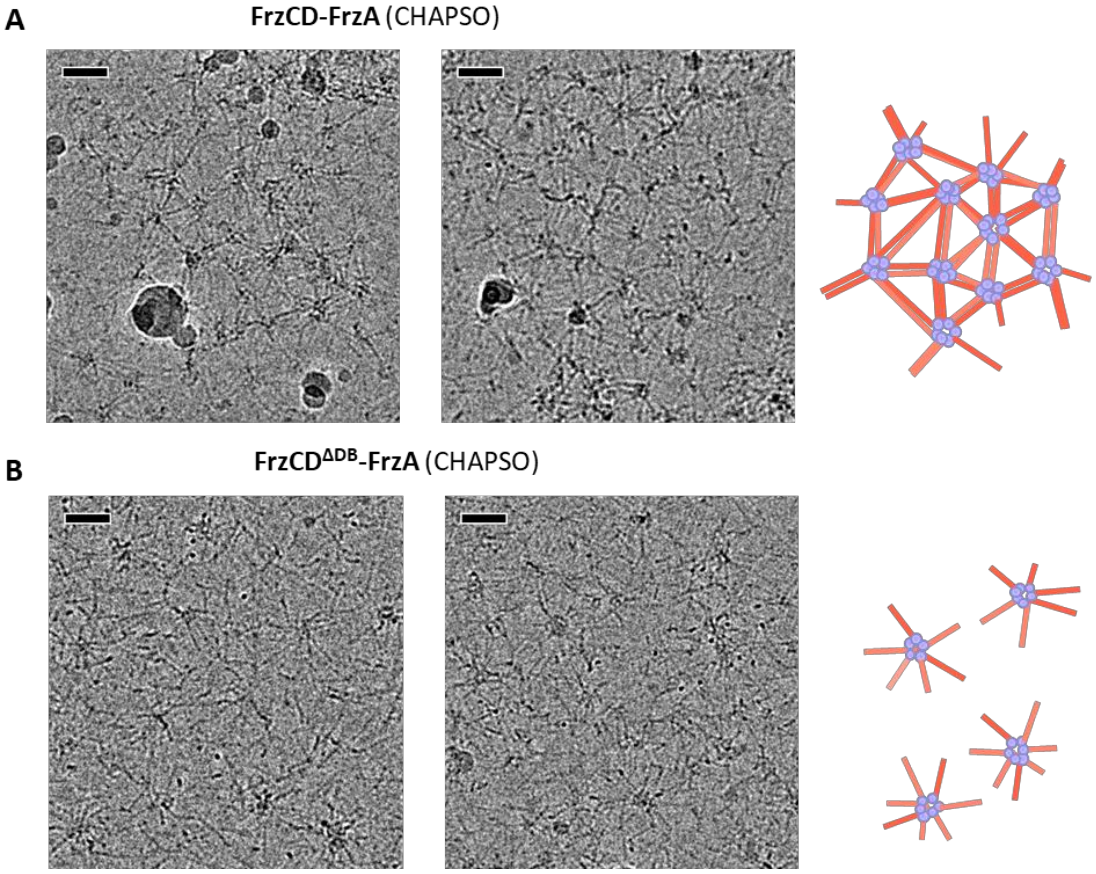


Figure 5.7 Atypical clusters observed for receptor-adaptor complex. (A) Triangle-like closed clusters of FrzCD-FrzA complex in presence of CHAPSO. (B) Atypical star-like cluster of FrzCD$^{\Delta DB}$-FrzA complex in presence of CHAPSO. Scale bar: 300 Å.

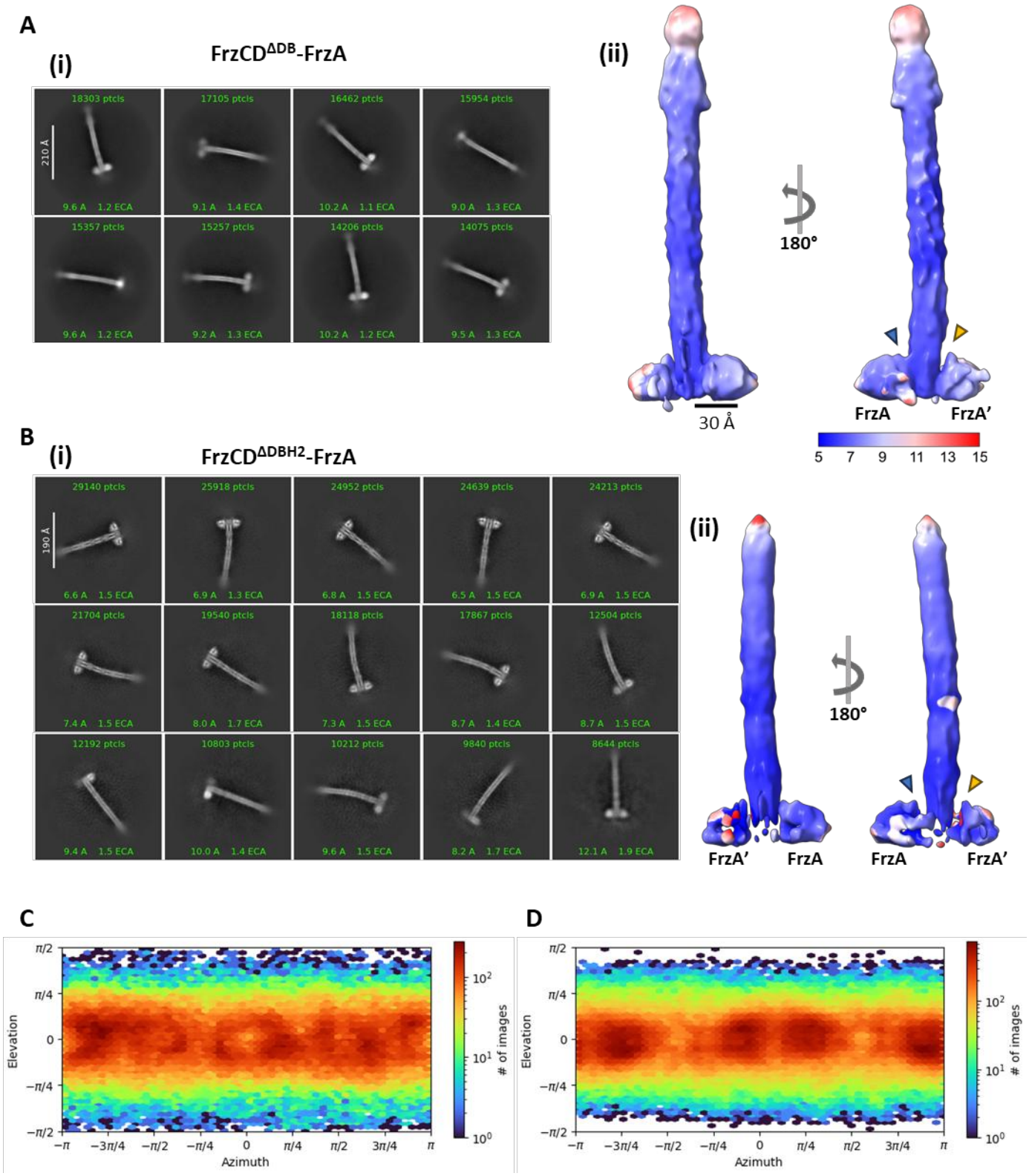


Figure 5.8 CryoEM density map of receptor-adaptor complex. (A) FrzCD$^{\Delta DB}$-FrzA (i) 2D classes, and (ii) CryoEM density map coloured according to local resolution estimation. (B) FrzCD$^{\Delta DBH2}$-FrzA (i) 2D classes, and (ii) electron density map coloured according to local resolution estimation. Blue triangle indicates the concave interface and the yellow triangle indicates the convex interface. Angular distribution plots of reconstructed maps of FrzCD$^{\Delta DB}$-FrzA (C) and FrzCD$^{\Delta DBH2}$-FrzA (D).

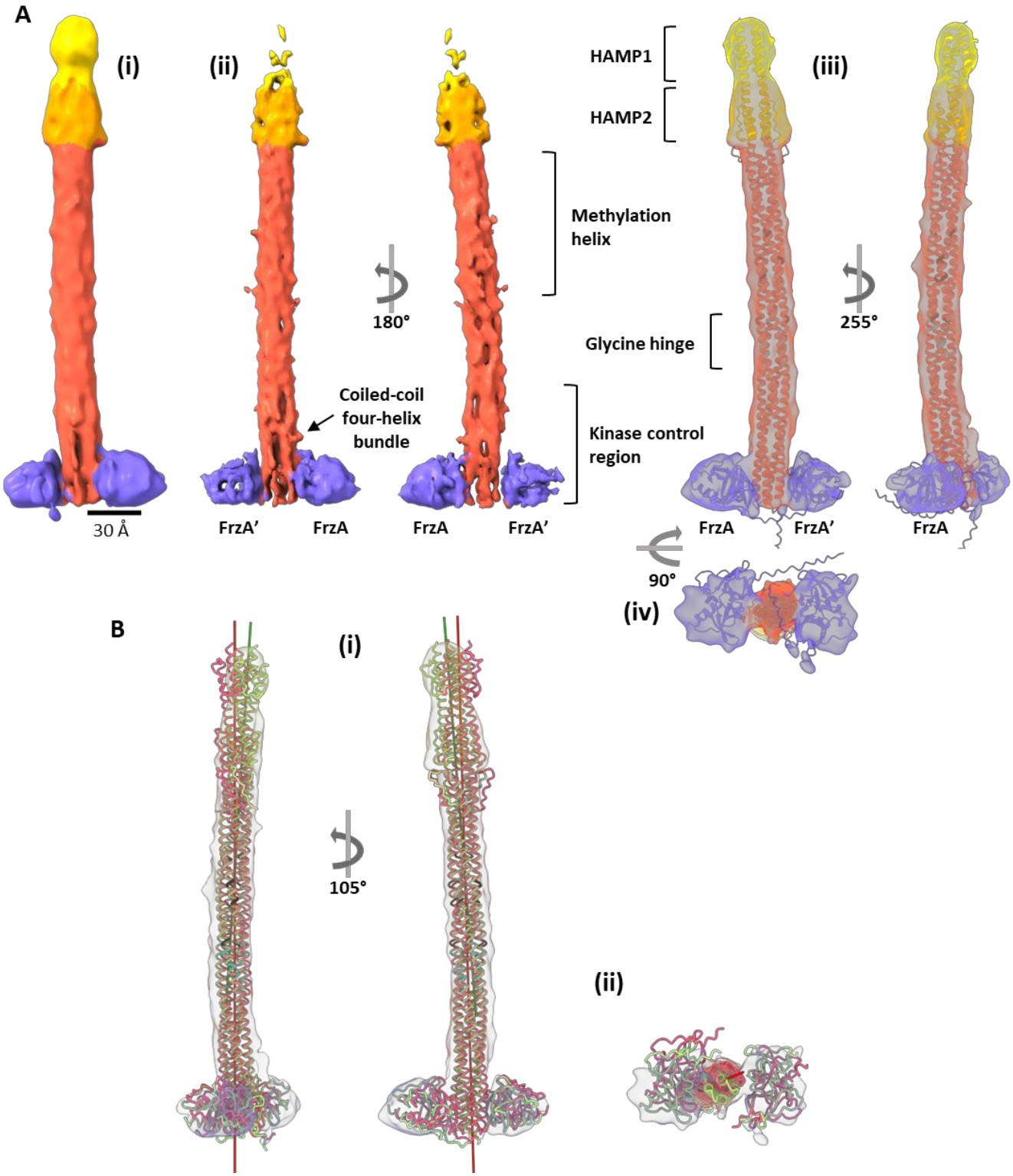


Figure 5.9 Structure of receptor-adaptor complex. (A) Domain architecture of FrzCD in the complex: (i) electron density map coloured according to different domains of FrzCD (HAMP1: yellow, HAMP2: orange, and MA: tomato) and FrzA (slate blue), (ii) sharp map highlighting the coiled-coil four-helix bundle and asymmetric FrzA density, (iii) AlphaFold3-generated model is fitted into the density using iMODFIT *(Lopéz-Blanco & Chacón, 2013)*, and (iv) view along longitudinal axis of FrzCD$^{\Delta DB}$-FrzA complex. (B) AlphaFold3-generated model (red) is fitted into the density using iMODFIT (green). Cyan marks glycine residues and black marks conserved aspartate and glutamate residues.

5.3.3 Glycine hinge contributes to a curved structure of the MCP coiled-coil domain

We observed a curvature in the dimeric FrzCD density, as opposed to a predicted straight two-fold symmetric model for the receptor-adaptor complex by AlphaFold3. We used iMODFIT *(Lopéz-Blanco & Chacón, 2013)* for flexible fitting of the AlphaFold3-generated receptor-adaptor complex model in the density **(Figure 5.9)**. To understand the changes to the AlphaFold predicted model, the AlphaFold3-generated model and the flexible-fitted iMODFIT-generated model were individually fitted into the observed density map in ChimeraX. Additionally, both models were superimposed, which revealed that the glycine hinge was responsible for the curvature of the dimeric FrzCD molecule and possibly a twist in the helices **(Figure 5.10A)**.

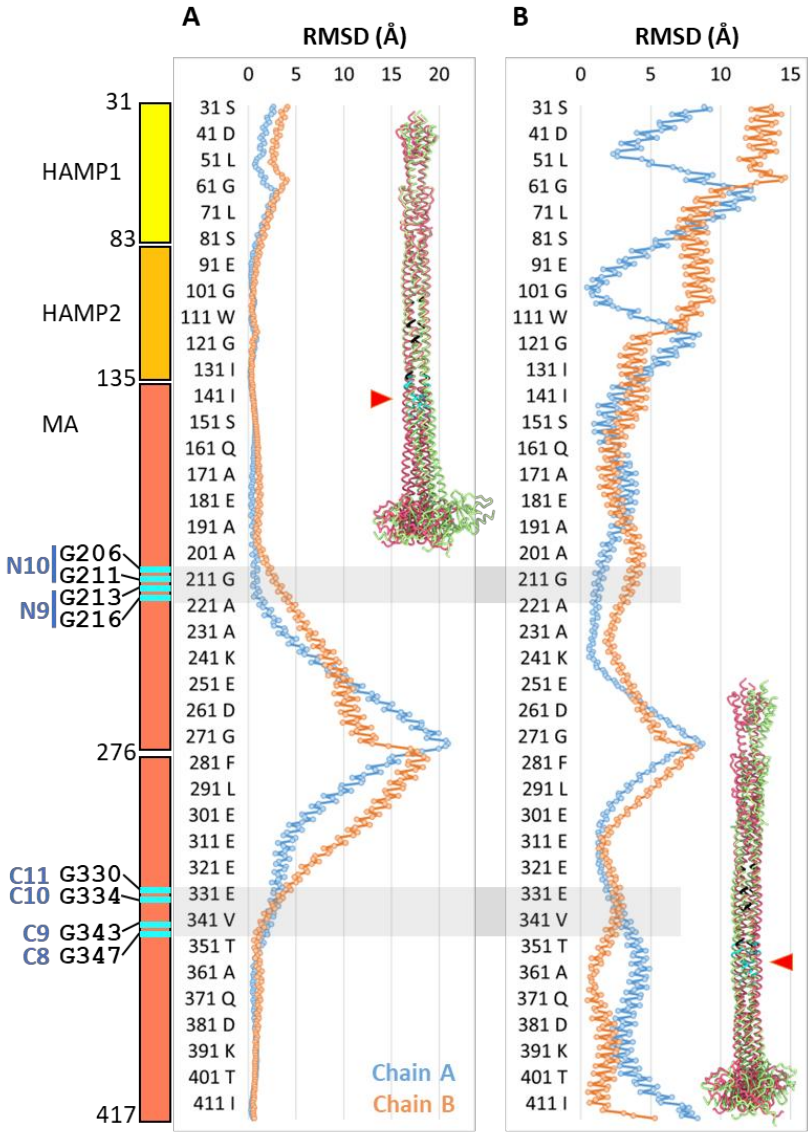


Figure 5.10 Glycine hinge contributes to the curvature of FrzCD. RMSD (Å) for each residue is plotted for individual chains of dimeric FrzCD – (A) superimposed AlphaFold3-generated model and flexible-fitted iMODFIT model, and (B) AlphaFold3-generated model and flexible-fitted iMODFIT models fitted into the CryoEM density map. Schematic

representation of domains of FrzCD on the left. Glycine residues in MA domain are highlighted in cyan and respective heptad number is labelled in blue. Models used to calculate RMSD are shown for respective plots, and a red triangle marks the glycine hinge in the structures. The AlphaFold3-generated model is coloured in red and flexible-fitted iMODFIT model is coloured green. Cyan marks glycine residues and black marks conserved aspartate and glutamate residues.

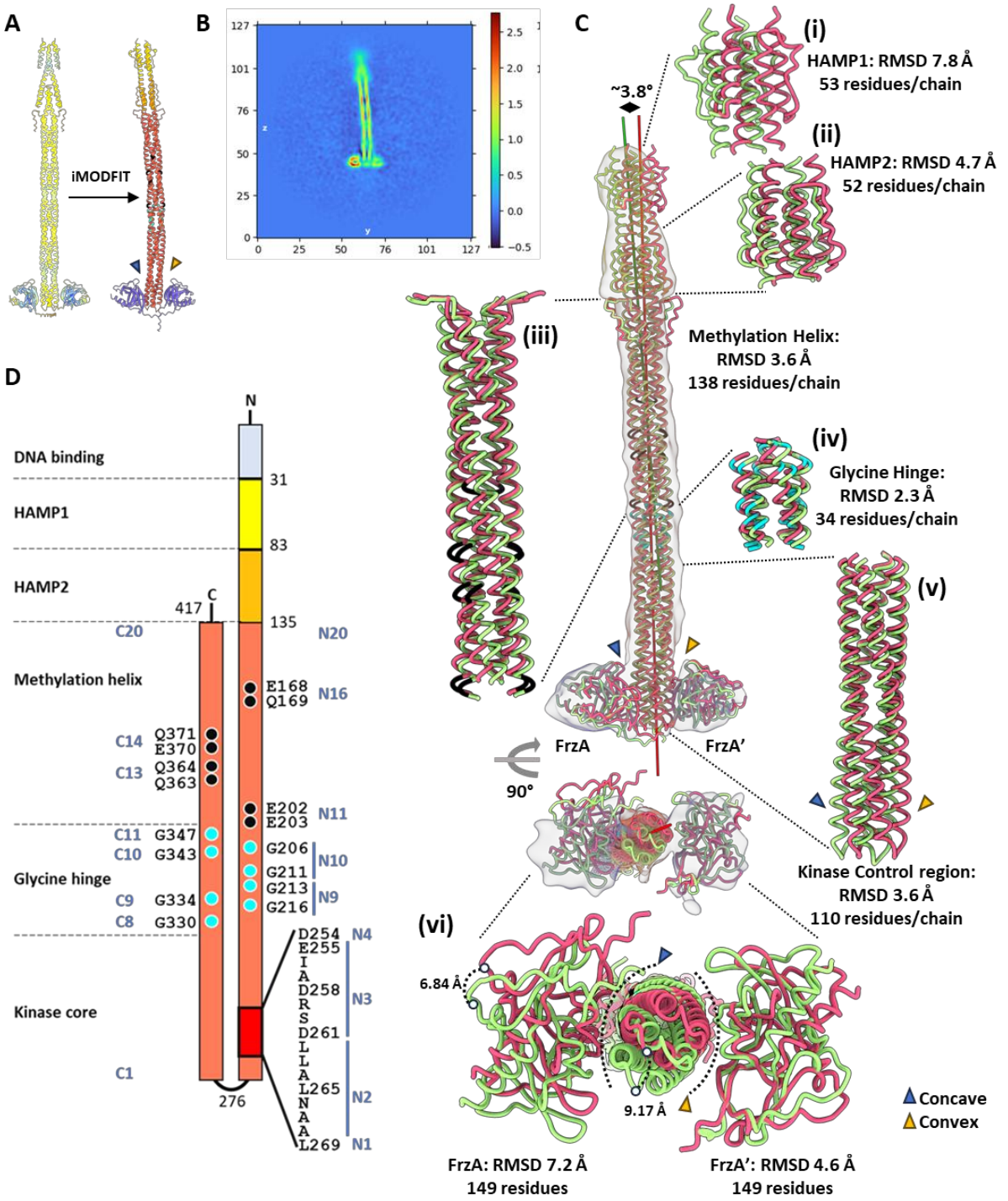


Figure 5.11 Curvature of FrzCD dimer. (A) AlphaFold3 generated model (coloured according to confidence, Figure 5.3A) and fitted model in the density (coloured according to domains, Figure 5.8C). (B) Real space slices from last round of Hetero refinement jobs of FrzCD$^{\Delta DB}$-FrzA (Figure 5.4). (C) RMSD between AlphaFold3 generated model and flexible fitted iMODFIT models fitted into the CryoEM density map for individual domains: (i)

HAMP1, (ii) HAMP2, (iii) methylation helix (calculated without C-terminal Strep tag, conserved aspartate and glutamate residues coloured in black), (iv) glycine hinge (glycine residues coloured in cyan), (v) kinase control region, and (vi) FrzA molecules (calculated from residue A9, without disorder N-terminal). The AlphaFold3-generated model is coloured in red and flexible-fitted iMODFIT model is coloured green. Asymmetric FrzCD-FrzA interface, concave by blue triangle and convex by yellow triangle, is marked as dotted line in (vi). (D) Schematic representation of domains of FrzCD. Aspartate and glutamate residues important for methylation-dependent adaptation is highlighted in black circles *(Astling et al., 2006)*. Glycine residues highlighted in cyan. Red square at the signalling tip corresponds to interface residues predicted by AlphaFold3. Heptads of coiled-coil region are labelled in blue.

Glycine residues (206, 211, 213 and 216 in the N-terminal arm, and 330, 334, 343 and 347 in the C-terminal arm) highlighted in **Figures 5.10 and 5.11C**, at the middle of the coiled-coil MA domain, act as a hinge for receptor FrzCD with an RMSD of 2.3 Å between the models. This facilitates an increased curvature of around 3.8° toward the N-terminal methylation helix (RMSD 3.6 Å), HAMP2 (RMSD 4.7 Å) and HAMP1 (RMSD 7.8 Å) **(Figure 5.11C)**. The hinge also induces a curvature in C-terminal kinase control region (RMSD 3.6 Å), where the glutamate residue (E276) at the signalling tip is shifted by 9.7 Å between the two structures, resulting in a curved concave interface for FrzA and a convex interface for FrzA' **(Figure 5.11C)**. FrzA at the concave interface shows a deviation of 7.2 Å (a shift by 6.8 Å is observed for Asp 122 of subdomain 1) while FrzA' shows a deviation of 4.6 Å **(Figure 511C.vi)**. Currently, due to resolution limitations, interactions contributing to the asymmetry of the FrzCD-FrzA interface are not identified. We believe that the concave interface may provide a more stable receptor adaptor interface, resulting in a more pronounced observed density of FrzA **(Figures 5.9 and 5.11B)**. However, this hypothesis remains to be validated.

5.3.4 Conformational changes between FrzCD$^{\Delta DB}$-FrzA and FrzCD$^{\Delta DBH2}$-FrzA complexes

Density maps of FrzCD$^{\Delta DB}$-FrzA and FrzCD$^{\Delta DBH2}$-FrzA were superimposed to see any conformational differences. We see a conformational shift of FrzA molecules at the signalling tip of the receptor. FrzA', in particular, shows a rotation along FrzCD longitudinal axis **(Figure 5.12)**. A rotational model had been proposed as a mechanism of signal regulation by di-HAMP domains, where the conformation of HAMP domain induces rotational changes in MA four-helix bundle *(Jazleena, Das, Guiseppi et al., 2025)*. Here, we see a rotation of FrzA at the convex interface, which we think to be a weaker interface for the FrzCD-FrzA complex. The region is poorly resolved to identify interacting residues or the rotation of coiled-coil helices

that might be responsible for observed rotational shift of FrzA **(Figure 5.12)**. Further processing of datasets is underway to improve the resolution of the structures.

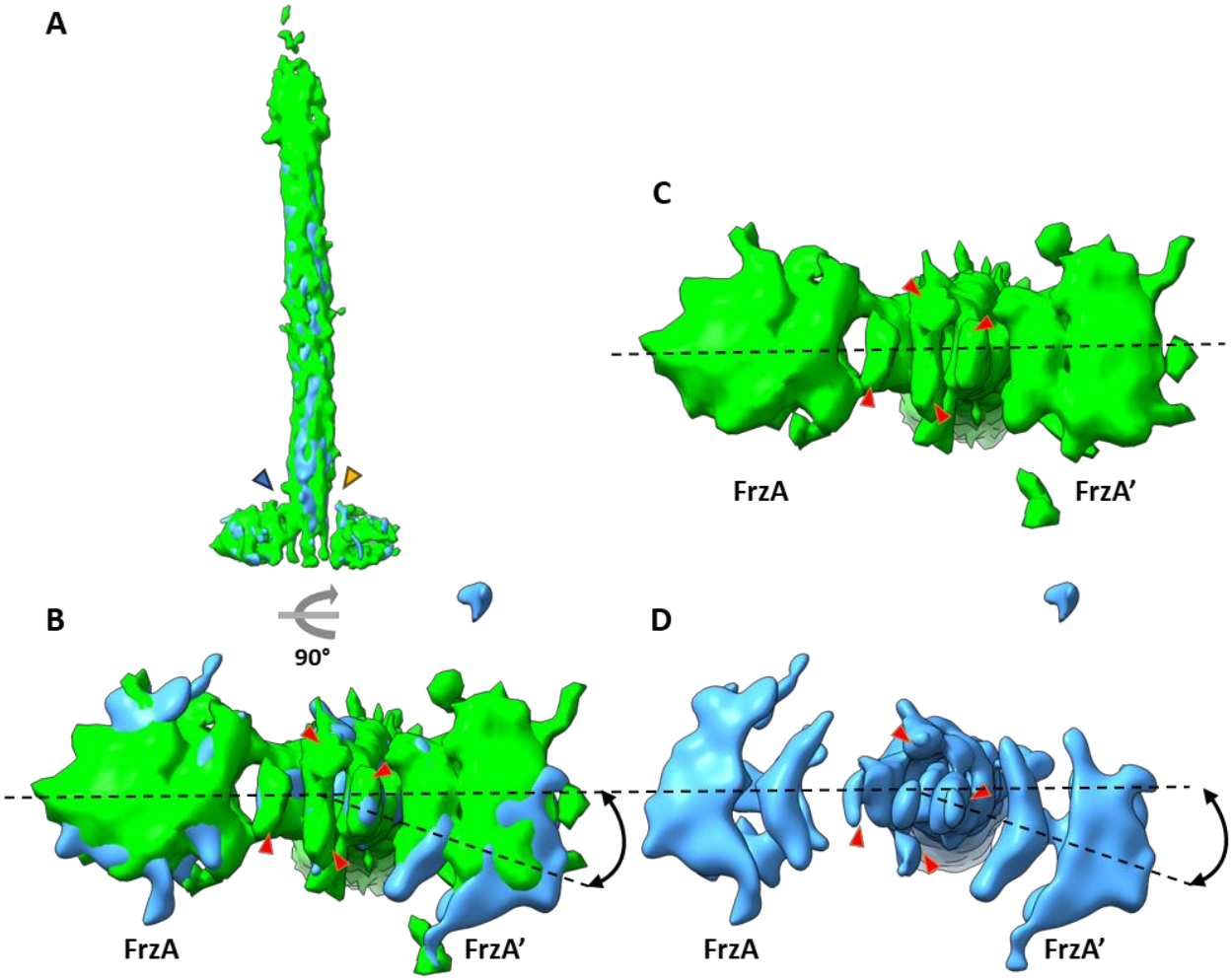


Figure 5.12 Conformational changes in receptor-adaptor complexes. (A) Overlay of FrzCD$^{\Delta DB}$-FrzA and FrzCD$^{\Delta DBH2}$-FrzA sharp density maps. Blue triangle indicates the concave interface and the yellow triangle indicates the convex interface. End-on view of (B) superimposed, (C) FrzCD$^{\Delta DB}$-FrzA, and (D) FrzCD$^{\Delta DBH2}$-FrzA density maps. Red arrows indicate the helices of the coiled-coil signalling tip. Black dotted line shows representative axis of the orientation of FrzA molecules in relation to dimeric FrzCD. Movement in FrzA' with respect to representative axis is marked by black curved arrow.

5.3.5 Flexibility of di-HAMP domains

The structure of receptor FrzCD$^{\Delta DB}$ features an N-terminal HAMP1 domain, which is poorly resolved, likely due to flexibility between HAMP1 and HAMP2. HAMP2 is continuous with MA domain, while HAMP1 and HAMP2 are connected by a small helical linker of around 11 residues, similar to the HAMP1 and HAMP2 domains of the Aer2 receptor from *P. aeruginosa (Jazleena, Das, Guiseppi et al., 2025)*. This may explain the flexibility observed in HAMP1

during the 3D classification of the FrzCD$^{\Delta DB}$-FrzA model **(Figure 5.13)**. The significance of the linker between HAMP1 and HAMP2 in inducing flexibility and, thereby, its significance remains to be explored.

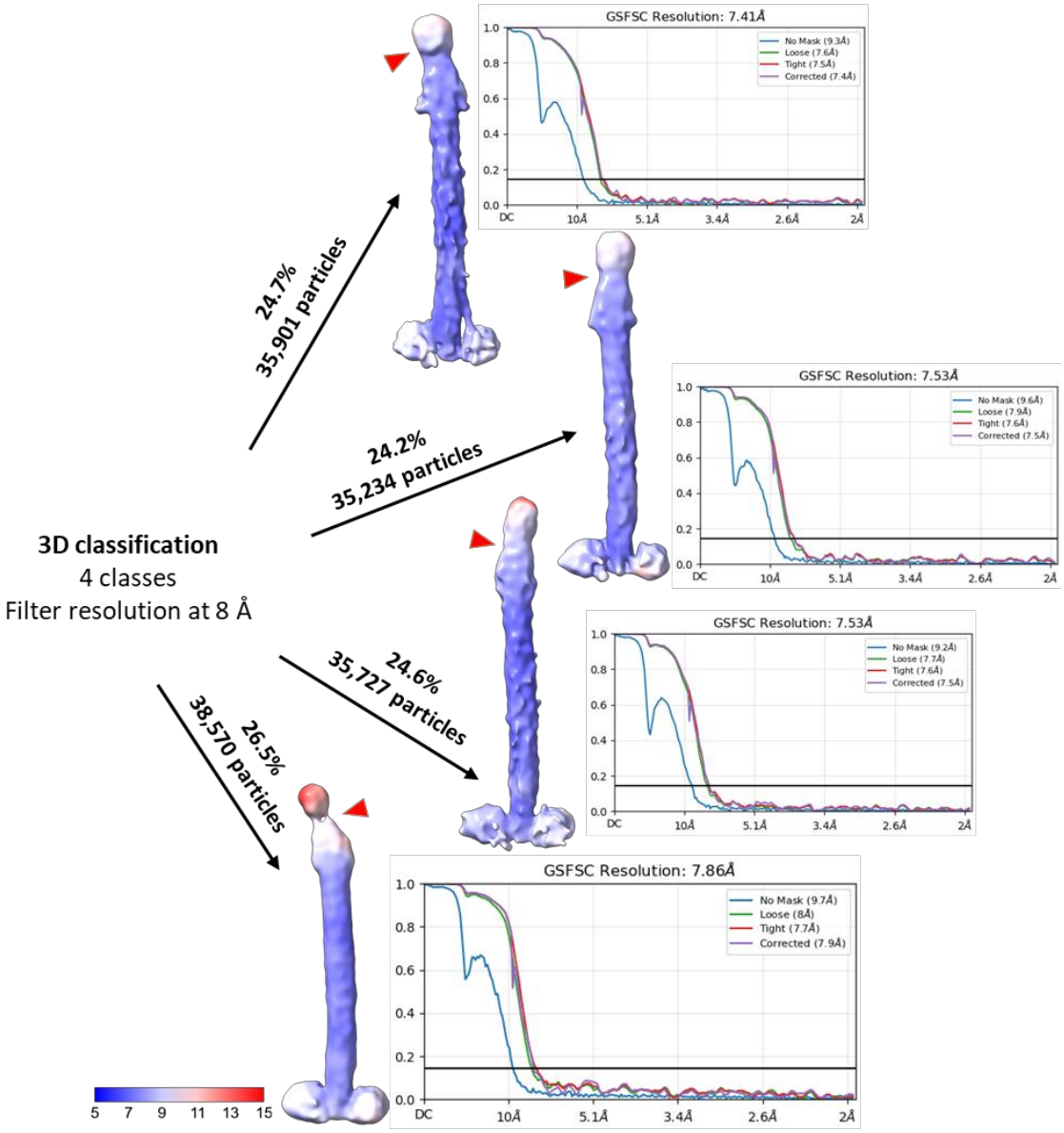


Figure 5.13 3D classification of FrzCD$^{\Delta DB}$-FrzA electron density at a filter resolution of 8 Å reveals movement of the HAMP1 domain. Four different 3D classes display changes in the orientation of HAMP1 domain, highlighted by red arrows.

5.4 Discussion

Alternate HAMP conformations are captured in crystal structure of the poly-HAMP domain of the Aer2 receptor from *P. aeruginosa,* where a helical insert separates HAMP 1 and HAMP 2, while HAMP 2 and HAMP 3 are concatenated *(Airola et al., 2010)*. HAMP 1 and HAMP 3 adopt similar conformations, while HAMP 2 displays an alternate conformation (**Figure 5.1D**) *(Airola et al., 2010)*. The two different HAMP conformers mediate alternate signalling in the MCPs *(Airola et al., 2013)*. Crystal structure of cytoplasmic MA region of MCP from *T. maritima* in complex with CheW and CheA kinase regulatory (P4-P5) module captures a conserved hydrophobic interface for CheA-P5 and CheW to form pseudo 6-fold symmetric rings *(X. Li et al., 2013; Briegel et al., 2012)*. Extensive cryoET studies confirmed conserved hexagonal architecture of chemosensory arrays in bacteria and archaea for membrane-bound and cytoplasmic chemosensory arrays (Riechmann & Zhang, 2023; Hadjidemetriou et al., 2022; Qin & Zhang, 2021; Briegel et al., 2015; Briegel, Ladinsky, et al., 2014; Briegel et al., 2009). Tomography studies combined with crystal structures and molecular modelling revealed a conserved array architecture, identified the core signalling unit, and explained how these arrays amplify and integrate signals. However, the exact mechanism of signal transduction in the MCP, regulation by methylation adaptation and kinase activation is not known.

Here, we characterized the structure of a cytoplasmic chemoreceptor FrzCD in complex with adaptor protein FrzA using CryoEM. Chemosensory complexes are reported to form atypical architecture *in vitro*. 'Zippers', or 'micelle-like' architecture are observed *in vitro* in absence of baseplate components *(Briegel, Wong, et al., 2014)*, and 'sandwich' array are observed for truncated receptors *in vitro* without a transmembrane domain in presence of baseplate components *(Briegel, Ladinsky, et al., 2014; Haglin et al., 2017)*. Interestingly, we observe 'star-like' clusters and 'triangle-like' arrays for FrzCD$^{\Delta DB}$-FrzA and FrzCD-FrzA complexes, respectively, in presence of CHAPSO. Such architecture is possibly mediated by interactions among FrzA **(Figure 5.7)**. Homo-hexameric rings by adaptor proteins are observed as part of arrays that mediate cooperativity and regulate sensitivity of arrays *(Piñas et al., 2022; Cassidy et al., 2020; Yang et al., 2018; Cassidy et al., 2015)*. Here, the mechanism of formation and significance of observed 'star-like' clusters and 'triangle-like' arrays remain to be explored.

The structure of FrzCD$^{\Delta DB}$-FrzA and FrzCD$^{\Delta DBH2}$-FrzA complexes were solved to a resolution of 6.13 Å and 6.19 Å, respectively. The structure though limited by resolution (possibly due to preferred orientation, absence of end-on views and flexible nature of the sample, Figure 5.8C

and D), highlights an important feature of glycine hinge induced flexibility, a feature not predicted in Alphafold generated models **(Figure 5.9B, 5.10)**. FrzCD$^{\Delta DB}$-FrzA confirms the presence of di-HAMP domains in FrzCD **(Figure 5.9)**. The di-HAMP domains of FrzCD are shown to modulate nucleoid array formation and downstream signalling *M. xanthus (Jazleena, Das, Guiseppi et al., 2025)*. The di-HAMP domains have a short helical insert between HAMP1 and HAMP2 *(Jazleena, Das, Guiseppi et al., 2025)*. We think that the linker helix provides flexibility to HAMP1 domain. Different orientations of HAMP1 were observed during the 3D classification of the FrzCD$^{\Delta DB}$-FrzA model **(Figure 5.13)**.

The di-HAMP domain is continuous with the methylation helix, followed by the glycine hinge and kinase control region of the coiled-coil MA domain **(Figure 5.9)**. The MA domain showed a curvature of around 3.8° **(Figure 5.11C)**. The curvature is due to the presence of glycine hinge in the MA domain **(Figure 5.10)**. Curvature of receptors is observed in tomography studies *(Cassidy et al., 2023, 2020; Burt et al., 2020; Briegel et al., 2012)*. Conserved glycine residues of MA domain regulate kinase coupling and signalling switching *(Coleman et al., 2005)*. The conformational freedom provided by the glycine hinge is essential for receptor structure and function *(Coleman et al., 2005)*. Flexible hinges were observed in nanodisc-embedded dimeric transmembrane chemoreceptors. Bending at two loci, one short hinge connecting HAMP and coiled-coil domain (0° to ∼13° bend), and a hinge corresponding to aligned glycines in the four-helix coiled-coil domain (0° to ∼20° bend), were independent of chemoreceptor signalling state *(Akkaladevi et al., 2018)*. Modelling showed that a narrow range of combinations of bend angles at the two flexible hinges avoids clashes in CSUs and arrays. Bending at the glycine hinge, without bending at the HAMP hinge, over a narrow range of experimentally observed angles supported CSU formation *(Akkaladevi et al., 2018)*. Additionally, the crystal structure of cytoplasmic region of transmembrane receptor from *E. coli* shows a bend of ∼10° at the glycine hinge *(Coleman et al., 2005; Kim et al., 1999)*. Flexibility of cytoplasmic chemoreceptor FrzCD may be important to avoid clashes during cluster formation. The hinges might also absorb strain imposed by the fluidic nature of scaffolds (membrane or nucleoid) and prevent disassembly of organized array at the baseplate.

The curvature in MA domain observed for FrzCD$^{\Delta DB}$-FrzA complex is similar to FrzCD$^{\Delta DBH2}$-FrzA complex **(Figure 5.12A)**. However, FrzA at the signalling tip showed rotation along FrzCD longitudinal axis **(Figure 5.12B-D)**. A rotational model is proposed as a mechanism of signal regulation by di-HAMP domains in FrzCD. The conformation of HAMP domain induces

rotational changes in MA four-helix bundle thereby exposing interface for methylation and oligomerization. The methylation state is different for either HAMP1/HAMP2 or both HAMP deleted constructs and it determines group motility and multicellular structure formation for *M. xanthus (Jazleena, Das, Guiseppi et al., 2025)*. Here, we see a rotation of FrzA at the convex interface. The region is poorly resolved to identify interacting residues or the rotation of coiled-coil helices that might be responsible for observed rotational shift of FrzA **(Figure 5.12)**. Further processing of the datasets will give possible insights about the interface and orientation of helices at the signalling tip.

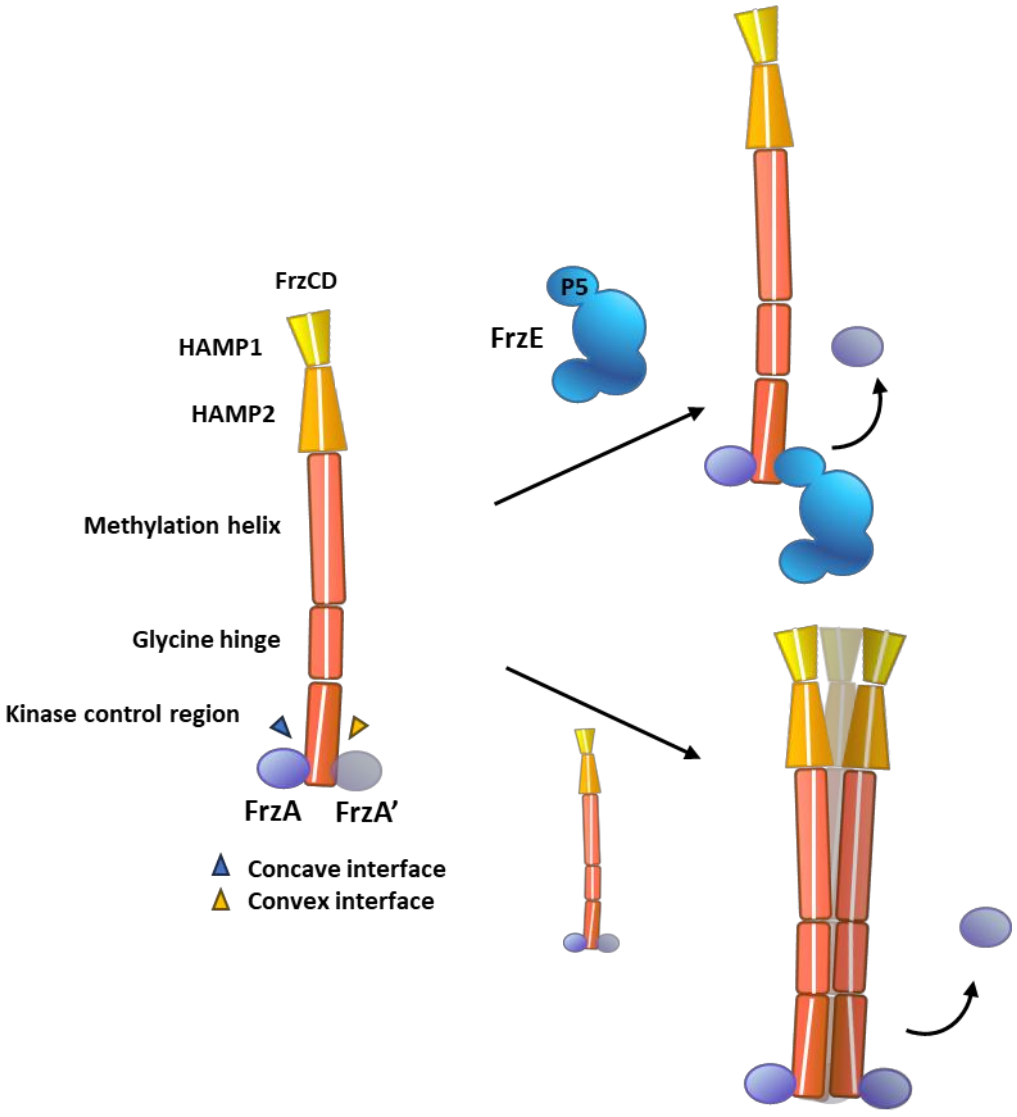


Figure 5.14 Model showing asymmetric interface of FrzCD which might result in a preferential FrzA binding interface at concave side and FrzE binding or oligomerization at convex interface. P5 domain of FrzE is homologous to CheW.

Interestingly we observe an asymmetry in FrzA density at binding interfaces in FrzCD dimer **(Figure 5.8 and 5.9)**. The curvature due to glycine hinge results in a concave and a convex

interface for FrzA interaction as opposed to two-fold symmetric model predicted using AlphaFold3. FrzA density is more pronounced at the concave interface **(Figure 5.8 and 5.9)**. We think that the asymmetric interface at the signalling tip has different affinities for FrzA molecules. FrzA at the concave interface may provide a more stable receptor adaptor interface, resulting in a more pronounced observed density of FrzA. CheW and CheA is reported to compete for the same binding site at receptor molecules *(Asinas & Weis, 2006)*. We propose a model where glycine hinge favours curvature of soluble dimeric FrzCD, observed for $FrzCD^{\Delta DB}$ and $FrzCD^{\Delta DBH2}$ in presence of FrzA. The curvature induces asymmetry in the binding interface for FrzA. We hypothesize that the convex interface which has less pronounced density for FrzA, might either prefer binding to FrzE in the cytoplasm of cells or support oligomerization of FrzCD in presence of DNA **(Figure 5.14)**. In absence of FrzE or DNA scaffold we see binding of FrzA to a lower extent on the convex interface. However, this hypothesis needs to be examined. Interestingly, we also see a rotational shift of FrzA molecules at the convex interface at the signalling tip of the receptor in $FrzCD^{\Delta DBH2}$ **(Figure 5.13)**. In line with our hypothesis, if FrzE prefers binding to the convex interface, the rotational shift might translate to kinase ON/OFF state, or the rotation shift will influence the signalling states of associated FrzCD molecules. Further investigation will provide insights into mechanism of signal transduction and activation of histidine kinases in chemosensory pathway. We believe that the soluble cytoplasmic Frz chemosensory pathway can serve as a model system to understand the mechanism of signal transduction in chemosensory clusters.

5.5 Acknowledgements

I would like to thank Professor Ben Luisi of the Department of Biochemistry at the University of Cambridge for hosting me in his laboratory, where I worked on the CryoEM of the FrzCD-FrzA complex. I am grateful to the SPARC grant for providing the opportunity and financial support for my travel and accommodations during my stay at Cambridge. Additionally, I thank Tiyasa Bain for cloning FrzCD$^{\Delta DBH2}$ into the pHis17 vector with a C-terminal Strep tag, and I appreciate her assistance during the purification of certain batches of receptor-adaptor complexes.

5.6 References

1. Abramson, J., Adler, J., Dunger, J., Evans, R., Green, T., Pritzel, A., Ronneberger, O., Willmore, L., Ballard, A. J., Bambrick, J., Bodenstein, S. W., Evans, D. A., Hung, C.-C., O'Neill, M., Reiman, D., Tunyasuvunakool, K., Wu, Z., Žemgulytė, A., Arvaniti, E., … Jumper, J. M. (2024). Accurate structure prediction of biomolecular interactions with AlphaFold 3. *Nature*, *630*(8016), 493–500. https://doi.org/10.1038/s41586-024-07487-w
2. Airola, M. V., Sukomon, N., Samanta, D., Borbat, P. P., Freed, J. H., Watts, K. J., & Crane, B. R. (2013). HAMP domain conformers that propagate opposite signals in bacterial chemoreceptors. *PLoS Biology*, *11*(2), e1001479. https://doi.org/10.1371/journal.pbio.1001479
3. Airola, M. V., Watts, K. J., Bilwes, A. M., & Crane, B. R. (2010). Structure of Concatenated HAMP Domains Provides a Mechanism for Signal Transduction. *Structure*, *18*(4), 436–448. https://doi.org/10.1016/j.str.2010.01.013
4. Akkaladevi, N., Bunyak, F., Stalla, D., White, T. A., & Hazelbauer, G. L. (2018). Flexible Hinges in Bacterial Chemoreceptors. *Journal of Bacteriology*, *200*(5), 10.1128/jb.00593-17. https://doi.org/10.1128/jb.00593-17
5. Aravind, L., & Ponting, C. P. (1999). The cytoplasmic helical linker domain of receptor histidine kinase and methyl-accepting proteins is common to many prokaryotic signalling proteins. *FEMS Microbiology Letters*, *176*(1), 111–116. https://doi.org/10.1111/j.1574-6968.1999.tb13650.x
6. Asinas, A. E., & Weis, R. M. (2006). Competitive and Cooperative Interactions in Receptor Signaling Complexes*. *Journal of Biological Chemistry*, *281*(41), 30512–30523. https://doi.org/10.1074/jbc.M606267200
7. Astling, D. P., Lee, J. Y., & Zusman, D. R. (2006). Differential effects of chemoreceptor methylation-domain mutations on swarming and development in the social bacterium Myxococcus xanthus. *Molecular Microbiology*, *59*(1), 45–55. https://doi.org/10.1111/j.1365-2958.2005.04926.x
8. Bain, T. (2025). *Structural characterization of components of the Frz chemoreceptor complex of Myxococcus xanthus* [Thesis]. http://dr.iiserpune.ac.in:8080/xmlui/handle/123456789/9981

9. Bi, S., & Lai, L. (2014). Bacterial chemoreceptors and chemoeffectors. *Cellular and Molecular Life Sciences: CMLS*, *72*(4), 691–708. https://doi.org/10.1007/s00018-014-1770-5

10. Briegel, A., Ames, P., Gumbart, J. C., Oikonomou, C. M., Parkinson, J. S., & Jensen, G. J. (2013). The mobility of two kinase domains in the Escherichia coli chemoreceptor array varies with signalling state. *Molecular Microbiology*, *89*(5), 831–841. https://doi.org/10.1111/mmi.12309

11. Briegel, A., Ladinsky, M. S., Oikonomou, C., Jones, C. W., Harris, M. J., Fowler, D. J., Chang, Y.-W., Thompson, L. K., Armitage, J. P., & Jensen, G. J. (2014). Structure of bacterial cytoplasmic chemoreceptor arrays and implications for chemotactic signaling. *eLife*, *3*, e02151. https://doi.org/10.7554/eLife.02151

12. Briegel, A., Li, X., Bilwes, A. M., Hughes, K. T., Jensen, G. J., & Crane, B. R. (2012). Bacterial chemoreceptor arrays are hexagonally packed trimers of receptor dimers networked by rings of kinase and coupling proteins. *Proceedings of the National Academy of Sciences of the United States of America*, *109*(10), 3766–3771. https://doi.org/10.1073/pnas.1115719109

13. Briegel, A., Ortega, D. R., Huang, A., Oikonomou, C. M., Gunsalus, R. P., & Jensen, G. J. (2015). Structural conservation of chemotaxis machinery across Archaea and Bacteria. *Environmental Microbiology Reports*, *7*(3), 414–419. https://doi.org/10.1111/1758-2229.12265

14. Briegel, A., Ortega, D. R., Tocheva, E. I., Wuichet, K., Li, Z., Chen, S., Müller, A., Iancu, C. V., Murphy, G. E., Dobro, M. J., Zhulin, I. B., & Jensen, G. J. (2009). Universal architecture of bacterial chemoreceptor arrays. *Proceedings of the National Academy of Sciences*, *106*(40), 17181–17186. https://doi.org/10.1073/pnas.0905181106

15. Briegel, A., Wong, M. L., Hodges, H. L., Oikonomou, C. M., Piasta, K. N., Harris, M. J., Fowler, D. J., Thompson, L. K., Falke, J. J., Kiessling, L. L., & Jensen, G. J. (2014). New Insights into Bacterial Chemoreceptor Array Structure and Assembly from Electron Cryotomography. *Biochemistry*, *53*(10), 1575–1585. https://doi.org/10.1021/bi5000614

16. Burt, A., Cassidy, C. K., Ames, P., Bacia-Verloop, M., Baulard, M., Huard, K., Luthey-Schulten, Z., Desfosses, A., Stansfeld, P. J., Margolin, W., Parkinson, J. S., & Gutsche, I. (2020). Complete structure of the chemosensory array core signalling unit in an E. coli minicell strain. *Nature Communications*, *11*(1), 743. https://doi.org/10.1038/s41467-020-14350-9

17. Cassidy, C. K., Himes, B. A., Alvarez, F. J., Ma, J., Zhao, G., Perilla, J. R., Schulten, K., & Zhang, P. (2015). CryoEM and computer simulations reveal a novel kinase conformational switch in bacterial chemotaxis signaling. *eLife*, *4*, e08419. https://doi.org/10.7554/eLife.08419

18. Cassidy, C. K., Himes, B. A., Sun, D., Ma, J., Zhao, G., Parkinson, J. S., Stansfeld, P. J., Luthey-Schulten, Z., & Zhang, P. (2020). Structure and dynamics of the E. coli chemotaxis core signaling complex by cryo-electron tomography and molecular simulations. *Communications Biology*, *3*(1), 24. https://doi.org/10.1038/s42003-019-0748-0

19. Cassidy, C. K., Qin, Z., Frosio, T., Gosink, K., Yang, Z., Sansom, M. S. P., Stansfeld, P. J., Parkinson, J. S., & Zhang, P. (2023). Structure of the native chemotaxis core signaling

unit from phage E-protein lysed E. coli cells. *mBio*, *14*(5), e00793-23. https://doi.org/10.1128/mbio.00793-23

20. Chen, J., Noble, A. J., Kang, J. Y., & Darst, S. A. (2019). Eliminating effects of particle adsorption to the air/water interface in single-particle cryo-electron microscopy: Bacterial RNA polymerase and CHAPSO. *Journal of Structural Biology: X*, *1*, 100005. https://doi.org/10.1016/j.yjsbx.2019.100005

21. Coleman, M. D., Bass, R. B., Mehan, R. S., & Falke, J. J. (2005). Conserved Glycine Residues in the Cytoplasmic Domain of the Aspartate Receptor Play Essential Roles in Kinase Coupling and On–Off Switching. *Biochemistry*, *44*(21), 7687–7695. https://doi.org/10.1021/bi0501479

22. Erbse, A. H., & Falke, J. J. (2009). The Core Signaling Proteins of Bacterial Chemotaxis Assemble To Form an Ultrastable Complex. *Biochemistry*, *48*(29), 6975–6987. https://doi.org/10.1021/bi900641c

23. Gumerov, V. M., Andrianova, E. P., & Zhulin, I. B. (2021). Diversity of bacterial chemosensory systems. *Current Opinion in Microbiology*, *61*, 42–50. https://doi.org/10.1016/j.mib.2021.01.016

24. Gushchin, I., Melnikov, I., Polovinkin, V., Ishchenko, A., Yuzhakova, A., Buslaev, P., Bourenkov, G., Grudinin, S., Round, E., Balandin, T., Borshchevskiy, V., Willbold, D., Leonard, G., Büldt, G., Popov, A., & Gordeliy, V. (2017). Mechanism of transmembrane signaling by sensor histidine kinases. *Science (New York, N.Y.)*, *356*(6342), eaah6345. https://doi.org/10.1126/science.aah6345

25. Hadjidemetriou, K., Kaur, S., Cassidy, C. K., & Zhang, P. (2022). Mechanisms of E. coli chemotaxis signaling pathways visualized using cryoET and computational approaches. *Biochemical Society Transactions*, *50*(6), 1595–1605. https://doi.org/10.1042/BST20220191

26. Haglin, E. R., Yang, W., Briegel, A., & Thompson, L. K. (2017). His-Tag-Mediated Dimerization of Chemoreceptors Leads to Assembly of Functional Nanoarrays. *Biochemistry*, *56*(44), 5874–5885. https://doi.org/10.1021/acs.biochem.7b00698

27. Hazelbauer, G. L. (2012). Bacterial Chemotaxis: The Early Years of Molecular Studies. *Annual Review of Microbiology*, *66*(Volume 66, 2012), 285–303. https://doi.org/10.1146/annurev-micro-092611-150120

28. Hulko, M., Berndt, F., Gruber, M., Linder, J. U., Truffault, V., Schultz, A., Martin, J., Schultz, J. E., Lupas, A. N., & Coles, M. (2006). The HAMP Domain Structure Implies Helix Rotation in Transmembrane Signaling. *Cell*, *126*(5), 929–940. https://doi.org/10.1016/j.cell.2006.06.058

29. Jazleena, P. J., Das, A., Guiseppi, A., Debard, F., Sharma, J., Yaikhomba, M., Mignot, T., Mauriello, E. M. F., & Gayathri, P. (2025). Di-HAMP domains of a cytoplasmic chemoreceptor modulate nucleoid array formation and downstream signaling. *mBio*, *16*(5), e00057-25. https://doi.org/10.1128/mbio.00057-25

30. Jumper, J., Evans, R., Pritzel, A., Green, T., Figurnov, M., Ronneberger, O., Tunyasuvunakool, K., Bates, R., Žídek, A., Potapenko, A., Bridgland, A., Meyer, C., Kohl, S. A. A., Ballard, A. J., Cowie, A., Romera-Paredes, B., Nikolov, S., Jain, R., Adler, J., … Hassabis, D. (2021). Highly accurate protein structure prediction with AlphaFold. *Nature*, *596*(7873), Article 7873. https://doi.org/10.1038/s41586-021-03819-2

31. Kim, K. K., Yokota, H., & Kim, S.-H. (1999). Four-helical-bundle structure of the cytoplasmic domain of a serine chemotaxis receptor. *Nature*, *400*(6746), 787–792. https://doi.org/10.1038/23512

32. Li, M., & Hazelbauer, G. L. (2004). Cellular Stoichiometry of the Components of the Chemotaxis Signaling Complex. *Journal of Bacteriology*, *186*(12), 3687–3694. https://doi.org/10.1128/jb.186.12.3687-3694.2004

33. Li, M., & Hazelbauer, G. L. (2011). Core unit of chemotaxis signaling complexes. *Proceedings of the National Academy of Sciences*, *108*(23), 9390–9395. https://doi.org/10.1073/pnas.1104824108

34. Li, X., Fleetwood, A. D., Bayas, C., Bilwes, A. M., Ortega, D. R., Falke, J. J., Zhulin, I. B., & Crane, B. R. (2013). The 3.2 Å Resolution Structure of a Receptor:CheA:CheW Signaling Complex Defines Overlapping Binding Sites and Key Residue Interactions within Bacterial Chemosensory Arrays. *Biochemistry*, *52*(22), 3852–3865. https://doi.org/10.1021/bi400383e

35. Liu, J., Hu, B., Morado, D. R., Jani, S., Manson, M. D., & Margolin, W. (2012). Molecular architecture of chemoreceptor arrays revealed by cryoelectron tomography of Escherichia coli minicells. *Proceedings of the National Academy of Sciences of the United States of America*, *109*(23), E1481–E1488. https://doi.org/10.1073/pnas.1200781109

36. Lopéz-Blanco, J. R., & Chacón, P. (2013). iMODFIT: Efficient and robust flexible fitting based on vibrational analysis in internal coordinates. *Journal of Structural Biology*, *184*(2), 261–270. https://doi.org/10.1016/j.jsb.2013.08.010

37. Meng, E. C., Goddard, T. D., Pettersen, E. F., Couch, G. S., Pearson, Z. J., Morris, J. H., & Ferrin, T. E. (2023). UCSF ChimeraX: Tools for structure building and analysis. *Protein Science*, *32*(11), e4792. https://doi.org/10.1002/pro.4792

38. Muok, A. R., Briegel, A., & Crane, B. R. (2020). Regulation of the chemotaxis histidine kinase CheA: A structural perspective. *Biochimica et Biophysica Acta (BBA) - Biomembranes*, *1862*(1), 183030. https://doi.org/10.1016/j.bbamem.2019.183030

39. Muok, A. R., Ortega, D. R., Kurniyati, K., Yang, W., Maschmann, Z. A., Sidi Mabrouk, A., Li, C., Crane, B. R., & Briegel, A. (2020). Atypical chemoreceptor arrays accommodate high membrane curvature. *Nature Communications*, *11*(1), 5763. https://doi.org/10.1038/s41467-020-19628-6

40. Pettersen, E. F., Goddard, T. D., Huang, C. C., Couch, G. S., Greenblatt, D. M., Meng, E. C., & Ferrin, T. E. (2004). UCSF Chimera—A visualization system for exploratory research and analysis. *Journal of Computational Chemistry*, *25*(13), 1605–1612. https://doi.org/10.1002/jcc.20084

41. Piñas, G. E., DeSantis, M. D., Cassidy, C. K., & Parkinson, J. S. (2022). Hexameric rings of the scaffolding protein CheW enhance response sensitivity and cooperativity in Escherichia coli chemoreceptor arrays. *Science Signaling*, *15*(718), eabj1737. https://doi.org/10.1126/scisignal.abj1737

42. Punjani, A., Rubinstein, J. L., Fleet, D. J., & Brubaker, M. A. (2017). cryoSPARC: Algorithms for rapid unsupervised cryo-EM structure determination. *Nature Methods*, *14*(3), 290–296. https://doi.org/10.1038/nmeth.4169

43. Qin, Z., Lin, W., Zhu, S., Franco, A. T., & Liu, J. (2017). Imaging the Motility and Chemotaxis Machineries in Helicobacter pylori by Cryo-Electron Tomography. *Journal of Bacteriology*, *199*(3), 10.1128/jb.00695-16. https://doi.org/10.1128/jb.00695-16

44. Qin, Z., & Zhang, P. (2021). Studying bacterial chemosensory array with CryoEM. *Biochemical Society Transactions*, *49*(5), 2081–2089. https://doi.org/10.1042/BST20210080

45. Riechmann, C., & Zhang, P. (2023). Recent structural advances in bacterial chemotaxis signalling. *Current Opinion in Structural Biology*, *79*, 102565. https://doi.org/10.1016/j.sbi.2023.102565

46. Wadhams, G. H., & Armitage, J. P. (2004). Making sense of it all: Bacterial chemotaxis. *Nature Reviews Molecular Cell Biology*, *5*(12), Article 12. https://doi.org/10.1038/nrm1524

47. Winski, A., Ludwiczak, J., Orlowska, M., Madaj, R., Kaminski, K., & Dunin-Horkawicz, S. (2023). *AlphaFold2 captures the conformational landscape of the HAMP signaling domain* [Preprint]. Bioinformatics. https://doi.org/10.1101/2023.05.23.541686

48. Wuichet, K., & Zhulin, I. B. (2010). Origins and Diversification of a Complex Signal Transduction System in Prokaryotes. *Science Signaling*, *3*(128), ra50–ra50. https://doi.org/10.1126/scisignal.2000724

49. Yang, W., Alvarado, A., Glatter, T., Ringgaard, S., & Briegel, A. (2018). Baseplate variability of Vibrio cholerae chemoreceptor arrays. *Proceedings of the National Academy of Sciences*, *115*(52), 13365–13370. https://doi.org/10.1073/pnas.1811931115

50. Yang, W., Cassidy, C. K., Ames, P., Diebolder, C. A., Schulten, K., Luthey-Schulten, Z., Parkinson, J. S., & Briegel, A. (2019). In Situ Conformational Changes of the Escherichia coli Serine Chemoreceptor in Different Signaling States. *mBio*, *10*(4), 10.1128/mbio.00973-19. https://doi.org/10.1128/mbio.00973-19

51. Zhang, P., Khursigara, C. M., Hartnell, L. M., & Subramaniam, S. (2007). Direct visualization of Escherichia coli chemotaxis receptor arrays using cryo-electron microscopy. *Proceedings of the National Academy of Sciences*, *104*(10), 3777–3781. https://doi.org/10.1073/pnas.0610106104

Chapter 6

Conclusions and Future Prospects

6.1 Summary of major findings

Although the architecture of chemosensory macromolecular complexes, as hexagonal arrays, is conserved in bacteria and archaea *(Briegel et al., 2012, 2009)*, the exact mechanism of signal transduction in these complexes is not well understood. The structural changes mediated by ligand binding, adaptational modification of conserved residues, cooperativity and signal integration among receptors, resulting in kinase output, have not been captured to a high resolution. Additionally, very few cytoplasmic chemosensory complexes have been characterized to date *(Ortega et al., 2020; Briegel et al., 2016, 2014)*. Here, we studied the cytoplasmic Frz chemosensory complex from *M. xanthus,* which forms chemosensory clusters on the nucleoid *(Guiseppi et al., 2019; Moine et al., 2017)* and regulates polarity reversals in the bacterium *(Bustamante et al., 2004)*. Our motivation was to reconstitute this soluble chemosensory complex *in vitro* for structure determination and structural studies to understand the mechanism of signal transduction in chemosensory complexes. Here, I summarize the major findings from my PhD research work.

Through multiple sequence alignment and homology modelling, we characterized the domain boundaries of the chemoreceptor FrzCD. The N-terminal DNA-binding domain has positively charged residues that mediate sequence-independent binding to DNA fragments. We identified di-HAMP domains between the DNA-binding domain and the coiled-coil signalling domain. We characterized the role of di-HAMP domains *in vitro* and *in vivo* in collaboration with Dr Emilia Mauriello at CNRS, France. *In vitro* experiments demonstrate that the di-HAMP domains restrict FrzCD to a dimeric form in solution and modulates FrzCD affinity for DNA. In contrast, the signalling domain stabilizes higher-order oligomeric assemblies upon DNA binding **(Chapter2, Figure 2.11A)**. Along with the *in vivo* observations of Frz clusters on the nucleoid, as well as group motility and development in the bacterium, a rotation model of the coiled-coil domain is proposed, which is regulated by DNA binding and di-HAMP domains **(Chapter2, Figure 2.11)**. We believe that DNA-binding induces conformational changes, which are then transduced by di-HAMP domains to the MA domain. This conformational change may reorient the MA helices to favour oligomer formation, possibly by axial rotation, allowing the exposure of an interface responsible for oligomerization. The conformation of the MA domain is possibly regulated by di-HAMP domains, which may exist in different conformers, affecting DNA binding as well as the exposed methylation sites within the MA domain. Thus, the di-HAMP domains modulated cluster formation on the nucleoid and

downstream signalling in the bacterium **(Chapter 2, Figure 2.11A)** *(Jazleena, Das, Guiseppi et al., 2025)*.

Next, we looked into the diversity of HAMP and ligand-binding domains (LBDs) in different MCP heptad classes as well as any preferences between membrane-bound and cytoplasmic MCPs. We noticed that, besides predominant MCP heptad classes (44H, 40H, 38H, and 36H), MCP classes with fewer heptads, such as 28H and 24H, were more common among cytoplasmic MCPs. Conversely, MCP classes with higher heptad counts are comparatively predominant in membrane-bound MCPs. Cytoplasmic MCPs predominantly lacked HAMP domains and most of the poly-HAMP domains were found to be concatenated. Beyond signal transduction, HAMP domains for cytoplasmic MCPs might have additional roles. The tri-HAMP region in cytoplasmic Aer2 MCPs regulate the cellular localization of receptors in *P. aeruginosa (Anaya et al., 2022)*, and di-HAMP domains in the cytoplasmic MCP FrzCD influence array formation on the nucleoid in *M. xanthus (Jazleena, Das, Guiseppi et al., 2025, mBio)*. Additionally, we identified the prevalence of certain LBDs for cytoplasmic MCPs that can sense small diffusible molecules or intracellular metabolites. We hypothesize that FrzCD might detect intracellular signals, such as changes in osmolality or small, diffusible molecules like short-chain alcohols. Changes in osmolarity is reported to alter the packing of the coiled-coils of *E. coli* MCPs, and ethanol molecules are reported to bind to the coiled-coil of transmembrane chemoreceptor McpB in *Bacillus subtilis (Tohidifar et al., 2020; Vaknin & Berg, 2006)*. We did not identify any MCP with an architecture and DB domain similar to FrzCD. This novel mechanism of cluster formation on nucleoid is proposed to aid in segregation of chemosensory complexes during cell division akin to segregation of membrane-bound chemosensory complexes *(Mauriello et al., 2018)*.

We successfully reconstituted receptor-adaptor complexes, FrzCD-FrzA/FrzB, and identified key residues that mediate hydrophobic and salt bridge interactions between receptor and adaptor molecules. Leucine 265 and 269 of FrzCD mediate hydrophobic interactions with the hydrophobic groove of adaptor proteins. Essential salt bridge interactions were observed between aspartate 285 of FrzCD with arginine 85 of FrzA. While two salt bridges (aspartate 258 and 261 of FrzCD with arginine 44 of FrzB, and glutamate 255 together with aspartate 258 of FrzCD interacts with arginine 39 of FrzB) were essential for FrzCD-FrzB complex formation. Since FrzB lacked β4 and β5 in subdomain 2, it cannot interact with FrzE to form the core signalling unit *(Guiseppi et al., 2019; Mauriello, 2020)*. Additionally, we observed

that FrzCD-FrzB complex was less stable than FrzCD-FrzA complex. We propose a model where the distinct characteristics of two adaptors in this CSS facilitate a division of labour in mediating multiple cluster formations on the nucleoid **(Chapter 4, Figure 4.15)**. FrzA interacts with receptor FrzCD to form stable complexes and, in the presence of histidine kinase FrzE, forms core signalling units via interactions at interface 1. Since FrzB cannot form CSU and forms a less stable complex with FrzCD, the core signalling complex between FrzCD, FrzA and FrzE is possibly preferred. Since both adaptor proteins have the same binding interface on FrzCD, it is the property of the interacting interface of FrzA and FrzB with FrzCD that provides competitive regulation for array propagation. FrzA, which stably interacts with FrzCD and FrzE-P5 at interface 1, promotes CSU formation and array propagation. However, binding of FrzB to FrzCD, possibly favoured by lower free FrzA concentration or as a stochastic event based on comparative binding affinities. FrzB fails to interact with FrzE and restricts array extension, thereby regulating the array size on the nucleoid and promoting multiple clusters.

Next, we carried out structural studies on the reconstituted receptor-adaptor complexes using single particle cryoEM. Structure of FrzCD$^{\Delta DB}$-FrzA and FrzCD$^{\Delta DBH2}$-FrzA confirmed the presence of N-terminal di-HAMP domains, which is continuous with the MA domain and FrzA molecules interact at the signalling tip. The HAMP1 domain within the di-HAMP exhibits significant flexibility, likely due to a helical linker between HAMP1 and HAMP2. The receptor displays a curvature induced by the glycine hinge, resulting in an asymmetric interface at the signalling tip. Additionally, our observations indicate that FrzA binding is preferentially present at the concave interface, as indicated by a more prominent density of FrzA at this site. We propose a model in which asymmetry at the signalling tip of dimeric FrzCD may result in asymmetric interfaces **(Chapter 5, Figure 5.13)**. We hypothesize that the convex interface which has a less pronounced density for FrzA, might prefer binding to FrzE in cytoplasm of cells or support oligomerization of FrzCD in presence of DNA. Furthermore, in the absence of the HAMP2 domain, FrzA demonstrates a rotational shift along the longitudinal axis of FrzCD, suggesting a mechanism of signal transduction in receptor adaptor complexes. Further processing of datasets is underway to improve the resolution of the structures.

Our study on this novel cytoplasmic chemosensory system serves as a promising step toward carrying out structural studies on reconstituted cytoplasmic chemosensory complexes to understand the mechanism of signal transduction in chemosensory arrays. The Frz chemosensory system could be an ideal model system for obtaining high-resolution

information on chemosensory complexes in general, as well as for identifying both unique and common features of such complexes.

6.2 Future prospects

6.2.1 Co-evolution studies on interface residues at receptor-adaptor complex

FrzCD-FrzA/FrzB interaction interface has negatively charged residues on FrzCD that forms salt bridge interactions with positively charged arginine residues on adaptor proteins. We believe that these anchoring interactions have co-evolved between receptors and their corresponding adaptor proteins. This will also provide insights into the interaction of the receptor with the P5 domain of histidine kinases and can explain how, despite having multiple CSSs in certain organisms, the selectivity and regulation of individual CSSs are mediated.

6.2.2 Mechanism of signal transduction in FrzCD

We have carried out structural studies on FrzCD$^{\Delta DB}$-FrzA and FrzCD$^{\Delta DBH2}$-FrzA complexes which showed that in the absence of the HAMP2 domain, FrzA demonstrates a rotational shift along the longitudinal axis of FrzCD. Structural studies on FrzCD$^{\Delta DBH1}$-FrzA and FrzCD$^{\Delta DBH2}$-FrzA will provide insights into other conformational changes to understand the mechanism of signal transduction. The samples exhibit a preferred orientation bias (absence of end-on views) and are flexible, which influences the resolution attained in the structures. Further processing of datasets and optimization of sample preparation are necessary to overcome challenges in understanding conformational changes, which are limited by resolution.

Studies should be carried out with mutations on conserved glutamate and aspartate residues of FrzCD that mimic opposing signalling states *(Astling et al., 2006)*. Mutations of E168-Q169 or Q363-Q364 to alanine activates the pathway while mutations of E202-E203 or E370-Q371 to alanine inhibits the pathway *(Astling et al., 2006)*. Structural studies of complexes with these mutations will provide insights into the mechanism of signalling regulation via the receptor.

The role of DNA binding in mediating structural changes in FrzCD to support oligomerisation remains to be explored.

6.2.3 Significance of asymmetric interface on FrzCD

Based on our observation, we hypothesize that asymmetric interfaces at the signalling tip may provide selective binding surface for FrzA, FrzE or oligomerization. This hypothesis needs to be tested, which will provide insights into how a symmetric interface of a dimeric molecule may have different binding surfaces due to curvature induced by the glycine hinge. The importance of flexibility between HAMP1 and HAMP2 mediated by a connecting helix, in signalling or cluster formation, remains to be explored.

6.2.4 *In vitro* reconstitution and structure of CSU

In our current study, we solved the structure of the receptor-adaptor complex. *In vitro* reconstitution of the FrzCD-FrzA-FrzE complex, followed by single particle cryoEM, will provide structural details of a novel cytoplasmic chemosensory cluster. Additionally, it will provide insights into how histidine kinase is regulated by different signalling states of the receptor (using different FrzCD mutants).

6.3 References

1. Anaya, S., Orillard, E., Greer-Phillips, S. E., & Watts, K. J. (2022). New Roles for HAMP Domains: The Tri-HAMP Region of Pseudomonas aeruginosa Aer2 Controls Receptor Signaling and Cellular Localization. *Journal of Bacteriology*, *204*(9), e00225-22. https://doi.org/10.1128/jb.00225-22
2. Astling, D. P., Lee, J. Y., & Zusman, D. R. (2006). Differential effects of chemoreceptor methylation-domain mutations on swarming and development in the social bacterium Myxococcus xanthus. *Molecular Microbiology*, *59*(1), 45–55. https://doi.org/10.1111/j.1365-2958.2005.04926.x
3. Briegel, A., Ladinsky, M. S., Oikonomou, C., Jones, C. W., Harris, M. J., Fowler, D. J., Chang, Y.-W., Thompson, L. K., Armitage, J. P., & Jensen, G. J. (2014). Structure of bacterial cytoplasmic chemoreceptor arrays and implications for chemotactic signaling. *eLife*, *3*, e02151. https://doi.org/10.7554/eLife.02151
4. Briegel, A., Li, X., Bilwes, A. M., Hughes, K. T., Jensen, G. J., & Crane, B. R. (2012). Bacterial chemoreceptor arrays are hexagonally packed trimers of receptor dimers networked by rings of kinase and coupling proteins. *Proceedings of the National*

Academy of Sciences of the United States of America, *109*(10), 3766–3771. https://doi.org/10.1073/pnas.1115719109

5. Briegel, A., Ortega, D. R., Mann, P., Kjær, A., Ringgaard, S., & Jensen, G. J. (2016). Chemotaxis cluster 1 proteins form cytoplasmic arrays in *Vibrio cholerae* and are stabilized by a double signaling domain receptor DosM. *Proceedings of the National Academy of Sciences*, *113*(37), 10412–10417. https://doi.org/10.1073/pnas.1604693113

6. Briegel, A., Ortega, D. R., Tocheva, E. I., Wuichet, K., Li, Z., Chen, S., Müller, A., Iancu, C. V., Murphy, G. E., Dobro, M. J., Zhulin, I. B., & Jensen, G. J. (2009). Universal architecture of bacterial chemoreceptor arrays. *Proceedings of the National Academy of Sciences*, *106*(40), 17181–17186. https://doi.org/10.1073/pnas.0905181106

7. Bustamante, V. H., Martínez-Flores, I., Vlamakis, H. C., & Zusman, D. R. (2004). Analysis of the Frz signal transduction system of Myxococcus xanthus shows the importance of the conserved C-terminal region of the cytoplasmic chemoreceptor FrzCD in sensing signals: Signal sensing by a cytoplasmic MCP. *Molecular Microbiology*, *53*(5), 1501–1513. https://doi.org/10.1111/j.1365-2958.2004.04221.x

8. Guiseppi, A., Vicente, J. J., Herrou, J., Byrne, D., Barneoud, A., Moine, A., Espinosa, L., Basse, M.-J., Molle, V., Mignot, T., Roche, P., & Mauriello, E. M. F. (2019a). A divergent CheW confers plasticity to nucleoid-associated chemosensory arrays. *PLoS Genetics*, *15*(12), e1008533. https://doi.org/10.1371/journal.pgen.1008533

9. Guiseppi, A., Vicente, J. J., Herrou, J., Byrne, D., Barneoud, A., Moine, A., Espinosa, L., Basse, M.-J., Molle, V., Mignot, T., Roche, P., & Mauriello, E. M. F. (2019b). A divergent CheW confers plasticity to nucleoid-associated chemosensory arrays. *PLOS Genetics*, *15*(12), e1008533. https://doi.org/10.1371/journal.pgen.1008533

10. Jazleena, P. J., Das, A., Guiseppi, A., Debard, F., Sharma, J., Yaikhomba, M., Mignot, T., Mauriello, E. M. F., & Gayathri, P. (2025). Di-HAMP domains of a cytoplasmic chemoreceptor modulate nucleoid array formation and downstream signaling. *mBio*, *16*(5), e00057-25. https://doi.org/10.1128/mbio.00057-25

11. Mauriello, E. M. F. (2020). How an unusual chemosensory system forms arrays on the bacterial nucleoid. *Biochemical Society Transactions*, *48*(2), 347–356. https://doi.org/10.1042/BST20180450

12. Moine, A., Espinosa, L., Martineau, E., Yaikhomba, M., Jazleena, P. J., Byrne, D., Biondi, E. G., Notomista, E., Brilli, M., Molle, V., Gayathri, P., Mignot, T., & Mauriello, E. M. F. (2017). The nucleoid as a scaffold for the assembly of bacterial signaling complexes. *PLOS Genetics*, *13*(11), e1007103. https://doi.org/10.1371/journal.pgen.1007103

13. Ortega, D. R., Kjær, A., & Briegel, A. (2020). The chemosensory systems of Vibrio cholerae. *Molecular Microbiology*, *114*(3), 367–376. https://doi.org/10.1111/mmi.14520

14. Mauriello, E. M. F., Jones, C., Moine, A., & Armitage, J. P. (2018). Cellular Targeting and Segregation of Bacterial Chemosensory Systems. *FEMS Microbiology Reviews*. https://doi.org/10.1093/femsre/fuy015

MBio.

Article: Di-HAMP domains of a cytoplasmic chemoreceptor modulate nucleoid array formation and downstream signaling

GENERAL INFORMATION

Request ID	600240818	**Request Date**	30 Dec 2025
Request Status	Awaiting Customer Reply		

ALL DETAILS

COMMENTS

Add Comment / Attachment(s)

06 Jan 2026 4:10:51 AM, by Publisher Representative

Hello:

Thank you for your request. As one of the article authors, you retain copyright of this article and therefore do not require permission from ASM for use of the article content. Please cancel this request and thank you again.

-ASM Journals View Less

30 Dec 2025 11:01:41 AM, by APURBA DAS

I want to reprint some sections of this article as part of my thesis chapter.

Edit Request | Cancel Request